Design and Synthesis of New Ligand Scaffolds and Transition Metal Complexes for Small Molecule Activation

A DISSERTATION

SUBMITTED TO THE FACULTY OF

UNIVERSITY OF MINNESOTA

BY

Deanna Lynn Miller

IN PARTIAL FULFILLMENT OF THE REQUIREMENTS

FOR THE DEGREE OF

DOCTOR OF PHILOSOPHY

Connie C. Lu, Advisor

August 2013

Acknowledgements

First and foremost, I would like to thank my advisor, Connie C. Lu. When we decided together that I would be her first student, I don't think we knew what the next five years would bring. We had a lot of firsts together and because of this, I have learned more than I ever could have imagined. I leave the Lu group with an abundance of scientific knowledge to take with me in my future endeavors. Most importantly, I leave the Lu group with a wealth of pride for what our group has become, and an unwavering confidence in what it will become in the years to come. It was an honor to be your first student, Connie.

Next I would like to thank the past and present members of the Lu Lab. Thank you for all the helpful discussions and for always making coming to work more fun. A special thanks to Kit Zall for joining the Lu Lab with me! I couldn't have made it through everything without your help and support.

I choose to come to Minnesota not only for the science, but also because I felt that I would really get along with everyone in the department. However, I didn't know that I would be leaving Minnesota with some of the best friends I will ever have. Thank you to Emily Pelton for being my best friend and always being my rock. Thank you to my Tit for Tat Brewery ladies, Emily, Jacqui and Maria, for all the fun brewing adventures, venting sessions, lunches, coffee excursions, trips and the list goes on. Laura, I'm very glad that you decided to come to grad school at Minnesota. I don't think I could have gotten through my last two years without you as my lab and officemate. Bess and Nora, thank you for all of your help and patience while teaching me and also for all of the awesome dinners and coffee breaks!

A huge thanks to my parents for always supporting me in everything I do. I wouldn't be where I am today without them!

Finally, thank you to Chase for always being there. Thank you for uprooting your life in Kansas and moving to Minnesota with me. It was definitely a long and stressful ride, but we made it through grad school!

Table of Contents

List of Tables

Chapter 2

Chapter 3

Chapter 4

List of Figures

Chapter 1

Chapter 2

List of Schemes

Chapter 1

Chapter 2

Chapter 3

Chapter 4

List of Symbols and Abbreviations

°	degree
18-crown-6 (18C6)	1,4,7,10,13,16-hexaoxacyclooctadecane
A	hyperfine coupling constant
Å	angstrom
avg	average
B	magnetic field
Bn	benzyl
BNAH	1-benzyl-1,4-dihydropyridine
br	broad
C	celsius
C_6D_6	deuterated benzene
C_6H_6	benzene
CASPT2	complete active space second order perturbation theory
CASSCF	complete active space self consistent field
$CDCl_3$	deuterated chloroform
CH_3CN	acetonitrile
$CHCl_3$	chloroform
cm	centimeter
cm^{-1}	wavenumber
CTV	cyclotriveratrylene
CV	cyclic voltammetry
d	density
d	doublet
D	zero-field splitting
d_6-DMSO	deuterated dimethyl sulfoxide
d_8THF	deuterated tetrahydrofuran
DCM	dichloromethane
dd	doublet of doublets
DFT	density functional theory
dH2O	distilled water
DHP	dihydropyridine
DMA	dimethylacetylamide
DME	dimethyloxyethane
DMF	dimethylformamide
DMSO	dimethylsulfoxide
dt	doublet of triplets
E/D	rhombicity
E°	standard electrode potential
$E_{1/2}$	reversible process
EBO	effective bond order
EFG	electric field gradient
E_{pa}	irreversible oxidation

E_{pc}	irreversible reduction
EPR	electron paramagnetic resonance
ESI-MS	electron spray ionization mass spectrometry
Et_2O	diethyl ether
EtOAc	ethyl acetate
FBO	formal bond order
Fc	ferrocene
g	gram
g	anisotropic *g* factor
G	Gauss
g_{eff}	effective g factor
GHz	gigahertz
HCl	hydrochloric acid
HRMS	high resolution mass spectrometry
hrs	hours
I	nuclear spin quantum number
^{i}Pr	isopropyl
J	coupling constant
K	Kelvin
kcal	kilocalorie
keV	kiloelectron volt
KH	potassium hydride
LMCT	ligand to metal charge transfer
m	multiplet
M	molarity
m/z	mass-to-charge ratio
Me	methyl
MeOH	methanol
mes	mesityl
mg	milligram
MHz	megahertz
min	minute
mL	milliliter
MLCT	metal to ligand charge transfer
mm	millimeter
mM	millimolar
mmol	millimole
MO	molecular orbital
mol	mole
m_s	electron spin quantum number
mV	millivolts
mW	milliwatts
NA	nicotinamide
NAD+	nicotinamide adenine dinucleotide

NADH	dihydronicotinamide adenine dinucleotide
NEt_3	triethylamine
NHE	normal hydrogen electrode
NIR	near infrared
nm	nanometers
NMR	nuclear magnetic resonance
pH	negative logarithm of hydrogen ion concentration
Ph	phenyl
pKa	pK for association
PPG	polypropylene glycol
PPh_4Cl	tetraphenylphosphonium chloride
ppm	parts per million
q	quartet
r	covalent ratio
reflns	reflections
r_M	covalent radii of metal (M)
rt	room temperature
s	singlet
s	second
S	spin state
s^{-1}	frequency
SQUID	superconducting quantum interference device
T	temperature
t	triplet
T	Tesla
TAME	1,1,1-tris(aminomethyl)ethane
$TBAPF_6$	tetrabutylammonium hexafluorophosphate
THF	tetrahydrofuran
TOF	time of flight
tren	tris(2-aminoethyl)amine
UV	ultraviolet
V	volts
V	volume
vis	visible
vs	versus
W	width
Z	number of independent structures in unit cell
δ	chemical shift
δ	isomer shift
ΔE_Q	quadrupole splitting
Δf'	Real component of the anomalous scattering factor
Δf''	Imaginary component of the anomalous scattering factor
ΔG°	Gibb's free energy
ε	molar absorptivity

θ	degrees of data collection
λ	wavelength
λ_{max}	maximum absorbance wavelength
μ	bridging
μ	absorption coefficient
μ_B	Bohr magnetons
μ_{eff}	effective magnetic moment
μL	microliter
μM	micromolar
π	pi
σ	sigma

Chapter 1

Introduction

1.1 Small Molecule Activation

1.1.1 Environmental Impact

World population is projected to increase over 20% in the upcoming years, reaching 9 billion by 2050.[1] With a growing population comes an increase in demand for energy as well. In the US, 82% of the total energy consumption is derived from fossil fuels, a supply chain that is finite and depleting rapidly. The decline of fossil fuels makes the development of new catalysts to generate energy rich chemicals, such as ammonia (NH_3), hydrogen (H_2), and methanol (CH_3OH), on an industrial scale necessary and urgent. Ideally, these useful chemical commodities would be generated from abundant and/or renewable feedstocks such as dinitrogen (N_2), water (H_2O), and carbon dioxide (CO_2).

Furthermore, the burning of fossil fuels generates CO_2, the most abundant greenhouse gas in our atmosphere.[2] Rising levels of greenhouse gases from human activity has provoked many researchers to study the sequestration and transformation of CO_2 into more useful chemical products, including CH_3OH, which has been identified as an alternative fuel source.[3,4] Industrially, CO_2 is hydrogenated to form carbon monoxide (CO) for its use as synthesis gas (syngas, CO/H_2) in the Fischer-Tropsch process to produce hydrocarbon fuels.

Another small molecule of interest is dinitrogen, as it is an abundant precursor for the production of NH_3. In 2010, 131 million metric tons of NH_3 were produced industrially, mainly for use as a fertilizer. The majority of ammonia is produced using the Haber-Bosch process: N_2 is hydrogenated using three equivalents of molecular hydrogen

(H_2). An iron catalyst is employed to drive the scission of the strong N_2 triple bond and facilitate the hydrogenation. Higher temperatures and pressures of hydrogen are also required to efficiently effect this difficult conversion.

The underlying issue with current industrial systems used to transform the small molecules of interest into more useful chemicals is the need for hydrogen as a co-reactant. Over 80% of bulk hydrogen is produced from the steam reformation of natural gas (***Eqn 1)***, coupled with the water gas-shift reaction (***Eqn 2***).[5]

$$CH_4 + H_2O_{(g)} \rightarrow CO + 3H_2 \quad (\boldsymbol{Eqn\ 1})$$

$$CO + H_2O_{(g)} \rightarrow CO_2 + H_2 \quad (\boldsymbol{Eqn\ 2})$$

While the catalysts utilized to carry out these reactions are efficient and cheap, the starting material, natural gas, is limited in supply. Moreover, the byproduct of these reactions is CO_2, which does not fit into a clean-energy future.

The desire for the production of clean energy drives the development of catalysts that can transform abundant molecules like CO_2 and N_2 into the chemicals necessary to provide the energy for human activity. However, these transformations are extremely difficult, given the strength of the chemical bonds in CO_2 and N_2.

1.1.2 Thermodynamics of Small Molecule Activation

The strong bonds of CO_2 and N_2 are difficult to reduce in one-electron steps. It is well established that the reduction of these molecules by multiple equivalents of protons and electrons in a single step is more thermodynamically favorable.[6-8] As shown in Figure 1.1, increasing numbers of protons and electrons added in one step causes the reduction potential to become more favorable (i.e. more positive).[9,10] The one-electron

reduction of CO_2 to form a CO_2 radical anion has a high energy cost, with a very negative reduction potential of -1.90 V. By adding two protons and two electrons at the same time, the reduction potential becomes milder at -0.61 V to generate formic acid (HCO_2H), and -0.53 V to generate CO and H_2O, which are 1.29 V and 1.37 V more favorable, respectively, than the one-electron reduction of CO_2. Arguably, the most useful single carbon chemical product from the reduction of CO_2 is CH_3OH. The reduction potential for the formation of CH_3OH can be fairly mild (-0.38 V) when six protons and electrons are added in one step. For the reduction of N_2, the most desired product, NH_3, is also the most thermodynamically favored product, with a reduction potential of 0.16 V. The thermodynamic advantage of adding multiple protons and electrons simultaneously is clear and provides a strong motivation for the development of catalysts that can support such processes.

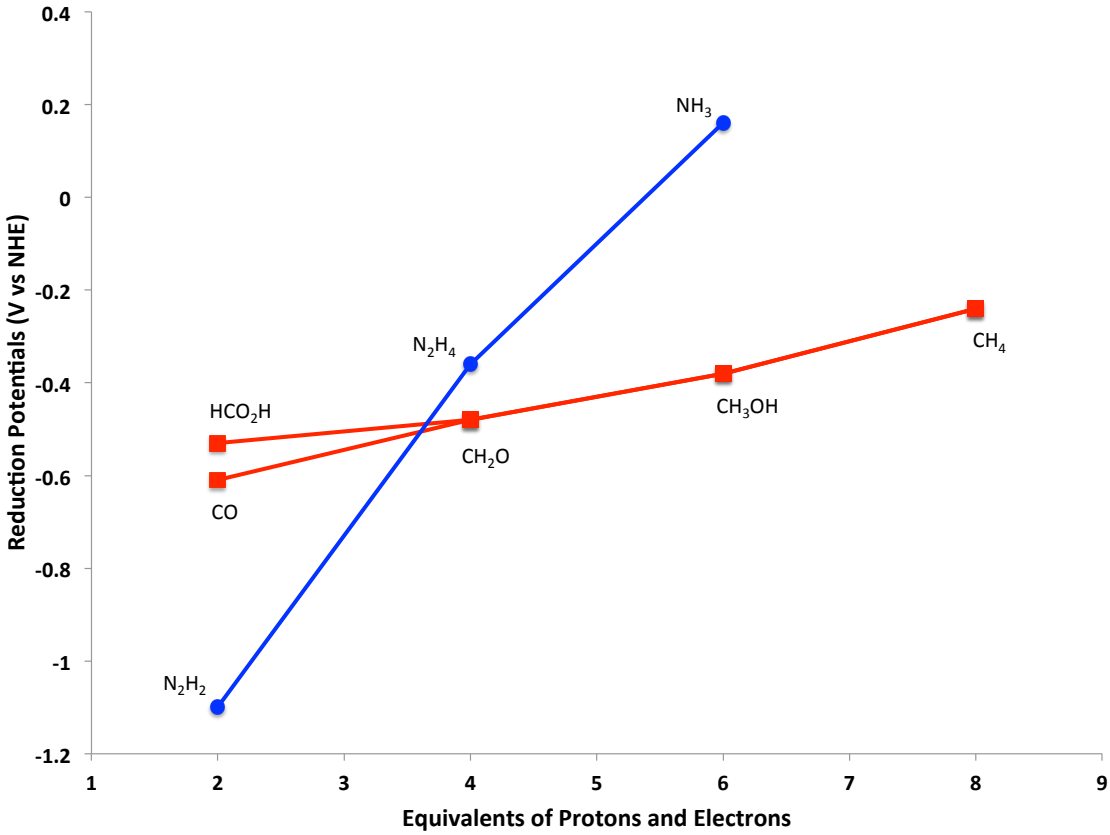

Figure 1.1 Reduction potential profile of CO_2 and N_2 versus the number of added protons and electrons. All reduction potentials are referenced to NHE at pH 7.[9,11]

However, developing catalysts to deliver multiple equivalents of protons and electrons is challenging. The use of first-row transition metals is desired because they are cheaper and more abundant than precious metals. One immediate issue is the tendency of first row transition metals to undergo one-electron redox events (e.g. Fe^{II}/Fe^{III} or Cu^{I}/Cu^{II}) instead of the more desirable two-electron (or more) redox processes. Metalloenzymes are nature's most efficient catalysts and utilize transition metal active sites to catalyze difficult transformations, such as the reduction of N_2 to NH_3. Although the transition metal is essential for enzymatic activity in metalloenzymes, the ligands

coordinating the transition metal and the secondary coordination sphere of the enzyme are also vital to the activity.

In order to facilitate small molecule activation using homogeneous first-row transition metal complexes, ligand design is of utmost importance. Historically, researchers have utilized many different ligand scaffolds to synthesize transition metal catalysts. Three strategies for effecting small molecule activation will be discussed herein: *(1) steric protection of a reactive metal center, (2) non-innocent functional group cooperation, and (3) using multiple transition metal centers.*

1.2 Current Synthetic Strategies for Small Molecule Activation

1.2.1 Steric Protection

Perhaps the best homogenous system for the reduction of N_2 to NH_3 hails from the laboratory of Richard Schrock. The system, a sterically protected, tris(arylamido)amine (aryl = 3,5-(2,4,6-*i*-$Pr_3C_6H_2)_2C_6H_3$) molybdenum complex, successfully reduces dinitrogen to ammonia under ambient pressure and temperature with 66% efficiency in four turnovers.[12,13] Before catalysis with sterically demanding ligands was realized, a series of molybdenum complexes were synthesized with a less sterically hindered tris(arylamido)amine (aryl = 4-*tert*-butylC_6H_4). The complexes bind dinitrogen upon reduction of the Mo(IV)Cl (**1**), forming a dimolybdenum bridging dinitrogen complex (**2**) (Scheme 1.1).[14,15] Increasing the steric bulk of the aryl group to terphenyl substituents allows for the functionalization of the dinitrogen adduct with electrophiles,

such as trimethylsilyl chloride (Me_3SiCl) and methyl tosylate (MeOTs), to form activated dinitrogen complexes **3** and **4**.[15]

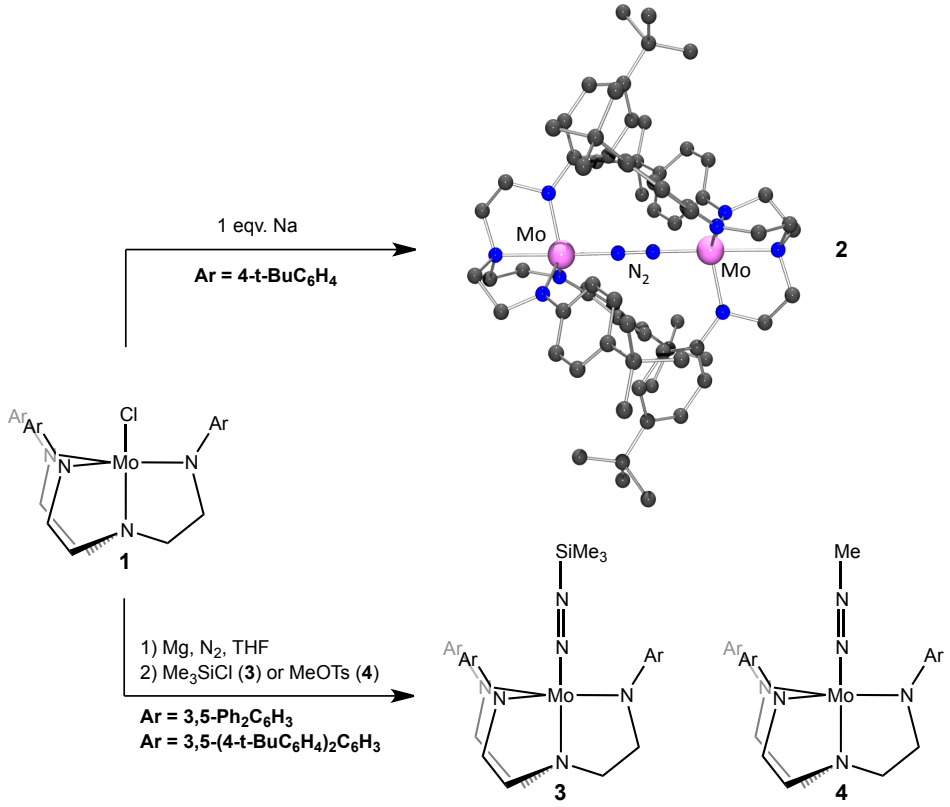

Scheme 1.1 Synthetic pathways to molybdenum dinitrogen complexes.[15]

In order to achieve catalytic dinitrogen reduction, the aryl substituents must be even bulkier. To do this, three isopropyl groups were added onto the phenyl groups of the terphenyl substituent (aryl = HIPT = 3,5-(2,4,6-*i*-$Pr_3C_6H_2)_2C_6H_3$) (Figure 1.2). The additional bulkiness allowed for the isolation of a mononuclear Mo(III) end-on dinitrogen complex (**5**).[12,13] The bound dinitrogen can be reduced to ammonia by mimicking the cycle initially proposed by Chatt for the stepwise addition of protons and electrons (Figure 1.2).[16] The sterically bulky molybdenum complex is, to date, the most efficient catalyst for N_2 reduction, second only to the metalloenzyme nitrogenase.[17]

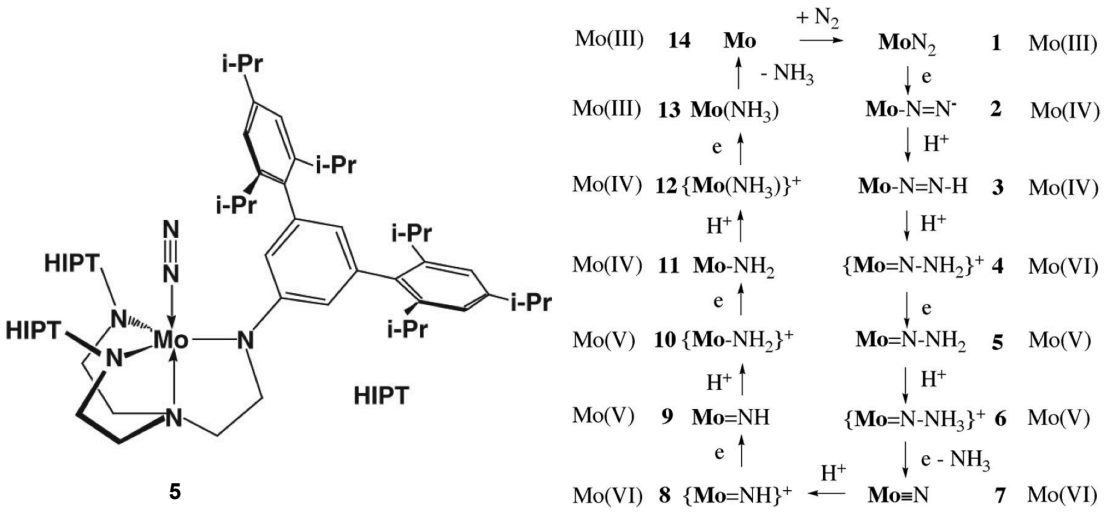

Figure 1.2 Mononuclear Mo(III) N_2 complex utilized in catalytic reduction of N_2 (left), and proposed intermediates in the reduction of N_2 at the Mo metal center through the stepwise addition of protons and electrons (right).[13]

Another example that displays the importance of ligand sterics in small molecule activation is the stoichiometric reaction between CO_2 and an electron rich tri(alkoxy)triazacyclononane uranium(III) complex.[18] The reduction of CO_2 is often plagued by bimolecular decomposition reactions, such as the loss of CO to form a M(μ-O)M species or the coupling of two CO_2 molecules to form oxalate. While formation of these products demonstrate CO_2 reduction, further reduced products, such as CH_3OH and CH_4, are more desirable, due to their potential use as fuel sources.[19,20] Meyer *et al*. observed that the reactivity of the electron rich uranium(III) complex (**6**) is determined by the sterics of the ligand (Scheme 1.2). When the R group is a *tert*-butyl substituent, a bimolecular reaction is observed via the formation of a stable diuranium μ-oxo bridged complex **7** and the loss of CO. Increasing the bulkiness of the ligand scaffold to an adamantyl group prevents the bimolecular reaction, favoring the formation of a linearly bound $CO_2^{\bullet-}$ (**8**).[21] Although further reactivity is not realized with this unique, linearly

bound CO_2 radical anion, it is proposed that this binding mode could lead to other carbon dioxide reduction products. Both of these examples of small molecule activation with transition metal complexes are strictly controlled by the sterics of the ligand environment, lending to the importance of ligand design in homogeneous catalysis.

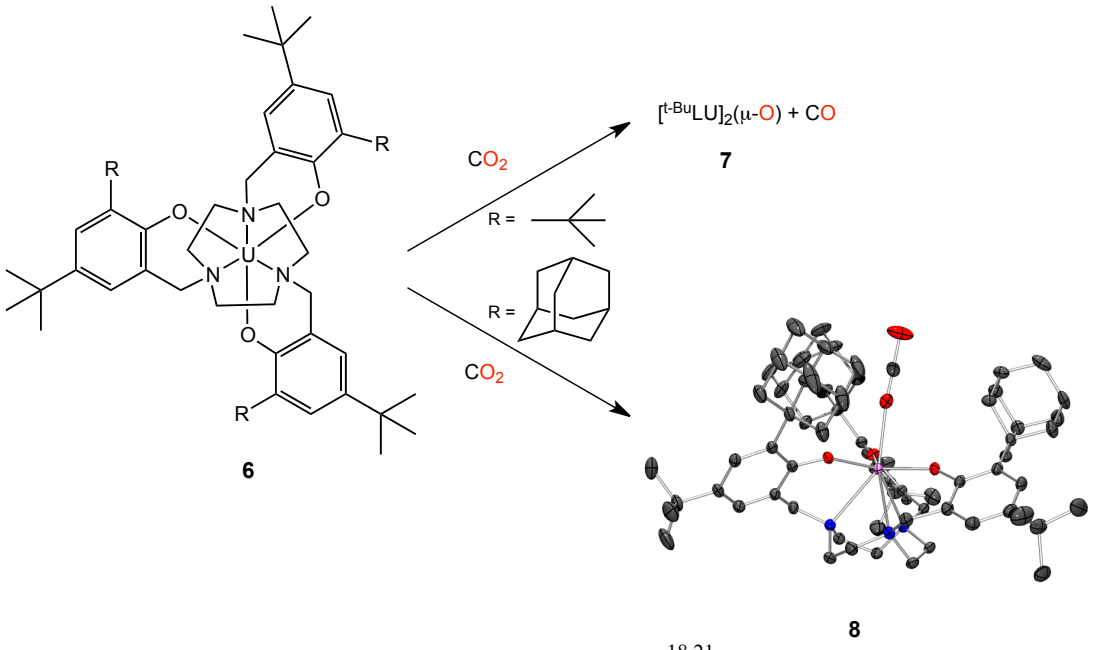

Scheme 1.2 Reactivity of U(III) complexes with CO_2.[18,21]

1.2.2 Ligand Functional Group Cooperativity

Recently, a nickel electrocatalyst was shown to have high turnover frequencies (>100,000 s^{-1}) for the production of H_2 from acid.[22] At the time of this report, it is the highest turnover frequency reported for H_2 production, even higher than the value reported for [FeFe] hydrogenase (9000 s^{-1}).[23] The key to the activity of these catalysts is the ligand design. Studies performed on various hydrogenase metalloenzymes suggest that an amine base situated close to the enzyme active site is responsible for acting as a proton relay to promote the production of H_2 (Figure 1.3a).[24]

Using nature as a guide, DuBois and coworkers have developed and tuned a variety of nickel electrocatalysts to efficiently produce H_2.[22,25-27] The pendent amines built into the phosphine ligand scaffold employed by DuBois have been shown to act as proton relays in the catalytic cycle.[28] The first generation of nickel electrocatalysts were ligated by a binucleating phosphine ligand with two pendant tertiary amines ($[NiP^R_2N^{R'}_2]^{2+}$) (Figure 1.3b). Catalytic activity with these first generation catalysts was realized with turnover frequencies around 1000 s^{-1}.[25] Theoretical calculations revealed the transition state for H_2 formation to be heterolytic in nature (Figure 1.3c). Mechanistic studies have revealed that this state is in equilibrium with a doubly protonated form, where the two protons are located on the pendant amines. However, when the two protonated amines are on opposite faces of the nickel, they have difficulty reaching the transition state (Figure 1.3c). Hence, it was proposed that removing one of the pendant amines on each ligand may shut down formation of these doubly protonated isomers and thus increase catalytic activity.[22]. Figure 1.3d displays the structure of the most active H_2 production catalyst to date, with only one pendant amine per diphosphine. This minor change to the ligand scaffold increased the catalytic activity for the production of H_2 100-fold.

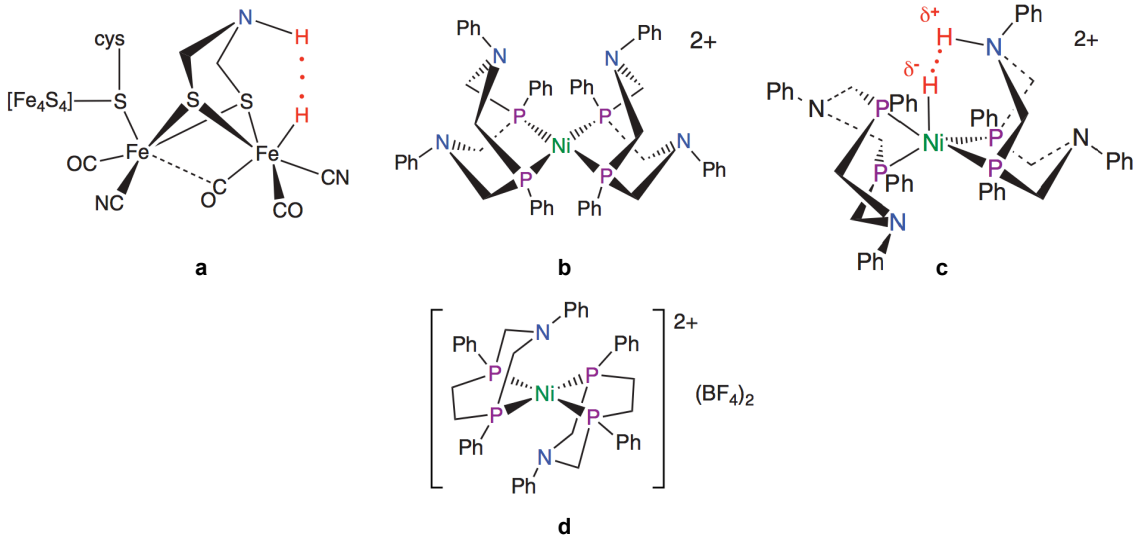

Figure 1.3 (**a**) Proposed structure of active site for [FeFe] hydrogenase.[24] (**b**) First generation nickel electrocatalyst active for H_2 production (1000 s^{-1}).[25] (**c**) Proposed transition state for the formation of H_2.[29] (**d**) Second generation nickel electrocatalyst capable of H_2 production with record turnover frequencies (>100,000 s^{-1}).[22]

Another great example of functional group cooperativity is displayed by a family of ligands, designed and synthesized by the Borovik group, with urea functionalities that act as a hydrogen-bonding cavity. A clear example of how changes in the ligand scaffold affects reactivity is displayed by a cobalt(II) complex supported by trianionic ligands with varying numbers of urea moieties.[30] When no urea substituents (i.e. no H-bonding groups) are present on the ligand scaffold, the Co(II) complex does not react with excess O_2. Modification of one ligand arm to a urea functionality changes the reactivity of the Co(II) complex with O_2 (Scheme 1.3). For example, exposure of cobalt complex **9** to excess O_2 shows spectroscopic evidence for reversible O_2 binding. Although not isolable, spectroscopic studies indicate formation of features associated with Co(III)-OH complexes.

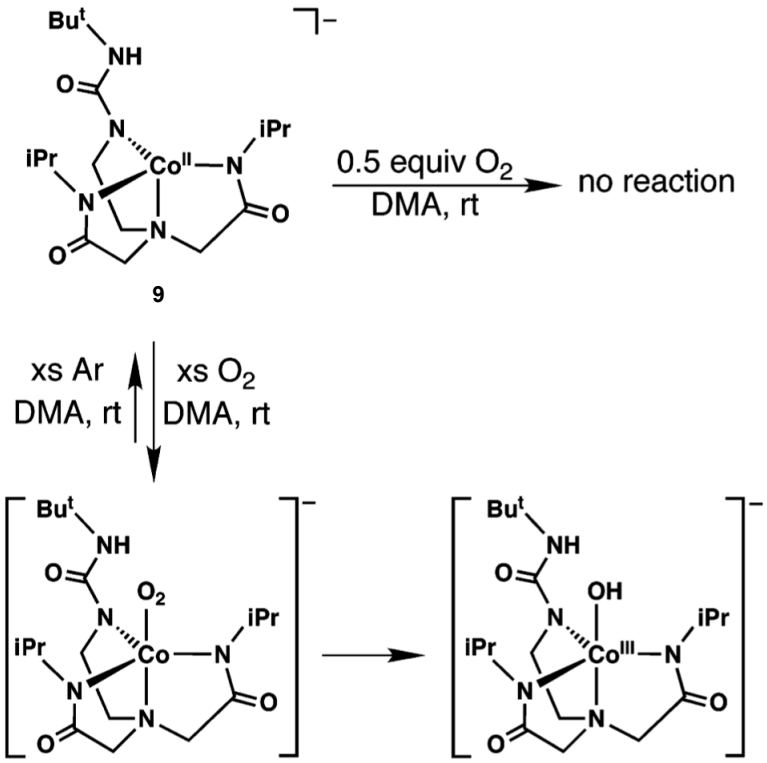

Scheme 1.3 Reaction of Co(II) complex supported by monourea ligand scaffold with O_2.[30]

When two or more urea groups are present in the ligand, reaction of Co(II) complex **10** with stoichiometric O_2 quantitatively yields a Co(III)-OH (**11**) (Scheme 1.4). This change in reactivity based on the number of urea groups present suggests that the hydrogen-bonding cavity is necessary to support the Co(III)-OH moiety.[30]

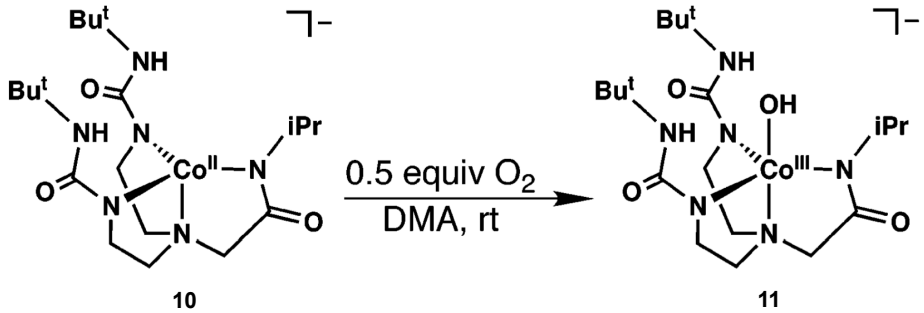

Scheme 1.4 Reaction of Co(II) complex supported by bisurea ligand scaffold with O_2.[30]

By capitalizing on these unique urea ligand scaffolds, a Mn(II) complex supported by a modified urea ligand scaffold has been shown to catalytically reduce O_2 to H_2O at room temperature with 1,2-diphenylhydrazine (DPH) as the hydrogen source (Figure 1.4).[31] Other Mn(II) complexes have been synthesized using the same ligand sets as the Co(II) complexes described above, and they also activate O_2 to form Mn(III)-OH complexes.[32] However, catalytic activity was not realized until the ligand was modified to be a dianionic ligand instead of a trianionic ligand. Thus, the urea functionalities are important in the catalytic cycle, as they are proposed to support the Mn(III)-oxo formed through hydrogen bonding. The solid-state structure of the Mn(III)-oxo complex is shown as part of the catalytic cycle in Figure 1.4.

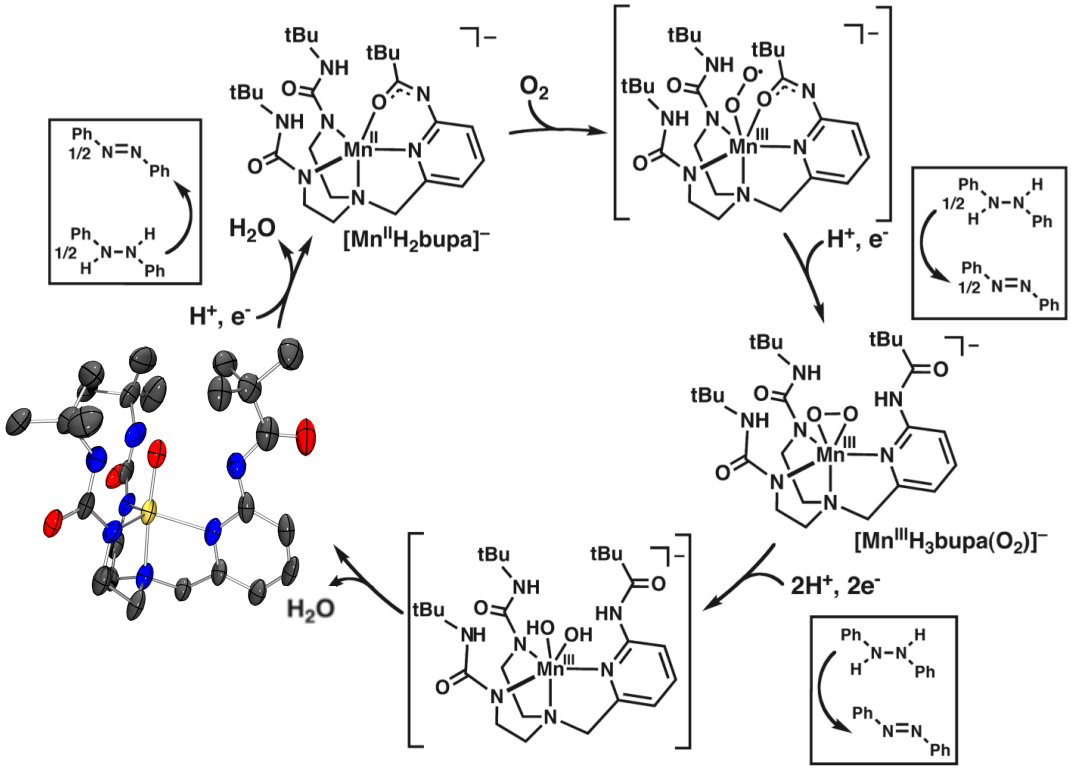

Figure 1.4 Catalytic cycle for reduction of O_2 to H_2O. Inset: Solid-state structure of Mn^{III}-oxo stabilized by hydrogen bonding, with hydrogen atoms omitted for clarity.[31]

1.2.3 Multi-metallic Approaches

In biology, metalloenzymes often employ multiple metal centers to effect multi-electron small molecule activation.[17,33-36] Challenges in this field include the controlled synthesis of multi-metallic complexes and achieving cooperative multi-electron reactivity. Betley and coworkers have synthesized families of iron, cobalt, and manganese trimetallic[37-42] and hexametallic[43] complexes and studied their reactivity toward small molecules. More recently, they have explored hetero-multimetallic complexes of iron and cobalt.[40] One hexairon complex (**12**) in particular can reduce six equivalents of nitrite ($[NO_2]^-$) to form a hexairon nitrosyl complex (**13**) in the presence of a proton source (Scheme 1.5).[43] Furthermore, the redox properties of many of the multi-metallic complexes synthesized by Betley and coworkers are extremely rich and span a large range of potentials, making their potential for multi-electron redox exciting.[44]

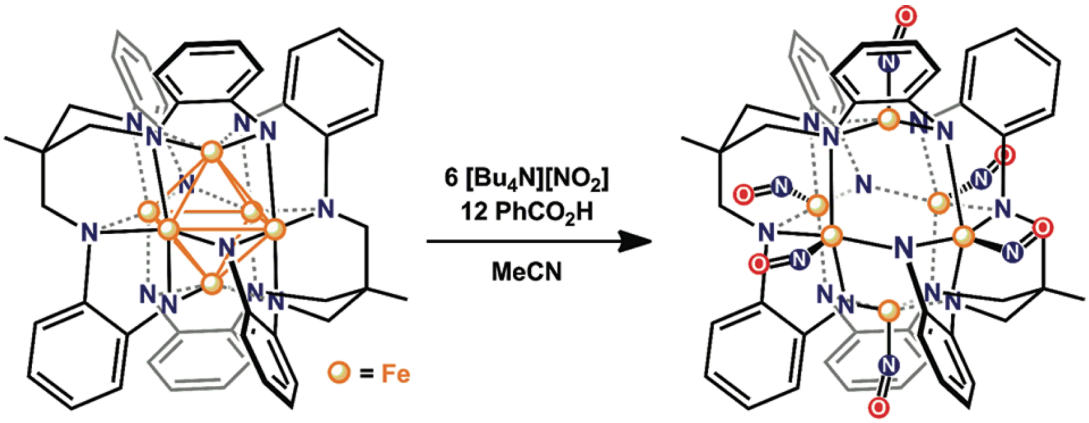

12 **13**

Scheme 1.5 Reaction of $[Fe^{II}]_6$ with NO_2^- to yield a hexairon nitrosyl complex.[43]

The Thomas laboratory has focused most of their efforts on synthesizing heterobimetallic complexes. One complex, an early-late heterobimetallic multiply bonded Zr-Co complex **14**, shows promising multi-electron reactivity with CO_2. The solid-state

structure of the product reveals that the CO_2 oxidatively adds across the Zr-Co bond to form an end-on CO bound to the cobalt metal center and a bridging oxide between the cobalt and zirconium metal centers (Scheme 1.6). A second equivalent of reductant, both in the presence and absence of more CO_2, yields rearranged products, but no reactivity to further reduce the CO or scavenge the oxide has been realized. The multiply bonded Zr-Co can use the electrons stored in the multiple bond to effectively reduce small molecules.

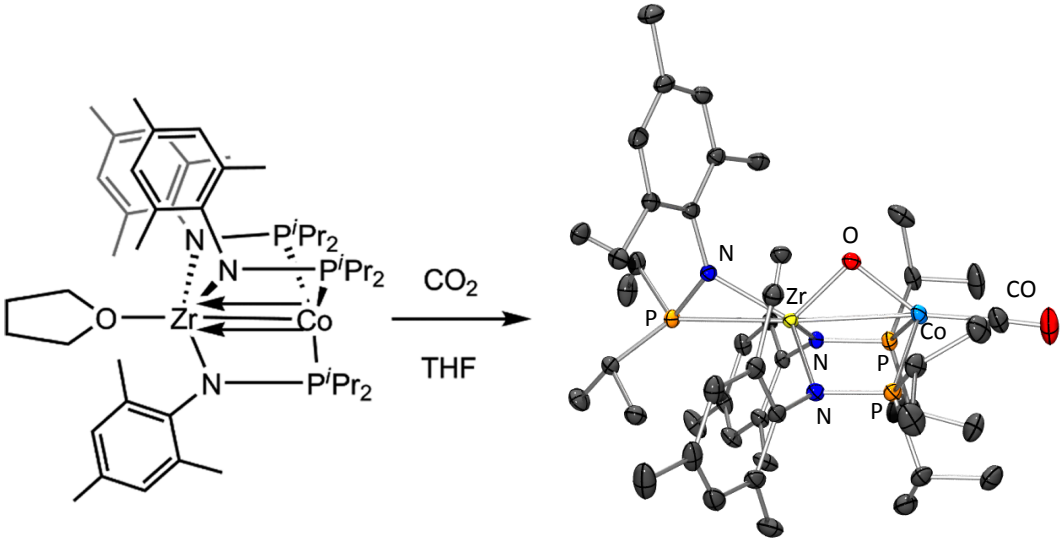

Scheme 1.6 Reaction of a heterobimetallic Zr-Co complex **13** with CO_2. The solid-state structure of Zr-Co product **14** is shown with hydrogens omitted for clarity.[45]

Another example of a metal-metal multiply bonded complex that can effect small molecule reactivity is a ditungsten complex (**15**) synthesized by the Berry group. Tetragonal ditungsten complexes **15** and **16** are supported by four monoanionic pyridyl amidinate ligands. Reaction of the ditungsten complex with oxo transfer reagents results in the formation of a ditungsten oxo **17** (Scheme 1.7). X-ray crystallography and resonance Raman spectroscopy indicate that **17** is a triply bonded tungsten oxo moiety.

Monometallic tungsten oxo complexes typically have a very strong bond and do not effect oxo transfer to organic compounds, but **17** reacts with alkyl phosphines to regenerate the multiply bonded ditungsten complex **15** and a trialkylphosphine oxide. Addition of the second metal to form a multiply bonded ditungsten complex allows for a four electron reduction process to proceed, while monometallic tungsten oxos are known to be unreactive.

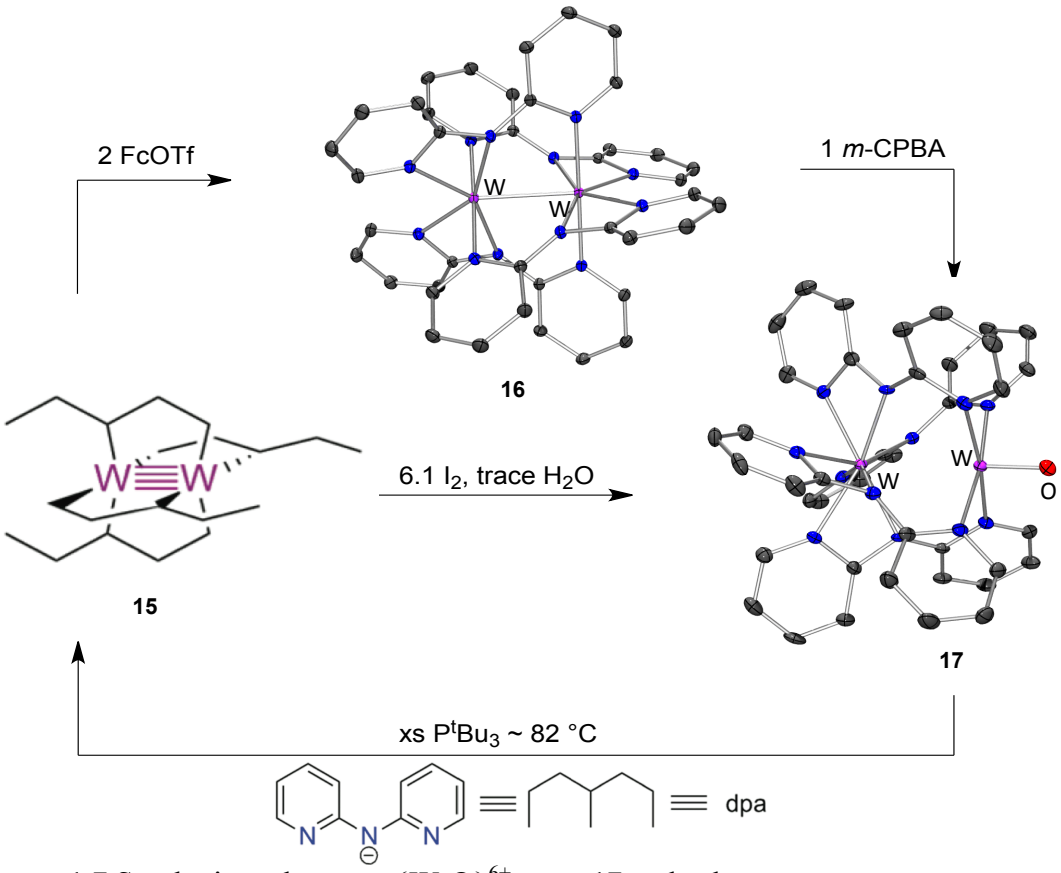

Scheme 1.7 Synthetic pathway to $\{W_2O\}^{6+}$ core **17** and subsequent oxygen atom transfer to P^tBu_3 to reform ditungsten **15**.[46]

1.3 Scope of Thesis

The objective of this thesis is to explore the synthesis of new ligand scaffolds designed to support late first row transition metals and to study their potential for small molecule activation. Many researchers have utilized sterically encumbered ligands to protect reactive metal centers. In the second chapter, the design and synthesis of novel cage ligands featuring a hydrophobic cavity to provide protection to reactive metal centers will be explored. Ideally, the cavity will effectively prevent bimolecular decomposition reactions that often plague small molecule activation. The synthesis and characterization of two cage ligands, a trianionic tri(amido)amine and a neutral tri(amino)amine variant, will be presented. Additionally, the preparation and characterization of the zinc(II) complex of the tri(amido)amine cage ligand will be discussed and its uptake of small molecules explored.

In addition to employing protection of reactive metal centers in ligand design, a bio-inspired ligand design will be explored. The biological cofactor dihydronicotinamide adenine dinucleotide (NADH) can efficiently reduce and oxidize substrates through the transfer of a hydride (or a proton and two electrons). The third chapter explores the design and synthesis of a NADH-type ligand scaffold. The systems presented herein have three NADH-like moieties built into the ligand, designed to reduce substrates via either hydride transfer or proton coupled electron transfer. Having three NADH moieties allows for the possibility of multi-electron redox chemistry. The synthesis and characterization of zinc(II) and cobalt(II) complexes will be discussed. Additionally, the reaction of both

the NADH ligand and the zinc(II) complex with known hydride acceptors will be explored.

Finally, in chapter four, the synthesis and characterization of a family of diiron and iron cobalt bimetallic complexes with a third type of ligand design will be presented. Previous work in the Connie Lu group has shown reactivity toward small molecules using heterobimetallic complexes supported by a tripodal phosphine amide ligand scaffold. Herein, the same ligand scaffold is applied to late transition metals to explore their synthesis, reactivity toward small molecules, and electronic and magnetic properties to allow for a better understanding of metal-metal bonding interactions.

Chapter 2

Design and Synthesis of Cage Ligands with Unique Hydrophobic Cavity

In part from:

Miller, D. L.; Lu, C. C. Encapsulating Zinc(II) Within a Hydrophobic Cavity. *Dalton Trans.* **2012**, *41*, 7464-7466.

2.1 Overview

A new family of macrobicyclic cage ligands was synthesized featuring a hydrophobic pocket. The synthesis of tri(amido)amine cage ligand **4** was achieved through both a convergent and a linear synthetic route. Despite the success of the convergent route, the linear route utilized a pyridyl thioester leaving group and improvement to yield and isolation of **4** was realized. Tri(amino)amine cage ligand **9** was synthesized by modifying the linear route to **4**. A zinc complex (**10**) was synthesized from tri(amido)amine cage ligand **4** and zinc dichloride. A complementary theoretical study on the cavity size of different cage ligands was also completed. The synthesis and characterization of tri(amido)amine cage ligand, tri(amino)amine cage ligand, and the zinc complex are reported herein.

2.2 Introduction

Metalloenzymes, some of nature's most efficient catalysts, are often mimicked by synthetic chemists hoping to gain an understanding of the reactivity and achieve comparable reactivity by modeling the structure of the metal binding pocket as well as the secondary coordination sphere.[1] The enzymatic pocket is intricately tuned to assist the transition metal active site to efficiently transform otherwise highly inert small molecules into useful products. For example, nitrogenase enzymes can efficiently catalyze the reduction of dinitrogen (N_2) to ammonia (NH_3).[2-5] Historically, when modeling enzyme active sites, chemists often rely on sterically bulky ligand systems in an attempt to isolate reactive complexes. In some cases, formation of dinuclear complexes stunt reactivity and

sterically hindering ligands must be utilized in order to isolate the reactive mononuclear complexes. For example, sterically bulky ligands are vital in the state of the art dinitrogen reduction catalyst by Schrock and coworkers (*vide supra*).[6,7]

Unfortunately, too much steric protection of the metal center can inhibit reactivity by limiting substrate access or even preventing the synthesis of the desired complex. Using an encapsulating, macrobicyclic ligand framework would enable the synthesis of monomeric, active species but still allow for substrate access. A few different types of encapsulating ligand systems, or cage ligands, have been extensively studied for a variety of applications including host-guest chemistry, catalysis, and molecular recognition chemistry. Herein we will focus only on cage ligands that utilize tris(2-aminoethyl)amine (tren) in combination with a protective cap to generate the cage ligand.[8,9]

Coupling two tren ligands together with an organic linker in between yields a class of binucleating cage ligands called hexaamino-cryptands; these ligands are derivatives in the general family of cryptands, known most notably for cation sequesteration.[10-12] Hexaamino-cryptands were studied for their use in host-guest chemistry and transition metal catalysis after the development of a one-pot synthesis via a cyclic [2+3] Schiff-base condensation by Nelson *et al*.[13] Since this development, a variety of hexaamino-cryptands have been synthesized with linkers such as furans, thiophenes, benzenes, benzyls, napthalenes, pyridines and many more.[13-15] The transition metal chemistry of hexaamino-cryptands and their reduced octaamino counterparts has mostly focused on late transition metals suitable for a neutral, tetradentate binding pocket such as copper.[16] Recently, Nocera and co-workers have synthesized a family of bimetallic

manganese, iron, cobalt, nickel and zinc complexes supported by a hexaanionic hexacarboxamide cryptand cage ligand (Scheme 2.1).[17-19] Interestingly, the iron and cobalt complexes can bind cyanide ($[CN]^-$) in the cavity between the two metals despite the small size of the cavity (M-M distance (Å): Fe-Fe, 6.30; Co-Co, 6.41). Furthermore, the distance between the two metals is contracted upon binding the $[CN]^-$ ligand to 5.39 and 5.33 Å for the iron and cobalt complexes, respectively.

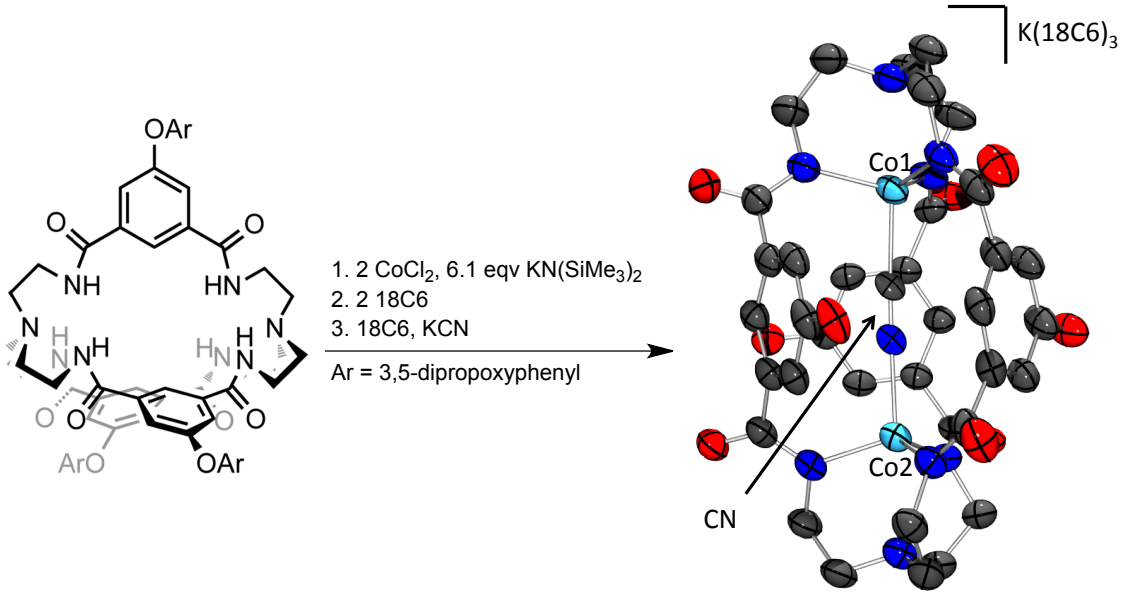

Scheme 2.1 Synthetic route to a dicobalt cyanide complex by Nocera *et al.* Solid-state structure shown with Ar groups, K, and 18C6 removed for clarity.[17]

Calix[6]arenes have also been widely used in host-guest chemistry, however their conformational flexibility due to facile ring inversion has presented obstacles.[20] Recent strides to overcome this obstacle have utilized tren to increase the rigidity of the calix[6]arene and constrain it to a cone conformation for more efficient and selective substrate binding (Figure 2.1). Calix[6]tren has been shown to coordinate Zn^{2+} and in turn the zinc complex has been shown to bind a variety of substrates.[21] Calix[6]tren can also coordinate copper and bind water, nitriles, carbon monoxide and dioxygen.[22] More

interestingly, host-guest chemistry is observed with the ligand alone. The charge of the ligand can be modulated by protonating the tren nitrogens. When only the apical amine is protonated the cavity attracts charged organic molecules such as ammonium ions. When the ligand is fully protonated, neutral organic molecules are attracted such as alcohols and dimethylforamide (DMF).[23].

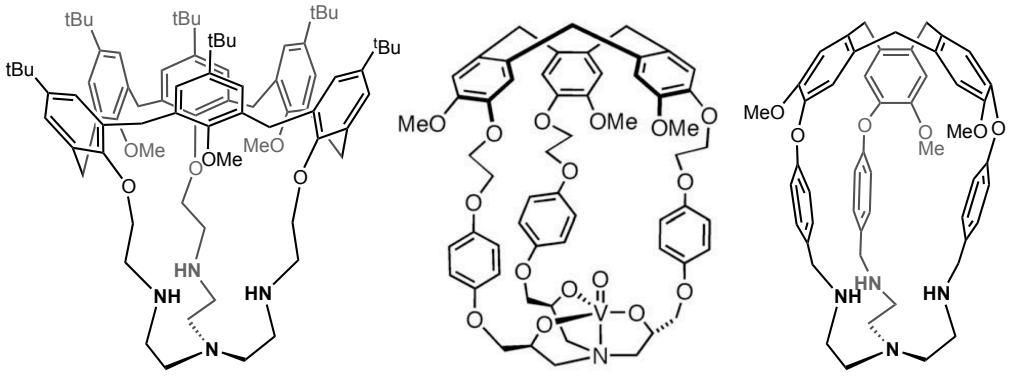

Calix[6]tren Hemicryptophane

Figure 2.1 Examples three macrobicyclic ligand systems.[23,24]

Cryptophanes represent another class of supramolecular catalysts and host-guest cage molecules. Cryptophanes have been used to encapsulate methane and for chiral selectivity in guest incorporation.[25] Dustasta and co-workers have synthesized a catalytically active hemicryptophane-oxovandium(V) complex by integrating a trialkanolamine unit with the traditional cryptophane unit cyclotriveratrylene (CTV).[26] The hemicryptophane vanadium complex is 6 times more catalytically active in the oxidation of sulfide to sulfoxide than a model complex without a cavity feature.[27,28] This result prompted the expansion of the hemicryptophane class to include tren as the metal coordination site.[29]

Despite improved reactivity of the hemicryptophane metal complexes, syntheses are time consuming, many steps, and extremely low yielding (overall 3%).[24] To combat this, Dustasta and co-workers developed a modular and efficient synthesis for these hemicryptophanes. An improved synthetic route to an aldehyde-containing CTV cap enabled the advancement of hemicryptophane synthesis.[30] Using the aldehyde-containing cap, a condensation reaction was used to couple the cap to the tren, followed by reduction of the resulting imine with sodium borohydride, which proceeded in high yields (77%). This convergent route improved the overall yield to 8% and more importantly reduced the number of steps in the synthesis from seven to four.[29] Dustasta and co-workers exploited the modularity of their new synthesis and developed seven new hemicryptophane cage ligands. Modifications of the linkers between the CTV and tren moieties will allow for a comparison of cavity volume and host-guest selectivity studies, which are currently on going.[29] With the exception of one naphthalene linker, all of the linkers included one benzene ring with substituents in varying positions and having varying electronic properties. The different substituents on these new hemicryptophanes should provide interesting comparisons in host-guest chemistry; however, what is lacking in this area is a comprehensive study of how the height of the cavity affects the ability of cage ligands to encapsulate small molecules.

Herein is a cooperative theoretical and synthetic study aimed at the design and synthesis of novel cage ligands. The theoretical study allows for a comprehensive picture of the factors that affect the cavity height and informs which ligands to target for

synthesis. Furthermore, a new synthetic strategy is realized, improving the overall yield for the synthesis of such cage ligands to 30%.

2.3 Results and Discussion

2.3.1 Theoretical Calculations

Density functional theory (DFT) calculations were performed on a variety of proposed cage ligands to gain insight on the cavity height in order to determine an appropriate synthetic target.[31,32] Two different metal binding pockets, tren and 1,1,1-tris(aminomethyl)ethane (tame) were investigated due to their rich coordination chemistry.[8,9] As previously discussed, similar ligand frameworks have utilized heteroatom-carbon linkages to ease the synthetic difficulties, however, heteroatom-carbon linkages are not always stable to reagents utilized in reactivity studies (e.g acids).[20,26,33] Thus, we desired a more robust cap for our cage ligands. One ligand cap that was envisioned consists of an apical aryl ring ("aryl cap") with three alkyl chains in the 1, 3, and 5 positions that each connect to a second aryl ring ("aryl arm"). Figure 2.2 displays two of the proposed cage ligands. We propose that changing the number of methylene linkers in the alkyl chain between the aryl cap and the aryl rings in the ligand arms should alter the size of the cavity. The nomenclature used to described the proposed cage ligands is as follows: identity of the metal binding pocket, e.g. tren versus tame, followed by the linker between the pocket and aryl arm, and finally the number of methylene linkers between the aryl cap and the aryl arms. (e.g. tame CH_2 4 in Figure 2.2).

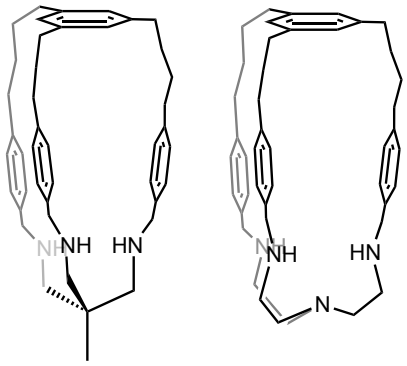

tame CH_2 4 **tren CH_2 4**

Figure 2.2 Two proposed cage ligands, tame CH_2 4 and tren CH_2 4.

These optimizations were performed using the Turbomole 5.10[34] program package; BP86 was chosen as the density functional due to its success in performing geometry and electron density optimization calculations on many large organometallic, fullerene, and metalloenzyme complexes.[35-37]. A minimal basis set, def-SV(P)[38], was used since we were interested in qualitative trends and not exact energies. In order to compare the cavity height of the cage ligands, a consistent methodology was used. The cavity height is defined as the distance between the metal ion and the centroid of the aryl cap. For the calculations, a few different metal ions were utilized. First, for the ligand derivatives with the tame base, a phosphorus atom was used. A phosphorus atom was chosen for several reasons; a phosphorus ion has a 3+ charge allowing for the overall complex to be charge neutral with the trianionic tame ligands. Also, the trigonal pyramidal coordination geometry of the phosphorus atom mimics the tetrahedral environment that would be expected from a M-X in this ligand environment.

Table 2.1 Cavity heights of proposed tame ligands optimized with DFT.

Entry	Ligand	Cavity Height (Å)
1	tame 2	4.93
2	tame 4	6.09
3	tame 5	5.84
4	tame 6	7.71
5	tame 7	7.01
6	tame 8	8.48
7	tame CH_2 4	7.43
8	tame CH_2 5	6.52
9	tame CH_2 6	9.52

The results from the geometry optimizations are shown in Table 2.1. Interestingly, the cavity height was not directly correlated with the number of carbons in the alkyl chain between the aryl cap and the aryl arm (Entries 2 and 3 for example). This deviation from a linear trend occurs in ligands with an odd number of carbons in the alkyl chain (tame 5 and tame 7). Examination of tame 5 in Figure 2.3 reveals an unfavorable eclipsed conformation in the methylene linkers in the alkyl chain. This unfavorable conformation required to make the connection to the aryl arm is likely the origin of the decrease in cavity height. A similar observation is made in the tame 7 case as well (Table 2.1, entry 5). Furthermore, linking the aryl ring directly to the amine pocket results in variable strain across the series, with the tame 2 ligand being the most strained based on the angle between P−N−C_{aryl} of 106°. The strain is relieved as more carbons are added to the alkyl chain between the aryl cap and the aryl arm largely due to enabling rotation around the N-aryl bond.

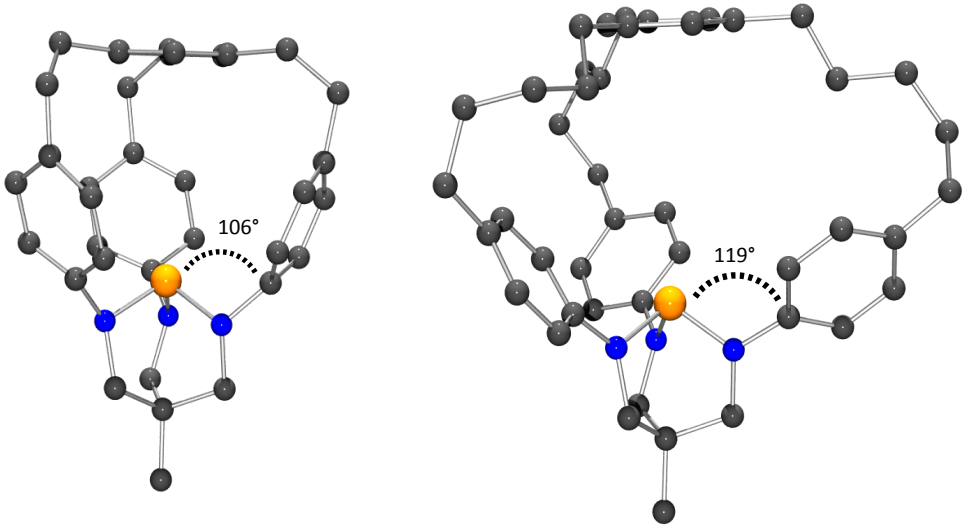

Figure 2.3 Ball-and-stick models of tame 2 and tame 5 geometry optimized structures. The angle between P−N−C_{aryl} as shown is 106° for tame 2 and 119° for tame 5. The atoms are represented as follows: P (orange), C (dark grey) and N (blue).

To perhaps circumvent undesirable strain in the ligands with fewer carbons in the alkyl chain between the aryl cap and aryl arm, a methylene linker was introduced between the nitrogen pocket and the aryl arm. For this study, only the 4, 5, and 6 carbon alkyl chain variants were optimized (Table 2.1, Entry 7-9). As expected the overall cavity heights increase, with the addition methylene linker, compared to those without. Tame CH_2 4 increases by approxiamately 1.3 Å compared to tame 4 (Table 2.1, Entry 2 and 7), while tame CH_2 5 only increases by around 0.7 Å compared to tame 5 (Table 2.1, Entries 3 and 8). As anticipated, an increased amount of flexibility was observed, and some of the optimized structures to deviate significantly from an idealized C_3 symmetry (Figure 2.4). The strain observed in the direct nitrogen-aryl linked variants is alleviated in all of the variants with a methylene linker between the nitrogen and aryl arm. The P−N−C_{aryl} angle is approxiamately 120° for all of the methylene linked variants. A similar non-

linear trend for the methylene linked variants was observed, with tame CH_2 5 being the outliner again. Despite increased rotational freedom within the structures, an unfavorable eclipsed conformation is still observed for the variant with an odd number of carbons in the alkyl chain again likely causeing a decreased cavity height compared to the variants with an even number of carbons in the alkyl chain (Table 2.1, Entry 7-9).

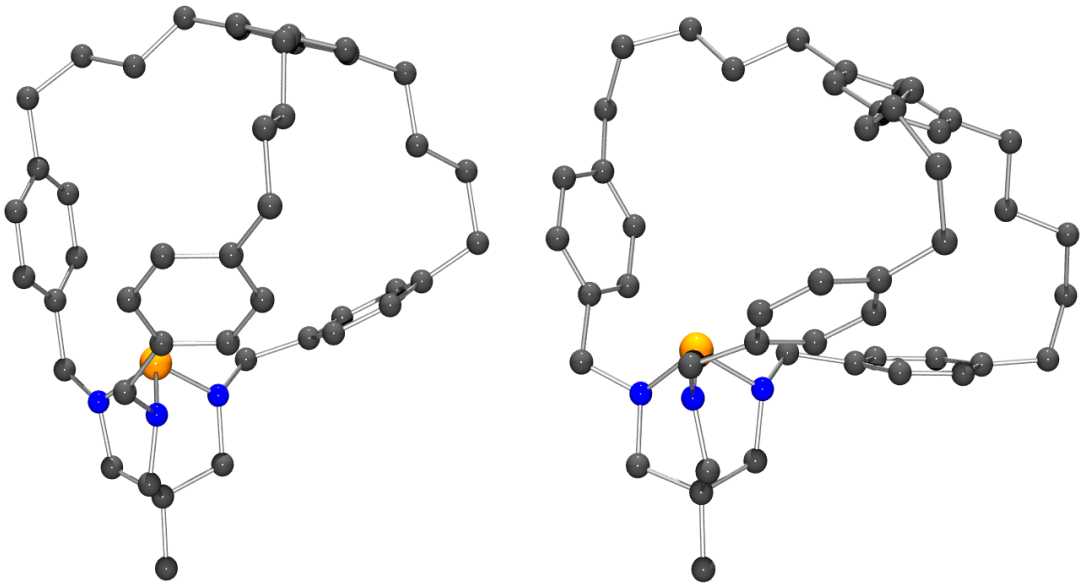

tame CH_2 4 tame CH_2 5

Figure 2.4 Ball-and-stick models of tame CH_2 4 and tame CH_2 5 optimized by DFT. The atoms are represented as follows: P (orange), C (dark grey) and N (blue).

Another series of calculations were completed using tren for the metal binding pocket. The tren ligands will invoke a tetradentate chelation around the metal center and will impose a trigonal bipyramidal geometry for M-X. This will lower the metal in nitrogen binding pocket compared to tame ligands and possibly increase the cavity height. The calculations for the tame series show that addition of a methylene linker between the nitrogen and aryl arm increased the flexibility of the molecule, which significantly affected the cavity height of the ligand as a result of the asymmetry. None of

the calculations were able to minimize to a C_3 symmetric structure. It is likely that in solution the cage ligands will be freely rotating, allowing for such asymmetric structures, and, if these motions are rapid, the solution-state structure should appear to be C_3 symmetric. Additionally, the asymmetric structures prevent an accurate measure of the true cavity height, as the cage ligands should have the largest cavity height when C_3 symmetry is adopted. As a result, we looked for a way to impose C_3 symmetry on the tren ligand systems in order to obtain a prediction for the true cavity height.

In order to evaluate the viability of obtaining a C_3 symmetric cage ligand, C_3 symmetric models were generated by multiplying the x,y,z coordinates of one arm with three-fold proper rotation matrices. Using these methods, the models were run with three different symmetry restrictions: symmetric (forcing C_3 symmetry within the DFT method and beginning with a C_3 symmetric input), no symmetry (no symmetry restrictions within the method, but beginning with a C_3 symmetric input), and asymmetric (no symmetry restrictions and asymmetric input). Figure 2.5 displays the overlays of the different methods for each of the different number of carbons in the alkyl chain.

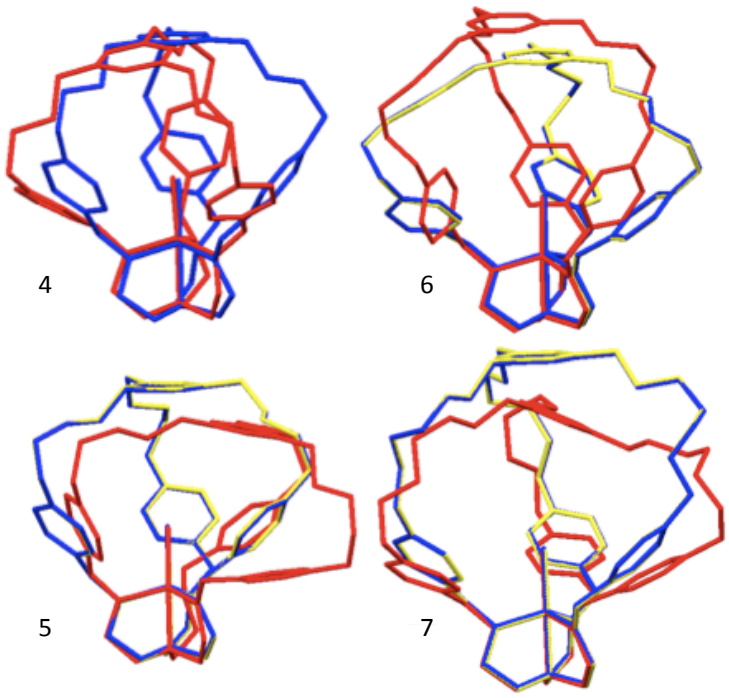

Figure 2.5 Overlay of DFT optimized structures with C_3 symmetric inputs with imposed C_3 symmetry (yellow), C_3 symmetric input with no method imposed C_3 symmetry (blue), and asymmetric input with no imposed C_3 symmetry (red).

The relative energies of each model were compared to see if there was a large enough difference to indicate that symmetric or asymmetric was more energetically favorable. The results in Table 2.2 reveal that the energy differences between the three different optimizations are small (< 10 kcal/mol). The low energy barriers between the optimized structures corroborates our assumption that the cage ligands are very flexible and can easily adopt variable cavity heights. Ideally, this variability will be dependent on substrate identity. Interestingly, the lowest energy structure for variants with an odd numbers of carbons in the alkyl chain results from the asymmetric input. This corroborates the conclusion above that an odd number carbons in the alkyl chain causes eclipsed angles along the alkyl chain and thus results in highly asymmetric structures.

Table 2.2 Energy differences in kcal/mol between three different inputs. The lowest energy input was set to zero.

Entry		4	5	6	7
1	Asymmetric input	+0.2	0	+4.9	0
2	C_3 input with forced C_3 symmetry	- [1]	+6.1	+0.1	+9.3
3	C_3 input with no symmetry	0	+6.0	0	+9.1

1. Calculation for the C_3 symmetric tren CH_2 4 did not converge.

The C_3 symmetric outputs (Table 2.2, Entry 2, Entry 3 for tren CH_2 4) were analyzed for trends in cavity height. Again, as shown in Table 2.3, the variants with an odd number of carbons in the alkyl chain have smaller cavity heights than what one would from a direct linear increase (Table 2.3, Entry 2 and 4). Enforcing C_3 symmetry seems to minimize this deviation, since an increase in cavity height is observed from tren CH_2 4 to tren CH_2 5 (Table 2.3, Entries 1 and 2) and only a slight decrease from tren CH_2 6 to tren CH_2 7 (Table 2.3, Entry 3 and 4).

Table 2.3 Cavity heights of proposed tren cage ligands optimized by DFT.

Entry	Structure	Cavity Height (Å)
1	tren CH_2 4	7.55
2	tren CH_2 5	7.67
3	tren CH_2 6	10.05
4	tren CH_2 7	9.41
5	tren amide 4	8.27
6	tren amide 5	8.33

Finally, tren cage ligands with an amide linkage were studied due to their proclivity to bind mid-late transition metals as well as enabling multiple synthetic routes to be explored later on if desired. Only the tren amide 4 and tren amide 5 variants were studied (Table 2.3, Entry 5 and 6) based on previous results for tren CH_2 and tame CH_2 and a zinc metal was used as it was proposed to be the first transition metal target. The cavity height did not change drastically when substituting an amide group for the methylene linker (Table 2.3, Entry 2-3 and 5-6 and Figure 2.6). In fact, we expected that

the cavity height might decrease slightly due to reduced flexibility in the bond linking the aryl arm to the nitrogen pocket; however, the ethylene groups in the tren backbone appear to absorb this reduced flexibility and still allow for a large amount of rotation in the ligand arms maintaining maximum cavity height.

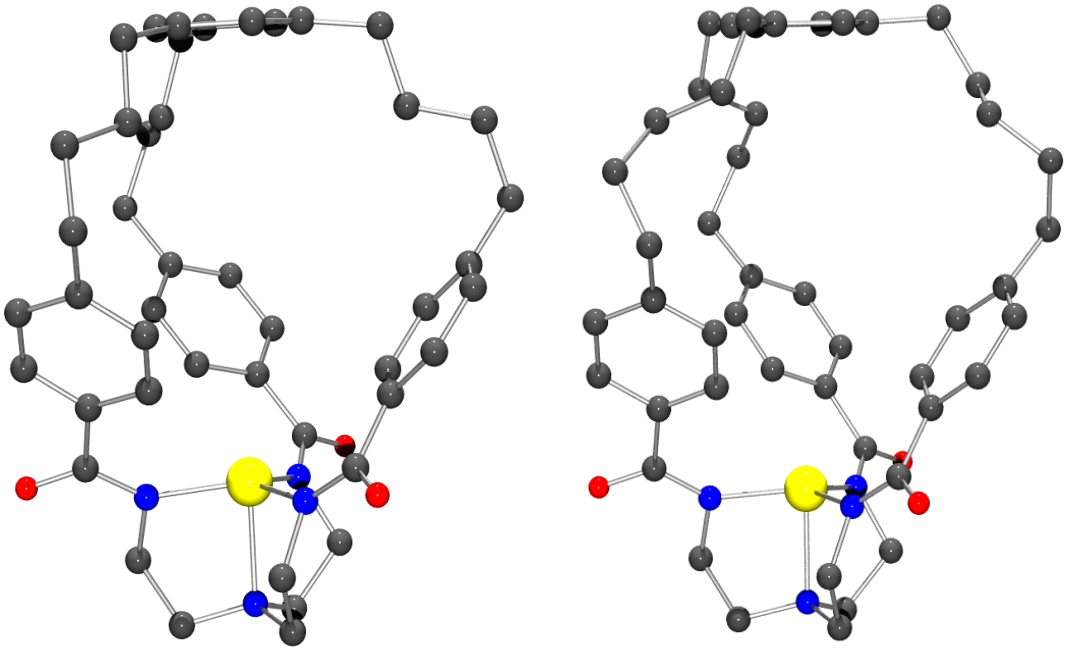

tren amide 4 **tren amide 5**

Figure 2.6 Ball-and-stick models of tren amide 4 and tren amide 5 optimized by DFT. Atoms are represented as follows: N (blue), C (grey), O (red), and Zn (yellow).

Based on the theoretical results, combined with relative ease of synthesis from commercially available starting materials, the first synthetic target was tren amide 4. Moving to 5 or 6 carbon linkers in the alkyl chain adds multiple synthetic steps and as mentioned previously, using the amide linker between the aryl arms and tren allows for both a convergent and linear synthetic routes to be explored.

*2.3.2 Synthesis and characterization of tri(amido)amine cage ligand (**4**)*

Traditionally, the synthesis of macrobicylic molecules is difficult and low yielding. The first macrobicylic triamido ligand was synthesized for anion capture studies via reaction of 3 equivalents of 2,6-pyridinedicarbonyl dichloride and two equivalents of tren in the presence of base. While this reaction is high yielding when a single tren unit is reacted, creating the macrobicylic ring reduces the yield to 10% after a column is used to remove undesired byproducts.[19] As discussed above, Nocera adapted this synthesis slightly by activating the linker further by generating a disuccimido ester and subsequently reacting it with two equivalents of tren;[17] however, the overall yield was still only 8% and a column was still necessary for purification. We investigated two different routes herein in an effort to improve the synthesis of triamido cage ligand systems.

One route was a convergent pathway involving the coupling of a cap and tren and the other took a linear approach, starting from the top of the complex and building it down. For the convergent pathway (Scheme 2.2), the triamido(amine), **1**, was formed from the reaction of 4-bromobenzoyl chloride and tren in the presence of a weak base, triethylamine (NEt_3) in high yields (>80%). Compound **1** was characterized by ^1H nuclear magnetic resonance (NMR) spectroscopy, ^{13}C NMR spectroscopy and electron spray ionization mass spectrometry (ESI-MS). In the ^1H NMR spectrum of **1**, the three amide protons were easily identified as a broad triplet at 8.4 parts per million (ppm). Compound **2** was synthesized according to a modified literature procedure from 1,3,5-tris(bromomethyl)benzene and allyl Grignard.[39] Hydroboration of **2** with 9-

borabicyclo[3.3.1]borane (9-BBN) generates **3**, which is primed to be coupled to tri(amido)amine **1**. Compounds **2** and **3** were both characterized by ^{1}H NMR and ^{13}C NMR spectroscopy. Complete conversion of **2** to **3** is evident by monitoring the disappearance of the vinyl peaks of **2** at 5.9, 5.1 and 5.01 ppm in the ^{1}H NMR spectrum.

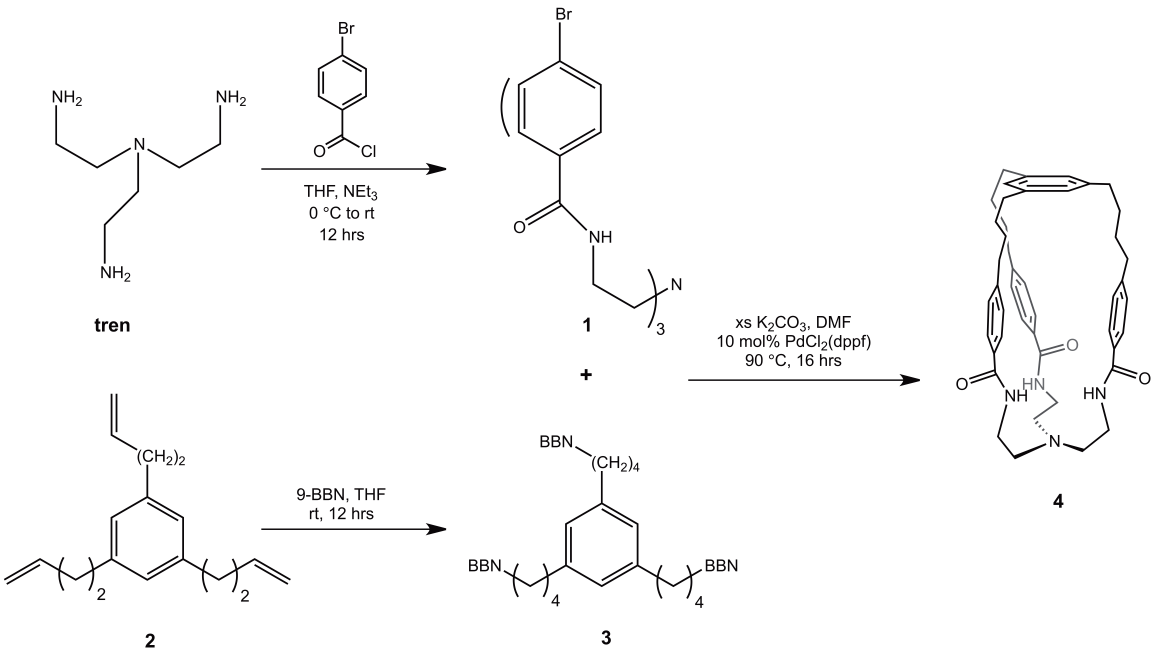

Scheme 2.2 Convergent synthetic route for the synthesis of cage ligand **4**.

Suzuki-Miyaura coupling conditions were utilized to couple **1** and **3** together and generate tri(amido)amine cage ligand **4**. Dilute conditions were required to prevent the formation of oligomers. Crude yields for this coupling were low, likely due to unidentified oligomers and isolation of **4** from coupling by-products and salts was difficult. Column chromatography afforded pure ligand when the eluting solvent was 10% MeOH / 90% DCM. Despite obtaining pure ligand, overall isolation yields for the synthesis of **4** using the convergent pathway were less than 10%. Although a convergent pathway is the most economical and would ideally give the highest overall yields, a new

route was investigated due to low yields of coupling and isolation difficulty due to use of column chromatography.

Scheme 2.3 illustrates the linear pathway for the synthesis of cage ligand **4**. Using the same Suzuki-Miyaura coupling condition as described above, **3** is coupled to 4-methyl iodobenzoate to generate compound **5** in moderate yield (60%) after column chromatography. Hydrolysis of **5** under basic conditions followed by an acidic work-up yields the tricarboxylic acid **6**. Conversion of triester **5** to tricarboxylic acid **6** was easily monitored via ^{1}H NMR spectroscopy by following the disappearance of the methyl peak of **5** at 3.9 ppm. Compounds **5** and **6** were characterized by ^{1}H NMR and ^{13}C NMR spectroscopy and ESI-MS.

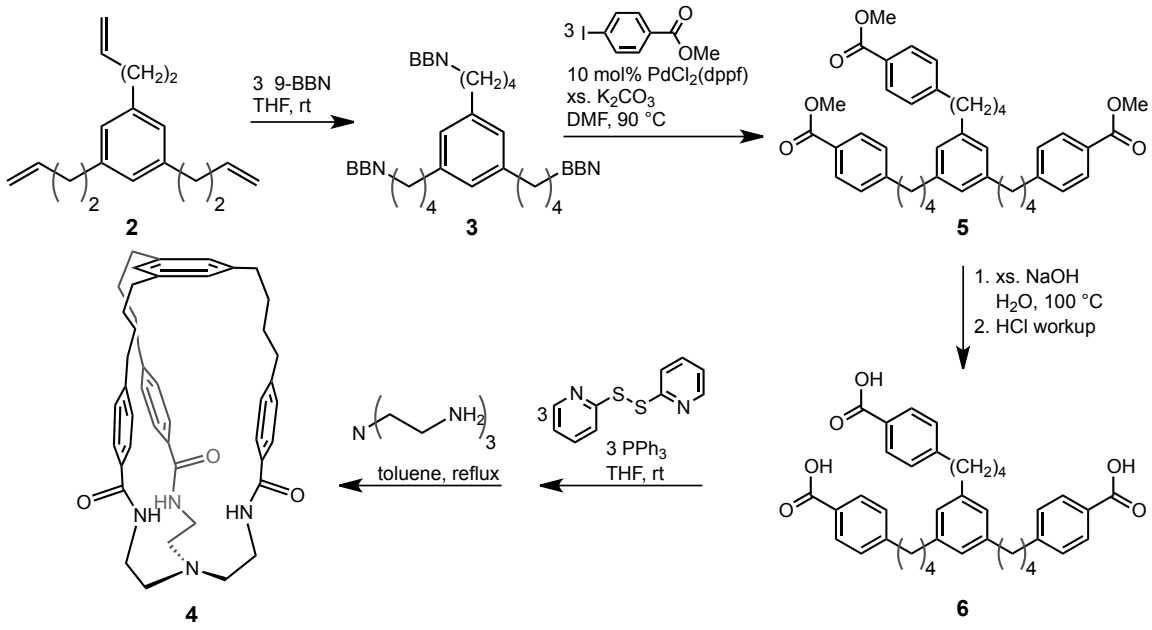

Scheme 2.3 Linear synthetic route for synthesis of cage ligand **4**.

Development of a new method for synthesizing macrobicyclic ligands with higher yields was necessary to achieve an efficient synthesis of triamido(amine) cage ligand **4**. The key innovation achieving higher yields of **4** in our hands was to use 2,2'-dipyridyl

disulfide (PySSPy) to activate the carboxylic acid group of compound **6**. As illustrated in Scheme 2.3, triphenylphoshine (PPh_3) drives the formation of the 2-pyridyl thiolester derivative of **6** by forming triphenylphosphine oxide (PPh_3O). As the reaction proceeds to completion, the mixture turns an intense yellow color, presumably due to the formation of the thioester, a useful colorometric indication of reaction completion. After removing the tetrahydrofuran (THF), the crude mixture is reconstituted in toluene and a solution of tren in toluene is added. A major improvement in this synthesis from the method described in Scheme 2.2 is the workup to obtain **4** as a pure material. Cage ligand **4** was obtained by filtration of reaction mixture to remove PPh_3O and possible oligomers, removal of toluene, reconstitution in diethyl ether (Et_2O) and finally filtration to collect solids, omitting the need for a lengthy column. The white solids were characterized by ^1H and ^{13}C NMR spectroscopy and high resolution ESI-MS and identified as tri(amido)amine cage ligand **4**.

Given the theoretical results, we were interested in whether the ligand arms would be flexible or in a locked conformation yielding diastereotopic protons The room temperature ^1H NMR of **4** is shown in Figure 2.7. The ^1H NMR shows 10 unique proton resonances (one peak is underneath the H_2O peak). This is consistent with a completely C_3 symmetric geometry in solution, indicating that the ligand has complete rotational freedom, corroborating our theoretical calculations.

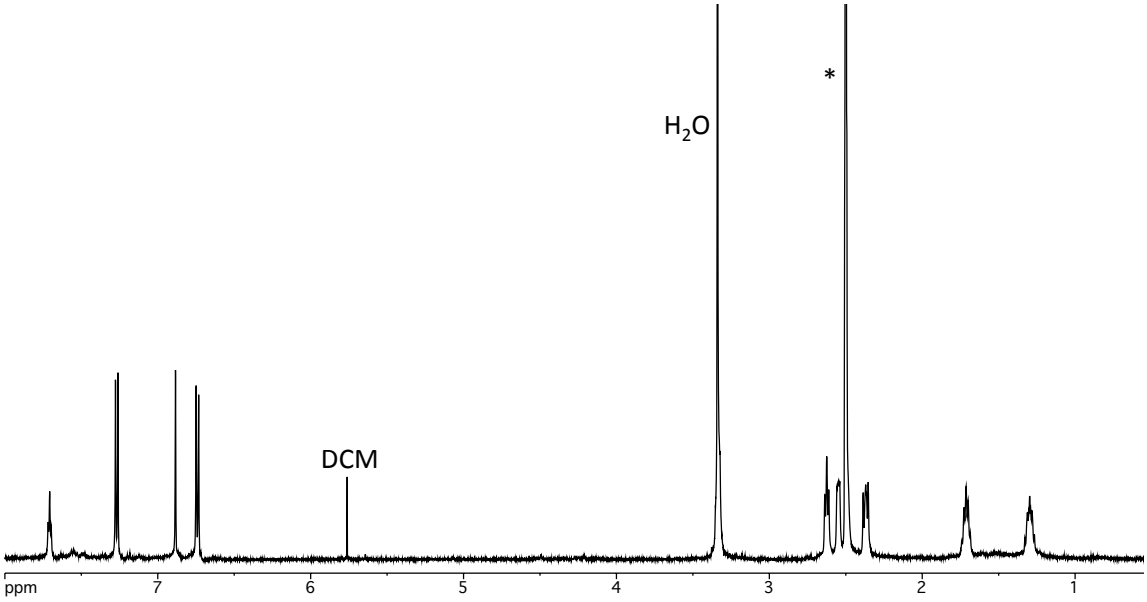

Figure 2.7 ^{1}H NMR spectrum of tri(amido)amine cage ligand **4** in d_6-DMSO. Asterisk represents residual solvent peak from d_6-DMSO.

Despite the increased number of steps in the linear pathway, six versus four in convergent pathway, the overall yield was increased from 4% to 30%. Furthermore, isolation of analytically pure material was achieved with much less effort with the linear pathway.

*2.3.3 Synthesis and characterization of tri(amino)amine cage ligand (**9**)*

An additional goal of this project was to create a synthetic scheme that would be highly modular. Small modifications to Scheme 2.3 allowed for the synthesis of a new cage ligand, featuring a neutral tetradentate metal binding pocket (Scheme 2.4). Tri(amino)amine cage ligand **9** was synthesized starting from the tricarboxylic ester **5**. Compound **5** was reduced to tribenzyl alcohol **7** using lithium aluminum hydride ($LiAlH_4$). Oxidation of **7** yields trialdehyde **8**. Both **7** and **8** are synthesized in high yields (> 70%) and have been characterized by ^{1}H and ^{13}C NMR spectroscopy.

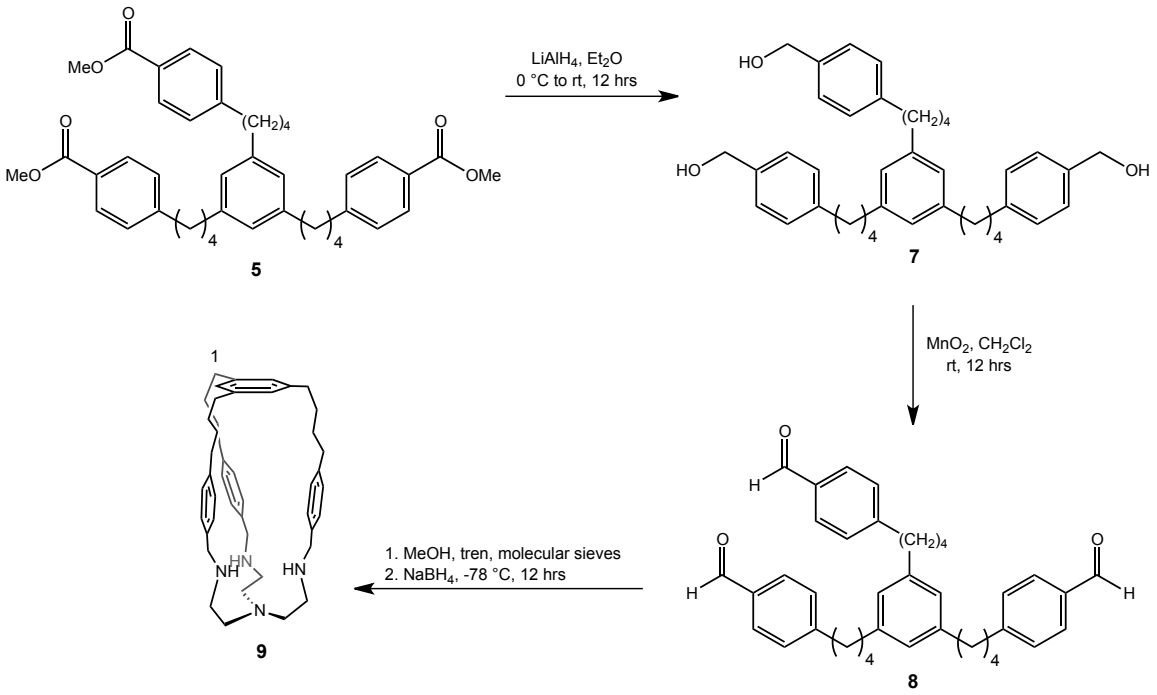

Scheme 2.4 Synthesis of tri(amino)amine cage ligand **9**.

Formation of tri(amino)amine cage ligand **9** requires dilute conditions (~ 0.1mM) in order to prevent oligomerization. The condensation reaction between the aldehyde and secondary amine is reversible and must be driven by removing the byproduct, water, using molecular sieves. When the reaction is carried out without the use of molecular sieves, an equilibrium mixture persists. In the presence of sieves an intermediate imine compound is formed and was identified by ^{1}H NMR spectroscopy. The intermediate imine is reduced directly without isolation using sodium borohydride to yield **9**. Tri(amino)amine cage ligand **9** is isolated after removal of salts by an aqueous extraction as an oil. The ^{1}H NMR spectrum of **9** is similar to tri(amido)amine cage ligand **4**, in that it exhibits complete rotational freedom as indicated by the presence of only 10 peaks (Figure 2.7 (**4**) and Figure 2.8 (**9**)). Furthermore, the area under each peak in the alkyl region integrates to two protons. In the tri(amido)amine cage ligand **4**, the doublets

corresponding to the aryl protons on the aryl arms differ by almost 1 ppm due to the electronic difference between the amide substituent versus the alkyl substituent (Figure 2.7). In the tri(amino)amine cage ligand **9**, it is evident that the electronic environments are very similar because the peaks corresponding to the aryl protons on the aryl arm overlap forming a doublet of doublets in the ^{1}H NMR spectrum (Figure 2.8).

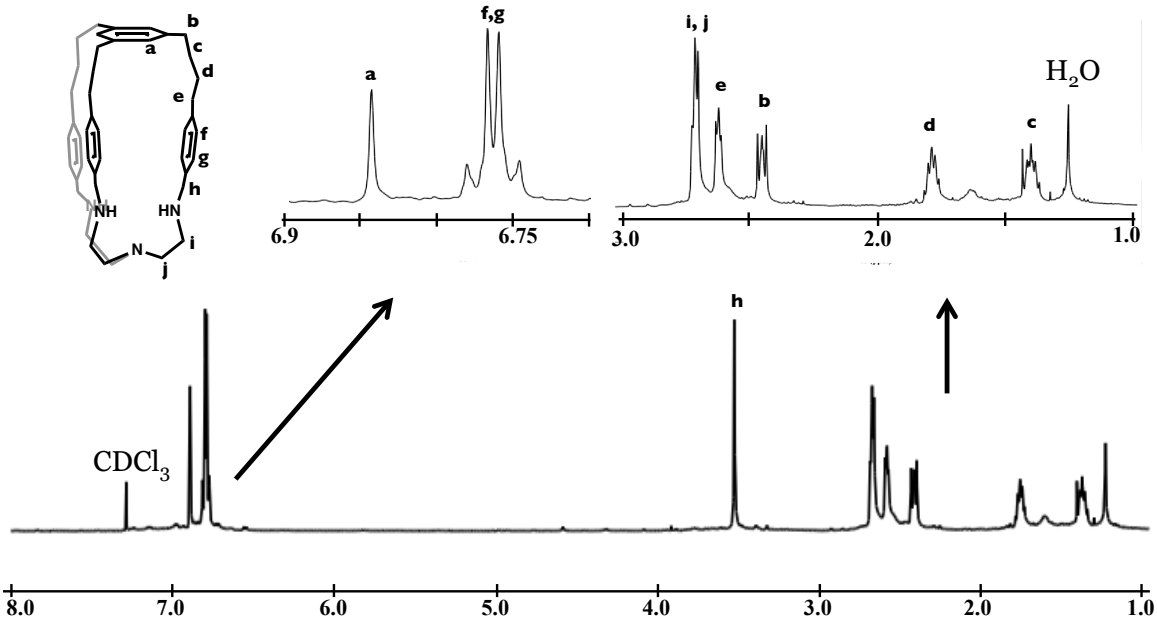

Figure 2.8 500 MHz ^{1}H NMR spectrum of tri(amino)amine cage ligand **9** in $CDCl_3$.

*2.3.4 Synthesis and characterization of tri(amido)amine Zn Complex (**10**)*

Tri(amido)amine cage ligand **4** was metallated with anhydrous zinc dichloride ($ZnCl_2$). The three amide moieties of **4** render it very insoluble in most organic solvents, limiting the choice of bases and solvent feasible for metallation. Slight modifications to methods developed by Borovik *et al.* for analogous tri(amido)amine ligand scaffolds enabled metallation of **4** with $ZnCl_2$ (Scheme 2.5). Complex **10** was synthesized in a 90% yield as a salmon-colored solid.

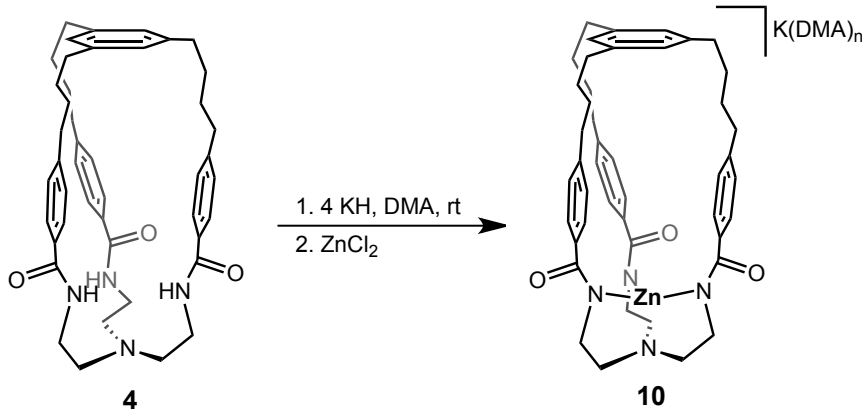

Scheme 2.5 Metallation of tri(amido)amine cage ligand **4** with $ZnCl_2$.[40]

The ^{1}H NMR spectrum of **10** indicated that the metallation proceeded cleanly as evident by the absence of the amide protons (Figure 2.9). The aryl region of the NMR spectra is distinctly different as well. The proton resonances most affected by the addition of the zinc metal center to **4** are the protons on the aryl arm near to the amide moiety, likely due to their close proximity to the zinc center. On the other hand, the singlet assigned to the aryl cap protons is barely affected by the presence of the zinc, and thus there is almost no change in chemical shift.

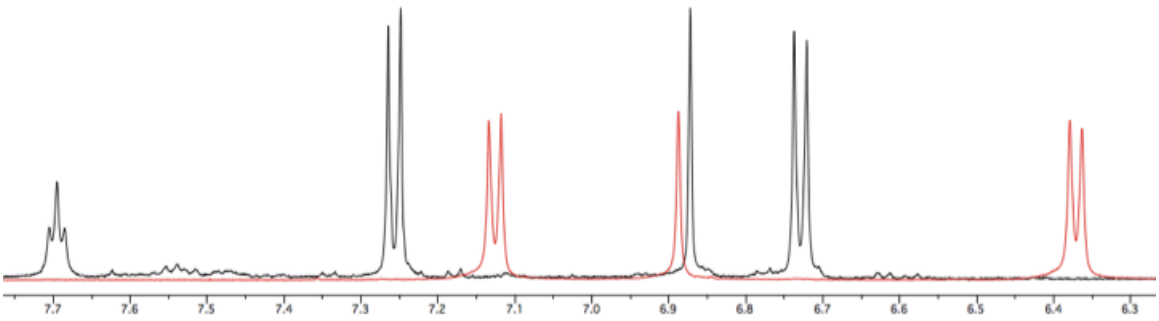

Figure 2.9 Overlay of ^{1}H NMR spectra of **4** (black) and **10** (red).

*2.3.5 Solid-State Structure of **10[PPh$_4$]***

In order to obtain crystals of **10** suitable for an X-ray diffraction study, the potassium counterion was exchanged with tetraphenylphosphonium ($[PPh_4]^+$) to increase solubility. Even with PPh_4 as the countercation, **10** was sparingly soluble THF and a concentrated solution was obtained by only after gentle heating. X-ray quality single crystals grew as yellow plates from a hot THF solution that was allowed to cool slowly. The structure of **10**[PPh_4] reveals a trigonal monopyramidal coordination geometry around the zinc (Figure 2.10a). The structure is nearly C_3 symmetric confirming the symmetry observed in the solution-state ^{1}H NMR spectrum and theoretical calulations. The flexible ligand arms dramatically twist by 40° (Figure 2.10b). The bond distances between the ligand and the zinc metal center are Zn-N_{ap}, 2.128(2) Å, and Zn-N_{eq}, 1.985(2) Å, on average. These distances are consistent with literature examples for a Zn^{2+} ion in a trigonal bipyramidal coordination environment. Particularly, these distances are very similar to those reported by Cummins and Nocera for a dizinc-cryptand complex where the Zn-N_{ap} and Zn-N_{eq} distances are 2.162 Å (average) and 1.973 Å (average), respectively. Important crystallographic information can be found in Table 2.4.

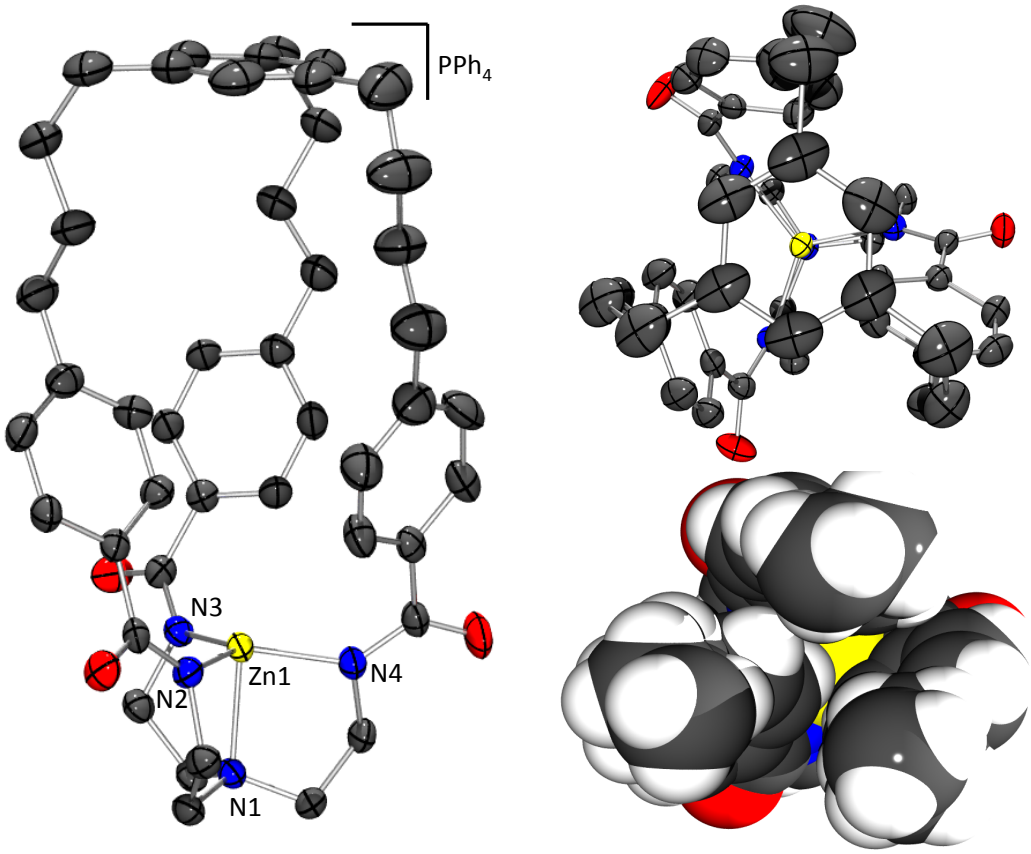

Figure 2.10 (a) Crystal structure of **10[PPh$_4$]** depicted at the 30% probability level. Hydrogen atoms, solvent and countercation were omitted for clarity. (b) Top view of **10[PPh$_4$]**. (c) Space-filling model with aryl cap removed for better visualization of the cavity. Selected bond lengths (Å) and bond angles (°): Zn1-N1, 2.128(2); Zn-N2, 1.977(2); Zn1-N3, 1.985(2); Zn1-N4, 1.992(2); N2-Zn1-N3, 119.23(9); N3-Zn1-N4, 120.34(9); N2-Zn1-N4, 119.06(9).

Table 2.4 Crystallographic information for **10[PPh$_4$]**.

	10[PPh$_4$]
chemical formula	$C_{73}H_{77}N_4O_4PZn$
formula weight	1170.73
crystal system	monoclinic
space group	$P2_1/n$
a (Å)	13.1597(8)
b (Å)	34.881(2)
c (Å)	14.5029(9)
α (deg)	90
β (deg)	92.8190(10)
γ (deg)	90
V (Å^3)	6649.1(7)
Z	4
d_{calcd} (g cm^{-3})	1.169
λ (Å), μ (mm^{-1})	0.71073, 0.443
T (K)	173(2)
Θ range (deg)	1.66 to 26.65
reflns collected	13959
unique reflns	9502
data/restraint/ parameters	13959 / 0 / 748
R_1, wR_2 ($I > 2\sigma(I)$)	0.0513, 0.1346

From the solid-state structure of **10[PPh$_4$]** we can obtain additional metrics on size of the cavity. Consistent with the theoretical calculations discussed above, the cavity height was determined by measuring the distance from the zinc center to the centroid of the aryl ring in the cap. The cavity of the crystal structure is nearly one nanometer tall (9.57 Å), which matches reasonably well with the predicted cavity height of 8.27 Å from the DFT calculations. The cavity height of the crystal structure is likely close to the maximum height of the cavity because the crystal structure has nearly perfect C_3 symmetry. Our theoretical studies indicated fluxional behavior in the cavity height; thus, we were interested in probing the geometry optimization of the crystal structure to determine if the cavity height would change. Using the exact same theoretical parameters

that were used for the tren amide 4 geometry optimizations discussed above, the crystal structure coordinates were optimized. The result is a lower energy solution by 10 kcal/mol compared to the original tren amide 4 optimization, and the cavity height is 9.29 Å, which is expectedly closer to that observed in the crystal structure. A comparison of these two optimized structures indicates that the cavity can readily adopt conformations with cavity height changes of at least ~1 Å at room temperature. It also suggests that the DFT optimizations are prone to fall into local minimums.

In addition to the cavity height, we were also interested in the volume of the cavity. Estimation of cavity volume can be obtained using PLATON/VOID a program designed to detect solvent accessible voids.[41] This program has been utilized to analyze solvent channels in $[Ru(bpy)]X_2$ complexes identified for Solid-state oxygen sensing.[42] When analyzing **10[PPh$_4$]** for solvent channels, it was determined that only short, disconnected channels existed in the entire crystalline lattice, perhaps unsurprisingly. However, the void of interest in the inside of the cavity of **10[PPh$_4$]** was found. Using the radius of the void found in Mercury, the volume of the void was calculated to be 4.72 Å^3. Figure 2.11 displays a space-filling model of **10** with the void inside the cavity. It is clear that the void, which is modeled as a perfect sphere does not fill the entire cavity and that the volume calculated for the void is estimated to be slightly smaller than the true volume of the cavity. Despite a relatively small volume, we believe encapsulation of small molecules is possible due to the encouraging results from the hexamido-cryptand iron and cobalt complexes.[17,18] The distance between the two metal centers is significantly shorter than the estimated height of the cavity of **10** (Fe-Fe, 6.30 Å; Co-Co, 6.41 Å; **10**, 9.57 Å),

and these complexes have demonstrated the binding of a cyanide anion, indicating that there is likely room lengthwise to fit small diatomic molecules in our system.

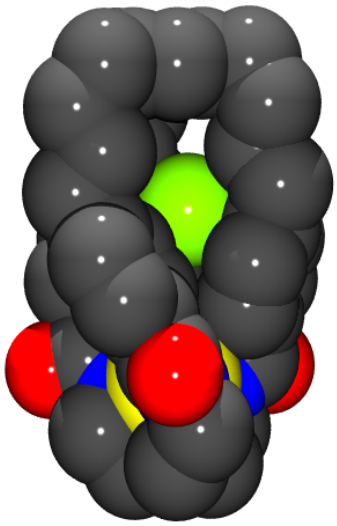

Figure 2.11 Space-filling model of **10[PPh$_4$]** and void space generated from PLATON/VOID analysis.

2.3.6 Reactivity studies

Host-guest chemistry of **10** was briefly explored with coordinating solvent molecules such as acetonitrile (CH_3CN), dimethylformamide (DMF), and dimethylsulfoxide (DMSO). The reactions were monitored by ^{1}H NMR spectroscopy, and no changes in the spectra were observed at room temperature or with mild heating (50 °C). Next, nonpolar substrates were explored. Weak interactions between C-H bonds and aromatic systems have been identified in crystal structures of organic molecules and have also been extensively studied by theorists. Particularly interesting to this project is the study the interaction of methane with benzene. Studies have shown that methane interacts with benzene in a monodentate fashion.[43,44] The unique hydrophobic pocket of **10** has four aromatic rings that could interact with methane. Literature host-guest

chemistry on the encapsulation of methane shows a dramatic shift in the ^{1}H NMR spectrum of methane when encapsulated;[45] thus, the reaction of **10** with methane was monitored by ^{1}H NMR spectroscopy. Unfortunately, only dissolved methane gas was observed both at room temperature and under mild heating (50 °C). Other nonpolar hydrocarbons such as pentane, hexane, benzene, and trifluorotoluene were investigated as well albeit with no success. The lack of reactivity can be rationalized by considering two factors: (1) the Lewis acidity of the Zn^{2+} center is significantly attenuated by the ligand's three anionic amide groups; and (2) the cavity is so narrow that it would exclude most of these substrates based on their size.

2.4 Conclusions

Two cage ligands featuring a hydrophobic pocket were successfully synthesized. Transition metal chelation was demonstrated via the synthesis of Zn complex **10**. X-ray crystallography revealed a cavity that is nearly one nanometer long. Theoretical and ^{1}H NMR spectroscopy studies indicated fluxional behavior in the ligand arms that could cause variation in the cavity height in solution. Despite this, substrate uptake was not observed. Still, an improved synthetic route to novel triamido(amine) and tri(amino)amine cage ligands has been developed. Even more promising is the possibility of modularity in this synthetic scheme by utilization of a different metal binding pocket, such as tame, or by using a different allyl Grignard to increase the number of methylene linkers. Possible avenues for future research include extending the coordination

chemistry to different transition metals, as well as expanding the cavity size by increasing the number of methylene linkers in the ligand arms.

2.5 Experimental Procedures

2.5.1 General considerations

Unless otherwise stated, all operations were performed in a VAC Atmosphere double-dry box under an atmosphere of purified nitrogen or using high vacuum standard Schlenk techniques under a nitrogen atmosphere. Anhydrous *n*-hexane, pentane, toluene, tetrahydrofuran, diethyl ether, acetonitrile, and benzene were purchased from Aldrich and dried with a SG Waters solvent purification system. Dimethoxyethane (DME) was dried over $LiAlH_4$ overnight, distilled and dried further with 4 Å activated alumina, filtered through a bed of activated alumina powder, and stored over 4 Å molecular sieves. Anhydrous DMF and DMA were purchase from Aldrich and further dried using 4 Å activated alumina, filtered through a bed of activated alumina powder and stored over 4 Å molecular sieves. Chloroform and Ethyl Acetate were purchased from Aldrich and used without further purification. $CDCl_3$ and d_6-DMSO were purchased from Cambridge Isotope Laboratory (CIL), degassed and stored over 4 Å molecular sieves. Celite, alumina, and 4 Å molecular sieves were activated under vacuum for four days at 350 ºC. All other chemicals were used as received. ^1H and ^{13}C NMR spectra were recorded on Varian 300 MHz NMR spectrometer and a Varian 500 MHz NMR spectrometer. ^1H and ^{13}C NMR shifts are reported with reference to solvent resonances (residual $CHCl_3$ in

$CDCl_3$, 7.27 ppm and 77.0 ppm or residual DMSO in d_6-DMSO, 2.50 ppm and 40.0 ppm).

2.5.2 Synthetic procedures

Synthesis of *N*,*N*',*N*''-(nitrilotris(ethane-2,1-diyl))tris(4-bromobenzamide) (1): A 500 mL round bottom charged with 2.66 g (18.19 mmol) of tren and 300 mL of THF was cooled to 0 ^oC. Triethylamine (6.63g, 65.48 mmol) was added slowly and the reaction was stirred for 15 min. While still at 0 ^oC a THF solution of 4-bromo benzoylchloride (13.17g, 60.03 mmol) was added drop wise over 25 min. The reaction allowed to warm to room temperature and stirred for 12 hours. The solvent was concentrated on the rotovap and the solid collected via vacuum filtration. The solid was purified through a series of solvent washes: Et_2O, dH_2O, $CHCl_3$, and hot THF to afford 11.07 g (88% yield) of white powder. For **1:** ^1H NMR (23 ^oC, 300 MHz, d_6-DMSO): δ 8.40 ppm (broad t, 3H, N*H*), 7.66 ppm (d, 6H, C_6H_4), 7.53 ppm (d, 6H, C_6H_4), 3.37 ppm (t, 6H, $NHCH_2CH_2N$), 2.67 ppm (t, 6H, $NHCH_2CH_2N$). ^{13}C NMR (23 ^oC, 75 MHz, d_6-DMSO): δ 165.46 ppm (*C*ONH), 133.82 ppm (C_6H_4), 131.56 (2C, C_6H_4), 129.39 (2C, C_6H_4), 124.87 ppm (C_6H_4), 53.02 ppm ($NHCH_2CH_2N$), 37.77 ppm ($NHCH_2CH_2N$).

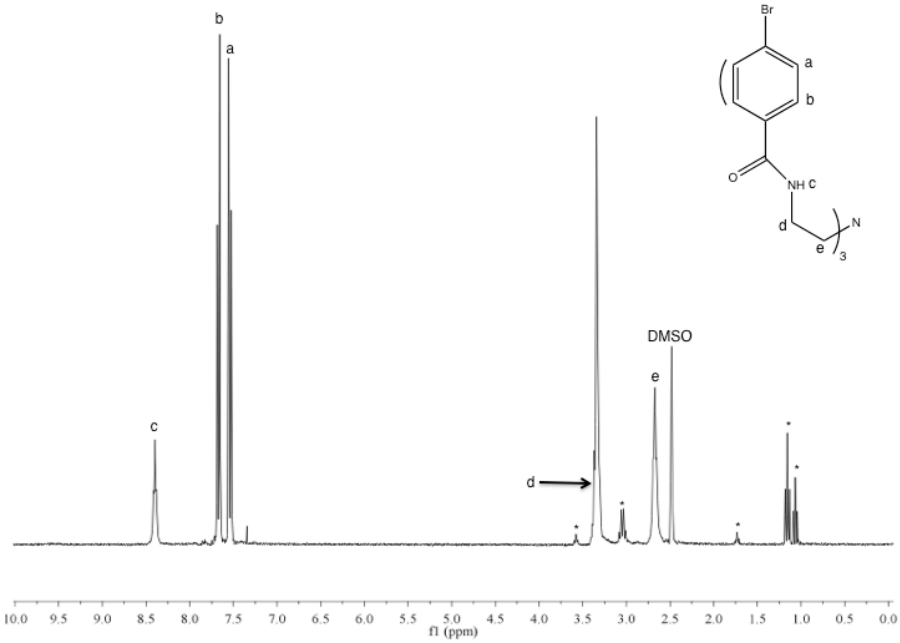

Figure 2.12 300 MHz ^{1}H NMR spectrum of **1** in d_6-DMSO. Asterisk marks extraneous THF and Et_2O.

Synthesis of 1,3,5-tri(but-3-en-1-yl)benzene (2): A round bottom flask charged with 1 g (2.8 mmol) of 1,3,5-bromomethylbenzene and 150 mL of DME was cooled to 0 ^{o}C in the cold well. Allyl magnesium bromide in Et_2O (11.2 mL, 11.2 mmol) was added drop wise with ample stirring. The reaction was stirred for 2 hours at room temperature after which the reaction was quenched with dH_2O and the product extracted with Et_2O. Removal of the solvent yielded 1.30 g (96%) of yellow oil. The oil was dried and purified through a short activated alumina plug to yield 0.89 g (66%) of colorless oil. For **2**: ^{1}H NMR (23 ^{o}C, 300 MHz, $CDCl_3$): δ 6.88 ppm (s, 3H, C_6H_3), 5.90 ppm (m, 3H, C*H*CH_2), 5.10 ppm (d, 3H, CHCH_2), 5.01 ppm (m, 3H, CHCH_2), 2.68 ppm (t, 6H, (C_6H_3)CH_2CH_2CH), 2.37 ppm (q, 6H, (C_6H_3)CH_2CH_2CH). ^{13}C NMR (23 ^{o}C, 75 MHz, $CDCl_3$): δ 141.61 ppm (C_6H_3), 138.07 ppm (C_6H_3), 125.90 ppm (*C*HCH_2), 114.54 ppm (CH*C*H_2), 35.43 ppm ((C_6H_3)*C*H_2CH_2CH), 35.15 ppm ((C_6H_3)CH_2*C*H_2CH).

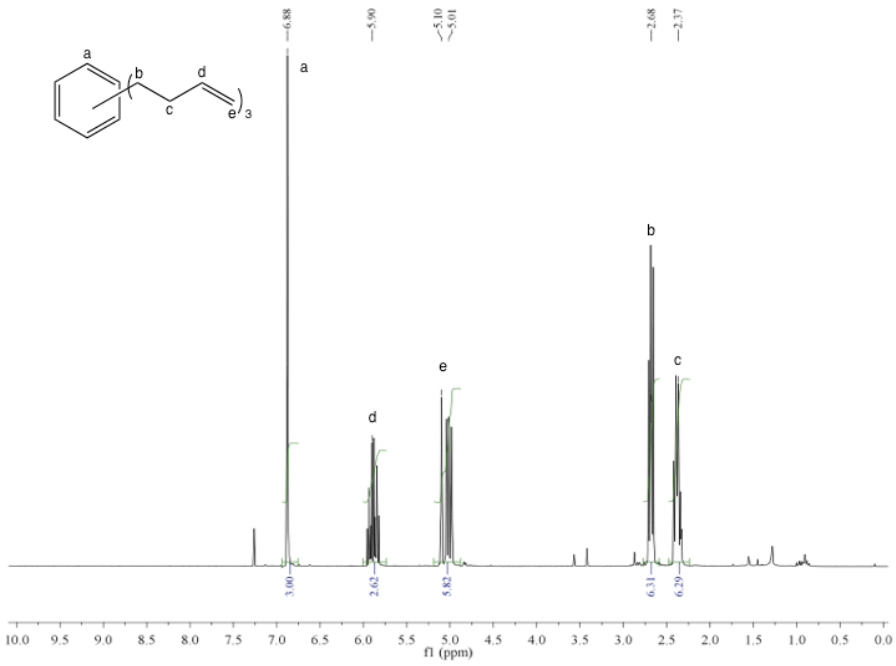

Figure 2.13 300 MHz ^{1}H NMR spectrum of **2** in $CDCl_3$.

Synthesis of 1,3,5-tris((9-borabicyclo[3.3.1]nonan-9-yl)butyl)benzene (3): Inside the glovebox, 1,3,5-tri(but-3-en-1-yl)benzene (10.2 g, 42.3 mmol) was dissolved in 300 mL of THF and a solution of 9-borabicyclo[3.3.1]-nonane dimer (9-BBN) (15.5 g, 63.4 mmol) was added portion wise at room temperature. The mixture was stirred for 12 hours and the solvent was removed to yield 24.4 g (95% yield) of thick yellow oil. For **3**: ^{1}H NMR (23 ^{o}C, 300 MHz, $CDCl_3$): δ 6.83 (s, 3H, C_6H_3), 2.58 (t, 6H, $(C_6H_3)CH_2CH_2CH_2CH_2B$), 1.84 (m, BBN), 1.69 (m, BBN), 1.56 (m, $(C_6H_3)CH_2CH_2CH_2CH_2B$), 1.39 (m, $(C_6H_3)CH_2CH_2CH_2CH_2B$), 1.20 (m, BBN). ^{13}C NMR (23 ^{o}C, 75 MHz, $CDCl_3$): δ 142.53 (C_6H_3), 125.37 (C_6H_3), 35.76 ($BCHCH_2CH_2$), 34.65 ($(C_6H_3)CH_2CH_2CH_2CH_2B$), 33.2 ($(C_6H_3)CH_2CH_2CH_2CH_2B$), 32.91 ($BCHCH_2CH_2$), 30.76 ($(C_6H_3)CH_2CH_2CH_2CH_2B$), 23.98 ($(C_6H_3)CH_2CH_2CH_2CH_2B$), 23.02 ($BCHCH_2CH_2$).

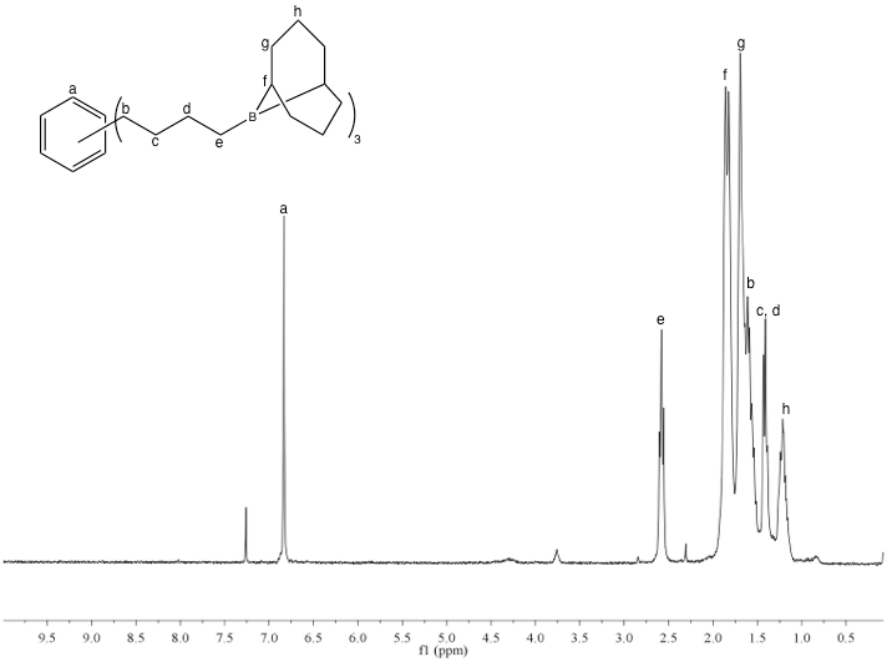

Figure 2.14 300 MHz ^{1}H NMR spectrum of **3** in $CDCl_3$.

Synthesis of tri(amido)amine cage ligand (4). Convergent Pathway (Scheme 2.2): A small bomb flask was charged with 241 mg (0.398 mmol) of **3**, 276.4 mg of **1** (0.398 mmol), 549.5 mg of K_2CO_3 (3.98 mmol), 32.4 mg of $PdCl_2(dppf)CH_2Cl_2$ (10 mol%), and 20 mL of DMF. The bomb was stirred at room temperature until the solution yielded a deep maroon color and then heated at 90 ^{o}C for 16 hours, after which the DMF was removed by vacuum distillation. The resulting residue was stirred vigorously in a DCM/dH_2O for 2 hours, extracted with DCM and hot DCM, and pumped down to yield a thick orange oil, 137 mg. This resin was washed with Et_2O to remove a yellow liquid and yield 51 mg (18%) of cream powder. The white powder was purified with column chromatography (alumina, 1% MeOH/DCM) to yield 25 mg (9%) of white powder.

Linear Pathway (Scheme 2.3) to 4: A round bottom was charged with **3** (1.05 g, 1.7 mmol) dissolved in THF and 1.18 g (5 mmol) of dipyridyl-disulfide was added as a THF

solution. Solid PPh_3 (1.41 g, 5 mmol) was added and the reaction turned yellow immediately. After stirring at room temperature for 12 hrs, the solvent was removed. The residue was dissolved in 450 mL of toluene and fitted with a 500 mL addition funnel charged with 258.7 μL (1.7 mmol) of tris(2-aminoethyl)amine (tren) in 450 mL of toluene. The tren solution was added drop wise over 4 hours and the reaction was refluxed for 12 hrs. After 12 hrs of refluxing, some white solids had precipitated. They were filtered off and the solvent was removed to yield a yellow residue. Et_2O was added and a white solid precipitate. The solid was collected to yield 0.766 g (64%) of **4**. For **4**: ^{1}H NMR (23 ^{o}C, 500 MHz, *d*$_6$-DMSO): δ 7.70 (broad, t, 3H, N*H*), 7.26 (d, 6H, (CH-$_2$)$_4$(C$_6$*H*$_4$)CH$_2$NH), 6.87 (s, 3H, C$_6$*H*$_3$), 6.74 (d, 6H, (CH$_2$)$_4$(C$_6$*H*$_4$)CH$_2$NH), 3.31 (br, NHCH$_2$C*H*$_2$N), 2.61 (t, 6H, NHC*H*$_2$CH$_2$N), 2.54 (m, 6H, (C*H*$_2$)$_4$), 2.36 (m, 6H, (C*H*$_2$)$_4$), 1.70 (m, 6H, (C*H*$_2$)$_4$), 1.29 (m, 6H, (C*H*$_2$)$_4$). ^{13}C NMR (23 ^{o}C, 75 MHz, *d*$_6$-DMSO): δ 166.72, 145.41, 140.93, 127.42, 126.95, 125.97, 53.53, 37.08, 35.07, 33.92, 29.06. ESI-TOF HRMS (MeOH) with PPG-500-800 *m/z*: $[M + Na]^+$ calculated for $C_{45}H_{54}N_4NaO_3$, 721.4094; found, 721.4087; 0.97 ppm error.

Synthesis Tris 1,3,5-(butyl-4-benzenoate) benzene (5): A bomb flask was charged with **3** (3.29 g, 543 mmol), 4-methyl iodobenzoate (7.12 g, 27.0 mmol), K_2CO_3 (11.25 g, 81.0 mmol), $PdCl_2(dppf)CH_2Cl_2$ (664 mg, 15 mol%), and 250 mL of DMF. The reaction was heated in a 50 °C oil bath for 36 hours, after which the DMF was removed via vacuum distillation. The resulting maroon residue was extracted into DCM. After the solvent was removed, the dark red residue was redissolved in minimal amounts of DCM and filtered through a pad of celite. The resulting oil was purified on a short silica plug with a 10%

EtOAc/Hexane eluting mixture. The orange oil was further purified by column chromatography (silica, gradient (5-10% EtOAc/Hexane) to yield 2.05 g (59%) of pure colorless oil. For **5**: ^{1}H NMR (23 ^{o}C, 500 MHz, $CDCl_3$): δ 7.95 (d, 6H, (C_6H_4)$COCH_3$), 7.23 (d, 6H, (C_6H_4)$COCH_3$), 6.77 (s, 3H, (C_6H_3)$(CH_2)_4$), 3.87 (s, 3H, (C_6H_4)$COCH_3$), 2.67 (t, 6H, (C_6H_3)$(CH_2)_4$), 2.56 (t, 6H, (C_6H_3)$(CH_2)_4$), 1.66 (m, 12H, (C_6H_3)$(CH_2)_4$). ^{13}C NMR (23 ^{o}C, 75 MHz, $CDCl_3$): δ 147.9 (COOMe), 142.0 (C_6H_3), 129.4 (C_6H_4), 128.2 (C_6H_4), 127.4 (C_6H_4), 125.7 (C_6H_3), 105.2(C_6H_4), 51.8 (COO*Me)*, 35.6 ($CH_2CH_2CH_2CH_2$), 35.4 ($CH_2CH_2CH_2CH_2$), 30.8 ($CH_2CH_2CH_2CH_2$), 30.6 ($CH_2CH_2CH_2CH_2$).

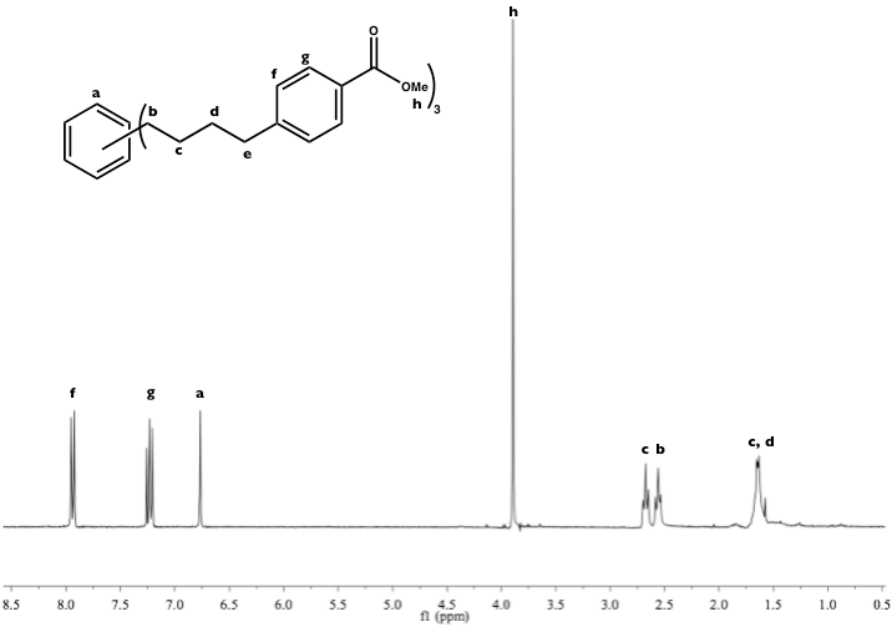

Figure 2.15 300 MHz ^{1}H NMR spectrum of **5** in $CDCl_3$.

Synthesis of Tris 1,3,5-(butyl-4-benzenoic acid) benzene (6): A round bottom was charged with **5** (4.0 g, 6.2 mmol) dissolved in a mixture of MeOH and H_2O (10:1). 250 mL of a 5M KOH solution was added to the stirring solution. After 24 hrs of stirring a

white precipitate had formed and the reaction was quenched with 250 mL of a 6M HCl solution. The product was extracted into Et_2O (3 x 100 mL) and isolated as a white solid (3.3 g) in an 87% yield. For **6**: ^{1}H NMR (23 ^{o}C, 500 MHz, d_6-DMSO): δ 12.77 (br s, 3H, COO*H*), 7.83 (d, 6H, C_6H_4), 7.27 (d, 6H, C_6H_4), 6.75 (s, 3H, C_6H_3), 2.63 (t, 6H, $(CH_2)_4$), 2.51 (t, 6H, $(CH_2)_4$), 1.54 (m, 12H, $(CH_2)_4$). ^{13}C NMR (23 ^{o}C, 75 MHz, d_6-DMSO): δ 167,79 (*C*OOH), 148.13 (C_6H_3), 142.30 (C_6H_4), 129.85 (C_6H_4), 128.12 (C_6H_4), 128.77 (C_6H_4), 126.20 (C_6H_3), 35.30 ((C_6H_3)*C*$H_2CH_2CH_2CH_2$(C_6H_4)), 30.99 ((C_6H_3)$CH_2CH_2CH_2CH_2$(C_6H_4)), 30.66 (((C_6H_3)$CH_2CH_2CH_2CH_2$(C_6H_4)).

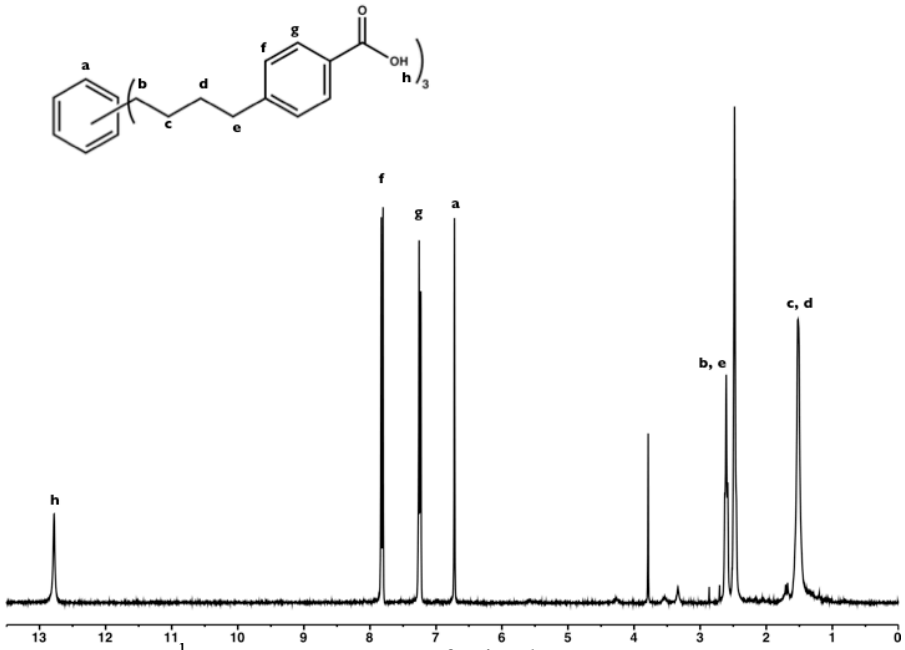

Figure 2.16 300 MHz ^{1}H NMR spectrum of **6** in d_6-DMSO.

Synthesis of tris-1,3,5-(butyl-4-benzylalcohol) (7): A solution of **5** (1.49 g, 2.3 mmol) in 200 mL Et_2O was added drop wise to a cooled slurry of $LiAlH_4$ (2.62 g, 69.0 mmol) and stirred overnight while warming to room temperature. 100 mL of MeOH and 100 mL of a saturated solution of Rochelle's Salt were added and the resulting solution was

stirred for 3 hours to quench the reaction and excess LAH. An aqueous/Et_2O extraction and removal of solvent yielded a clear oil (896 mg, 69% yield). For **7**: ^{1}H NMR (23 ^{o}C, 500 MHz, $CDCl_3$): δ 7.25 (d, 6H, $(CH_2)_4C_6H_4$), 7.15 (d, 6H, $(CH_2)_4C_6H_4$), 6.79 (s, 3H, C_6H_3), 4.64 (s, 6H, (C6H4)CH2OH), 2.60 (dt, 12H, CH_2(C6H4)), 1.87 (br, OH), 1.65 (m, 12H, $CH_2(CH_2)_2CH_2$).

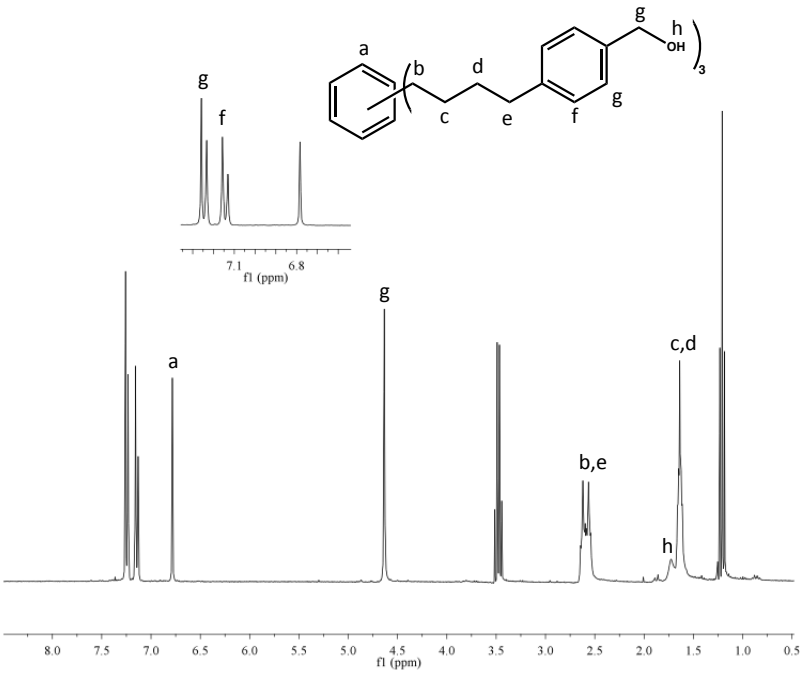

Figure 2.17 300 MHz ^{1}H NMR spectrum of **7** in $CDCl_3$.

Synthesis of tris-1,3,5-(butyl-4-benzaldehyde) (8): Excess MnO_2 (2.8g, 32.2 mmol) was added as a solid to a DCM solution of **7** (896 mg, 1.58 mmol) and stirred overnight at room temperature. After filtration to remove excess MnO_2 and removal of solvent in vacuo, a colorless oil remained (700 mg, 79% yield). For **8**: ^{1}H NMR (23 ^{o}C, 500 MHz, $CDCl_3$): δ 9.97 (s, 3H, CO*H*), 7.78 (d, 6H, $(CH_2)_4C_6H_4$), 7.38 (d, 6H, $(CH_2)_4C_6H_4$), 6.78 (s, 3H, C_6H_3), 2.71 (t, 6H, CH_2(C6H4)), 2.58 (t, 6H, $(C_6H_3)CH_2$), 1.67 (m, 12H,

$CH_2(CH_2)_2CH_2$). ^{13}C NMR (23 ^oC, 75 MHz, $CDCl_3$): δ 191.6, 149.9, 142.1, 134.2, 129.7, 129.0, 125.7, 35.8, 35.4, 30.8, 30.5.

Figure 2.18 300 MHz ^1H NMR spectrum of **8** in $CDCl_3$.

Synthesis of tri(amino)amine cage ligand (9): 8 (169 mg, 0.303 mmol) was dissolved in 800 mL of MeOH and a solution of tren (44.3 mg, 0.303 mmol) was added with stirring. An excess of molecular sieves were added to the reaction to remove the water from the reaction. The reaction was stirred overnight and then filtered through a pad of Celite. The resulting solution was cooled to -78 °C using a dry ice acetone bath. After cooling, the solution was cannula transferred into a Schlenk flask charged with an excess of $NaBH_4$ (45.3 mg, 10 mmol) in MeOH. The reaction was stirred at room temperature overnight and 90 mg (47% yield) of product was isolated after an H_2O/CH_2Cl_2 extraction and washing with hexane. For **9**: ^1H NMR (23 ^oC, 500 MHz, $CDCl_3$): δ 6.79 (s, 3H, C_6H_3), 6.67 (dd, 12H, $(CH_2)_4(C_6H_4)CH_2NH$), 3.41 (s, 6H, $(C_6H_4)CH_2NH$), 2.62 (m, 6H,

NHCH_2CH$_2$N), 2.58 (m, 6H, NHCH$_2$CH_2N), 2.49 (m, 6H, (CH_2)$_4$), 2.34 (m, 6H, (CH_2)$_4$), 1.70 (m, 6H, (CH_2)$_4$), 1.34 (m, 6H, (CH_2)$_4$).^{13}C NMR (23 ^{o}C, 75 MHz, $CDCl_3$): δ 141.3, 141.1, 136.4, 127.7, 127.6, 126.2, 54.1, 53.5, 47.7, 35.3, 29.6, 29.1.

2.5.3 X-Ray Crystallographic Data Collection and Refinement of the Structures

Single crystals of **10[PPh$_4$]** were grown from a concentrated solution of THF. Colorless plates of **10[PPh$_4$]** (0.30 x 0.20 x 0.15 mm^3) were placed on the tip of a glass capillary and mounted on a Bruker APEX II CCD diffractometer for data collection at 173(2) K.[46] The data collection was carried out using Mo-Kα radiation (graphite monochromator). The data intensity was corrected for absorption and decay (SADABS).[47] Final cell constants were calculated from the xyz centroids of 13595 strong reflections from the actual data collection after integration (SAINT).[48] The structure was solved using SHELXS-97 and refined using SHELXL-97.[49] The space group P2(1)/n was determined based on systematic absences and intensity statistics. A direct-methods solution was calculated which provided most non-hydrogen atoms from the E-map. Full-matrix least squares / difference Fourier cycles were performed which located the remaining non-hydrogen atoms. All non-hydrogen atoms were refined with anisotropic displacement parameters. All hydrogen atoms were placed in ideal positions and refined as riding atoms with relative isotropic displacement parameters. The final full matrix least squares refinement converged to $R1 = 0.0513$ and $wR2 = 0.1346$ (F^2 , all data). Crystallographic data is summarized in Table 2.4. Void space analysis parameters were measured using PLATON/VOID.[41,50] The detection of voids by PLATON/VOID is completed as described herein. The unit cell is filled with the atoms from the structural model and each

specific atom is assigned its respective van der Waals radius. A grid search generates a list of grid points with a minimum distance of 1.2 Å from the nearest van der Waals surface. This list of grid points is then used to produce a new list of grid points that makes up the void areas. The diameter and volume of the void is determined.

Chapter 3

Bio-inspired Ligand Scaffolds Containing Three NADH-Like Moieties

3.1 Overview

A novel tripodal ligand system featuring three NADH-like moieties has been synthesized and characterized. The ligand system, $H_3[(^{Bn}NADH)tren]$ (**3**) has been metallated with zinc, $PPh_4[Zn(^{Bn}NADH)_3tren]$ (**7**), and cobalt, $PPh_4[(^{Bn}NADH)trenCo]$ (**8**). Both complexes were characterized by ^1H NMR spectroscopy, and zinc complex **7** has been characterized by X-ray crystallography and paramagnetic cobalt complex **8** has been characterized by EPR. Theoretical studies reveal a hydricity of $\Delta G_{H^-} = 63$ kcal/mol for NADH analogue **3**. Interestingly, theoretical calculations predict that chelation of a transition metal (Zn or Co) increases the hydricity by 10 kcal/mol compared to ligand **3**. Preliminary hydride transfer studies show that the tripodal NADH analogue can transfer all three hydrides to the hydride acceptor CPh_3BF_4.

3.2 Introduction

The thermodynamic cost of reducing small molecules, such as CO_2 and N_2 into more useful chemicals is significantly decreased when multiple protons and electrons are added simultaneously or in fast sequential steps (*vida supra)*. Practically, delivering multiple equivalents of protons and electrons simultaneously is challenging; however, biology can provide some insight into achieving this goal. On particular source of inspiration is the biological cofactor nicotinamide adenine dinucleotide (NAD^+) and its two electron reduced counterpart dihydronicotinamide adenine dinucleotide (NADH) (Figure 3.1) These cofactors can efficiently reduce and oxidize a variety of substrates through the transfer of a hydride (or a proton and two electrons).

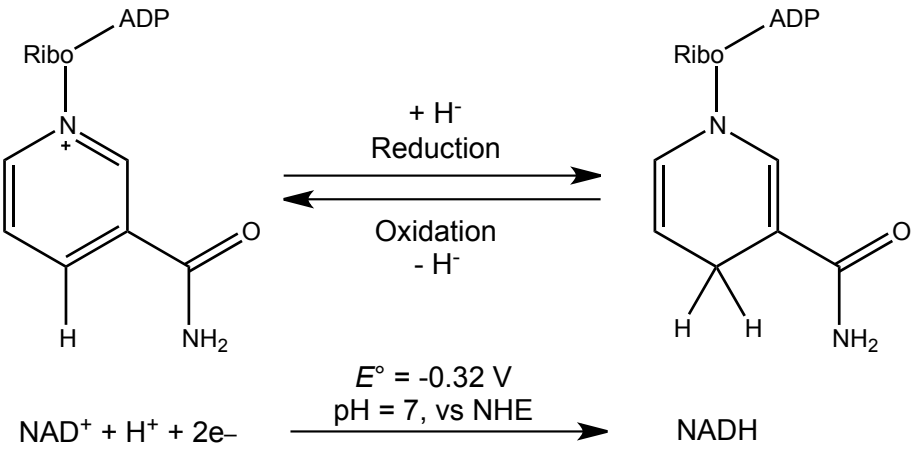

Figure 3.1 Biological cofactors NADH and NAD^+.

The NADH cofactor operates at a relatively negative potential of E° = -0.32 V vs NHE at pH = 7.[1] The NADH/NAD^+ redox couple is essential during cellular respiration by both accepting and delivering hydride equivalents.[2] In the first two steps of cellular respiration (glycolysis and Kreb's cycle) NAD^+ oxidizes substrates such as glucose and pyruvate by accepting hydride equivalents. More interesting though is the oxidation of NADH back to NAD^+ during the last step of cellular respiration known as the electron transfer chain. In this step, NADH reduces the small molecule dioxygen (O_2) to water by transferring its hydride through redox mediators (***Eqn 1***). It is this final step of hydride delivery that is of particular interest.

$$NADH + O_2 + 2H^+ \rightarrow NAD^+ + 2H_2O \quad (\boldsymbol{Eqn\ 1})$$

Many scientists have studied NADH models as hydride sources in organic catalysis. Two common NADH models studied are 1-benzyl-1,4-dihydronicotinamide (BNAH) and the Hantzsch ester (Figure 3.2). Initially, the reactivity of such organic hydrides was limited to electron-poor carbon-carbon double bonds and required heat. Improved reactivity was realized when a photosensitizer ($Ru(bpy)_3^{2+}$ (bpy = 2,2'-

bipyridine) is utilized. Olefins unreactive toward BNAH in the dark are reduced by BNAH upon selective photoexcitation of $Ru(bpy)_3^{2+}$ through a proposed mechanism of sequential electron transfer.[3] Unfortunately, BNAH is susceptible to radical decomposition products under irradiating conditions.[4] Recently, BNAH was successfully used as a catalyst in the reduction of α-β-epoxy ketones to β-hydoxy ketones with a BNAH catalytic loading of 1-5 mol% in the presence of excess NaS_2O_4 and $NaCO_3$ in water to regenerate BNAH from the BNA^+ by-product.[5].

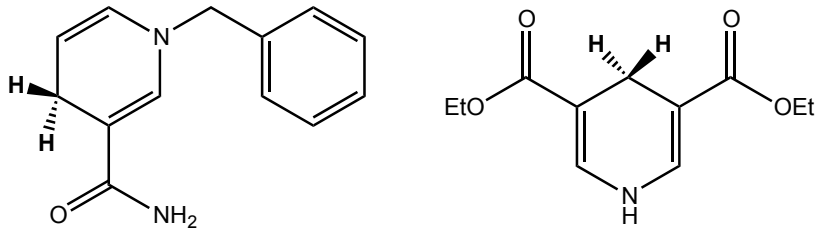

BNAH **Hantzsch Ester**

Figure 3.2 Examples of NADH model compounds.

The Hantzsch ester has recently been used a stoichiometric hydrogen transfer reagent in the enantioselective reduction of α,β–unsaturated aldehydes.[6-8] This application was quickly extended to the enantioselective reduction of α,β–unsaturated ketones,[9] imines,[10] and enamides.[11] While the Hantzsch ester is widely versatile as a hydrogen transfer reagent, all of the current reactions are stoichiometric as the Hantzsch ester cannot be regenerated.

Given the application towards organic catalysis, we were particularly interested in a system that couples the hydride donating abilities of NADH analogues to a reactive transition metal complex to cooperatively transfer multiple equivalents of protons and electrons simultaneously. While this goal has not yet been achieved, the inter- and

intramolecular reaction of transition metal complexes and NADH models has been studied. One example is the intermolecular hydride transfer to high-valent metal oxo complexes. Transition metal oxos are known to have extremely strong bonds that are difficult to activate. Studies on a manganese(V)-oxo porphyrin (formed via disproportionation of a Mn(IV)-oxo) show that BNAH can transfer a hydride to yield a Mn(III)-OH complex. Mechanistic studies reveal that the BNAH is operating through direct hydride transfer, not sequential hydrogen atom transfer followed by electron transfer.[12]

Appending an NADH analogue to a transition metal ligand scaffold allows for the study of intramolecular hydride transfer. Recently, a BNAH moiety was built into a cyclen ligand scaffold that binds Zn(II) (Figure 3.3). The Zn(II) can bind flavin, which is subsequently reduced by the appended BNAH. Kinetic studies showed that the intramolecular reduction of the flavin molecule was 175 times faster than the intermolecular reaction with BNAH.[13]

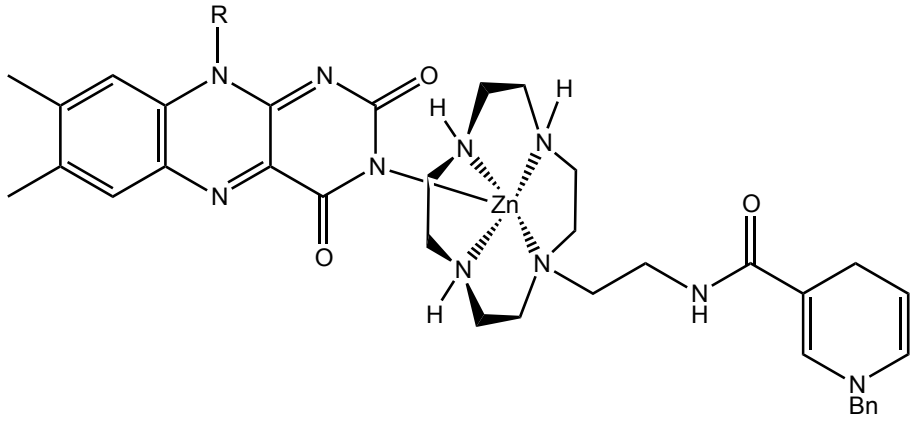

Figure 3.3 Zn(II) NADH anlogue binding flavin.

Recently, Tanaka and coworker have demonstrated a NADH/NAD^+ type redox couple with a $Ru(bpy)_2(pbn)$ (pbn = 2-(2-pyridyl)benzo[b]-1.5-naphthyridine). The reduced NADH-like species ($pbnH_2$) is formed by irradiation of the Ru complex in the presence of a sacrificial electron donor. By utilizing an intramolecular NADH-type moiety, photodecomposition products, observed in similar intermolecular systems, are avoided.[3] This system can electrochemically reduce acetone to isopropanol at a voltage of -1.14 V (vs Fc/Fc^+, Fc = Ferrocene) in an acidic media.[14,15] Tanaka and coworkers are currently investigating these complexes toward the reduction of CO_2.[16]

As illustrated by the examples above, combination of a transition metal complex with NADH analogues is not unprecedented. However, a system that can offer multiple equivalents of hydride, or protons and electrons stored as a hydride, in one step or in quick sequential steps is largely unexplored. Herein we describe a new ligand scaffold that incorporates three NADH moieties onto a well-known transition metal chelating tetraamine, tren (tris(2-aminoethyl)amine). The synthesis, characterization and reactivity of the NADH-like ligand scaffold as well as coordination complexes with Zn and Co are discussed.

3.3 Results and Discussion

3.3.1 Synthesis and Characterization of NADH-like Ligand $H_3[^{Bn}(NADH)_3tren]$ ***3***

The NADH analogue, N,N',N''-tris(1-benzyl-1,4-dihydropyridine-3-carboxamide)triethylamine ($H_3[^{Bn}(NADH)_3tren]$ **3**) was synthesized in three steps, starting with the synthesis of proligand, 2,2',2''-tris(*n*icotin*a*mide)triethylamine (H-

$_3$[(NA)$_3$tren] **1**) (Scheme 3.1). Proligand **1** was synthesized via amide formation from the reaction of nicotinyl chloride with tren in the presence of triethylamine (NEt_3). The reaction is high yielding (64%) and the crude product requires no further purification, as observed by ^{1}H NMR spectroscopy and ESI-MS. In the ^{1}H NMR spectrum the four aryl nicotinamide protons have distinctive shifts at 8.95, 8.65, 8.11, and 7.42 ppm. The amide protons have a chemical shift of 8.62 ppm and are distinctive by their pseudo-triplet peak shape from coupling with ^{14}N.

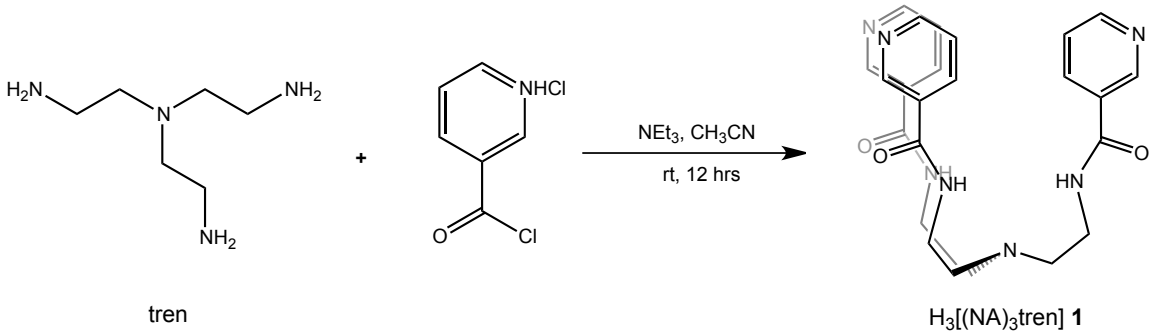

tren

H$_3$[(NA)$_3$tren] **1**

Scheme 3.1 Synthesis of proligand, H$_3$[(NA)$_3$tren] **1**.

Synthesis of the NAD^+ analogue, 2,2',2''-tris(1-benzyl-pyridinium-3-carboxamide)triethylamine hydrochloric acid ($H_3[^{Bn}(NAD^+)_3tren]Br_3HCl$, **2**) was modeled off of the synthesis of BNA^+ with minor modifications due to the tren backbone (Scheme 3.2). The tertiary apical amine is susceptible to alkylation under the reported conditions; thus, it must be protected prior to alkylation using hydrochloric acid (HCl). Once the apical amine has been protected, reaction with three equivalents of benzyl bromide yields the trisbenzylated pryidinium HCl salt **2**. Precipitation from Et_2O resulted in pure product. The NAD^+ analogue was characterized by ^{1}H NMR spectroscopy and ESI-MS. The ^{1}H NMR spectrum has four downfield shifted aryl peaks compared to proligand **1**, characteristic of pyridinium compounds, at 9.74, 9.31, 9.04, and 8.28 ppm.

For synthetic ease, $H_3[^{Bn}(NAD^+)_3tren]Br_3HCl$ was isolated as the hydrochloride salt because deprotection is not required for subsequent steps; however, if desired the HCl salt can be deprotonated using an excess of sodium tert-butoxide. The ^1H NMR spectrum of the deprotonated form remains unchanged with the exception of the methylene protons of the tren backbone closest to the tertiary amine, which shift upfield by about 1 ppm.

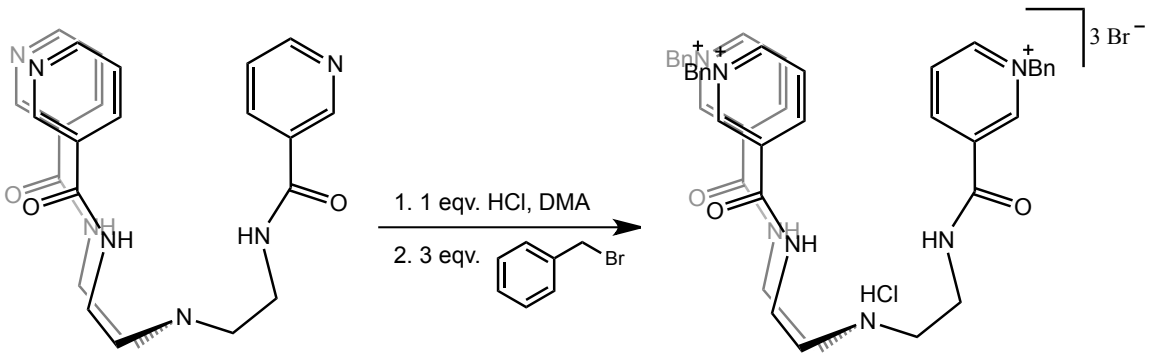

$H_3[(NA)_3tren]$ **1** $H_3[(^{Bn}NAD^+)_3tren]Br_3HCl$ **2**

Scheme 3.2 Synthesis of NAD^+ analogue, $H_3[(^{Bn}NAD^+)_3tren]Br_3HCl$ **2**.

The last and most synthetically challenging step in the synthesis of the NADH analogue is the reduction of the pyridinium moiety in **2** to form the 1,4 dihyropyridine (1,4-DHP) moiety in NADH analogue, $H_3[(^{Bn}NADH)_3tren]$ **3**. Traditional hydride sources, such as $LiAlH_4$, sodium borohydride ($NaBH_4$) and sodium hydride (NaH), are too strong to afford the singly reduced dihydropyridine product. Instead, the pyridnium ring is fully saturated with these hydride sources. Literature procedures for the synthesis of BNAH utilize sodium dithionite ($Na_2S_2O_4$) as the two-electron reductant in an alkaline media to selectively yield the 1,4-DHP product. A combined experimental and theoretical study proposed a thermodynamic argument for the preferential formation of 1,4-DHP over the formation of the other two conformations (1,2-DHP and 1,6-DHP). According to theoretical studies on BNAH, the 1,4-DHP is preferred by 3 kcal/mol over the other two

conformers. Furthermore, each conformer was identified by ^{1}H and ^{13}C NMR spectroscopy, and in the case of BNAH the 1,4-DHP and the 1,6-DHP conformers were observed in a 95% and 5% yield, respectively and no 1,2-DHP was not observed.[17]

Using a variation of this method, the synthesis of **3** was successful via reduction of **2** using $Na_2S_2O_4$ in a biphasic toluene and alkaline aqueous solution (Scheme 3.3). Although the procedure for the synthesis of **3** is very similar to the reported synthesis of BNAH, some modifications to reaction times were required. A biphasic solvent mixture of water and toluene easily separated the reduced product and the salts formed during the reaction. Interestingly, alternative procedures suggested refluxing for 24 hours, however, we observed increased amounts of undesired products with long reactions times (presumably 1,2-DHP and 1,6-DHP). In order to prevent formation of undesired conformers, reaction times must be kept between 8 to 10 minutes. The modifications afford the NADH analogue, **3**, as a bright orange foam in 62% yield with approximately 90% purity. Many reaction conditions were interrogated in attempts to optimize the reaction conditions to obtain higher purity, albeit without success. Further purification of **3** after isolation was also explored, but unfortunately did not yield a higher purity product. The product was characterized by ^{1}H NMR spectroscopy and ESI-MS. Most notably, in the ^{1}H NMR spectrum, the downfield pyridinium protons of **2** disappear and three new peaks associated with the 1,4-DHP moiety at 6.61, 5.90, and 5.97 ppm appear. The resonances at 5.90 and 5.97 ppm have splitting indicative of vinylic protons.

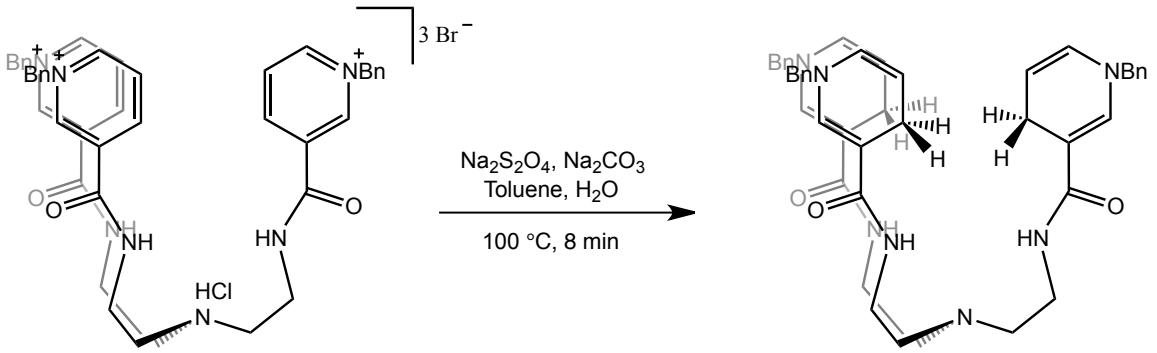

$H_3[(^{Bn}NAD^+)_3Br_3HCl$ **2** $H_3(^{Bn}NADH)_3tren]$ **3**

Scheme 3.3 Synthesis of NADH analogue, $H_3[^{Bn}(NADH)_3tren]$ **3**.

For this ligand family, ^1H NMR spectroscopy is an extremely useful tool to monitor electronic changes occurring on the pyridine ring throughout the family. An overlay of the ^1H NMR spectra of $H_3[(NA)_3tren)]$ **1**, $H_3[^{Bn}(NAD^+)_3tren]Br_3HCl$ **2** and $H_3[^{Bn}(NADH)_3tren]$ **3** is shown in Figure 3.4. In the overlay, asterisks identify the protons associated with the pyridine ring in each species. The four protons in the pyridine ring shift dramatically from one complex to the next (*vide supra*). Particularly useful is the difference between the pyridinium protons in **2** and the 1,4-DHP protons in **4**. The distinctiveness of these two species by ^1H NMR spectroscopy will allow for spectroscopic analysis of hydride transfer.

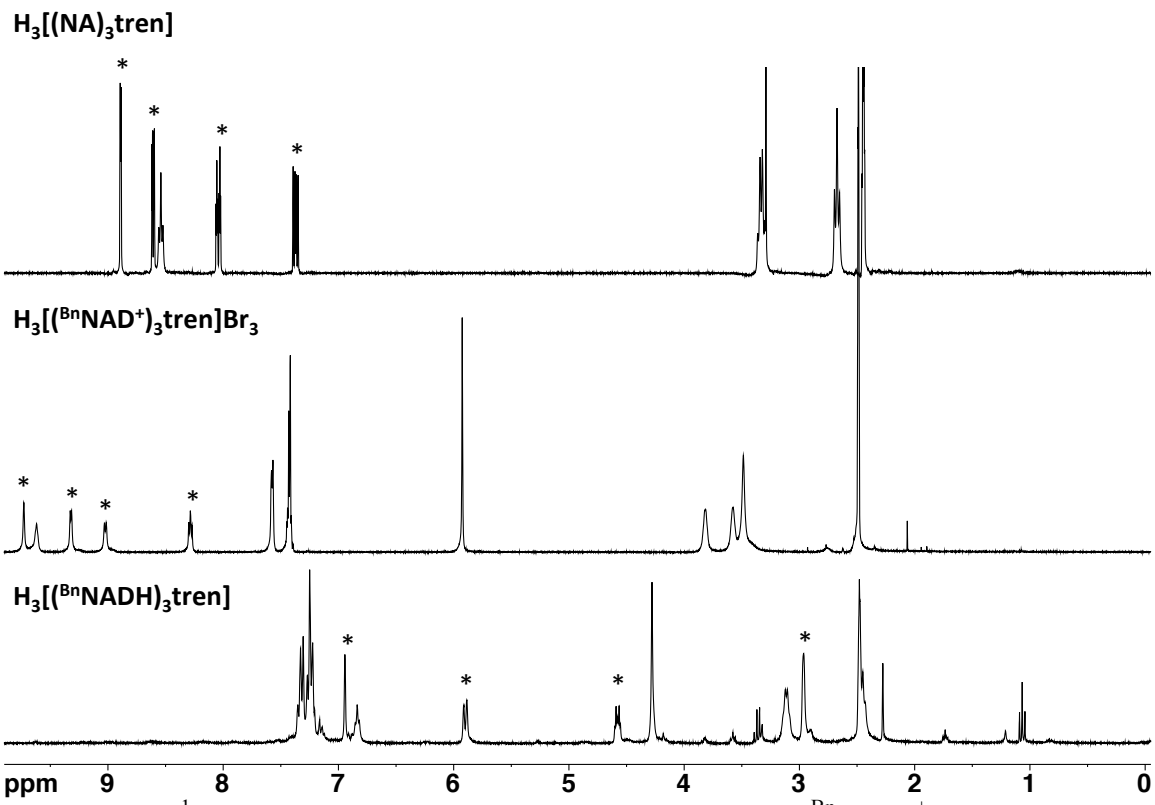

Figure 3.4 ^{1}H NMR spectra of $H_3[(NA)_3tren)]$ **1**, $H_3[^{Bn}(NAD^+)_3tren]Br_3HCl$ **2**, $H_3[^{Bn}(NADH)_3tren]$ **3**.

*3.3.2 Synthesis and Characterization of [M(NA)$_3$tren)] Complexes, where M = Zn (**4**), Co (**5**), and Fe (**6**)*

The coordination chemistry of proligand **1** was explored with first row transition metals. Proligand **1** was metallated with iron, cobalt and zinc as outlined in Scheme 3.4. Potassium hydride (KH) was used to deprotonate $H_3[(NA)_3tren)]$ in dimethylacetylamide (DMA) due to the insolubility of **1**. Complexes **4**, **5**, and **6** are isolated by precipitation from the DMA solution using copious amounts of diethyl ether (Et_2O).

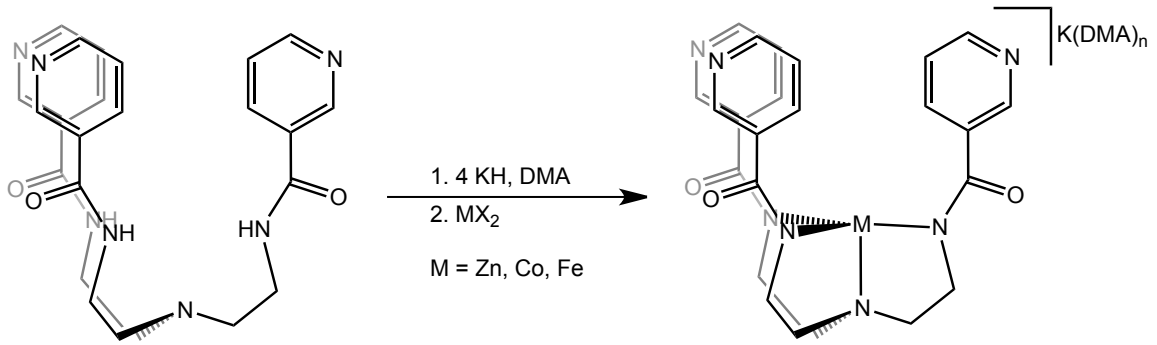

$H_3[(NA)_3tren]$ **1**

$K(DMA)_n[M(NA)_3tren]$

M = Zn **4**
Co **5**
Fe **6**

Scheme 3.4 Synthesis of $K(DMA)_n[M(II)(NA)_3tren)]$, where M = Zn **4**, Co **5**, Fe **6**.

Complex **4** was isolated as a salmon colored solid in 43% yield. The ^1H NMR spectrum of **4** revealed a C_3 symmetric species with six unique proton resonances. The four aryl resonances of $K(DMA)_n[Zn(NA)_3tren)]$ **4** shift upfield compared to those of $H_3[(NA)_3tren)]$ **1** in the ^1H NMR spectrum (Figure 3.5). The amide proton resonance is also absent, further supporting the formation of **4**. Complex **5** was isolated as a turquoise colored solid in an 89% yield. The ^1H NMR spectrum has five paramagnetically broadened proton resonances ranging from 80 to -6 ppm. It is likely that the last proton for complex **5** is too paramagnetically broadened to see using a 300 MHz spectrometer. Complex **6** was isolated as a yellow solid in 83% yield. Similar to **5**, complex **6** is also paramagnetic. However, the ^1H NMR spectrum of **6** has six distinct proton resonances from 66 to -57 ppm. This likely a result of less paramagnetic broadening in **6,** as evidenced by the sharpness of the peaks.

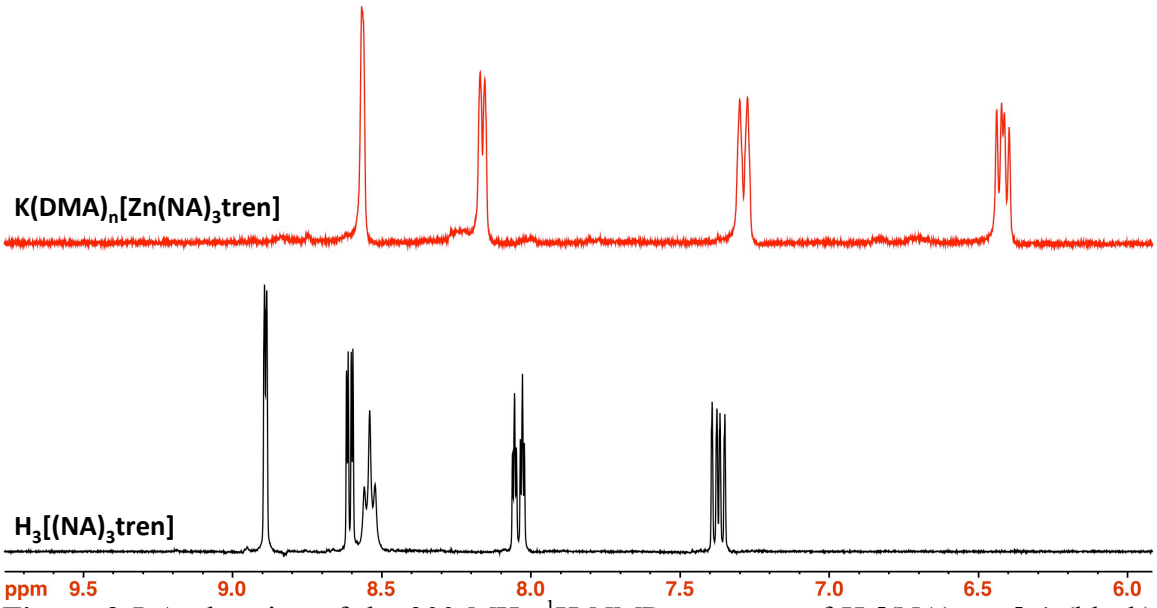

Figure 3.5 Aryl region of the 300 MHz ^{1}H NMR spectrum of $H_3[(NA)_3tren]$ **1** (black) and $K(DMF)_n[Zn(NA)_3tren]$ **4** (red).

3.3.3 Synthesis and Characterization of $PPh_4[M(^{Bn}NADH)_3tren)]$, where M = Zn and Co

Metallation of NADH analogue $H_3[(^{Bn}NADH)_3tren]$ **3** was completed using zinc and cobalt. The synthesis of $PPh_4[M(^{Bn}NADH)_3tren)]$, (Zn **7**, Co **8**) was achieved in a very similar fashion to the synthesis for complexes **4-6**. Two small deviations improved the isolation of complexes **7** and **8** (Scheme 3.5). First, NADH analogue **3** is soluble in THF unlike proligand **1**, thus a 1:10 mixture of DMF:THF was used in these metallations. Furthermore, isolation of the potassium salts proved to be difficult, largely due to solubility; as a result, the potassium countercation was exchanged for tetraphenylphosphonium cation (PPh_4^+) *in situ* using PPh_4Cl.

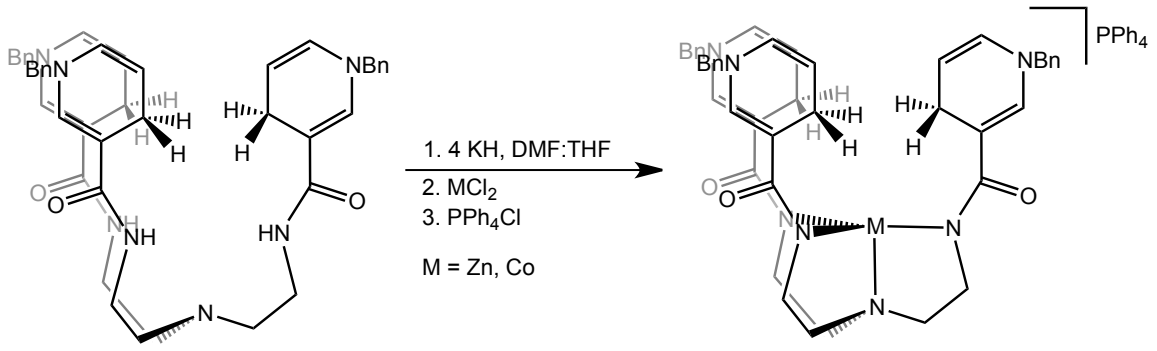

$H_3[(^{Bn}NADH)_3tren]$ **1**

$PPh_4[Zn(^{Bn}NADH)_3tren]$

M = Zn **7**
Co **8**

Scheme 3.5 Synthesis of $PPh_4[M(^{Bn}NADH)_3tren)]$, where M = Zn **7** and Co **8**.

The diamagnetic nature of zinc(II) enables reaction monitoring using ^{1}H NMR spectroscopy. An overlay of the ^{1}H NMR spectra of **3** and zinc complex **7** is shown in Figure 3.6. The first indication of a successful synthesis was the disappearance of the amide protons at 6.85 ppm. Paramagnetic cobalt complex **8** has a paramagnetically broadened ^{1}H NMR spectrum with approxiamately four peaks ranging from -10 ppm to 65 ppm. Interestingly, the aryl protons from the benzyl ring are removed enough from the paramagnetic cobalt metal center and are not shifted, relatively sharp, and remain unaffected by the paramagnetism.

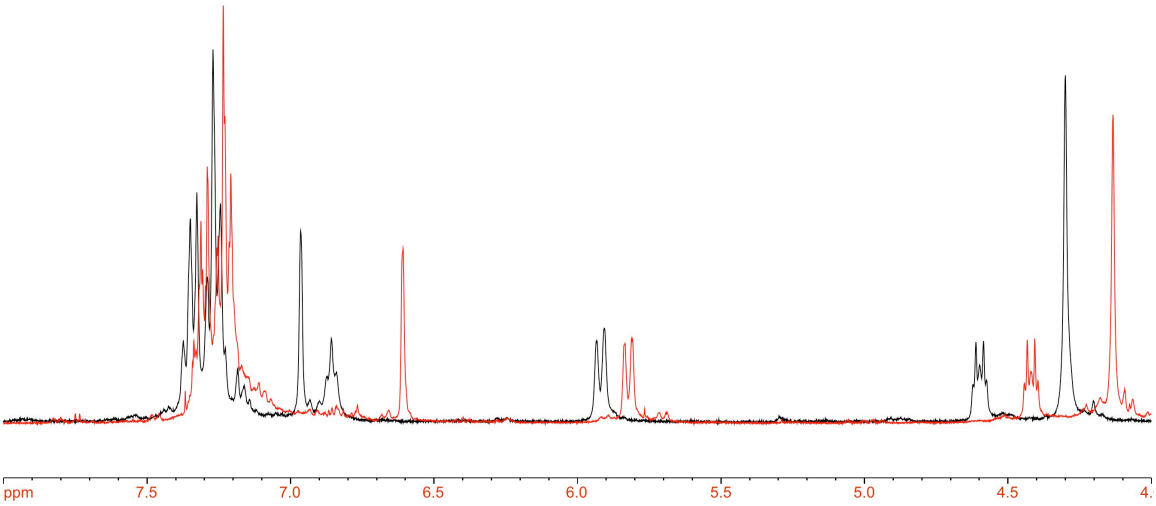

Figure 3.6 ^{1}H NMR spectrum of $H_3[(^{Bn}NADH)_3tren)]$, (black) and $K(DMF)_n[Zn(^{Bn}NADH)_3tren)]$, (red) in d_6-DMSO.

*3.3.4 Solid-State Structures of Complexes **4, 5,** and 7*

X-ray quality single crystals of K[Zn(NA)$_3$tren)], **4** were grown from vapor diffusion of dichloromethane (DCM) into a concentration DMSO solution. The crystals were analyzed by single crystal X-ray diffraction (Figure 3.7). The complex crystallized in a perfectly C_3 symmetric manner with the potassium counterion situated on top of the complex, interacting with the three pyridine rings. Only one of the arms is crystallographically unique, leading to only 14 atoms in the asymmetric unit (Table 3.1). The unit cell of **4** has three complete molecules related by three-fold axis that runs through the potassium, zinc and apical nitrogen. The potassium ion also interacts with three oxygen atoms of three different molecules, creating a polymeric chain. The potassium ion is six-coordinate, coordinating to the three pyridine nitrogens and an oxygen of three other molecules The zinc – nitrogen bond lengths of 2.155(9) Å and 1.979(9) Å for Zn-N_{ax} and Zn-N_{eq}, respectively, match well with literature values for a

zinc(II) ion in a similar environment. A tris(amido)amine Zn(II) complex synthesized previously in our group exhibits similar bond lengths of 2.128(2) Å and 1.984(2) Å (avg) for the Zn-N_{ax} and Zn-N_{eq} bonds, respectively (*vide supra*, Chapter 2).

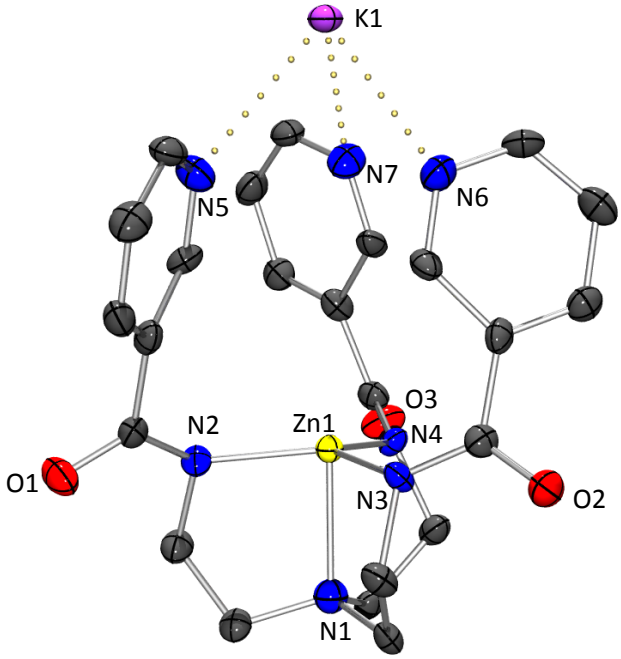

Figure 3.7 Solid-state structure of **4** at 50% probability. Selected bond lengths (Å) and angles (°): Zn1-N1: 2.155(9), Zn1-N2: 1.979(4), N5-K1: 2.952, N2-Zn1-N3: 119.4(2), N1-Zn1-N2: 85.5(3).

Single crystals of **5** were grown by encapsulating the potassium cation with 18-crown-6 (1,4,7,10,13,16-hexaoxacyclooctadecane). The 18-crown-6 (18C6) increases the solubility of the complex and X-ray quality crystals were grown from diffusion of Et_2O into a concentrated THF solution (Figure 3.8). Crystallographically, the 18-crown-6 decreases the symmetry of the complex as it crystallizes in a triclinic space group (Table 3.1). There are two molecules in the unit cell that are related through the inversion center in the space group P_{-1}. The lack of symmetry in the solid-state structure is evident in the bond angles in the Co-N_{eq} plane: N2-Co1-N3: 117.8(1), N2-Co1-N4: 118.8(1), N3-Co1-

N4: 121.5(1). Of note, the Co1-N2 bond length is slightly lengthened at 1.985(3) Å compared to the other Co1-N_{eq} distances of 1.974(3) and 1.973(2) Å; this is potentially be due to N2 being associated with the amide group that interacts with the potassium cation.

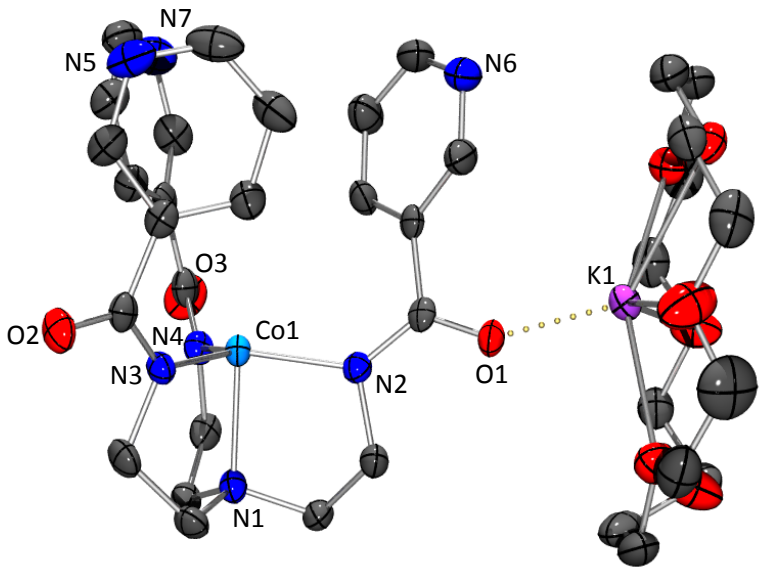

Figure 3.8 Solid-state structure of **K(18C6)[5]** at 50% probability. Selected bond lengths (Å) and angles (°): Co1-N1: 2.101(3), Co1-N2: 1.985(3), Co1-N3: 1.974(3), Co1-N4: 1.973(2), O1-K1: 2.705(3), N1-Co1-N2: 85.3 (1), N2-Co1-N3: 117.8(1), N2-Co1-N4: 118.8(1), N3-Co1-N4: 121.5(1),.

Single crystals suitable for X-ray diffraction of K[Zn(^{Bn}NADH)$_3$tren)] were grown by slow vapor diffusion of Et_2O into a concentrated solution of DMF. The crystal structure reveals a trigonal monopyramidal coordination geometry around the zinc(II) center (Figure 3.9). Examination of the Zn-N_{eq} bond lengths and N_{eq}-Zn-N_{eq} angles suggest a pseudo-C_3 symmetric complex as observed by ^{1}H NMR spectroscopy; however, the dihydropyridine groups are twisted and the benzyl groups are highly rotationally disordered supporting the lack of C_3 symmetry in the crystal structure. We postulate that this is due to crystal packing, and that in solution these moieties are freely rotating, explaining the observed C_3 symmetry in the ^{1}H NMR spectrum. The bond lengths around

the zinc metal center in **[7]K** are very similar to those of the proligand complex **[4]K**. The Zn-N_{ax} bond length shortens by 0.06 Å and the Zn-N_{eq} bond lengthens by an average of 0.02 Å. The solid-state structure also confirms the formation of a 1,4-DHP moiety. The C1-C2 bond length in the 1,4-DHP is elongated to 1.508 Å (compared to a bond length of 1.351 Å in **4**) and distinctly different than the C2-C3 bond length of to 1.328 Å, indicating loss of aromaticity.

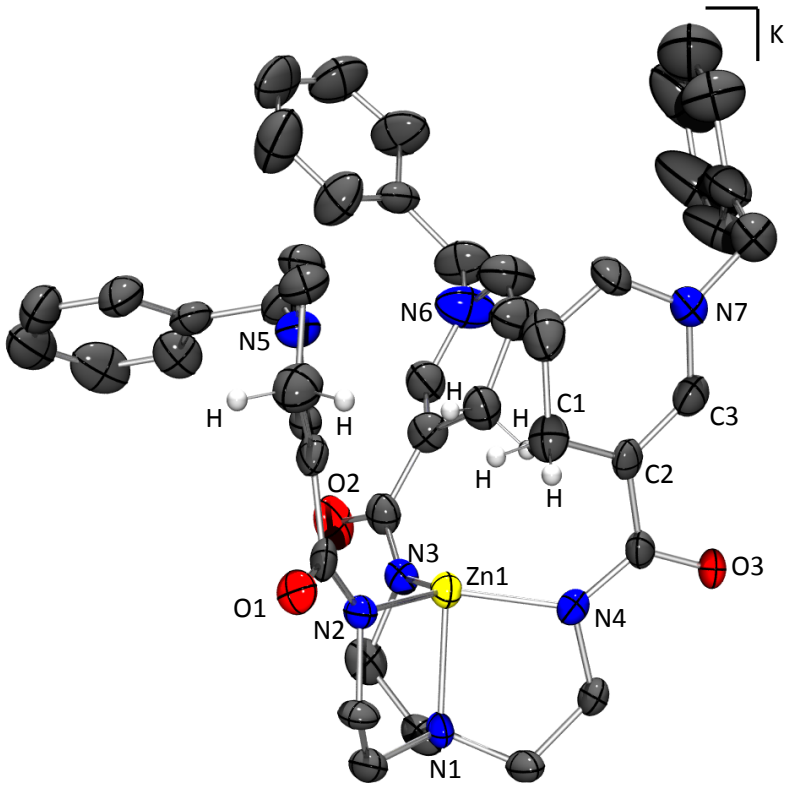

Figure 3.9 Solid-state struction of **[7]K** at 50% probability. Selected bond lengths (Å) and angles (°): Zn1-N1, 2.092(4); Zn1-N2, 1.999(5); Zn1-N3, 2.004(5); Zn-N4, 2.009(5); C2-C3, 1.328(9); C1-C2, 1.508(7), N1-Zn1-N2, 86.8(2), N2-Zn1-N3, 118.3(2), N2-Zn-N4, 120.4(2); N3-Zn1-N4, 120.3(2).

Table 3.1 Crystallographic information for solid-state structures of **[4]K**, **[5]K(18C6)**, **[7]K**.

	[4]K	**[5]K(18C6)**	**[7]K**
chemical formula	$C_{24}H_{24}N_7O_3ZnK$	$C_{36}H_{48}N_7O_9CoK$	$C_{45}H_{48}N_7O_3ZnK$
formula weight	562.97	820.84	839.37
crystal system	trigonal	triclinic	monoclinic
space group	R_3	P_{-1}	$P2_1/c$
a (Å)	10.147(2)	11.9328(19)	20.450(2)
b (Å)	10.147(2)	13.950(2)	10.5063(13)
c (Å)	23.408(5)	13.982(2)	20.450(2)
α (deg)	90	112.657(2)	90
β (deg)	90	105.237(2)	113.58(8)
γ (deg)	120	101.715(3)	90
V (Å^3)	2087.2(8)	1931.2(5)	4026.8(8)
Z	3	1	4
D_{calcd} (g cm^{-3})	1.358	1.412	1.385
λ (Å), μ (mm^{-1})	0.71073, 1.069	0.71073, 0.614	0.71073, 0.764
T (K)	173(2)	173(2)	173(2)
Θ range (deg)	2.48 to 25.08	1.69 to 27.58	2.00 to 21.21
reflns collected	5071	22312	13432
unique reflns	1545	8733	4351
data/restraint/ parameters	1545/1/109	8733/ 6 / 494	4351/12/539
R_1, wR_2 ($I > 2\sigma(I)$)	0.0533, 0.1460	0.0617, 0.1049	0.0487, 0.1041

*3.3.5 UV-Vis and Cyclic Voltammetry Characterization of **3**, 7, and **8***

UV-Vis spectroscopy has been widely utilized to study the transformation of NADH analogues to their NAD^+ counterparts due to the characteristic NADH absorption at around 340 nm. Likewise, $H_3[(^{Bn}NADH)_3tren)]$ **3** also has an intense absorption at 354 nm (ε = 1750 $M^{-1}cm^{-1}$). This intense band is associated with the 1,4-dihydropyridine group and shifts to slightly higher energies for complexes **7** and **8**, with λ_{max} values of 342 and 340 nm, respectively (Figure 3.10). Both complexes **7** and **8** also exhibit a broad, low intensity shoulder between 430 nm and 550 nm.

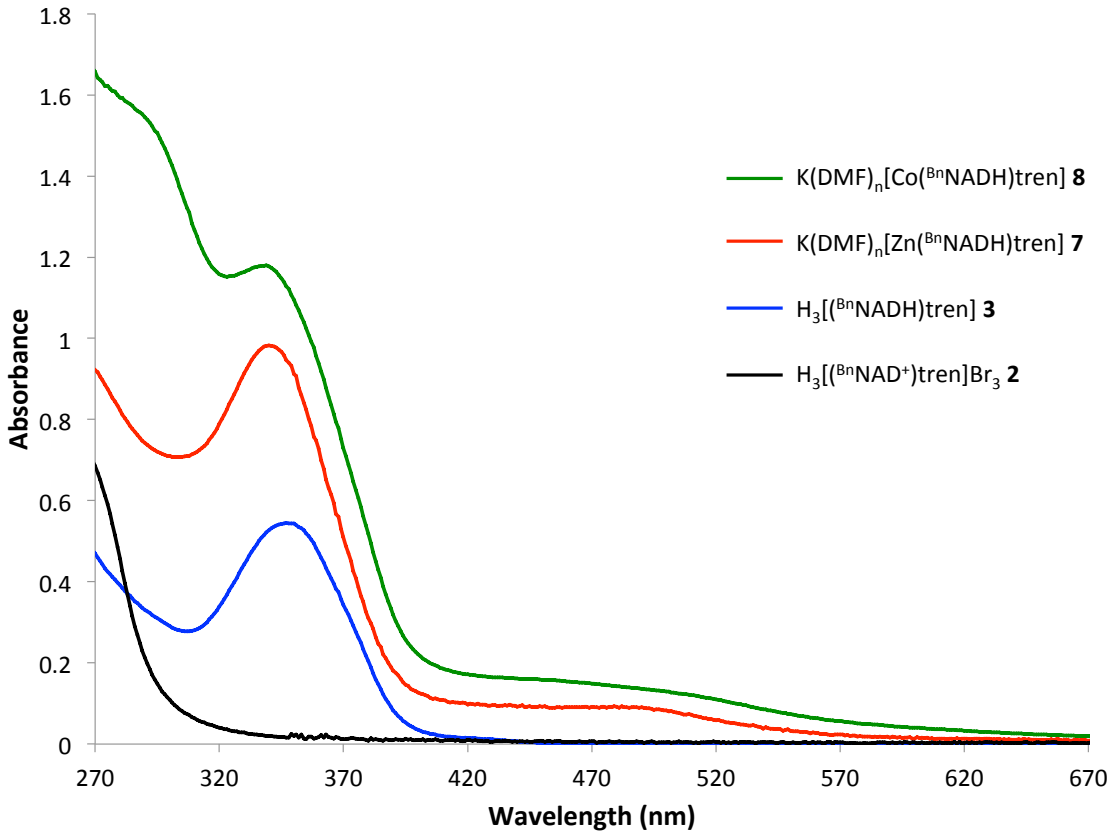

Figure 3.10 Overlay of UV-Vis spectra of $H_3[(^{Bn}NADH)_3tren]$ **3**, $H_3[(^{Bn}NAD^+)_3tren]Br_3$ **2** and $K(DMF)_n$ $[M(^{Bn}NADH)_3tren]$, where M = Zn (**7**) and Co (**8**) in DMF.

Electrochemical studies on $H_3[(^{Bn}NADH)_3tren)]$ **3** and complexes **7** and **8** were completed. The redox properties of BNAH have been studied extensively in the literature. In DMF, BNAH has an irreversible oxidation at E_{pa} = 0.015 V (vs Fc/Fc^+, 10 mV/s). The irreversibility is predicted to be due to the instability of the cationic radical $BNAH^{\square+}$, which quickly loses a proton and additional electron to form BNA^+.[18] The NADH analogue, **3** and complexes **7** and **8** each exhibit multiple irreversible oxidation waves since each compound has three possible hydrides to be oxidized. As a result, meaningful interpretation of the voltammograms is difficult. The first irreversible oxidation wave of $H_3[(^{Bn}NADH)_3tren)]$ **3** occurs at E_{pa} = - 0.04 V (vs Fc/Fc^+ in DMF, 10 mV/s). The first

anodic waves of complexes **7** and **8** shift to more negative potentials by almost 300 mV to -0.3 and -0.33 V, respectively. Other cobalt complexes in similar environments have a Co(II)/Co(III) redox couple near the potential of the first observed wave in **8**.[19] However, no metal-based redox events can be assigned due to the complicated redox properties inherent in 1,4-DHP moieties.

3.3.6 EPR of PPh_4[Co(^{Bn}NADH)$_3$tren)] ***8***

Cobalt complex **8** is paramagnetic, has an odd number of electrons, and can be studied by electron paramagnetic resonance (EPR). Figure 3.11 shows the X-Band EPR spectrum of PPh_4[Co(^{Bn}NADH)$_3$tren)] in DMSO at 20 K. The spectrum reveals an axial signal with g_{eff} values around 4 and 2. This is consistent with the $m_s = \pm ½$ doublet that arises from the S = 3/2 ground state. The hyperfine coupling around g_{eff} of 2 is due to the $I = 7/2$ nuclear spin of the cobalt metal center. The spectrum was globally fit and the following anisotropy parameters were determined: g = 2.2, 2.2, 2.0, W (G) = 140, 150, 300, and A (cm^{-1}) = 0, 0, 90. The zero-field splitting parameters were modeled as D = 2.0 cm^{-1} and no rhombicity (E/D) was observed. Although EPR spectroscopy cannot confirm structural details of complex **8**, there is only one EPR active electronic species observed indicating that the cobalt has not likely undergone any redox chemistry from the ligand. Thus we propose that the identity of **8** is indeed PPh_4[Co(^{Bn}NADH)$_3$tren)] with all three hydrides still intact. Furthermore, the EPR spectrum observed is consistent with other Co(II) systems in a trianionic trigonal monopyramidal coordination environment in the literature.[20]

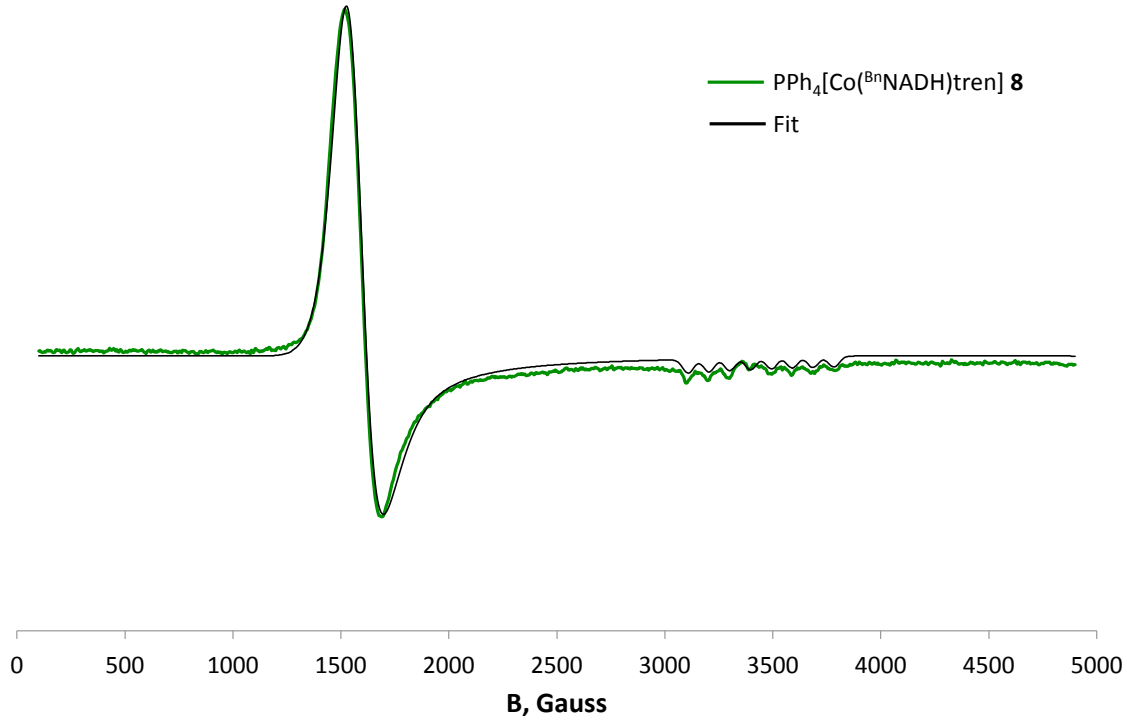

Figure 3.11 X-Band EPR of $PPh_4[Co(^{Bn}NADH)_3tren)]$ **8** in DMSO (1mM, 20K, frequency = 9.646 GHz, modulation = 1 G, power = 2.01 mW (green). The spectrum was simulated (black) by adopting $S = 3/2$ with the following anisotropic values, g = (2.2, 2.2, 2.0), line widths, W = (150, 300, 0), A = (0, 0, 90.0), and zero-field splitting parameters $D = 2.0\ cm^{-1}$.

3.3.7 Theoretical Chemistry

Since hydride transfer is a burgeoning area of research, Dubois and coworkers set out to generate a common scale of hydricity in order to compare hydride moieties of each compound.[21,22] The hydricity of a compound can also be used to compare the hydride donating ability of the different complexes. The hydricity or free energy of hydride transfer (ΔG°_{H-}) of a compound is determined by the summation of the free energies of each discrete step of the reaction. For direct hydride transfer, the summation would be:

$$\Delta G^{\circ}_{H-}(HA) = (\Delta G^{\circ}(A^{-}) + \Delta G^{\circ}(H-)) - \Delta G^{\circ}(HA) \quad (\boldsymbol{Eqn\ 2})$$

The value can be determined both experimentally and theoretically.[18,21] Dubois and coworkers have determined the ΔG°_{H-} of BNAH experimentally to be 59 kcal/mol by determining both the pK_a and the reduction potential.[21] Because our system is inherently more complex than BNAH alone, developing a theoretical method to determine the ΔG°_{H-} and using DFT was particularly attractive. In order to test our methods, BNAH was studied as a control.

$$\Delta G^{\circ}_{H-}(BNAH) = (\Delta G^{\circ}(BNA^{+}) + \Delta G^{\circ}(H-)) - \Delta G^{\circ}(BNAH) \quad (\boldsymbol{Eqn\ 3})$$

Each of the species in ***Eqn 3*** were optimized using the M06L density functional and the Conductor-like Polarizable Continuum Model (COSMO) in the Gaussian09 program.[23,24] The literature value of -404.7 kcal/mol for the ΔG°(H-) was used. Using our methods, the ΔG°_{H-}(BNAH) was calculated to be 58.2 kcal/mol, which matches well with the experimentally determined value of 59 kcal/mol.

$$\Delta G^{\circ}_{H-}(H_3[(^{Bn}NADH)_3 tren]) =$$

$$(\Delta G^{\circ}([(^{Bn}NAD^{+})_3 tren]) + 3\Delta G^{\circ}(H-)) - \Delta G^{\circ}(H_3[(^{Bn}NADH)_3 tren]) \quad (\boldsymbol{Eqn\ 4})$$

Using the same methods, NADH analogue **3** was studied according to *Eqn 4*. The ΔG°_{H-} of ($H_3[(^{Bn}NADH)_3tren)]$) **3** was determined to be 63.2 kcal/mol per hydride. Because our analogue only varies slightly from BNAH, a small change in the ΔG°_{H-} was expected. As expected, this is in range with what was determined for the very close analogue BNAH. The ΔG°_{H-} was also determined for a series of zinc(II) complexes with different R groups on the dihydropyridine moiety using the same theoretical method (Table 3.2). For the experimentally isolated Zn(II) complex **7** (Table 3.2, Entry 3), the hydricity was calculated to be ΔG°_{H-} = 52.0 kcal/mol per hydride. Furthermore, the ΔG°_{H-} for

$[Co(^{Bn}NADH)_3tren)]^+$ was determined to be 52.1 kcal/mol. Based on these results, it appears as though addition of a transition metal to **3** lowers the hydricity of the complex by approximately 10 kcal/mol, and the identity of the transition metal causes less of a deviation, at least for M = Zn and Co. Also, substituents on the 1,4-DHP group appear to have very little effect on ΔG°_{H-} (Table 3.2, Entries 1-3)

Table 3.2 ΔG_{H-} in kcal/mol for $[Zn(^{Bn}NADH)_3tren)]^+$ complexes, where R = H, Me, Bn.

Entry	R =	ΔG_{H-} (kcal/mol)
1	H	52.0
2	Me	50.7
3	Bn	52.0

During hydride transfer a charge build up occurs on the NAD^+ byproduct, and in the tripodal NADH analogue, **3**, up to three hydrides can be transferred increasing the potential for unfavorable charge to accumulate during the formation of the NAD^+ analogue **2**. Thus, the ΔG°_{H-} was studied for each sequential hydride transfer step using **Eqn 5**, **Eqn 6**, and **Eqn 7**, rather than in a single transfer as before.

$$\Delta G^\circ_{H-}(H_3[(^{Bn}NADH)_3tren])) =$$

$$(\Delta G^\circ(H_3[(^{Bn}NADH)_2(^{Bn}NAD^+)tren]) + \Delta G^\circ(H-)) - \Delta G^\circ(H_3[(^{Bn}NADH)_3tren]) \quad (\boldsymbol{Eqn\ 5})$$

$$\Delta G^\circ_{H-}(H_3[(^{Bn}NADH)_2(^{Bn}NAD^+)tren]) =$$

$$(\Delta G^\circ(H_3[(^{Bn}NADH)(^{Bn}NAD^+)_2tren]) + \Delta G^\circ(H-)) - \Delta G^\circ(H_3[(^{Bn}NADH)_2(^{Bn}NAD^+)tren]) \quad (\boldsymbol{Eqn\ 6})$$

$$\Delta G^\circ_{H-}(H_3[(^{Bn}NADH)(^{Bn}NAD^+)_2tren]) =$$

$$(\Delta G^\circ(H_3[(^{Bn}NAD^+)_3tren])) + \Delta G^\circ(H-)) - \Delta G^\circ(H_3[(^{Bn}NADH)(^{Bn}NAD^+)_2tren]) \quad (\boldsymbol{Eqn\ 7})$$

The first hydride is the most hydridic with a ΔG°_{H-} of 47.6 kcal/mol (**Eqn 5**). The second and third hydrides have ΔG°_{H-} of 52.0 and 56.6 kcal/mol, respectively (**Eqn 5** and **Eqn 6**), indicating a decrease in hydricity for each subsequent hydride. This is consistent with unfavorable charge accumulation with each hydride transfer. Importantly, the

difference in hydricity between the hydrides is not large gap (approximately 5 kcal/mol between each sequential hydride); thus, we predict that all three hydrides could be transferred from both the complex K[Zn(^{Bn}NADH)$_3$tren)] **7** and ligand, H$_3$[(^{Bn}NADH)$_3$tren)] **3**.

3.3.8 Hydride Transfer Studies

In order to determine the viability of **3** and **7** as hydride donors, the transfer of the hydrides to simple hydride acceptors must be demonstrated. In this case, the hydride acceptor used is triphenylcarbenium tetrafluoroborate (CPh_3BF_4), which in the presence of a hydride converts rapidly to triphenylmethane (CPh_3H). This conversion can be studied by both ^{1}H NMR and UV-Vis spectroscopy. Table 3.3 contains the molar absorptivities (ε, $M^{-1}cm^{-1}$) of the compounds of interest in the hydride transfer studies. By monitoring the disappearance of the distinctive absorption in the NADH-like compounds (λ_{max} = 345 and 347, Table 3.3, Entries 2 and 4), we can follow the hydride transfer reaction. Furthermore, the products of the hydride transfer reactions (BNA^+, H$_3$[(^{Bn}NAD$^+$)tren]X$_3$ and CPh_3H) have no distinctive features in the visible region (Table 3.3, Entries 1,3, and 5).

Table 3.3 Molar absorptivities, ε ($M^{-1}cm^{-1}$) at the λ_{max} for compounds of interest.

Entry	Complex	λ_{max}	ε ($M^{-1}cm^{-1}$)
1	CPh_3H	260	13000
2	BNAH	347	6504
3	BNA^+	260	5965
4	H$_3$[(^{Bn}NADH)$_3$tren)] **3**	345	13810
5	H$_3$[(^{Bn}NAD$^+$)$_3$tren)]X$_3$ **2**	260	11680

First, to test this methodology, the simple reaction of BNAH with CPh_3BF_4 was studied. When BNAH is reacted with CPh_3BF_4, the bright orange of BNAH disappears and the solution turns colorless. By ^1H NMR spectroscopy, the distinctive 1,4-DHP peaks in the alkene region disappear and the aryl proton resonances of the pyrdinium ring in BNA^+ appear. Integration of the ^1H NMR spectrum reveals near 100% conversion of BNAH to BNA^+ with concurrent formation of CPh_3H.

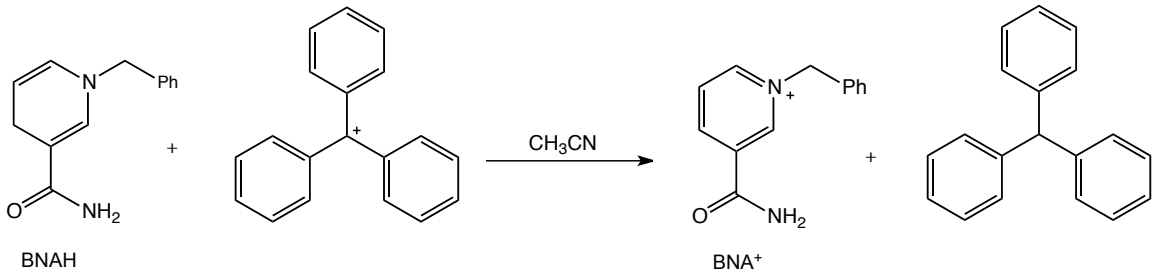

BNAH BNA^+

Scheme 3.6 Hydride transfer studies on BNAH.

The results of the UV-Vis study are shown in Figure 3.12. The absorption arising from BNAH (λ_{max} = 345 nm) decreases rapidly while features in the UV region appear, presumably as a result of formation of BNA^+ and CPh_3H. Again, conversion of the reaction was calculated to be 97%, in good agreement with the NMR result. A slight shift in the λ_{max} was observed immediately after the addition of CPh_3BF_4 to the solution. The origin of this blue shift is unknown at this time.

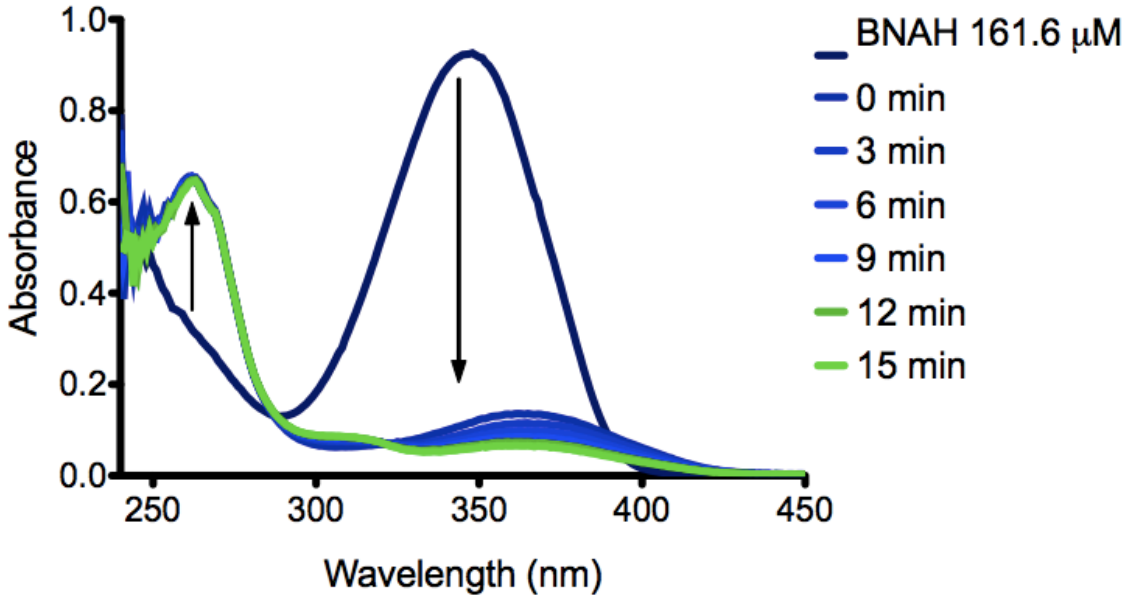

Figure 3.12 UV-Vis study of the reaction of BNAH with hydride acceptor CPh_3BF_4.

The same study was repeated using tripodal NADH analogue, $H_3[(^{Bn}NADH)tren]$ **3**. Similar to the reaction of CPh_3BF_4 with BNAH, the ^1H NMR spectrum revealed a disappearance of the 1,4-DPH proton resonances and the appearance of the aryl protons associated with the pyridinium moiety. The reaction was also studied by UV-Vis spectroscopy (Figure 3.13); as anticipated, the distinct absorption at λ_{max} = 347 nm disappears rapidly, and new features in the UV region grow in. Conversion of $H_3[(^{Bn}NADH)_3tren]$ **3** to $H_3[(^{Bn}NAD^+)_3tren]X_3$ **2** was quantified as a 95% yield.

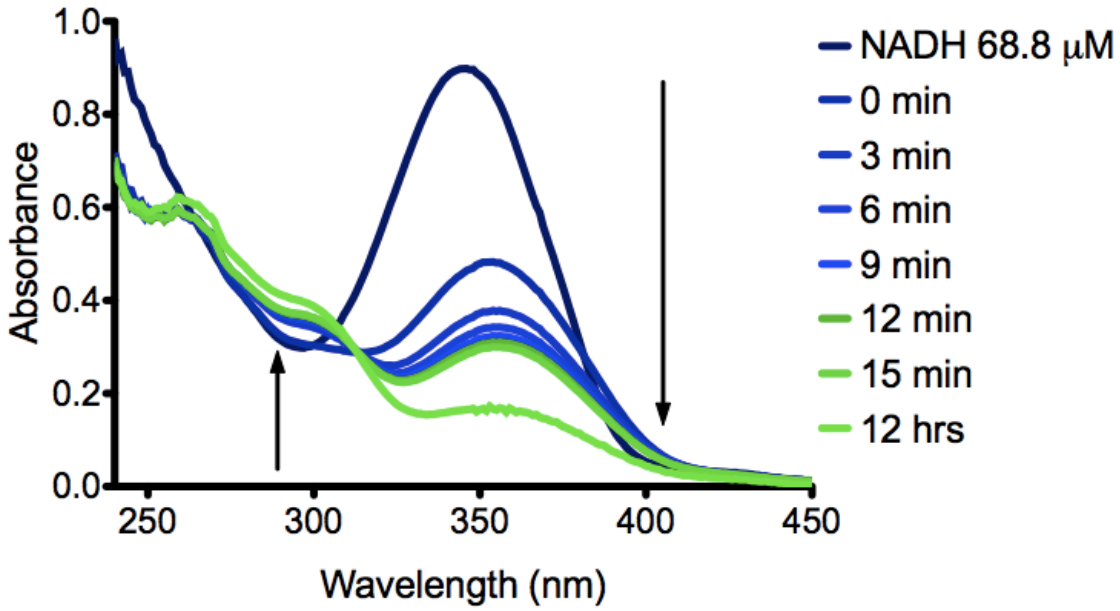

Figure 3.13 UV-vis analysis of the reaction of $H_3[(^{Bn}NADH)tren]$ **3** and hydride acceptor CPh_3BF_4.

3.3.9 Future Studies

Preliminary studies have been completed to study the hydride transfer abilities of $PPh_4[Zn(^{Bn}NADH)tren]$ **7**. Analysis of the ^1H NMR spectrum of the reaction of **7** with CPh_3BF_4 seem to indicate hydride transfer, but also that demetallation is occurring as evident by the appearance of amide protons once again. The cause of this demetallation is unknown at this time, since all reagents were rigorously dried to remove trace H_2O. Furthermore, independent synthesis of $[Zn(^{Bn}NAD^+)_3tren]X_4$ proved unsuccessful. The methylene protons on the benzyl ring in the pyridinium moiety was highly susceptible to decomposition when base is added for deprotonation. Hydride transfer to other small molecules such as trifluoroacetophenone and thiobenzophenones, have been studied with BNAH, however they require an acidic media to drive the reaction.[25,26] Initial studies of

$H_3[(^{Bn}NADH)tren]$ **3** with trifluoroacetophenone in acidic media show that even **3** is not stable to the acids used for the reaction (e.g lutidinium HCl), resulting in the formation of $H_3[(^{Bn}NAD^+)tren]X_3$ **2** without the formation of reduced substrate. Due to the instability of **3** to acids, we find it unlikely that a metal complex supported by **3** will be stable. As a result, moving to a monoanionic framework may enable acid stable metal complexes able to afford the desired reactivity.

3.4 Conclusions

Herein a new ligand featuring three NADH moieties has been synthesized. The metallation of $H_3[(^{Bn}NADH)tren]$ **3** was demonstrated using zinc(II) **7** and cobalt(II) **8**. These complexes have been characterized by X-ray crystallography (**7**), EPR (**8**) and ^1H NMR spectroscopy (**7**, **8**). Theoretical studies show that the hydricity of NADH analogue **3** is 63.2 kcal/mol. This value is on par with, but slightly more hydridic than a similar NADH analogue, BNAH (ΔG°_{H-} = 58 kcal/mol). Theoretical studies predict a decrease in hydricity by almost 10 kcal/mol upon addition of Zn(II) or Co(II) to **3**. Hydride transfer studies using UV-Vis and ^1H NMR spectroscopy reveal that **3** can transfer all three equivalents of hydride to the hydride acceptor CPh_3BF_4 in high yields. Preliminary studies transferring hydrides from zinc complex **7** indicate hydride transfer to CPh_3BF_4 is possible, if demetallation issues can be solved.

3.5 Experimental Procedures

3.5.1 General Considerations

Unless otherwise stated, all operations were performed in a VAC Atmosphere double-dry box under an atmosphere of purified nitrogen or using high vacuum standard Schlenk techniques under a nitrogen atmosphere. Anhydrous *n*-Hexane, pentane, toluene, tetrahydrofuran, diethyl ether, acetonitrile and benzene were purchased from Aldrich and dried on an SG Waters solvent purification system. Anhydrous dimethylactelyamide (DMA) was purchased from Aldrich dried over 4 Å activated alumina, filtered through a bed of activated alumina powder and stored over 4 Å molecular sieves. $CDCl_3$ and d_6-DMSO were purchased from Cambridge Isotope Laboratory, degassed and stored over 4 Å molecular sieves. Celite, alumina, and 4 Å molecular sieves were activated under vacuum for four days at 350ºC. All other chemical were used as received. ^1H and ^{13}C NMR spectra were recorded on Varian 300 MHz NMR spectrometer. ^1H and ^{13}C NMR resonances are reported with reference to solvent resonances (residual $CHCl_3$ in $CDCl_3$, 7.27 ppm and 77.0 ppm or residual DMSO in d_6-DMSO, 2.50 ppm and 40.0 ppm).

3.5.2 Synthetic Procedures

H_3[(NA)$_3$tren] 1: Nicotinyl HCl (88.28 mmol) was suspended in CH_3CN and excess NEt_3 (214.02 mmol) was added dropwise to the stirring suspension. Tren (26.75 mmol) was added as a CH_3CN solution in 10 mL portions. The reaction was stirred for 12 hours at room temperature. After 12 hours the solution was red and had a large amount of precipitate. The solid was collected and dissolved in minimal amounts of dH_2O (50 mL). The solution was brought to pH = 10 with NaOH pellets. The product was extracted with

$CHCl_3$ (3x 100 mL), dried over $MgSO_4$, and the solvent was removed in vacuo to yield 7.71 g (64%) of white solid. For **1**: ^{1}H NMR (23 ^{o}C, 300 MHz, d_6-DMSO): δ 8.95 (s, 3H), 8.65 (dd, 3H), 8.62 (t, 3H, NH), 8.11 (dt, 3H), 7.42 (m, 3H), 3.38 (q, 6H), 2.73 (t, 6H).

H_3[(^{Bn}NADH)$_3$tren]Br_3HCl (2): 1 (0.063 mol) was dissolved in minimal amounts of DMA (50mL) and acidified with 1M HCl in DMA (0.063 mol). Benzyl bromide (0.22 mol) was added to the solution in 1 mL portions. The reaction was heated at 100 °C for 16 hrs. With vigorous stirring, 400 mL of Et_2O is added to the reaction and the product precipitated out of the solution as a yellow solid. The mixture is filtered and the solid is washed with CH_3CN to yield a light yellow solid (4.68 g, 74%). For **2**: ^{1}H NMR (23 ^{o}C, 300 MHz, d_6-DMSO): δ 9.74 (s, 3H), 9.63 (t, 3H,), 9.31 (d, 3H), 9.04 (dd, 3H), 8.28 (m, 3H), 7.58 (m, 6H), 7.43 (m, 9H), 5.93 (s, 6H), 3.81 (m, 6H), 3.58 (m, 6H).

H_3[(^{Bn}NADH)$_3$tren] (3): 2 (2.47 g, 2 mmol) was dissolved in 500 mL dH_2O and a biphasic mixture of $Na_2S_2O_4$ (60 mmol) and K_2CO_3 (60 mmol) in dH_2O and toluene (500 mL dH_20 and 1 L of toluene) was added quickly to a preheated dH_2O solution of **2**. Solids precipitated immediately and the color of the solution was yellow. The reaction was equipped with a condenser and refluxed at 100 °C for 8 to 10 minutes. While still warm, the reaction mixture was separated and the organic fractions were washed with a saturated solution of sodium bicarbonate, dried over $MgSO_4$ and evaporated in vacuo. The product was isolated as orange foam (1.115 g, 62%). For **3:** ^{1}H NMR (23 ^{o}C, 300 MHz, d_6-DMSO): δ 7.31 (m, 9H), 7.25 (m, 6H), 6.94 (s, 3H), 6.84 (t, 3H), 5.90 (d, 3H), 4.57 (m, 3H), 4.28 (s, 6H), 3.12 (q, 6H), 2.96 (s, 6H), 2.45 (t, 6H).

$K(DMA)_n[Zn(NA)_3tren]$ (4): 1 (1.0 g, 2.16 mmol) was dissolved in 15 mL of DMA. A slurry of KH (347.6 mg, 8.66 mmol) in 5 mL of DMA was added to the stirring solution. After the solution was stirred for 3 hours, a 5 mL DMA slurry of $ZnCl_2$ (295.3 mg, 2.16 mmol) was added to the reaction and it was stirred overnight at room temperature. The resulting dark yellow solution was filtered through Celite. The yellow solution was stirred vigorously while copious amounts of Et_2O (100 mL) was quickly added. A yellow solid crashed out of solution, and collected via filtration and washed with a small amount dichloromethane (DCM) to yield 524 mg of salmon-colored solid (43% yield). ^{1}H NMR (23 ^{o}C, 300 MHz, d_6-DMSO): δ 8.55 (s, 3H), 8.16 (d, 3H), 7.29 (d, 3H), 6.40 (dd, 3H), 3.38 (t, 6H), 2.67 (t, 6H).

$K(DMA)_n[Co(NA)_3tren]$ (5): 1 (498 mg, 1.08 mmol) was dissolved in 10 mL of DMA. A slurry of KH (173 mg, 4.32 mmol) in DMA was added to the stirring solution. After the solution was stirred for 3 hours, a slurry of $CoCl_2(THF)_{1.5}$ (211 mg, 1.08mmol) was added to the reaction and it was stirred overnight at room temperature. The resulting green solution was filtered through celite. The green solution was stirred vigorously while copious amounts of Et_2O (50 mL) was quickly added. A dark green solid crashed out of solution. The solid was collected and washed with a small amount dichloromethane (DCM) to yield ~ 600 mg of solid. The crude solid was purified via crystallization by vapor diffusion of DCM into a concentrated solution of DMSO to yield 301 mg of crystalline solid (49% yield). ^{1}H NMR (23 ^{o}C, 300 MHz, d_6-DMSO): δ 80.8, 63.2, 10.5, -4.2, -6.2.

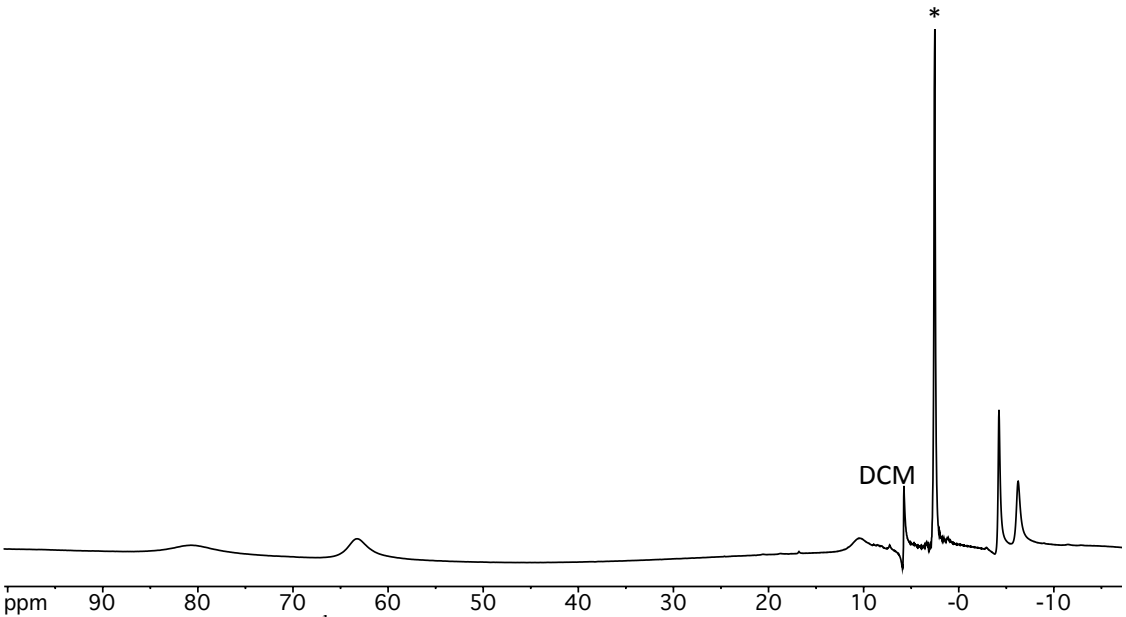

Figure 3.14 300 MHz ^{1}H NMR spectrum of **K(DMA)$_n$[Co(NA)$_3$tren] (5)**. Asterisks represents residual solvent peak.

K(DMA)$_n$[Fe(NA)$_3$tren] (6): 1 (200 mg, 0.43 mmol) was dissolved in 10 mL of DMA. A slurry of KH (70 mg, 1.73 mmol) in 5 mL of DMA was added to the stirring solution. After the solution was stirred for 3 hours, a slurry of $Fe(OAc)_2$ (75 mg, 0.43 mmol) was added to the reaction and it was stirred overnight at room temperature. The resulting dark yellow solution was filtered through celite. The yellow solution was stirred vigorously while copious amounts of Et_2O (50 mL) was quickly added. A yellow solid crashed out of solution. The solid was collected and washed with a small amount dichloromethane (DCM) to yield 205 mg of yellow solid (83% yield). ^{1}H NMR (23 ^{o}C, 300 MHz, *d$_6$*-DMSO): δ 66.7, 29.9, 22.8, 19.8, 13.1, -56.9 ppm.

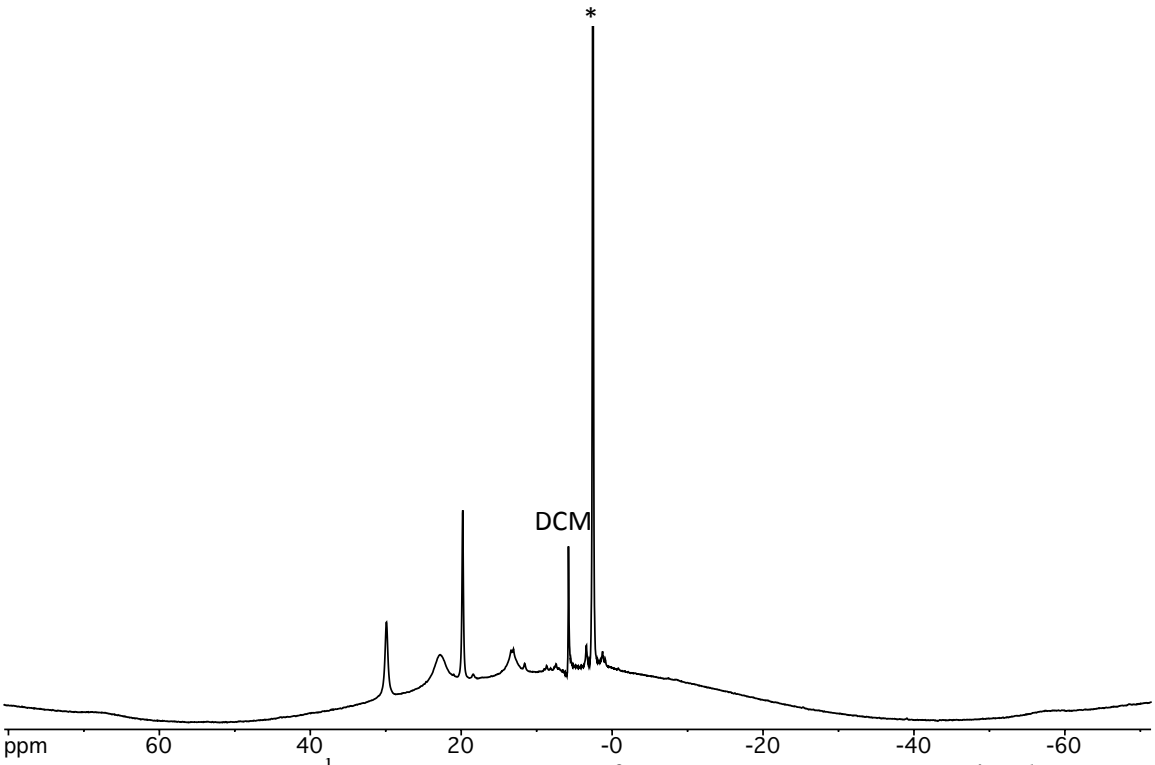

Figure 3.15 300 MHz ^{1}H NMR spectrum of **K(DMA)$_n$[Fe(NA)$_3$tren]** in d_6-DMSO. Asterick respresents residual DMSO peak in d_6-DMSO.

PPh$_4$[Zn(^{Bn}NADH)$_3$tren] (7): 3 (105.3 mg, 0.153 mmol) was dissolved in 5 mL of THF. While stirring, a slurry of KH (25 mg, 0.611 mmol) in 3 mL of DMF was added dropwise to the solution. Immediately the solution became darker and evolution of H_2 was observed. $ZnCl_2$ (21 mg, 0.151 mmol) was dissolved in 3 mL of THF and added to the solution. After 4 hours, the solution was a dark orange-red color. PPh_4Cl (57 mg, 0.153 mmol) was slurried in THF and added to the solution. After stirring overnight at room temperature the solvent was removed in vacuo to yield a orange-yellow solid. The solid was reconstituted in 10 mL of CH_3CN, filtered and the solvent removed in vacuo to yield a orange-yellow solid in a 67% yield. For **7**: ^{1}H NMR (23 ^{o}C, 300 MHz, d_6-DMSO): δ 7.29 (m, 9H), 7.25 (m, 6H), 6.61 (s, 3H), 5.82 (d, 3H), 4.42 (m, 3H), 4.13 (s, 6H), 3.19 (q, 6H), 3.01 (s, 6H), 2.46 (t, 6H).

PPh_4[Co(^{Bn}NADH)$_3$tren] (8): 3 (98.5 mg, 0.141 mmol) was dissolved in 5 mL of THF. While stirring, a slurry of KH (23 mg, 0.564 mmol) in 3 mL of DMF was added dropwise to the solution. Immediately the solution became darker and evolution of H_2 was observed. $CoCl_2(THF)_{1.5}$ (27.6 mg, 0.141 mmol) was dissolved in 3 mL of THF and added to the solution. After 4 hrs the solution was a yellow-green color. PPh_4Cl (53mg, 0.141 mmol) was slurried in 3 mL of THF and added to the solution. After stirring overnight at room temperature the solvent was removed in vacuo to yield a brown-green solid. The brown-green solid was reconstituted 10 mL of CH_3CN, filtered and the solvent removed in vacuo to yield a green solid (60% crude yield). For **8**: ^{1}H NMR (23 ^{o}C, 300 MHz, d_6-DMSO): δ 68.1, 19.2, 7.8-7.0 (overlapping broad features), 5.5, -11.9.

3.5.3 X-Ray Crystallographic Data Collection and Refinement of the Structures

Single crystals of **K[4]**, **K(18C6)[5]**, **K[7]** were grown by vapor diffusion of DCM into DMSO for **K[4]** or by vapor diffusion of Et_2O into a concentrated solution of THF for **K(18C6)[5]** and **K[7]**. Colorless needles of **K[4]** (0.10 x 0.10 x 0.2 mm^3), green needles of **K(18C6)[5]** (0.25 x 0.10 x 0.05 mm^3), and orange plates of **K[7]** (0.4 x 0.2 x 0.2 mm^3) were placed on the tip of a glass capillary and mounted on a Bruker APEX II CCD diffractometer for data collection at 173(2) K.[27] The data collection was carried out using Mo-Kα radiation (graphite monochromator). The data intensity was corrected for absorption and decay (SADABS).[28] Final cell constants were obtained from least squares fits of all measured reflections after integration (SAINT).[29] The structure was solved using SHELXS-97 and refined using SHELXL-97.[30] A direct-methods solution was calculated which provided most non-hydrogen atoms from the E-map. Full-matrix least

squares / difference Fourier cycles were performed which located the remaining non-hydrogen atoms. All non-hydrogen atoms were refined with anisotropic displacement parameters. All hydrogen atoms were placed in ideal positions and refined as riding atoms with relative isotropic displacement parameters. For **K[4]**, the PLATON program, SQUEEZE function, was used to remove disordered solvent in the asymmetric unit.[31] A total of 174 electrons were removed in a total volume of 391 $Å^3$ per unit cell, equally distributed between three positions at (0, 0, 0), (0.3, 0.6, 0.9), and (0.6, 0.3, 0.66) in the asymmetric unit. The number of electrons is consistent with removal one disordered DMSO molecule at each position. Crystallographic data is summarized in Table 3.1.

3.5.4 Physical Measurements

NMR spectra were collected on a Varian Inova 300 MHz spectrometer. UV-visible data were collected on a Cary 300 Bio UV-Visible spectrophotometer. Perpendicular-mode X-band EPR spectra were recorded on a Bruker EPP 300 spectrometer equipped with an Oxford ESR 910 liquid helium cryostat and an Oxford temperature controller. X-band EPR spectra were simulated using the ESIM program written by Eckhard Bill.

3.5.5 Computational Details

Theoretical calculations were carried out using density functional theory (DFT). No symmetry constraints were used. The geometry optimizations were performed with the M06-L functional in the Gaussian09 program package.[23] For C, O and H atoms, the double-ζ quality basis sets def-SV(P) was used, whereas the triple-ζ quality basis set def-

TZVP was employed for N and Co. The COSMO solvent model was employed to emulate solvent effects.[24]

Chapter 4

Synthesis, Characterization and Electronic Structure of a New Family of Diiron and Iron-Cobalt Complexes

4.1 Overview

Bimetallic complexes of diiron and iron-cobalt have been synthesized and characterized as a formally diiron(II,II) chloride, diiron(II,I), iron-cobalt(II,II) chloride and an iron-cobalt(II,I). Notably, the divalent diiron species is the direct precursor for heterobimetallic divalent iron-cobalt species, and hence, it is the common precursor of both mixed-valent species. The entire family of bimetallic complexes have high-spin ground states and can be described as two strongly ferromagnetically coupled metal centers. DFT and multi-configurational CASSCF confirm the experimental high-spin ground states for all complexes. The natural orbitals derived from the CASSCF calculations reveal a weak bonding interaction in the divalent diiron(II,II) chloride and iron-cobalt(II,II) chloride complexes. Excitingly, a covalent interaction is observed in mixed-valent diiron(II,I) and iron-cobalt(II,I) species.

4.2 Introduction

The reduction of small molecules by one-electron is thermodynamically challenging, thus multi-electron reduction approaches are more desired.[1,2] For example, the reduction of CO_2 by one-electron has a redox potential of -1.90 V, a value that decreases significantly to -0.61 V when two protons and two electrons are introduced simultaneously (*vide supra*).[3] In biology, many metalloenzymes use multi-metallic active sites to achieve difficult transformations. For example, nitrogenase uses metallic clusters (FeMo, Fe-only, VFe) to convert N_2 to NH_3.[4-6] The mechanistic details of these processes are largely unresolved. However, it is proposed that the multi-metallic clusters aid the transformation by facilitating multi-electron redox processes.[7,8]

Achieving redox cooperativity between multiple metal centers can be difficult. Many researchers have achieved electronic cooperativity by invoking strong metal-metal bonds, and several homogeneous systems containing metal-metal bonds have shown encouraging multi-electron reactivity with small molecules (*vide supra*). However, these systems have mostly utilized 2nd and 3rd row transition metals. Furthermore, only stoichiometric reactions have been observed largely due to the formation of stable metal oxides. When designing sustainable catalysts, the use of 1st row transition metals is desired because they are earth-abundant and inexpensive, especially compared to noble and precious metals.[9]

Examples of first-row bimetallic complexes with metal-metal bonds are limited compared to those of 2nd and 3rd row bimetallics.[10-14] Out of the first-row bimetallics, diiron complexes are some of the most widely studied bimetallics. However, the majority of these diiron complexes are supported by carbonyls and other strong field ligands, causing the iron metal centers to antiferromagnetically couple, yielding a low spin complex. The small class of diiron complexes not ligated by carbonyls is of interest because of their unique electronic and magnetic properties as well as their potential for multi-electron redox chemistry.[15,16]

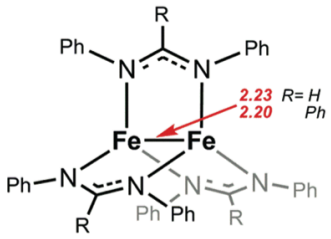

Murillo, Cotton
Fe(II)Fe(I)
S = 7/2
Fe-Fe: 2.23 (R = H)
Fe-Fe: 2.20 (R = Ph)

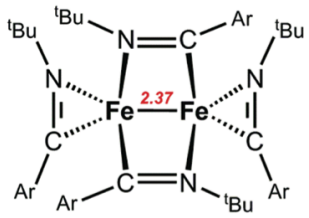

Klose, Floriani
Fe(II)Fe(II)
S = 3
Fe-Fe: 2.37

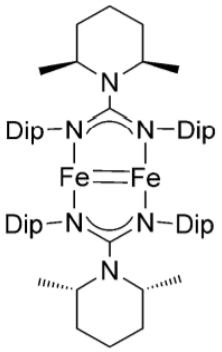

Jones
Fe(I)Fe(I)
S = HS
Fe-Fe: 2.13

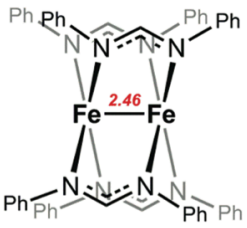

Murillo, Cotton
Fe(II)Fe(II)
S = 4
Fe-Fe: 2.46

Figure 4.1 Examples of diiron bimetallics with strong Fe-Fe bonds. The Fe-Fe bond lengths, spin states and formal oxidation states are given.[17-20]

An archetypical example is the high-spin, trigonal-lantern $Fe_2(DPhF)_3$ (DPhF = diphenylformamidinate) synthesized by Cotton *et al*. [17,18] and recently reinvestigated by Lu *et al* (Figure 4.1).[21] $Fe_2(DPhF)_3$ exhibits strong ferromagnetic coupling between two high-spin iron centers with an extremely short Fe-Fe bond length of 2.23 Å, which is even shorter at 2.20 Å when R = Ph. Cotton *et al*. have also explored the electronics of a tetragonal diiron complex coordinated with DPhF, and it also has a high-spin ground state and a relatively short Fe-Fe bond length of 2.46 Å.[18] Reactivity studies with $Fe_2(DPhF)_3$ have been limited due to its extreme H_2O and O_2 sensitivity yielding to its propensity to form stable iron oxides. Recently, a low coordinate diiron(I,I) complex supported by two

guanidinate ligands was synthesized by Jones *et al.* This diiron complex has the shortest Fe-Fe bond distance to date at 2.13 Å.[20]

The Betley group has synthesized a variety of triiron and hexairon complexes supported by hexadentate, tripodal hexa(amide) ligand scaffolds (Figure 4.2a). These complexes exhibit intriguing electronic and magnetic properties. For example, in one set of triiron complexes, the magnetic behavior is modified by the nature of the ancillary ligand (e.g. THF vs PR_3), giving rise to spin states ranging from $S = 6$ to $S = 2$. The triiron complex with THF as an ancillary ligand is displayed in Figure 4.2b. Current studies are underway to study the electronic structure of these complexes during redox processes. Another interesting system investigated by Betley *et al.* is a hexairon complex in which the iron centers form an octahedral core (Figure 4.2c). This complex has an impressive multi-electron redox profile that spans six oxidative sates, ranging from the all ferrous $[Fe^{II}]_6$ to the all ferric $[Fe^{III}]_6$ core. The spin states of these different redox states range from $S = 6$ to $S = 0$. Excitingly, multi-site reactivity was observed when the $[Fe^{II}]_6$ core is reacted with 6 equivalents of nitrite ($[NO_2]^-$) to yield a hexairon nitrosyl complex ($(^{H}L)_2Fe_6(NO)_6$) in the presence of exogenous acid. This conversion of nitrite by an $[Fe^{II}]_6$ core exhibits the potential for the use of high-spin ferromagnetically coupled metal-metal complexes in the multi-electron reduction of small molecules.

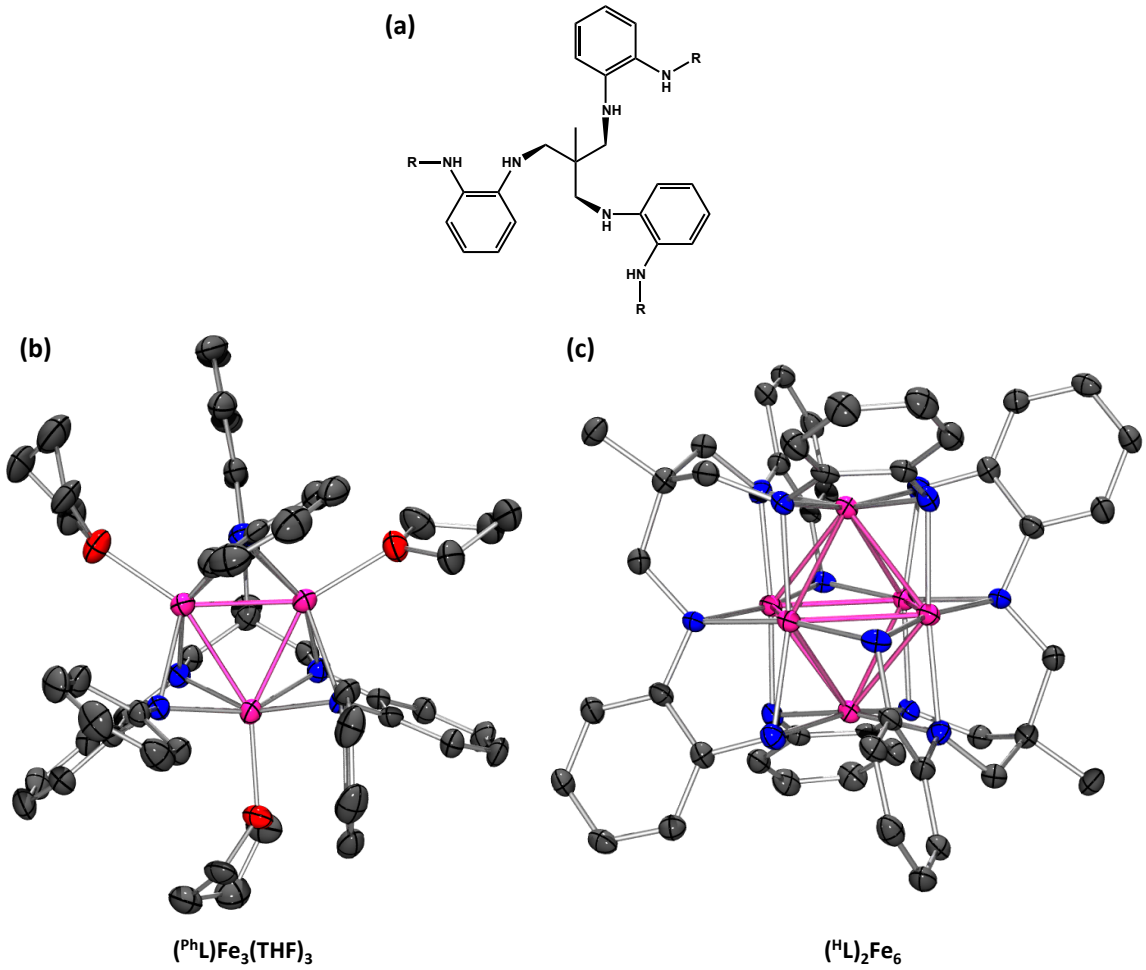

Figure 4.2 Multi-metallic iron complexes synthesized by Betley *et al.*[22,23] (**a**) Hexadentate ligand scaffold (R = H, Ph). (**b**) Solid-state structure of triiron complex with ancillary THF ligand ($(^{Ph}L)Fe_3(THF)_3$). (**c**) Solid-state structure of hexairon complex ($(^{H}L)Fe_6$). In solid-state structures, atoms are represented as follows: Fe (pink), N (blue), O (red), and C (grey).

Thus far, only diiron complexes with similar ligand environments at both iron centers have been discussed. However, bimetallic complexes between late transition metals with electronically distinct ligand environments at each iron center are underrepresented and show promise for interesting redox properties and reactivity as a result of the polarization of the metal-metal bond.[24,25] The Thomas group has synthesized diiron complexes using a phosphinoamide ($^{R}NHPR'_3$) ligand scaffold that has proved

successful in supporting an early-late heterobimetallic Zr-Co complex capable of reducing CO_2 (*vide supra*).[26,27] Figure 4.3 reveals the synthetic pathway to three different diiron(II,II) complexes, as well as a route to a diiron(II,III) imide. The metal-metal interaction of diiron(II,II) complexes support by various phosphinoamide ligands are best described as two high-spin iron metals strongly ferromagnetically coupled. While the redox profile of these diiron complexes is not as rich as the hexairon core described above, they can be reduced by one-electron to yield formally diiron(II,I) complexes stabilized by an additional axial ligand (PMe_3 or another phosphinoamide ligand) (Figure 4.3). These reduced diiron species shown promising multi-electron processes via their reaction with organic azides to from diiron(II,III) imides. The magnetic properties of the diiron(II,III) imides are best described as two non-interacting metal centers, a high-spin Fe(II) and a low-spin Fe(III) imide. Current efforts are underway to study the transfer chemistry of the imide moiety as well as studying the redox properties of the unique diiron imide complexes.[15]

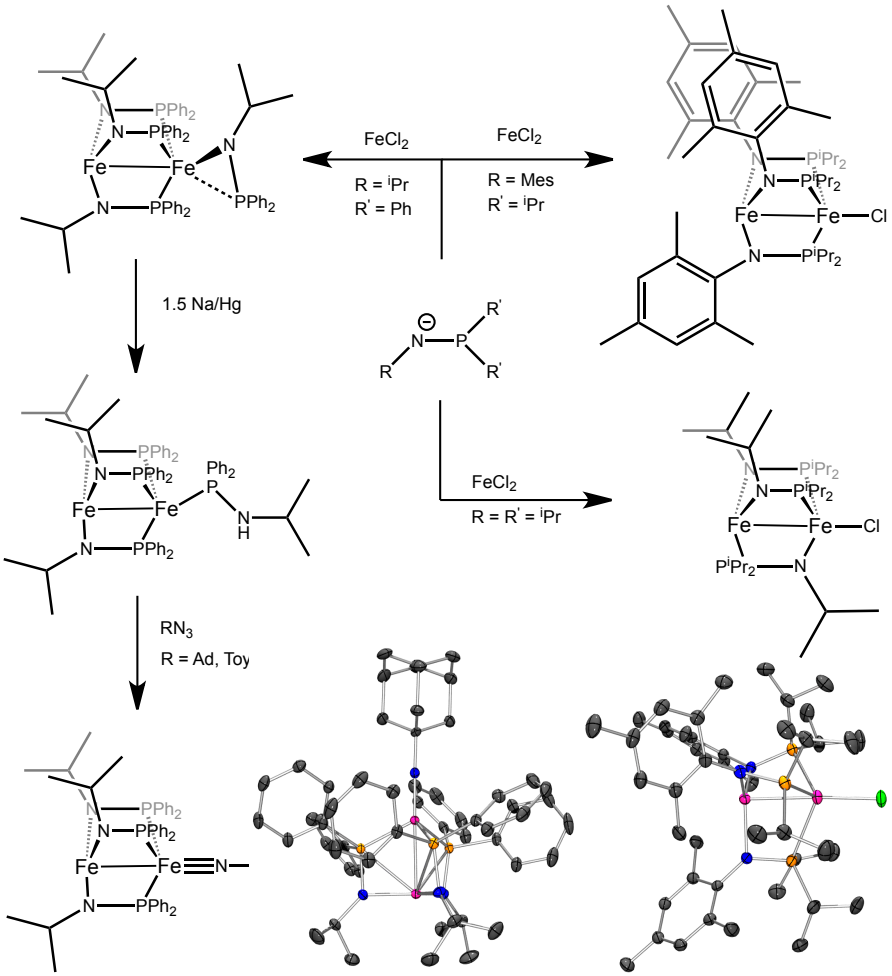

Figure 4.3 Synthetic routes to diiron(II,II) chloride, diiron(II,I) phosphinoamide, and diiron(II,III) imide complexes synthesized by Thomas *et al*.[15,28] Solid-state structures of diiron(II,II) chloride complex where R = R = Mes, R' = ^{i}Pr (right) and diiron(II,III) imide where R = adamantyl are shown. Atoms are represented as follows: Fe (pink), N (blue), P (orange), Cl (green), and C (grey).

The Lu group also utilizes a tripodal ligand system that offers two disparate ligand environments while promoting metal-metal bonding. Heterobimetallic complexes synthesized using ^{iPr}L (2,2′,2″-tri(diisopropylphosphinomethylamino)triphenylamine) have shown promising reactivity toward the activation of small molecules. For example, preliminary studies of a [^{iPr}LCrFe]K(18C6) heterobimetallic complex, which features an extremely short metal-metal bond (1.96 Å), reduces CO_2 to form oxalate.[29] Current

studies are underway to determine its promise for catalytic activity. Furthermore, ^{iPr}L stabilizes a low-valent iron (formally Fe(-1)) as an anionic aluminum-iron heterobimetallic complex.[30] The binding of dinitrogen to this low valent iron center allows for the functionalization of N_2 using silylchloride reagents (Figure 4.4).[31]

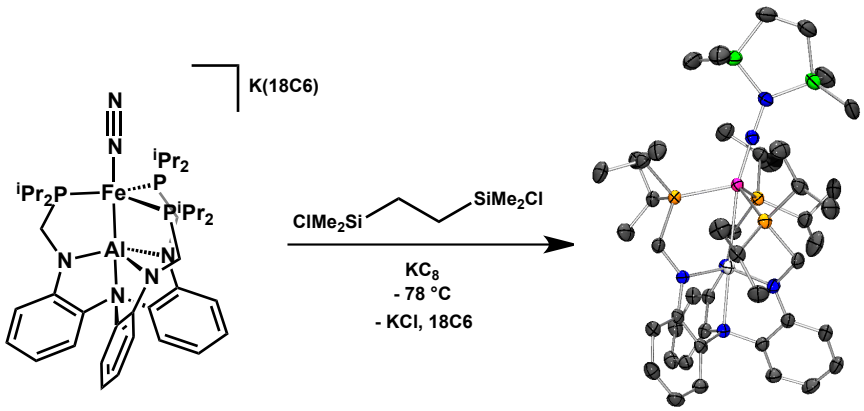

Figure 4.4 Synthetic pathway to a functionalized N_2 complex. Solid-state structure of ^{iPr}LAlFeN$_2$((SiMe$_2$)C$_2$H$_2$) is shown. Atoms are represented as follows: Al (lt. grey), Fe (pink), N (blue), Si (green), C (grey).

The synthesis of diverse heterobimetallic complexes supported by ^{iPr}L and their exciting propensity for reactivity prompted the study of late-late bimetallic complexes with this ligand. ^{iPr}L provides a phosphine plane for one iron and a trianionic amide plane for the second, similar to the phosphinoamide (^{R}NPR$'_3$) ligands utilized by Thomas *et al*. In contrast to ^{R}NPR$'_3$, ^{iPr}L offers a tethered ligand support that restricts the binding of the iron centers and also limits reactivity to one site. Herein we describe the synthesis of four complexes: formally diiron(II,II) chloride, diiron(II,I), iron-cobalt(II,II) chloride, and iron-cobalt(II,I). By using the synthetic route shown in Scheme 4.2, the diiron(II,II) chloride is the precursor for all of the other bimetallic complexes.

4.3 Results and Discussion

4.3.1 Synthesis and ^{1}H NMR Spectroscopy

Historically, diiron complexes with direct metal-metal interactions have been prepared in several ways (Scheme 4.1). The simplest synthetic route (Eqn 1) is a one-pot reaction. For example, Thomas *et al.*, prepared a diiron chloride complex using two equivalents of $FeCl_2$ and three equivalents of deprotonated ligand.[28] Alternatively, others have successfully synthesized diiron complexes by first isolating a mononuclear iron complex and then reacting two of these together, in the presence of reductant (Eqn 2).[18,21,32-34] In some cases, the mononuclear iron complexes dimerize into diiron μ-halide diamond cores (Eqn 3). These complexes can also be reduced to form diiron complexes.[20,35]

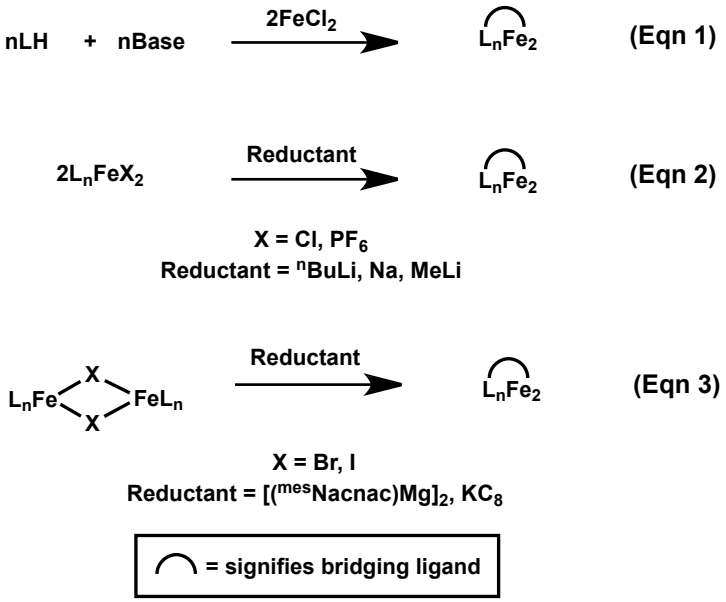

Scheme 4.1. Synthetic routes to diiron complexes. [18,20,21,28,32-35]

Using the route described by **Eqn 2**, we have successfully synthesized diiron(II,II) chloride (**1**) by adding two equivalents of $FeCl_2(THF)_{1.5}$ to $[^{iPr}L]^{3-}$ (Scheme

4.2). Complex **1** is isolated in ~70% crystalline yield as a deep blue solid. The ^{1}H NMR spectrum of **1** exhibits 10 sharp paramagnetically shifted resonances between -87 and 120 ppm. For a completely symmetric complex (C_{3v} symmetry) there should be 8 unique protons. Previous work with $H_3{}^{iPr}L$ has shown complexes often exhibit C_3 symmetry with 12 peaks in the ^{1}H NMR spectrum. Loss of the mirror plane causes the methylene protons and all the methyl groups on the isopropyl substituents to become inequivalent. Likely, complex **1** is a C_3 symmetric complex where the missing two peaks are either too paramagnetically broadened to be detectable or they are coincident with other peaks. The related diiron(II,II) bromide (**1-Br**) was synthesized in the same manner using $FeBr_2$. The ^{1}H NMR spectrum of **1-Br** is nearly identical to **1** with 10 paramagnetically broadened peaks that are slightly shifted compared to the shifts of **1** (Appendix A, Figure A.1).

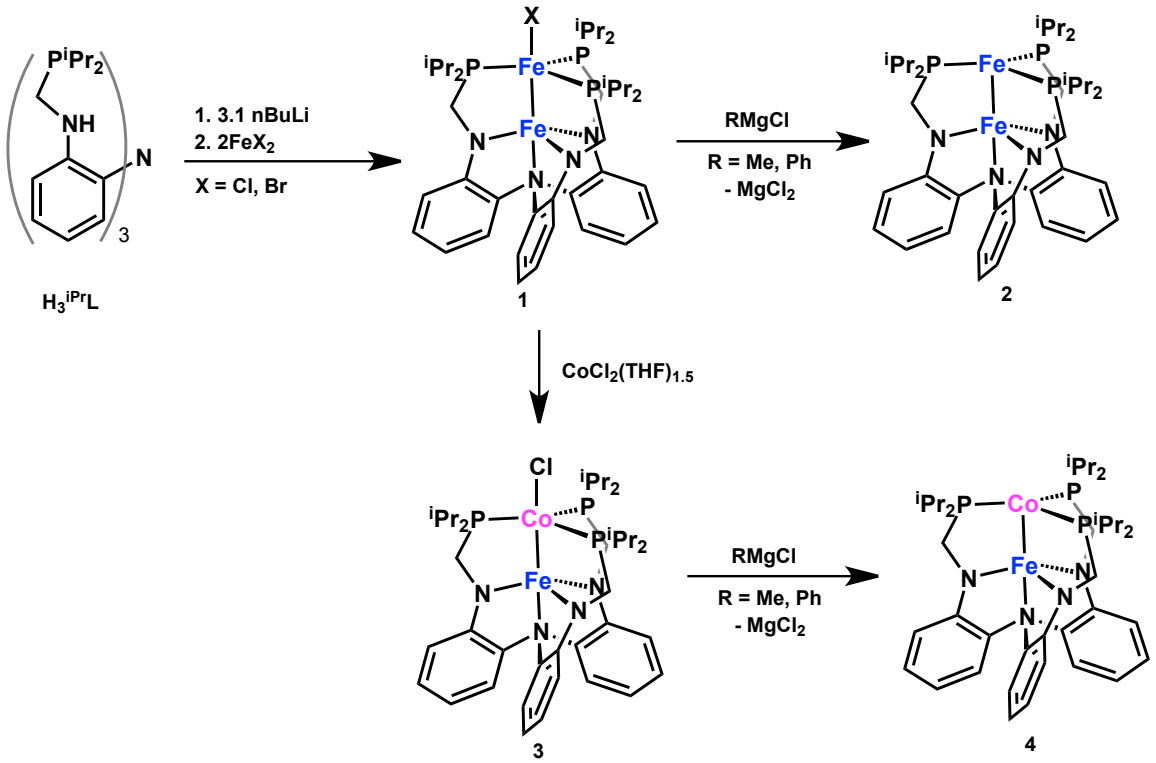

Scheme 4.2 Synthetic route to a family of homo- and heterobimetallic diiron and iron-cobalt complexes.

As illustrated in Scheme 4.1, a wide variety of reducing agents have been used to synthesize low- and mixed-valent diiron complexes.[15,20,21,32,34,35] Several of these reducing agents were used to reduce our diiron(II,II) chloride to the formally mixed-valent diiron(II,I) **2**. For example, ^{n}BuLi was reacted with diiron(II,II) chloride **1**; however, instead of isolating **2**, single crystal X-ray crystallography confirmed the formation of a LiCl adduct of **2** (**2-LiCl**, Appendix A, Figure A.2 and Table A.1). In contrast, Grignard reagents, such as PhMgCl or MeMgCl, reliably yielded the salt-free product. When PhMgCl is added to a THF solution of **1** an immediate and drastic color change to red is observed. The mixed-valent diiron(II,I), **2**, is isolated after reconstitution in benzene and filtration to remove the magnesium salts. Use of a Grignard as the reductant allows for the isolation of **2** without a salt adduct. Formation of a new species is confirmed by a new ^{1}H NMR spectrum that exhibits significant paramagnetic broadening compared to that of **1** and has only 5 peaks (Appendix A, Figure A.3). The ^{1}H NMR spectrum of **2** is extremely paramagnetically broadened, making it difficult to identify specific peaks.

A common method for synthesizing heterobimetallic complexes uses two sequential metallation steps.[36,37] Our group has successfully isolated a variety of heterobimetallic complexes by first synthesizing monometallic complexes and then in a separate reaction adding a second metal, generally in the presence of reductant.[29,30] In this case, however, we needed an alternative route to heterobimetallics due to difficulty in isolating a monoiron species. Recently, Betley and coworkers reported a new strategy, wherein transmetallation of a homotrimetallic complex with a MCl_2 (M = Co) resulted in

formation of the corresponding heterotrimetallic complex.[38] When $CoCl_2(THF)_{1.5}$ is added to a THF solution of **1** an immediate color change to a deep purple solution is observed. The putative iron-cobalt(II,II) chloride **3** is isolated by filtration of a toluene solution to remove the iron salts. A new ^{1}H NMR spectrum is observed for **3**, which when compared to the diiron(II,II) chloride **1** has a similar peak range, but is more paramagnetically broadened and has fewer peaks. Figure 4.5 compares the ^{1}H NMR spectra of complexes **1** and **3**. The reduced mixed-valent heterobimetallic iron-cobalt(II,I) complex (**4**) was synthesized analogously as **2**. Analysis by ^{1}H NMR spectroscopy indicated formation of a new species, with 6 resonances paramagnetically shifted between -60 and 135 ppm (Appendix A, Figure A-4).

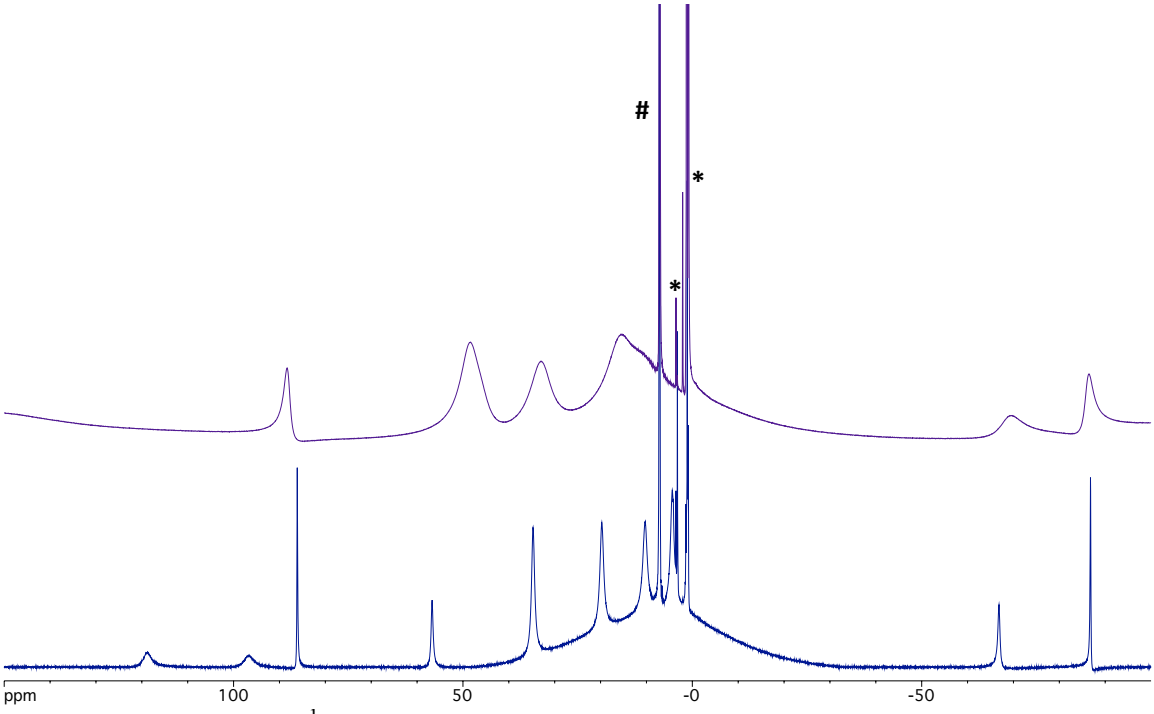

Figure 4.5 500 MHz ^{1}H NMR spectrum of diiron(II,II) chloride **1** (blue) and iron-cobalt(II,II) chloride **3** (purple). The residual C_6H_6 peak is identified by # and extraneous THF is identified by *.

4.3.2 Solid-state Structures

Single crystals suitable for X-ray diffraction of divalent species **1**, **1-Br**, and **3** were grown from layering pentane onto a concentrated toluene solution. The solid-state structures of **1**, **1-Br**, and **3** are shown in Figure 4.6. All three structures crystallize in the same space group, $P2_1/c$, and have similar unit cell parameters (**Table 4.1**). The structures lack perfect three-fold symmetry as indicated by the Fe-M-Cl angle of 168.80(3) for **1**, 169.33(3) for **1-Br**, and 169.56 (3) for **3**, as well as the asymmetry in the Fe-N_{eq} and M-P bond lengths and N_{eq}-M-N_{eq} angles (**Table 4.2**). Complexes **1** and **1-Br** have nearly identical bond metrics, with the exception of the Fe-X bond length, which is 2.2622(2) for **1** and 2.4109(4) for **1-Br**. Transmetallation of the top iron in **1** for a cobalt in **3** predominantly affects the Fe-M bond length, which shortens by 0.04 Å, and the M-P bond lengths, which shorten by ~ 0.1 Å each. Furthermore, the M-N_{ap} bond length is lengthened by 0.04 Å from **1** to **3**, consistent with the shortening of the Fe-M bond length. All of these bond metric changes are consistent with the transmetallation of the iron for a cobalt ion, which has a smaller covalent radius. However, the significant shortening of the Co-P bonds versus the Fe-P bonds cannot be accounted for by their differences in covalent radii alone (r_{Co} = 1.157, r_{Fe} = 1.165).[39] The more electron-rich Co center likely has better back bonding to the phosphine ligands.

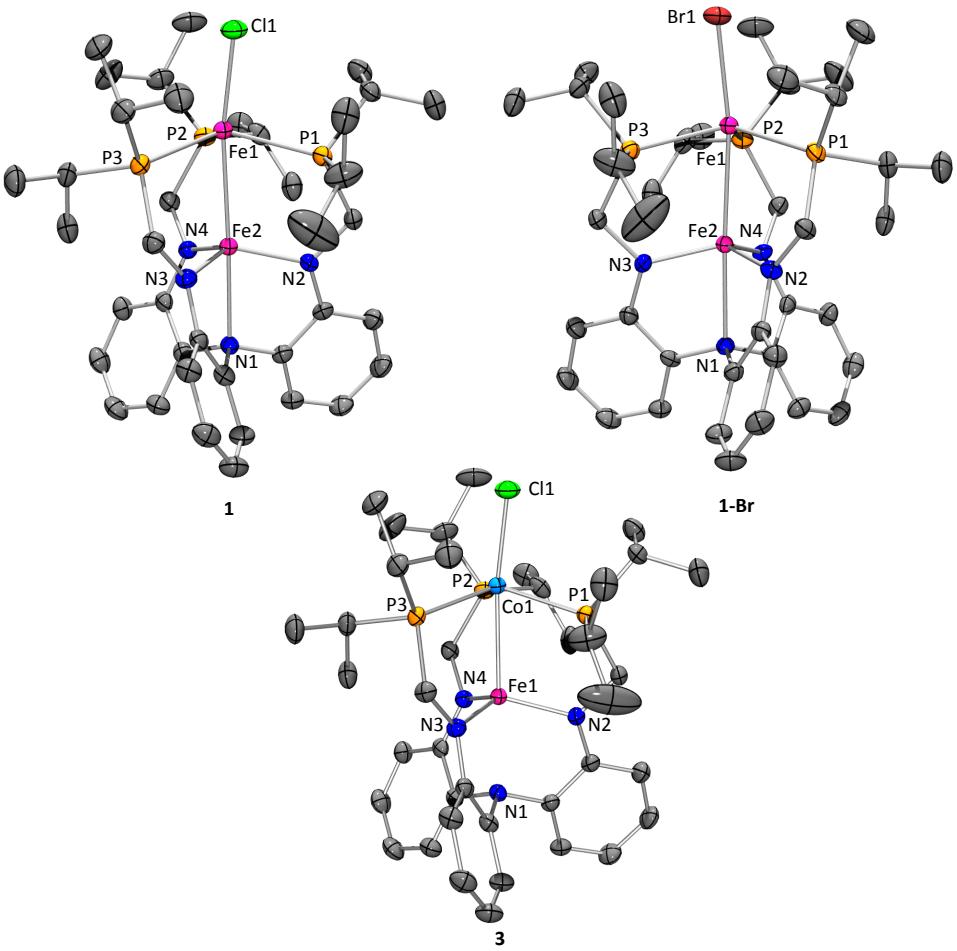

Figure 4.6 Solid-state structure of **1**, **1-Br**, and **3** at 50% probability. Hydrogen atoms are omitted for clarity.

The diiron(II,II) chloride and iron-cobalt(II,II) chloride have Fe-M bond lengths of 2.6251(5) Å and 2.5899(6) Å, respectively. The Fe-Fe bond distance in complex **1** falls on the longer end of the spectrum of formally diiron(II,II) complexes in the literature. The most relevant for comparison are the Fe-Fe complexes synthesized by Thomas *et al.* that are also supported by phosphinoamide ligand systems and have Fe-Fe bond lengths ranging from 2.5855 Å to 2.8684 Å depending on the ligand substituents.[28] Also relevant are triiron complexes synthesized by the Betley group with Fe-Fe bond lengths ranging between 2.4377 Å and 2.6074 Å.[23] Heterobimetallic iron-cobalt complexes are much

more rare in the literature compared to homobimetallic diiron complexes. As discussed previously, Betley *et al.* has recently reported heterotrimetallic complexes of iron and cobalt that have Fe-Co bond lengths ranging from 2.501 Å and 2.549 Å. Iron-cobalt(II,II) chloride **3** described herein is slightly longer (2.5899 Å) but compares well with the few literature structures available.

Perhaps a better measure for discussing the M-M bond in bimetallic complexes is the single-bond ratio, r, which is defined as the ratio of the M-M bond length to the sum of the single-bond radii of the two metal centers.[13,39-41] For **1** and **3**, the single-bond ratios are 1.13 and 1.11, respectively. The expected value of r for a single bond is 1.00. The covalent ratio of **1** and **3** indicate a weak interaction between the two metal ions, as the values are too high to indicate a single bond.

Table 4.1 Crystallographic and refinement details for complexes **1 - 4**.

	^{iPr}LFeFeCl **1**	^{iPr}LFeFeBr **1-Br**	^{iPr}LFeFe **2**	^{iPr}LFeCoCl **3**	^{iPr}LFeCo **4**
chemical formula	$C_{39}H_{60}N_4P_3Fe_2Cl$	$C_{39}H_{60}N_4P_3Fe_2Br$	$C_{39}H_{60}N_4P_3Fe_2$	$C_{39}H_{60}N_4P_3FeCoCl$	$C_{39}H_{60}N_4P_3FeCo$
formula weight	824.97	869.43	789.52	828.05	792.06
crystal system	monoclinic	monoclinic	trigonal	monoclinic	monoclinic
space group	$P2_1/c$	$P2_1/C$	P_{321}	$P2_1/c$	$P2_1$
a (Å)	11.8838(14)	11.8696(5)	15.8611(16)	11.8500(7)	11.837(2)
b (Å)	16.2331(18)	16.2190(7)	15.8611(16)	16.2123(10)	15.715(3)
c (Å)	23.986(3)	24.3507(11)	11.7814(12)	23.9996(14)	11.986(2)
α (deg)	90	90	90	90	90
β (deg)	101.070(2)	100.5650(10)	90	101.4750(10)	101.343(2)
γ (deg)	90	90	120	90	90
V (Å^3)	4541.1(9)	4608.4(3)	2566.8(4)	4518.5(5)	2186.1(8)
Z	4	4	2	4	2
D_{calcd} (g cm^{-3})	1.207	1.253	1.022	1.217	1.204
λ (Å), μ (mm^{-1})	0.71073, 0.883	0.71073, 1.630	0.71073, 0.684	0.71073, 0.883	0.71073, 0.850
T (K)	173(2)	296(2)	173(2)	173(2)	173(2)
Θ range (deg)	1.52 to 27.46	1.52 to 26.26	1.48 to 26.32	1.53 to 27.48	2.16 to 27.48
reflns collected	51260	48121	9070	51323	9688
unique reflns	10355	9291	3453	10290	9688
data/restraint/ parameters	10355 / 0 / 453	9291 / 0 / 442	9070 / 0 / 145	10290/ 0 / 452	9688 / 0 / 447
R_1, wR_2 ($I > 2\sigma(I)$)	0.0395, 0.0959	0.0363, 0.0856	0.0385, 0.0748	0.0362, 0.0897	0.0498, 0.1228

Table 4.2 Selected bond lengths and angles from solid-state structures of complexes **1-4**.

	^{iPr}LFeFeCl **1**	^{iPr}LFeFeBr **1-Br**	^{iPr}LFeFe **2**	^{iPr}LFeCoCl **3**	^{iPr}LFeCo **4**
Fe-M, Å	2.6251(6)	2.6203(5)	2.3252(2)	2.5899(6)	2.2599(4)
M-Cl, Å	2.2622(2)	2.4109(4)	-	2.2476(9)	-
Fe−N_{eq}, Å	1.973(2)	1.960(2)	1.9879(1)	1.968(2)	1.9891(4)
	1.980(2)	1.9753(2)		1.970(2)	1.9751(3)
	1.963(2)	1.976(2)		1.957(2)	1.9640(2)
Fe−N_{ax}, Å	2.2653(9)	2.275(2)	2.2927(2)	2.300(3)	2.2405(4)
M-P, Å	2.4847(9)	2.4607(7)	2.3656(2)	2.3671(8)	2.3032(4)
	2.4568(9)	2.4656(7)		2.3672(7)	2.2945(4)
	2.4610(9)	2.4874(7)		2.4099(8)	2.3119(3)
N_{eq}−Fe−N_{eq}, ^{o}	114.86(9)	117.32(8)	116.59(1)	115.62(7)	115.7(2)
	117.71(9)	116.09(8)		114.27(7)	117.0(2)
	116.09(9)	115.21(8)		116.97(7)	118.5(2)
P−M−P, ^{o}	114.57(3)	114.71(3)	119.40(5)	116.36(2)	117.31(7)
	119.41(3)	119.42(2)		114.78(2)	120.38(7)
	114.19(3)	114.61(3)		116.35(2)	122.07(7)
M-M-Cl, ^{o}	168.80(3)	169.33(2)	-	169.56(3)	-
r	1.13	1.12	1.00	1.11	0.97

Single crystals of **2** were grown from a concentrated benzene solution and analyzed by X-ray diffraction (Figure 4.7). In contrast to the diiron(II,II) chloride, **2** exhibits trigonal symmetry and crystalizes in the trigonal space group P_{321} (**Table 4.1** and **Table 4.2**). A significant contraction in the Fe-Fe bond is observed from **1** to **2**, decreasing from 2.6251(6) Å in **1** to 2.3252(2) Å in **2**, which is consistent with the formation of an Fe-Fe single bond. The formation of a single bond is also evident by examination of the r value of 1.00 for **2**. The Fe-Fe bond length of mixed-valent complex **2** is comparable to the Fe-Fe bond lengths of mixed-valent diiron species in the literature. Specifically, diiron(II,I) species with similar phosphinoamide ligands synthesized by Thomas *et al.* have Fe-Fe bond lengths of 2.4694 Å and 2.4645 Å when the axial ligand is another phosphinoamide ligand or PMe_3, respectively.[15] The bond length of these diiron systems with an apical ligand match very closely to the diiron lithium chloride adduct (**2-LiCl)** described above when diiron(II,II) chloride is reduced using ^{n}BuLi (Fe-

Fe bond length: 2.454 Å). Other diiron(II,I) complexes in the literature synthesized by Cotton *et al.* have Fe-Fe bond lengths of 2.23 Å.[33] Diiron(II,I) **2** exhibits a shorter bond length than Thomas's complex (0.14 Å shorter), yet longer than those reported by Cotton (0.09 Å longer). This difference is likely due to the lack of an axial donor on the Fe(I) center in **2**, like in Thomas's complexes and addition of an apical nitrogen donor to the Fe(II) center, which is absent in Cotton's complexes.

A more important analysis of the bond metrics than the Fe-Fe bond length is the comparison of the Fe-P and Fe-N_{eq} bond lengths in complexes **1** and **2**. Comparison of these values may provide some insight as to whether or not the one electron reduction occurred at the top or bottom iron center. The Fe-P bond lengths decrease by 0.102 Å from the diiron(II,II) chloride to the formally diiron(II,I) complex. The Fe-N_{eq} bond distances only change by 0.03 Å. Together, these bond metric comparisons indicate that the one electron reduction occurs primarily at the iron in the phosphine ligand plane, herein referred to as Fe_P.

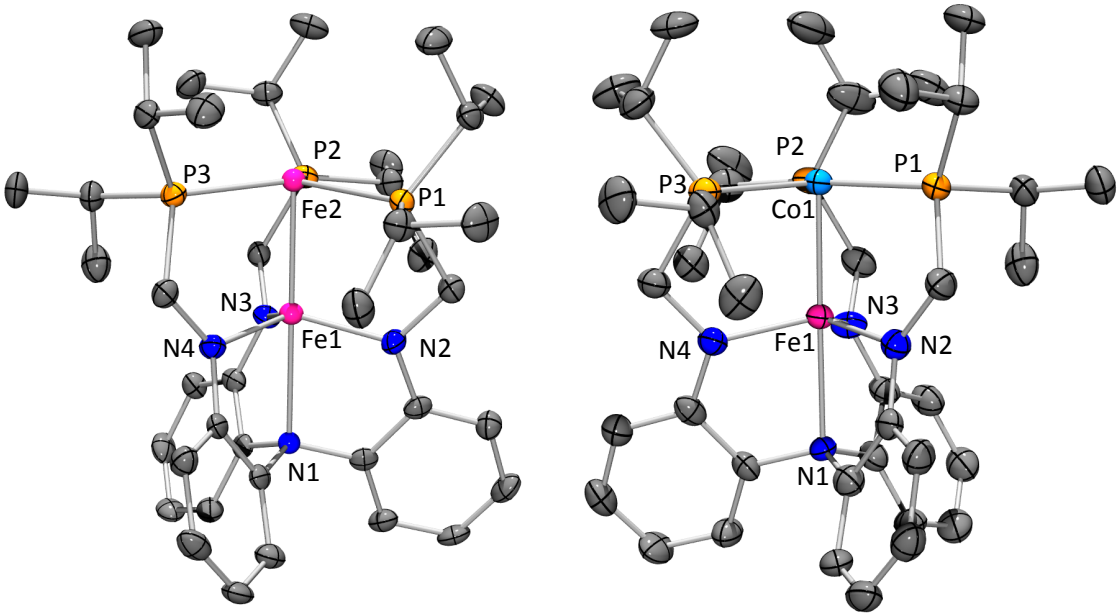

2 **4**

Figure 4.7 Solid-state structure of **2** and **4** at 50% probability. Hydrogen atoms are omitted for clarity.

Single crystals of mixed-valent iron-cobalt(II,I) **4** were grown from diffusion of Et_2O into a concentrated THF solution and analyzed by X-ray diffraction (Figure 4.7). The Fe-Co bond length of **4** is 2.2599(4) Å, which is 0.33 Å shorter than the Fe-Co bond length of 2.5899(6) Å for complex **3**. As previously mentioned, there are very few Fe-Co complexes not ligated by carbonyl groups to compare bond metrics against. An Fe-Co complex synthesized by our group with a trisamidinate ligand system has a Fe-Co bond length of 2.214 Å.[42] Further comparison of the solid-state structures of divalent **3** and mixed-valent **4** reveals an average shortening of 0.078 Å of the Co-P bond distances. This contraction, combined with the lack of difference in the Fe-N_{eq} bond distances in **4** (0.005 Å difference between **3** and **4**) also indicate a localized reduction of the cobalt metal ion.

The covalent ratios of mixed-valent reduced species **2** and **4** are 1.00 and 0.97, respectively. These covalent ratios are indicative of M-M single bonding interactions.

4.3.3 Anomalous Scattering Studies

Heterobimetallic iron-cobalt(II,II) chloride **3** was synthesized by exploiting the lability of the top iron in diiron(II,II) chloride **1**, a phenomenon that has also been observed in triiron complexes as well.[38] This lability lends concern when it comes to determining the position of each metal within the ligand scaffold. Despite the fact that comparison of the bond metrics from the solid-state structures of **1** and **3** reveals evidence for a more electronegative metal atom occupying the phosphine plane, standard X-ray techniques cannot alleviate the valid concerns about the metal ion positions in the ligand scaffold. To assist in delineating this concern, X-ray anomalous diffraction techniques were performed. This technique has been effective in quantifying the occupancies of metal ions in single crystals.[38,43]

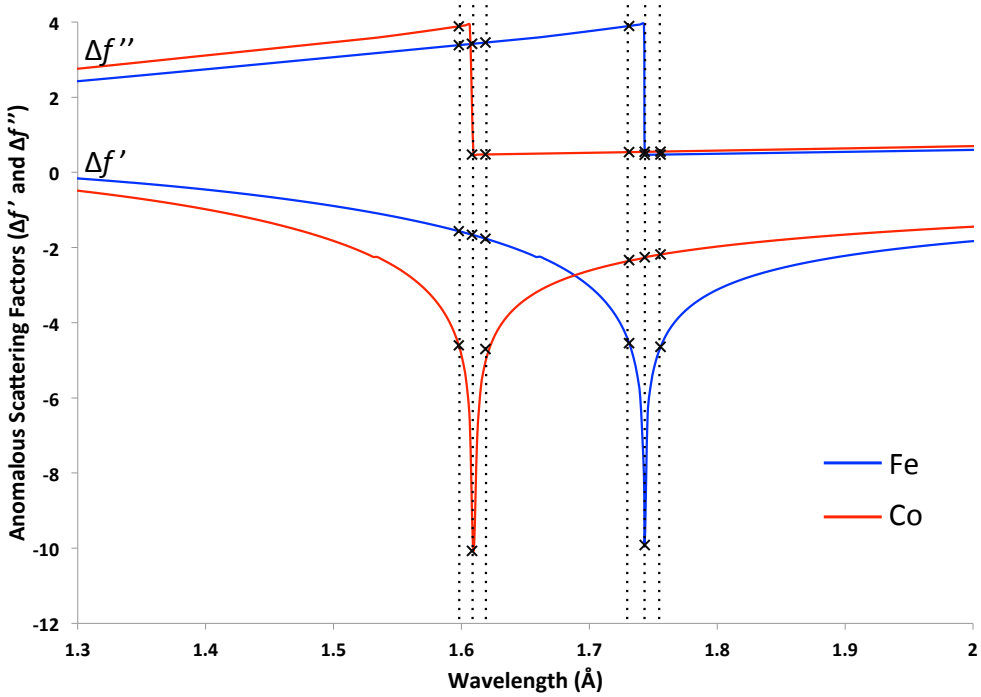

Figure 4.8 The anomalous dispersion corrections to normal scattering factors, including the real ($\Delta f'$) and imaginary ($\Delta f''$) components, for Fe (blue) and Co (red) as a function of wavelength (Å). The six dotted lines represent the experimental energies for the anomalous experiments at 1.755 Å, 1.743 Å, and 1.731 Å, which were selected to span the iron K-edge and at 1.619 Å, 1.608 Å, and 1.598 Å, which were selected to span the Co K-edge. The cross marks (×) indicate the Fe and Co anomalous scattering factor values used in the least-squares refinement to determine the metal occupancies. Figure courtesy of Laura J. Clouston.[42]

The anomalous diffraction data sets were collected using synchrotron radiation at the ChemMatCARS 15-ID-B beam line at the Advanced Photon Source (Argonne National Laboratory). The anomalous scattering factors ($\Delta f'$ and $\Delta f''$) for each metal change considerably when examined at the K-edge of each metal (Figure 4.8). To determine the occupancies of each metal in the ligand scaffold, three anomalous diffraction experiments were collected for each metal to take advantage of the change in the anomalous scattering factors Δf' and Δf'' at the metal's K-edge. For each metal, one collection was done just before the metal's K-edge, just at the K-edge, and just beyond

the K-edge, resulting in six total anomalous diffraction data sets. These six data sets are then refined collectively against a high energy structural model in a least-squares refinement to determine the Fe/Co occupancies at the two metal sites.[44]

The high-energy structural model was collected at 30 keV, to provide a high-resolution (0.5 Å) structure away from both K-edges. Table 4.3 compares the two data collections for iron-cobalt **3**. The high-resolution structure solution compares very well to the original structure determined by standard X-ray diffraction to 0.84 Å resolution. Of the selected bond lengths and angles, only a few of the angles change by more than 1%. Specifically, the Fe-Co bond length changes by only 0.001 Å, which is within experimental error.

Table 4.3 Comparison of bond lengths and angles from 0.84 Å structure and 0.5 Å structure from anomalous diffraction studies.

	^{iPr}LFeCoCl **3**	^{iPr}LFeCoCl **3** 0.5 Å
Fe-M, Å	2.5899(6)	2.5886(3)
M-Cl, Å	2.2476(9)	2.2468(4)
Fe−N_{eq}, Å	1.968(2)	1.963(1)
	1.970(2)	1.970(1)
	1.957(2)	1.962(1)
Fe−N_{ax}, Å	2.300(3)	2.303(1)
M-P, Å	2.3671(8)	2.3626(4)
	2.3672(7)	2.3650(4)
	2.4099(8)	2.4017(4)
N_{eq}−Fe−N_{eq}, ^{o}	115.62(7)	115.18(4)
	114.27(7)	117.67(5)
	116.97(7)	114.21(5)
P−M−P, ^{o}	116.36(2)	116.88(1)
	114.78(2)	114.84(1)
	116.35(2)	115.85(1)
M-M-Cl, ^{o}	169.56(3)	169.57(1)

In order to discuss the results of the refinement on the anomalous diffraction data, the phosphine plane of ^{iPr}L will be referred to as *site 1* and the nitrogen plane of the ^{iPr}L

will be referred to as *site 2*. The least squares refinement of the data leads precise occupancies for each *site.* For *site 1* the occupancies refine to 13.4% iron and 86.6% cobalt. For *site 2* the occupancies refine to 93.3% iron and 6.7% cobalt. If purely statistical mixing within the two metal sites is assumed, then the percentages of each possible metal-metal pair can be determined from these occupancies. The single crystal of **3** contains 80.8% ^{iPr}LFeCoCl, 12.5% ^{iPr}LFeFeCl, 5.8% ^{iPr}LCoFeCl, and 0.9% ^{iPr}LCoCoCl. Although some metal mixing is observed, that the major component of complex **3** does indeed have iron in the nitrogen plane (*site 2*) and cobalt in the phosphine plane (*site 1*). Diiron, ^{iPr}LFeFeCl, is the second highest percentage bimetallic, which is reasonable considering that ^{iPr}LFeCoCl **3** is synthesized directly from ^{iPr}LFeFeCl. The 5.8% composition associated with ^{iPr}LCoFeCl indicates that the Fe_N metal center in the diiron(II,II) chloride starting material is somewhat labile. The very small percentage of ^{iPr}LCoCoCl suggests that during the reaction of ^{iPr}LFeFeCl **2** with $CoCl_2(THF)_{1.5}$, complete iron demetallation does not occur.

4.3.4 Vis-NIR Data

The deep blue and purple colors of **1** and **3**, respectively, lead to rich electronic absorption spectra. As shown in Figure 4.9, **1** and **3** each have two strong absorptions in the visible (Vis) region at λ_{max} = 504 and 631 nm (ε = 5400, 7800 M^{-1} cm^{-1}) and λ_{max} = 509 and 593 nm (ε = 5000, 4400 M^{-1} cm^{-1}), respectively. The near infrared (NIR) region is more distinct as **1** has one absorbance at λ_{max} = 1073 nm (ε = 400 M^{-1} cm^{-1}) while **3** has two absorbances at λ_{max} = 1007 and 1525 nm (ε = 320, 418 M^{-1} cm^{-1}, respectively). Again, compared to literature values of similar complexes the molar absorptivity of the

transitions are unusually large. Particularly interesting is the comparison to Thomas *et. al.* diiron phosphinoamide complexes, for which only weak visible transitions were reported with no NIR transitions.[28] Similar visible transitions are observed in the triiron complexes synthesized by the Betley group. The high-spin triiron complex (^{Ph}L)$Fe_3(THF)_3$ has the most rich absorption spectrum with λ_{max} = 428 (5800), 590 (2000), 760 (1700). Again, no NIR transitions were not reported.[23] Interpretations are lacking and future theoretical studies would be useful to understand the underlying nature of these transitions. However, based on the molar absorptivity one would predict that the visible transitions are a result of metal-ligand charge transfers (MLCT) or ligand-metal charge transfers (LMCT). Perhaps they could be assigned as MLCT since the transitions shift to higher energy from diiron(II,II) chloride **1** to iron-cobalt(II,II) chloride **3**. Comparison to other bimetallic complexes synthesized in the Lu group allows for the tentative assignment of the NIR transition as spin- and dipole-allowed *d*-*d* electronic transitions.[21,42]

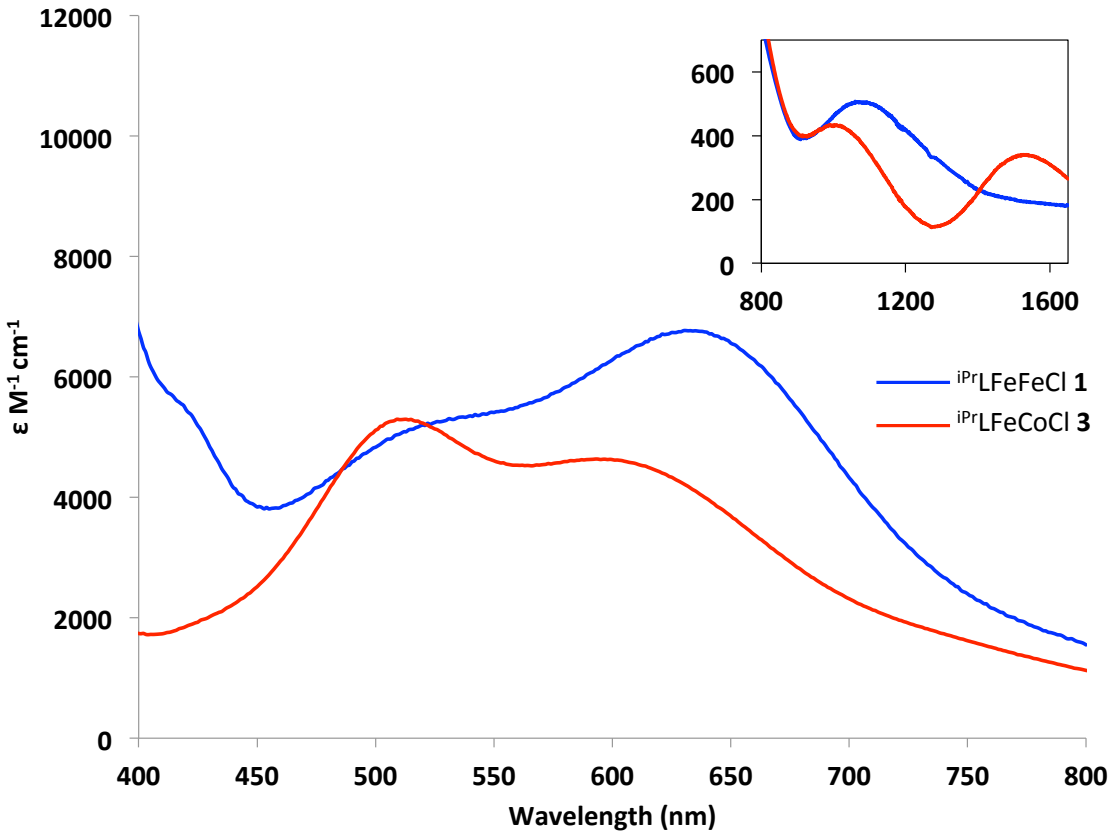

Figure 4.9 Vis-NIR spectra (ε vs. nm) of **1** (in blue) and **3** (in red) in THF at rt. Inset shows NIR region (ε vs. nm).

The visible region of the mixed-valent species **2** and **4** also exhibit intense features, however they are shifted to higher energies (Figure 4.10). Diiron(II,I) **2** has a strong absorbance exhibited on the shoulder of the UV absorbances at λ_{max} 350 = nm (ε = 6275 M^{-1} cm^{-1}) as well as three weaker absorbances at λ_{max} = 420 nm (ε = 2090 M^{-1} cm^{-1}), λ_{max} = 538 nm (ε = 1295 M^{-1} cm^{-1}) and λ_{max} = 663 nm (ε = 766 M^{-1} cm^{-1}). One strong absorbance at λ_{max} 415 = nm (ε = 9000 M^{-1} cm^{-1}) that trails off into a shoulder at λ_{max} = 530 nm (ε = 3000 M^{-1} cm^{-1}) and a weak band at λ_{max} 761 = nm (ε = 500 M^{-1} cm^{-1}) define heterobimetallic iron-cobalt(II,I) **4**. Similar higher energy transitions are

observed in the mixed-valent diiron(II,I) species synthesized by Thomas *et al* (e.g. λ_{max} = 366 nm (ε = 7500 M^{-1} cm^{-1}) and λ_{max} = 506 nm (ε = 2200 M^{-1} cm^{-1})).

The NIR features decrease in intensity for complexes **2** and **4**, compare to divalent complexes **1** and **3** ($\varepsilon \sim 400$ M^{-1} cm^{-1}). Interestingly, the NIR absorption at λ_{max} 1056 = nm (ε = 212 M^{-1} cm^{-1}) is very close in energy to that observed for diiron(II,II) chloride **1**, λ_{max} 1073 nm. Furthermore, two NIR transitions were observed for iron-cobalt(II,II) chloride, whereas only one lower energy absorption is observed for iron-cobalt(II,I) **4** (λ_{max} 1521 = nm (ε = 100 M^{-1} cm^{-1})). Based on the molar absorptivity, the NIR transitions for complexes **2** and **4** are tentatively assigned as *d-d* transitions, though whether they are intermetal or intrametal *d-d* is not yet known.

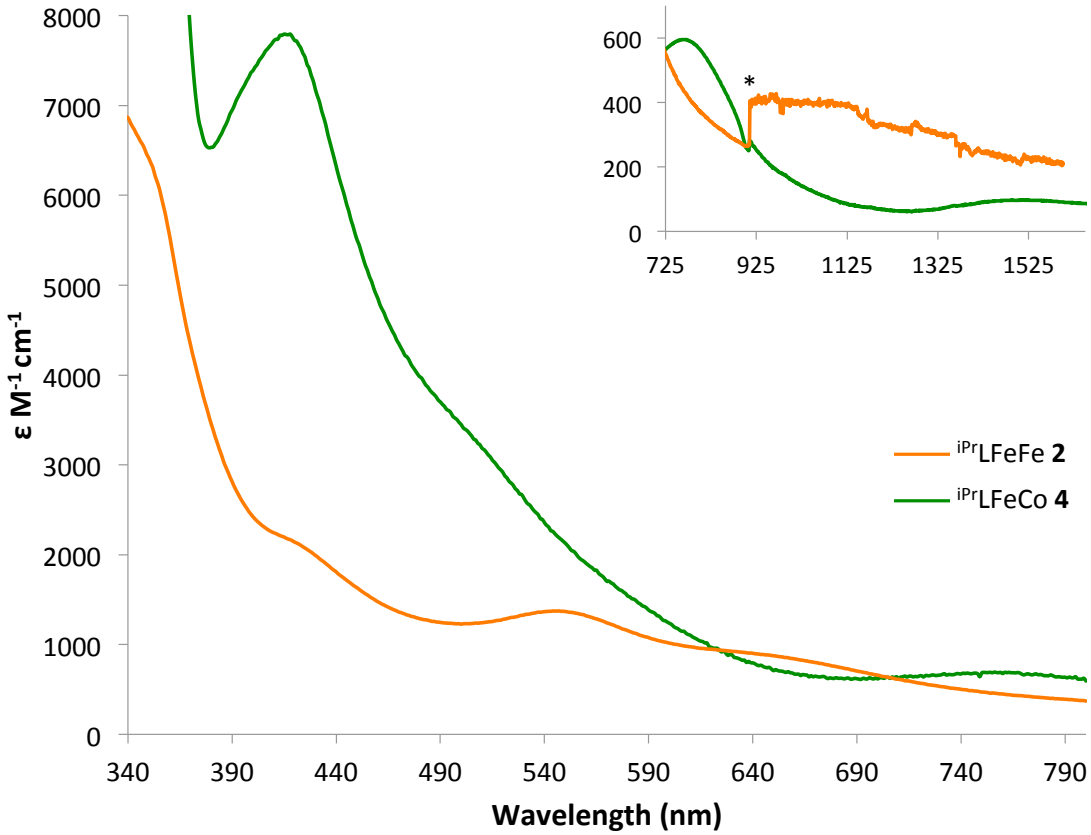

Figure 4.10 Vis-NIR spectra (ε vs. nm) of **4** in THF at rt. Inset shows NIR region (ε vs. nm). Asterisk denotes a change in lamp.

4.3.5 Magnetic Measurements

We are interested in investigating the electronic structure of late transition metal divalent species, diiron(II,II) chloride **1** and iron-cobalt(II,II) chloride **3**, and mixed-valent species diiron(II,I) **2** and iron-cobalt(II,I) **4**. Furthermore, we are interested in determining if swapping the top iron with cobalt has an effect on the electronic structure. To determine their ground spin states, complexes **1 - 4** have been studied in the solid state using superconducting quantum interference device (SQUID) magnetometry.

From 40K to 290 K, the effective magnetic moments, μ_{eff}, is essentially temperature independent with values of ~9.75 μ_B and ~8.00 μ_B, for **1** and **3** respectively.

These values are consistent with well-isolated nonet and octet states, which have spin only values of 8.94 and 7.94 μ_B, respectively. Figure 4.11 shows the effective magnetic moment plotted versus temperature. The plot for **1** can be fitted as two strongly ferromagnetically coupled (J > 200 cm^{-1}) $S = 2$ iron centers by adopting g-values of 2.2 and a zero-field splitting parameter $D = 3.0$ cm^{-1} for each iron center. Similarly, the plot of complex **3** can be simulated as two strongly ferromagnetically coupled (J > 200 cm^{-1}) $S = 2$ and $S = 3/2$ high-spin iron and coblat metal centers, respectively, with g-values of 2.0 and a zero-field splitting parameter of $D = 2.0$ cm^{-1} for each metal.

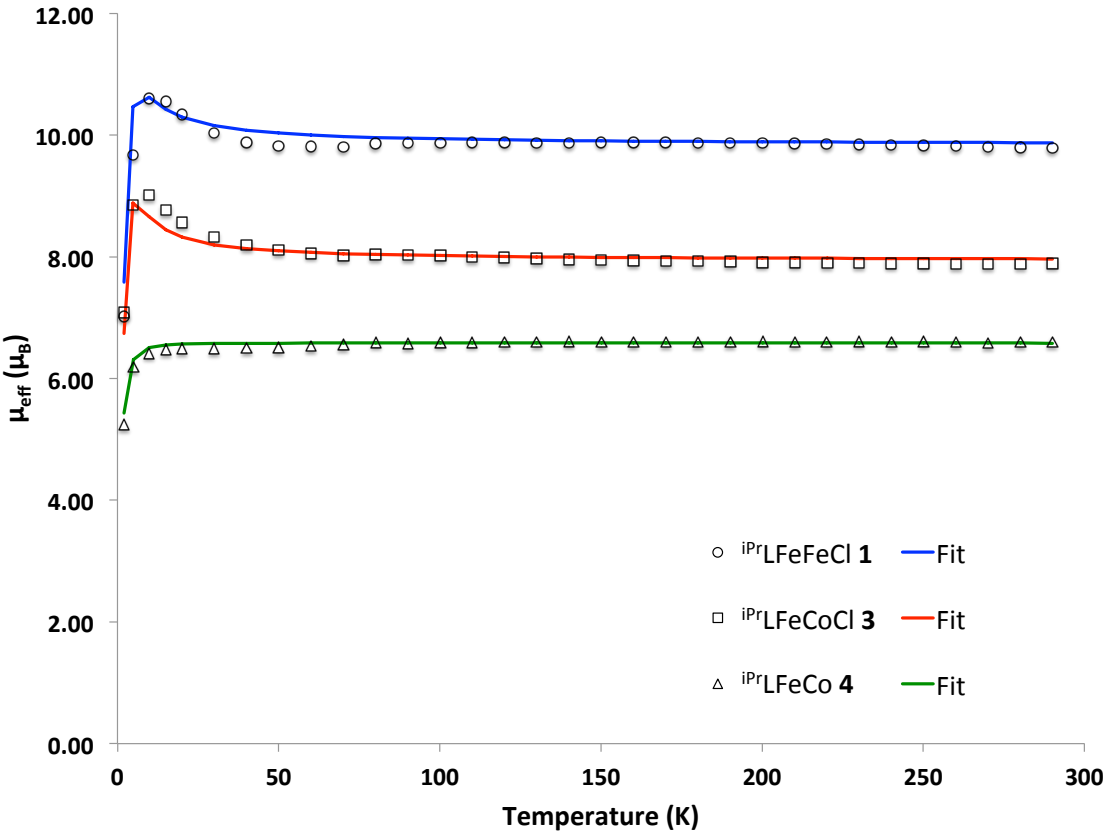

Figure 4.11 Variable temperature magnetic susceptibility of **1** (circles, blue), **2** (squares, red) and **4** (triangles, green) at 1 T from 2 to 290 K.

Variable-temperature magnetic susceptibility measurements of **4** are plotted in Figure 4.11 as μ_{eff} versus temperature (triangles). From 5K to 290K, complex **4** is temperature independent with an effective magnetic moment of ~ 6.6 μ_B. This is consistent with a well-isolated septet ground state, which has a spin-only magnetic moment of 6.93 μ_B. The green line represents a fit of the data using a two spin model consisting of one iron and one cobalt center, formally high-spin Fe(II) and Co(I) with S = 2 and S = 1, respectively. The fit reveals effective g values of 1.9 for both the iron and cobalt metal centers. The two high-spin metal centers are strongly ferromagnetically coupled (J > 200 cm^{-1}) and the magnetic data is best fit with a zero field splitting parameter of D = 2 cm^{-1}.

4.3.6 Mössbauer Spectroscopy

In order to further investigate the electronic structure of complexes **1-4**, ^{57}Fe Mössbauer spectroscopy was performed. The most important parameters derived from the Mössbauer experiment are the isomer shift (δ) and the quadrupole splitting ($|\Delta E_Q|$). The isomer shift can provide insight into the oxidation state of the iron centers due to its correlation to the *s* electron density at the iron center. The quadrupole splitting arises from the interactions of the nucleus and the electric field gradient (EFG), which can be affected by the asymmetry of either the electronic environment or the ligand environment. The isomer shift and quadrupole splitting for each complex is outlined in Table 4.4. The zero-field Mössbauer spectra of **1** at 80K reveals a broad quadrupole doublet that is best fit with two Lorentzian lines of nearly equal intensity with isomer shifts at 0.43 and 0.46 mm/s and quadrupole splittings of 1.26 and 0.71 mm/s,

respectively (Figure 4.12). Diiron(II,II) chloride **1** has two unique iron centers each with formal oxidation states of Fe(II), which is consistent with the similarity of their isomer shifts. The Mössbauer spectroscopy of **1-Br** also contains two quadrupole doublets (Figure 4.13). One doublet, $\delta = 0.41$ mm/s and $|\Delta E_Q| = 1.15$, matches well with one of the quadrupole doublets of **1** ($\delta = 0.43$ mm/s and $|\Delta E_Q| = 1.26$), while the other doublet has a higher isomer shift of 0.61 mm/s. Comparing the isomer shifts of **1** and **1-Br** allows for the assignment of the isomer shifts to either the Fe_N or Fe_P ligand planes. The lower isomer shifts (0.41 mm/s and 0.43 mm/s) are assigned to the Fe_N plane, which should be similar in both complexes, and the higher isomer shifts (0.46 mm/s and 0.61 mm/s for **1** and **1-Br**, respectively) are assigned to the Fe_P ligand plane.

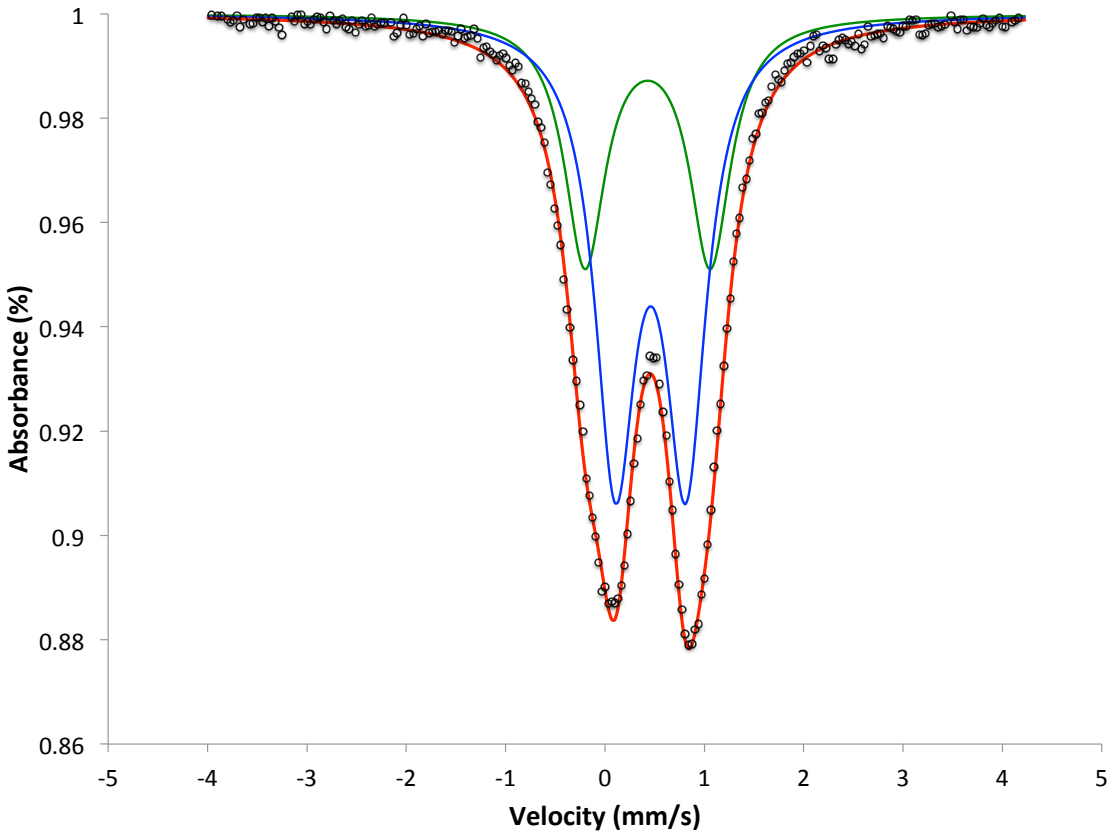

Figure 4.12 Zero-field ^{57}Fe Mössbauer spectrum of **1** at 80 K, fitted as two quadrupole doublets (red) at 36% (δ = 0.43 mm/s, $|\Delta E_Q|$ = 1.26 mm/s, green) and 64% (δ = 0.46, $|\Delta E_Q|$ = 0.71, blue) intensity.

The Mössbauer parameters for **1** and **1-Br** can be compared to other Fe(II) complexes in the literature. First, the isomer shifts assigned to the Fe_P center for **1** and **1-Br**, 0.43 and 0.60 mm/s, respectively, can be compared to other iron halide complexes in a trigonal phosphine environment. Once again, the most similar literature comparisons are the diiron(II,II) complexes synthesized by the Thomas group. The isomer shifts assigned to the Fe_p coordination sphere range from 0.51 to 0.69 mm/s for the three diiron(II,II) complexes.[28] Additionally, the Peters group has synthesized a mononuclear iron complex supported by a trisphosphineborane ligand system ($PhB(CH_2P^iPr_2)_3FeCl$) with comparable Mössbauer parameters of δ = 0.58 mm/s, $|\Delta E_Q|$ = 1.65 mm/s.[45] The 0.60

mm/s isomer shift of **1-Br** compares well to these literature examples, however, the isomer shift of 0.43 in complex **1** is slightly lower. At this time, it is unclear as to why complex **1** has a lower isomer shift than previously observed for high-spin Fe(II) chloride complexes supported by trigonal phosphine ligand scaffolds in the literature. Comparison of the isomer shifts assigned to the Fe_N ligand plane of complexes **1** and **1-Br** (0.41 and 0.43 mm/s, respectively) is interesting. Generally, compared to mononuclear three coordinate high-spin Fe(II) complexes in the literature, the isomer shifts for complexes **1** and **1-Br** are lower than what is typically observed (0.6 – 0.8 mm/s).[46-48] Comparison to diiron, triiron, and hexairon complexes with direct iron-iron interactions is perhaps more useful. However, nearly all of these iron complexes also have isomer shifts more in the normal range for high-spin Fe(II) complexes (0.51 – 0.85 mm/s) (Table 4.4). One triiron ($^{H}LFe_3(PMe_2Ph)_3$) complex and one hexairon ($(^{H}L)_2Fe_6$) complex synthesized by Betley *et al*. deviate from the trend similarly to complexes **1** and **1-Br**. The lower isomer shift of the triiron complex (δ = 0.38 mm/s) is likely attributed the ground spin state of S = 1, compared to the other triiron complexes in this family which have higher ground spin states (S = 2 to S = 6). Interestingly, the hexairon complex, $(^{H}L)_2Fe_6$, has an isomer shift of 0.48 mm/s and has a high-spin ground state. This complex provides the best comparison for the Mössbauer parameters observed for the Fe_N plane of complexes **1** and **1-Br**, 0.41 and 0.43 mm/s, respectively.

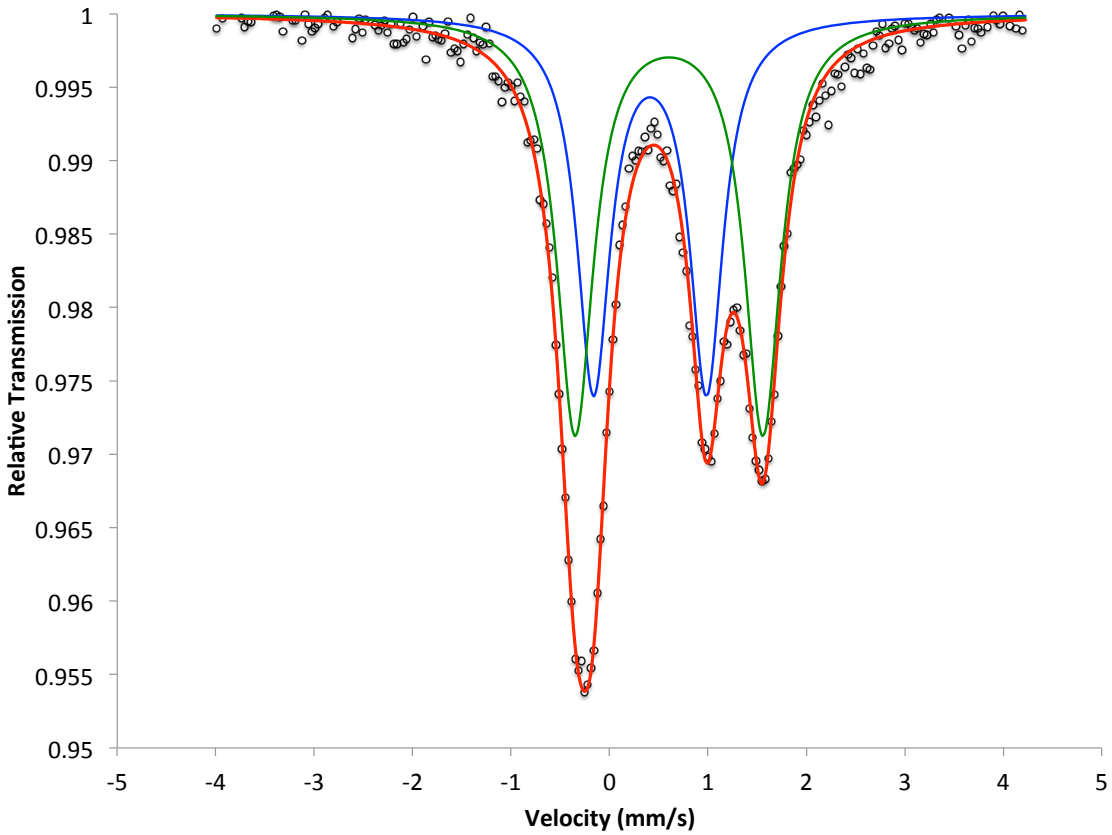

Figure 4.13 Zero field Mössbauer spectrum of **1-Br** at 80 K, fitted as two quadrupole doublets (red) at 55% (δ = 0.60 mm/s, $|\Delta E_Q|$ = 1.91 mm/s, green) and 45% (δ = 0.41, $|\Delta E_Q|$ = 1.15, blue) intensity.

Table 4.4 Mössbauer parameters for complexes **1-4** and select literature examples.

Complex	Fe_N			Fe_P or neutral donor for examples		
This work	**δ (mm/s)**	**$\|\Delta E_Q\|$ (mm/s)**	**%**	**δ (mm/s)**	**$\|\Delta E_Q\|$ (mm/s)**	**%**
^{iPr}LFeFeCl **1**	0.43	1.26	36	0.46	0.71	64
^{iPr}LFeFeBr **1-Br**	0.41	1.15	45	0.60	1.91	55
^{iPr}LFeFe **2**	0.68	0.23	100			
^{iPr}LFeCoCl **3**	0.28	1.71	100			
^{iPr}LFeCo **4**	0.39	1.06	100			
Thomas[28]						
$(^{iPr}NPPh_2)_3FeFe(^{iPr}NPPh_2)$	0.57	2.17	55	0.51	1.67	45
$(^{Mes}NP^iPr_2)_3FeFeCl$	0.63	1.16	38	0.69	2.63	62
$(^{iPr}NP^iPr_2)_2(^{iPr}NP^iPr_2)FeFeCl$	0.60	1.80	100			
Betley[22,23,38]						
$(^{Ph}L)Fe_3(THF)_3$	0.79	1.25	100			
$(^{Ph}L)Fe_3(py)_3$	0.82	1.48	71	0.85[a]	2.20	29
$(^{Ph}L)Fe_3(PMe_2Ph)_3$	0.77	1.43	68	0.77[a]	2.30	32
$(^{H}L)Fe_3(PMe_2Ph)_3$	0.38	1.04	100			
$(^{H}L)_2Fe_6$	0.48	1.79	100			
$(^{Ph}L)_2Fe_2CoCl(NCCH_3)$[b]	0.83	1.41	57	-0.01	2.36	22
				0.21	2.92	21
Peters[45]						
$PhB(CH_2P^iPr_2)_3FeCl$	0.58	1.65	100			
Cotton[21,33]						
$Fe_2(DPhF)_3$	0.65	0.32	100			
Lu[42]						
(LPh)FeCo[c]	0.65	0.64	100			

[a]The author attributes these to a different spin states rather than a separate iron environments. [b]Three quadrupole doublets were observed. [c]LPh = tripodal trisamidinate ligand scaffold.

The Mössbauer spectrum of **2** is much less resolved compared to **1** and **1-Br** and shows a very broad signal, likely due to paramagnetic relaxation effects. It can be fit to a single quadruple doublet with an isomer shift of 0.68 mm/s and a quadrupole splitting of 0.23 mm/s (Figure 4.14). The broad spectrum, single isomer shift, and small quadrupole splitting are similar to the $Fe_2(DPhF)_3$ (DPhF = diphenylformamidinate) system by Cotton *et al.* and recently reinvestigated by our group.[21,32] The $Fe_2(DPhF)_3$ system has an isomer shift of 0.65 mm/s and a quadrupole splitting of 0.23 mm/s and these features were attributed to a delocalized $Fe^{1.5}Fe^{1.5}$ core. This interpretation does not align with mixed-valent diiron(II,I) **2** on the basis of disparate ligand environments, the experimental solid-state structure of **2**, and theoretical investigations (*vide infra*). First, if

the electron density were delocalized across the two iron centers, the ligand environment around the irons would be different and should result in distinct quadrupole doublets for each iron. Second, the solid-state structure bond metrics suggest that the reduction from **1** to **2** is localized on Fe_P. The appearance of only one quadrupole doublet in **2** could also be coincidental. Of note, the isomer shift increases upon reduction from **1** to **2**, which suggests a decrease in *s*-electron density. The addition of a *d*-electron possibly increases shielding, which would result in lower *s*-electron density and thus an increase in isomer shift.[49]

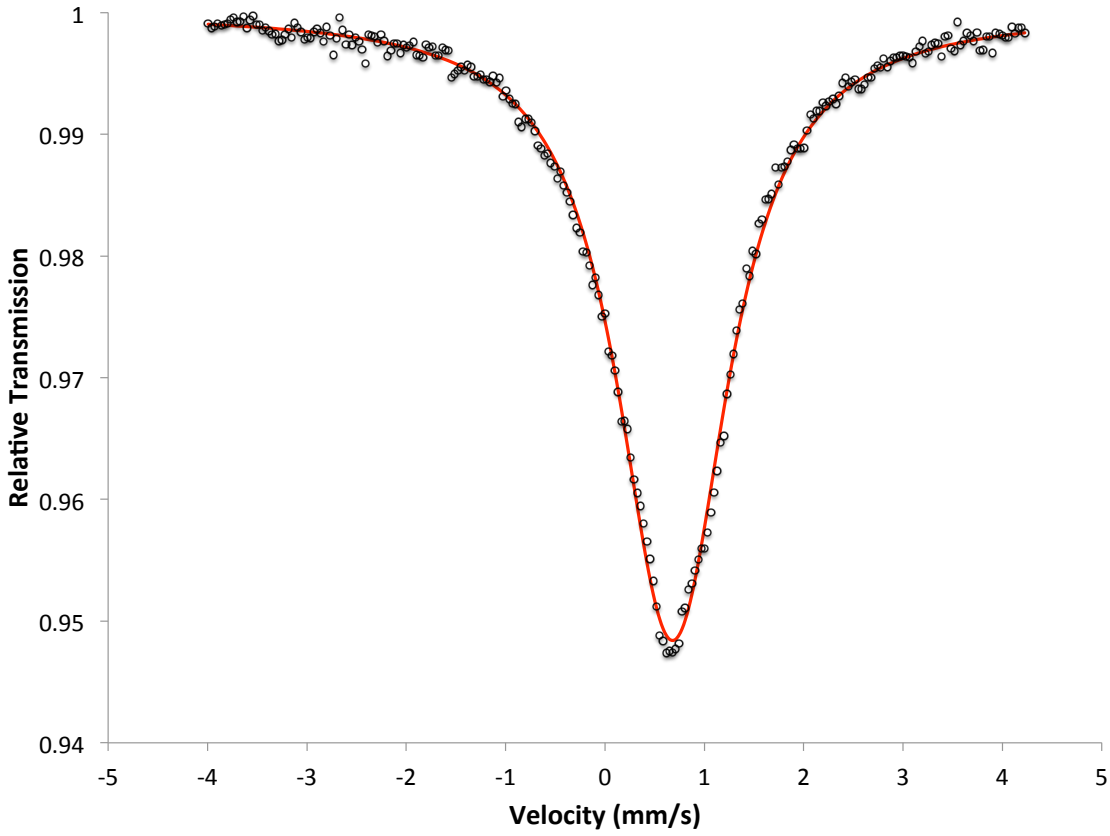

Figure 4.14 Zero-field Mössbauer spectrum of **2** at 80 K, fitted as a quadrupole doublet at 100% (δ = 0.68 mm/s, ΔE_q = 0.23 mm/s, red) intensity.

Initial zero-field Mössbauer experiments performed on iron-cobalt(II,II) chloride **3** show a broadened spectrum that could not be resolved enough to reveal the Mössbauer parameters desired accurately (Appendix A, Figure A-5); thus, we turned to applied-field ^{57}Fe Mössbauer spectroscopy. The spectra was globally fitted with an isotropic $g_{7/2} = 2.0$, $D_{7/2} = -8.3$ cm^{-1}, $E/D_{7/2} = 0$ cm^{-1}, and the Mössbauer parameters $\delta = 0.28$ mm s^{-1} and $\Delta E_q = 1.71$ mm s^{-1} (Figure 4.15). The values obtained for *g*, *D*, and *E/D* correspond reasonably well to the values observed in the magnetic susceptibility measurements (*g* = 2.0, *D* = 2.0, and *E/D* = 0). The decrease in isomer shift from diiron(II,II) chloride **1** to iron-cobalt(II,II) chloride **3** is unexpected because as stated before, increasing the d-electron count around the iron center should cause more shielding of the s-electrons and thus an increase in the isomer shift.[49] The Mössbauer parameters for a heterotrimetallic diiron cobalt complex ((^{Ph}L)$_2$Fe$_2$CoCl(NCCH$_3$)) synthesized by Betley *et al*. could provide some insight for the unique isomer shift observed in iron-cobalt(II,II) chloride **3**. While a large percentage (57%) of the complex exhibits an isomer shift typical of high-spin Fe(II) metal centers (δ = 0.83 mm/s), two smaller percentage components have lower isomer shifts similar to **3** (δ = -0.01 (22%) and 0.21(21%)).

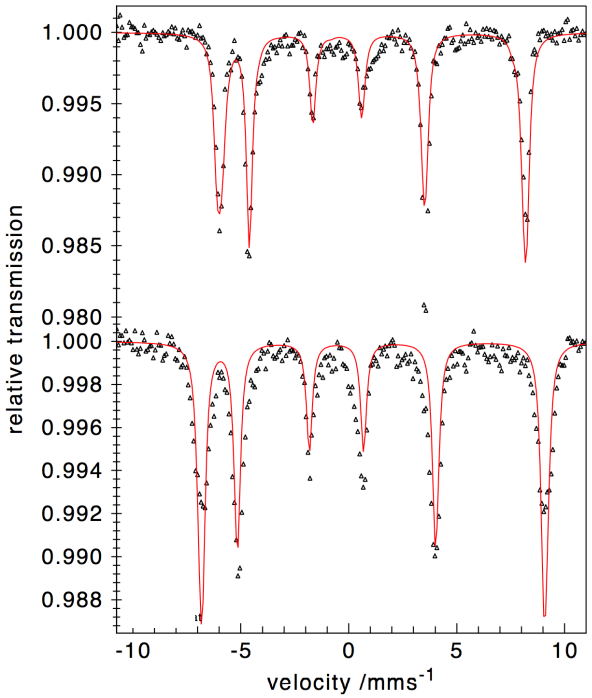

Figure 4.15 Variable-field ^{57}Fe Mössbauer spectrum of **3** at 1 T (top) and 7 T (bottom).

Iron-cobalt(II,I) **4** has also been characterized by Mössbauer spectroscopy (80K, zero applied field) and the spectrum revealed a single, well-resolved quadrupole doublet (Figure 4.16). Mössbauer parameters of δ = 0.39 mm s^{-1} and ΔE_q = 1.06 mm s^{-1} were determined from the global fit. As observed with complexes **1** and **2**, the isomer shift increases upon reduction from **3** (0.28 mm/s) to **4** (0.39 mm/s).

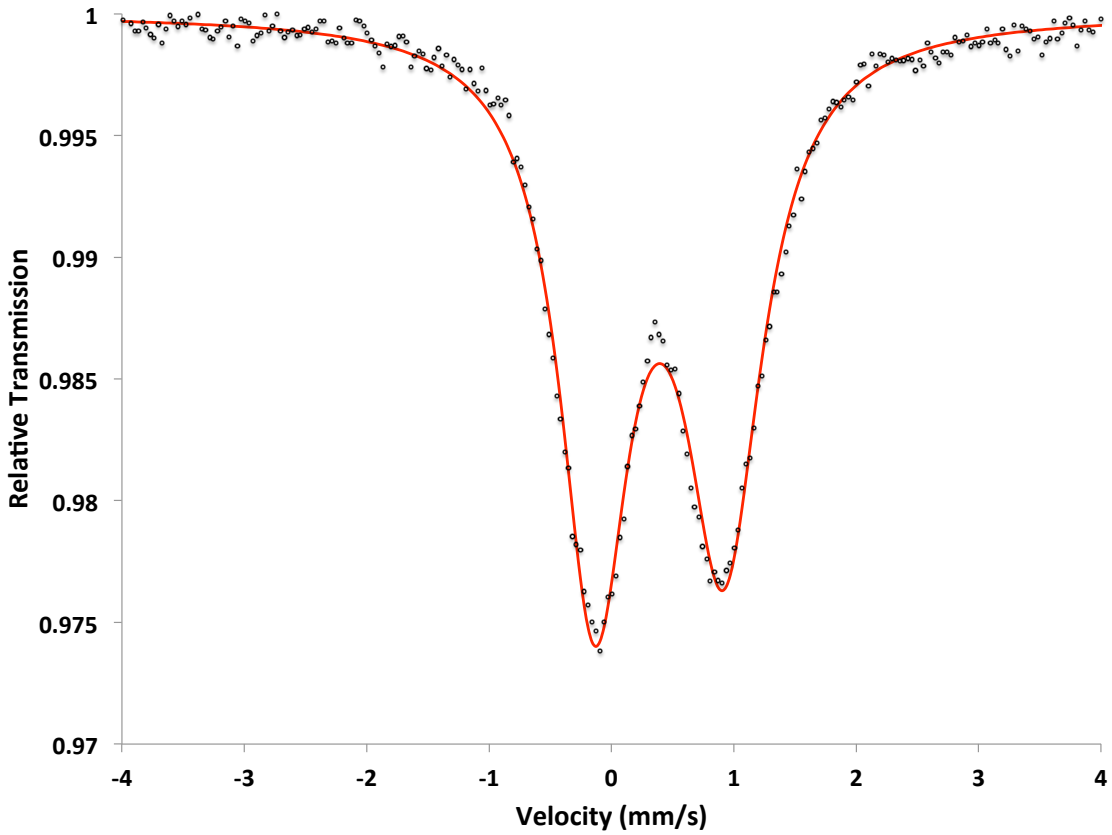

Figure 4.16 Zero field Mössbauer spectrum of **4** at 80 K, fitted as a quadrupole doublet at 100% (δ = 0.39 mm/s, ΔE_q = 1.06 mm/s, red) intensity.

4.3.7 Cyclic Voltammetry

The redox properties of diiron(II,II) chloride **1** and iron-cobalt(II,II) chloride **3** were studied using cyclic voltammetry (CV). The CV of both complexes were measured in a 0.4 M [TBA][PF_6] solution in THF and the redox potentials were referenced against an internal ferrocene standard. Complex **1** exhibits a single quasi-reversible reduction wave at -1.48 V (Figure 4.17) with a peak-to-peak separation of 150 mV. This quasi-reversible wave is assigned to the Fe^{II}/Fe^{I} redox couple and based on the solid-state structural analysis of **1** and **2** as well as theoretical investigations (*vide infra*), we assign

this to the Fe_P. The cyclic voltammogram of **1** also exhibits an irreversible oxidation wave (E_{pa} = 0.11 V) and an irreversible reduction wave (E_{pc} = -2.61) (Table 4.5).

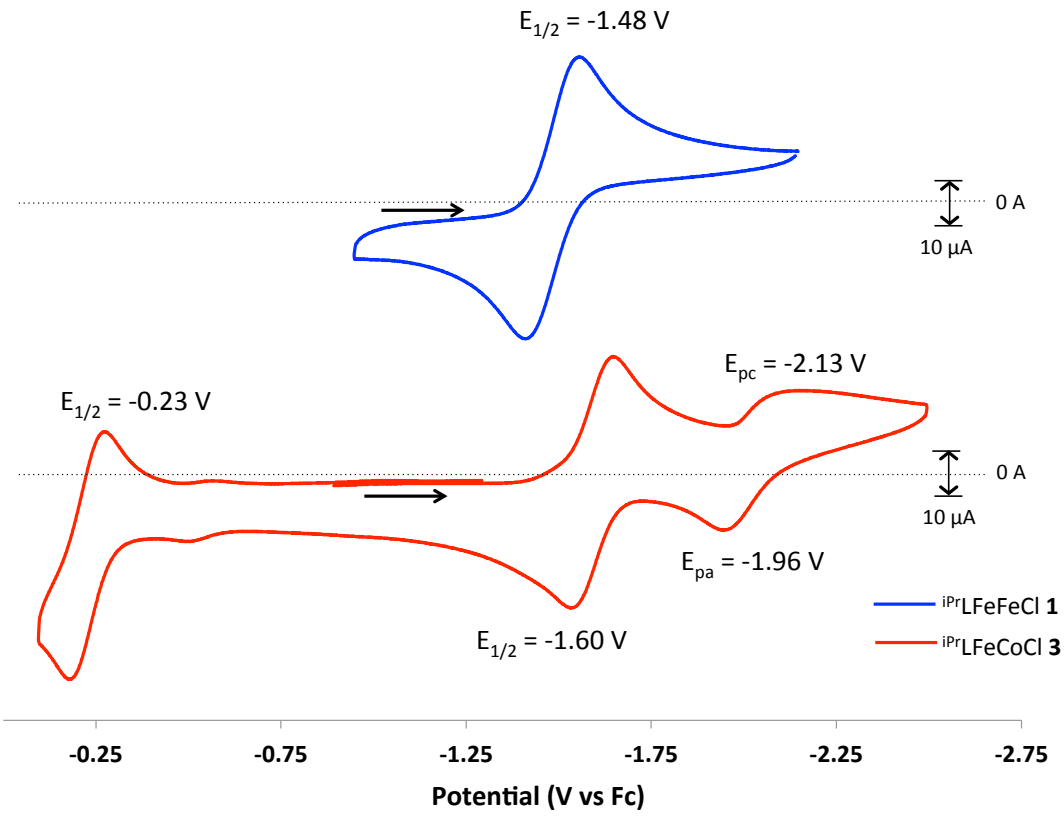

Figure 4.17 Cyclic voltammograms of **1** and **3** in 0.4 M [TBA][PF_6] THF solution. Scan rate is 300 mV/s.

The cyclic voltammogram of complex **3** shows one reversible redox wave and two quasi-reversible waves compared to the single reduction wave observed in complex **1**. The first reduction wave at -1.60 V has a peak-to-peak separation of 92 mV at a scan speed of 300 mV/s. This reduction is assigned to the Co^{II}/Co^{I} couple. Switching out the iron for a cobalt results in a shift in the reduction potential of 0.12 V. Complex **3** also exhibits a quasi-reversible reduction wave at -2.05 V. This wave has half of the current that the one electron reversible waves exhibit, however it is consistent and likely

represents a redox event that generates a complex that is unstable on the electrochemical timescale. Interestingly, complex **3** has a quasi-reversible oxidation wave at -0.23 V, which was irreversible in the case of diiron **1**. Based on the fact that this oxidation is irreversible in complex **1** and reversible in complex **3**, it would be reasonable to assign this oxidation to the Co^{III}/Co^{II} couple.

Table 4.5 Redox potentials of **1** and **3** referenced against the Fc/Fc^+ redox couple in a 0.4M [TBA][PF_6] solution.

	Redox Potentials (V vs Fc)		
	Oxidation	**1st Reduction**	**2nd Reduction**
^{iPr}LFeFeCl **1**	0.11[d]	-1.48[b]	-2.61[c]
^{iPr}LFeCoCl **3**	-0.23[b]	-1.60[a]	-2.13[c], -1.96[d]

[a]$E_{1/2}$ for a reversible process. [b]$E_{1/2}$ for a quasi-reversible process. [c]E_{pc} for an irreversible reduction. [d] E_{pa} for an irreversible oxidation process.

Assignment of the redox couples for complexes **1** and **3** is not trivial given that two redox active metal centers are involved. Mononuclear iron and cobalt halide complexes ligated with similar donors can provide insight. Peters *et al.* has synthesized a tris(phosphine)borane ligand system ($PhBP^iPr_3$) and iron chloride and cobalt iodide complexes have been isolated and studied using electrochemical methods.[45] Similarly to the complexes discussed herein, the $(PhBP^iPr_3)_3FeCl$ exhibited only one reversible reduction (-1.64 V vs Fc/Fc^+) while $(PhBP^iPr)_3CoI$ has one reversible reduction and one quasireversible oxidation (-1.27 V and 0.01 V vs Fc/Fc^+, respectively). As discussed previously, analysis of the solid state structures of complexes **1-4** also indicated that the reductions occur on the phosphine ligated metal center due to the lack of change in the Fe-N_{eq} bond lengths from diiron(II,II) chloride **1** to diiron(II,I) **2** and iron-cobalt(II,II) chlroride **3** to iron-cobalt(II,I) **4** (0.016 Å and 0.005 Å, respectively). Although the Fe-N_{ax} bond lengths change slightly more (0.03 Å and 0.06 Å for diiron and iron-cobalt

complexes, respectively), the change is still minimal relative to the change in the M-P bond lengths upon reduction (0.1019 Å and 0.0782 Å for diiron and iron-cobalt, respectively). Lastly, the natural orbitals from CASSCF calculations reveal that the valence electrons are highly localized on each metal center rather then delocalized between the two metal centers. The lowest singly occupied molecular orbital for the diiron is a localized Fe_P orbital and for the iron-cobalt complex it is a Co orbital.

Another comparison of interest is the effect of the bottom iron on the electronic structure of the top metal. When iron(II) halide and cobalt(II) halide are in a triphosphino ligand environment, the cobalt complexes generally have more positive redox potentials (i.e. easier to reduce).[45] In the case of complexes **1** and **3**, complex **1** is 0.12 V more positive than complex **3**, suggesting that the iron metal center is easier to reduce than the cobalt metal center. Comparison of the iron and cobalt reduction potentials of the $(PhBP^iPr_2)_3MX$ complexes discussed above reveals a 0.37 V difference with the cobalt complex being more positive. The effect of the borane on the iron and cobalt metal centers is defined as weak, as illustrated by the similar trend in the reduction potentials to other mononuclear iron and cobalt complexes. Of note, an Al-M series recently published by our group using the same ligand herein, exhibits an astonishing negative shift (1.2 v) in the M^{-1}/M^0 redox couple when cobalt is replaced with iron.[30] This trend observed for the Al-M series and complexes **1** and **3** is flipped compared to monometallic iron and cobalt complexes, suggesting that even weak interactions between the two metal centers could affect the redox properties of the complex.

4.3.8 Theoretical Calculations

Density functional theory (DFT) at the PBE/def-TZVP level of theory was used to explore the electronic structure of complexes **1-4**.[50-53] A variety of spin states were considered for each complex and geometry optimizations were performed for all cases using the Turbomole 6.1 program package.[54] Initial geometries were obtained from the solid-state structures, and the isopropyl groups were trunctated to methyl groups to lessen computational cost. Previous DFT work using ^{iPr}L have shown this to have little to no effect on computational results.[30] The DFT optimized geometries were compared with experimental bond metrics and they are in good agreement with the structure obtained for the ground state (Appendix A, Table A.1, A.2, A.3 and A.4). The calculated relative energies in kcal/mol for each complex are outlined in **Table 4.6**. At the PBE level of theory, DFT predicts the ground state of complexes **2, 3,** and **4** to have high-spin configurations, $S = 7/2$, $S = 7/2$, and $S = 3$, respectively. For diiron(II,II) chloride **1**, DFT predicted the ground state to be $S = 3$; however, magnetic susceptibility studies indicate that the ground state of **1** is a well-isolated nonet ($S = 4$). The relative energies of the septet and nonet spin states of **1** are only different by 0.59 kcal/mol, which is within the accepted error of the method.

Recent work by our group in collaboration with Prof. Laura Gagliardi's group has shown that metal-metal complexes often have multi-configurational ground states, thus, all of the complexes were further analyzed using the complete active space self-consistent field (CASSCF)[55] with corrections to the energy from second-order perturbation theory (CASPT2).[56] The CASSCF/PT2 calculations were performed with the Molcas7.4

program package using the DFT optimized geometries. For each complexes **1**, **2**, and **4**, a complete active space consisting of all of the d-electrons for each metal ion (e.g. 12 for ^{iPr}LFeFeCl **2**) distributed over 15 orbitals. The active space was optimized to include all of the 3d orbitals for each metal ion and five 4d orbitals, which are included for correlation effects between the third and fourth shell of the metal ions. For complex **3**, an AS of 9 electrons in 13 orbitals was utilized. Compared to the active space used for **1**, **2**, and **4**, this active space excluded two double-occupied 3d cobalt orbitals that are not involved in the bonding picture for the complex.

With the exception of diiron(II,II) chloride **1**, DFT predicts high-spin ground spin states, thus only selected spin states were studied by CASSCF/PT2 calculations. The septet and nonet spin states of complex **1** were very close in energy at the DFT level and experimental data predicts a nonet ground state. Accordingly, only the three highest spin states were studied with a higher level of theory. For the mixed-valent species **2** and **4**, the lowest spin states, doublet and triplet, respectively, were ~ 10 kcal/mol higher in energy than the predicted high-spin ground state by DFT and were subsequently not studied by CASSCF/PT2. Lastly, all of the possible spin states were studied for iron-cobalt(II,II) chloride **3** due to the minimal energy difference between the doublet and octet by DFT. The relative energies for each complex at the CASPT2 level are summarized in **Table 4.6**. The CASPT2 results confirm that all of the complexes have a high-spin ground state, in agreement with the magnetic measurements for complexes **1**, **3**, and **4**.

Table 4.6 Relative energies in kcal/mol for several spin states of complexes **1 - 4** at the DFT and CASPT2 level of theory.

^{iPr}LFeFeCl **1**	**DFT**	**CASPT2**
triplet	4.15	-
quintet	5.30	27.32
septet	0	2.78
nonet	0.59	0

^{iPr}LFeFe **2**	**DFT**	**CASPT2**
doublet	9.50	-
quartet	2.71	12.34
sextet	1.65	5.02
octet	0	0

^{iPr}LFeCoCl **3**	**DFT**	**CASPT2**[a]
doublet	1.61	46.79
quartet	3.44	88.40
sextet	1.72	148.44
octet	0	0

^{iPr}LFeCo **4**	**DFT**	**CASPT2**[b]
triplet	10.03	-
quintet	1.69	14.27
septet	0	0

[a]Octet geometry from DFT utilized
[b]Septet geometry from DFT utilized

DFT orbitals tend to be over delocalized and as a result interpreting the Kohn-Sham orbitals can be challenging. The natural orbitals obtained from CASSCF calculations are more localized and allow for additional analysis of the electronic configuration of complexes **1-4**, particularly with respect to the degree of interaction between the two metal centers. Moreover, the contribution of the individual electronic configurations to the total CASSCF wavefuction is obtained. The natural orbitals comprising of linear combinations of the valence 3d-orbitals of FeFeCl **1** are shown in Figure 4.18. Inspection of the MO diagram for FeFeCl reveals only two delocalized MOs, σ and σ*. The remaining MOs are localized at one of the two iron centers. The nonet ground state wavefunction is dominated by one configuration (90%) that has a formal bond order (FBO) of 0.5. Despite the sigma interaction, there is only a weak interaction

between the two iron centers primarily due to the high-spin configuration causing the σ* MO to be partially occupied. This analysis corresponds with the covalent ratio for diiron(II,II) chloride **1** of r = 1.13, higher than what is expected for a single bond, r = 1.00.

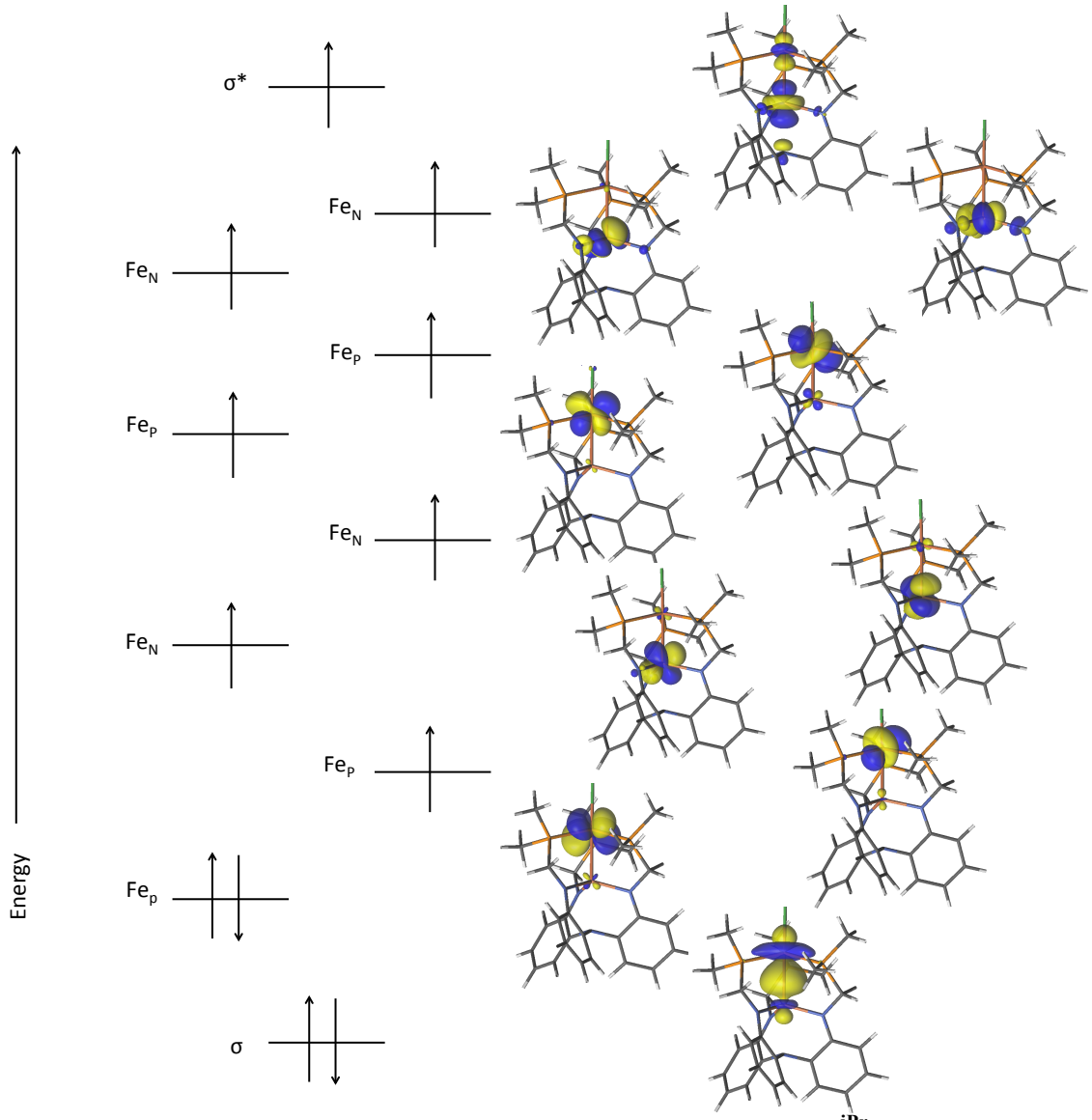

Figure 4.18 Qualitative MO diagram showing the natural orbitals for ^{iPr}**LFeFeCl 1**. The dominating electronic configuration (90%) from the CASSCF calculation is shown.

Analysis of divalent iron-cobalt(II,II) chloride **3** MOs reveals similar metal-metal interactions. The dominant electronic configuration (97%) of the octet ground state also has a FBO of 0.5 (Figure 4.19). Similar to diiron(II,II) chloride **1**, the d-electrons are localized at either the iron or cobalt metal centers, with the exception of the σ and σ* orbitals. It is noteworthy that the delocalization of the electron density in σ and σ* is less significant in the iron-cobalt(II,II) complex compared to the diiron(II,II) case. Again, the FBO and localized natural orbitals from CASSCF indicate only a weak interaction between the iron and cobalt metal centers. The covalent ratio for complex **3**, like complex **1**, is also significantly larger than the value expected for a single bond.

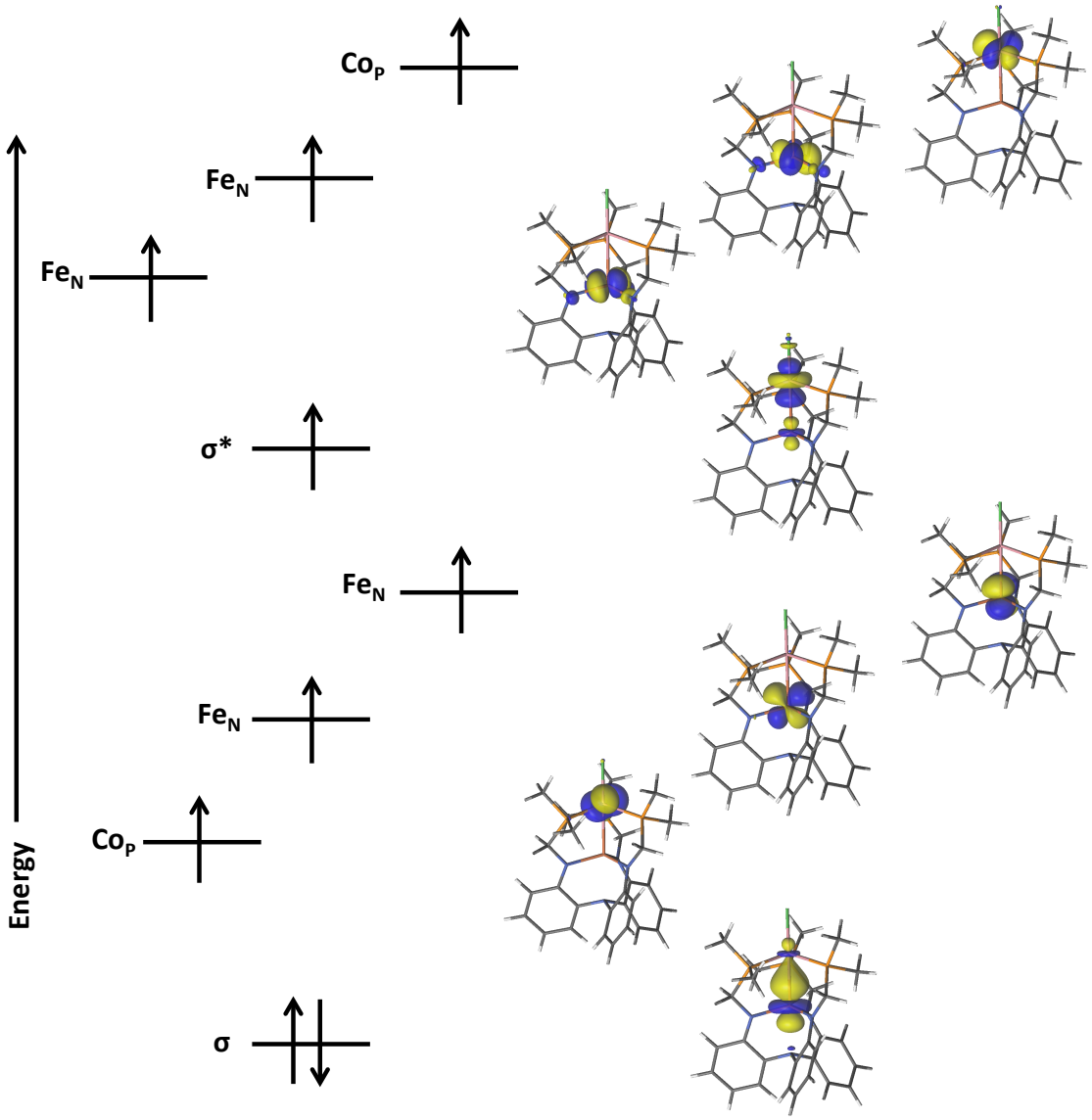

Figure 4.19 Qualitative MO diagram showing the natural orbitals for **3**. The dominating electronic configuration from CASSCF is shown (97%).

Furthermore, the CASSCF calculations reveal that complexes **1** and **3** have one main configuration that have large contributions to the ground state (90% and 97%, respectively). However, the total ground state wavefunction for each complex warrants discussion. The ground state electron configuration of diiron(II,II) chloride **1** is $(\sigma)^{1.91}(Fe_p)^{1.96}(Fe_P)^{0.99}(Fe_N)^{1.00}(Fe_N)^{1.00}(Fe_N)^{1.00}(Fe_N)^{1.00}(Fe_P)^{0.99}(Fe_P)^{0.99}(\sigma^*)^{1.03}$ where the

superscripts correspond to the natural orbital occupation numbers. From this picture, an effective bond order (EBO) can be computed. The EBO is equal to the sum of the natural orbital occupation numbers of the bonding orbitals minus the sum of the natural orbital occupation numbers for the anti bonding orbitals divided by two. The EBO for this system is 0.44. The effective bond order takes into account partial occupation of the σ* orbital. The total ground state wavefunction for iron-cobalt(II,II) chloride **3** also reveals a lower EBO of 0.48 with a ground state electron configuration of $(Co)^{2.00}(Co)^{2.00}(\sigma)^{1.97}(Fe)^{0.99}(Fe)^{0.99}(Co)^{1.00}(\sigma^*)^{1.00}(Fe)^{0.99}(Fe)^{0.99}(Co)^{1.00}$. The EBOs further support the presence of a weak interaction between the two metal centers in the divalent complexes **1** and **3**.

In the mixed-valent species **2** and **4**, the bond distance between the two metals is significantly shorter than their divalent parents **1** and **3** (by 0.301 Å and 0.33 Å, respectively) in the solid-state structures. Analysis of the MO diagram derived from CASSCF calculations can shed light on the origin of this bond shortening. For mixed-valent diiron(II,I) **2**, the natural orbitals arising from the dominant configuration (82%) for the octet ground state are shown in Figure 4.20. The FBO arising from the dominant configuration is 1.5, indicating the presence of a bond between the two metals. Excitingly, in addition to the σ and σ* orbitals, two π and two π* orbitals arise in the MOs. Similar to the divalent diiron(II,II) chloride, the remaining *d* electrons are localized on one of the two iron metal centers. Of note, the σ and σ* orbitals are completely delocalized between the two iron centers, whereas the π and π* orbitals are more localized on the top and bottom iron centers, respectively. The electronic configuration

for the ground state is $(\sigma)^{1.87}(\pi)^{1.93}(\pi)^{1.93}(Fe_P)^{0.99}(Fe_P)^{0.99}(\pi^*)^{1.01}(\pi^*)^{1.01}(\sigma^*)^{1.02}(Fe_N)^{1.00}$ $(Fe_N)^{1.00}$ with an EBO of 1.34. This EBO is slightly lower than the formal bond order obtained from the major electronic configuration again due to the partial occupation of the bonding orbitals being slightly less than two electrons and the anti-bonding orbitals having occupancies larger than one. The EBO combined with a covalent ratio of r = 1.00 predicts that there is only a single bond between to the two metal centers despite the fact that π interactions are observed.

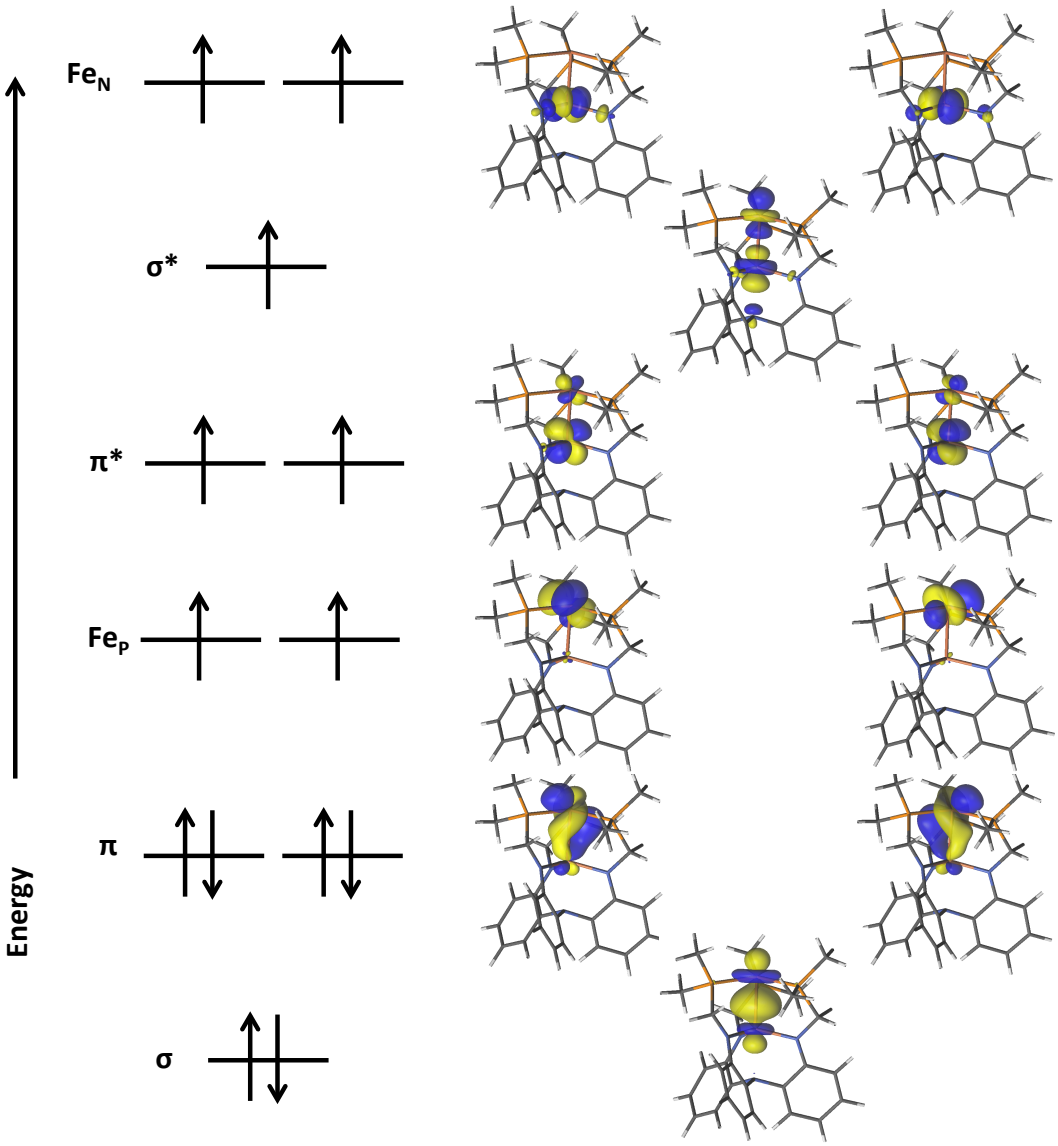

Figure 4.20 Qualitative MO diagram showing the natural orbitals for **2**. The dominating electronic configuration from CASSCF is shown (82%).

The CASSCF calculations performed on iron-cobalt(II,I) gave similar results to mixed-valent diiron(II,I). The natural orbitals from the major configuration (86%) are shown in Figure 4.21, and the FBO arising from the occupation of the σ, σ *, π, and π* MOs is 1.5. In the ground state of **4**, the electronic configuration is $(\sigma)^{1.90}(\pi)^{1.95}(\pi)^{1.95}(Co_P)^{1.96}(\pi^*)^{1.01}(\pi^*)^{1.01}(\sigma^*)^{1.01}(Fe_N)^{1.00}(Fe_N)^{1.00}(Co_P)^{0.99}$. Additionally,

the EBO of 1.38 is again lower than the FBO but by slightly less than was found in the mixed-valent diiron(II,I) species. This is consistent with the decrease in the covalent bond ratio to 0.97 compared to 1.00 in **2**. While the bonding interaction in **4** is still consistent with a single bond, the decreased covalent bond ratio and increased EBO indicate a slightly stronger covalent bonding interaction than in the case of diiron(II,I).

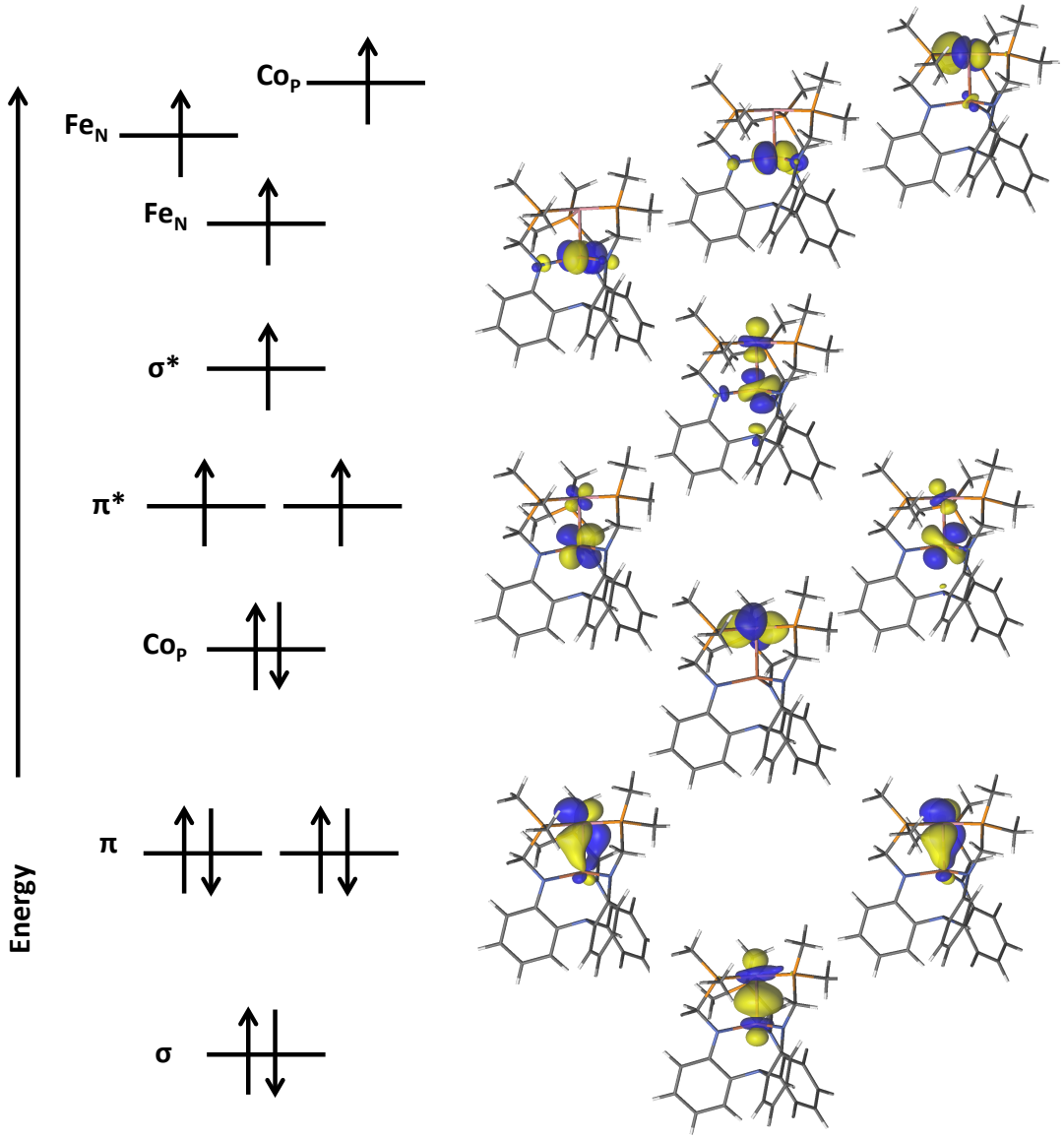

Figure 4.21 Qualitative MO diagram showing the natural orbitals for **2**. The dominating electronic configuration from CASSCF is shown (86%).

Lastly, CASSCF calculations can help to identify the oxidation states of the iron and cobalt metal centers in complexes **1-4**. The *d*-electron population of each of the metal centers can be calculated as a tool to quantify the amount of electron density on each metal center (Table 4.7). For complexes **2-4**, the *d*-electron counts were consistent with the formal oxidation states predicted yielding two mixed-valent (II,I) species, diiron **2** and iron-cobalt **4**, respectively, and one divalent heterobimetallic complex iron-cobalt(II,II) **3**. Interestingly, the calculated spin densities for **1** indicate some amount of delocalization between the two metal centers as more electron density is predicted to reside on the Fe in the phosphine plane.

Table 4.7 Calculated *d*-electron counts from the CASSCF total ground state electronic configurations.

	***d*-electron counts**	
	M_P	**Fe_N**
^{iPr}LFeFeCl **1**	6.72	5.31
^{iPr}LFeFe **2**	7.34	5.66
^{iPr}LFeCoCl **3**	6.97	6.03
^{iPr}LFeCo **4**	8.32	5.68

4.4 Conclusions

Herein a new family of late-late transition metal homo- and heterobimetallic complexes have been synthesized and characterized: diiron(II,II) chloride **1**, diiron(II,I) **2**, iron-cobalt(II,II) chloride **3**, and iron-cobalt(II,I). This provided a unique opportunity to compare the electronic and magnetic properties of homo and heterobimetallic complexes of iron and cobalt. All of the complexes exhibit similar magnetic properties with high-spin ground states that are best modeled by two strongly ferromagnetically coupled iron and cobalt metal centers. The Mössbauer spectroscopy showed interesting trends.

Overall, the Fe(II) metal centers have lower isomer shifts than generally observed in the literature for high-spin Fe(II) complexes in similar environments. However, in both the divalent and mixed-valent species, replacing Fe_P with Co results in a decreased isomer shift for Fe_N, an interesting result since an increase in d-electrons typically increases the isomer shift. Consistent with literature examples, the isomer shifts do increase upon reduction of complexes **1** and **3** to mixed-valent species **2** and **4**, respectively. Excitingly, theoretical studies indicate a σ-bond in mixed-valent complexes **2** and **4**. This is consistent with the short bond lengths observed in the solid-state structures (2.32 Å and 2.26 Å, respectively) and the covalent ratios of r = 1.00 and r = 0.97, respectively. Preliminary reactivity studies show promising results for the reaction of **2** and **4** with small molecules, such as CO, and organic azides.

4.5 Experimental Procedures

4.5.1 General Considerations

Unless otherwise stated, all operations were performed in a VAC Atmosphere double-dry box under an atmosphere of purified nitrogen or using high vacuum standard Schlenk techniques under a nitrogen atmosphere. Anhydrous *n*-Hexane, pentane, toluene, tetrahydrofuran, diethyl ether, acetonitrile and benzene were purchased from Aldrich and dried on an SG Waters solvent purification system. C_6D_6 and d^8-THF were purchased from Aldrich, distilled over calcium hydride, degassed and stored over 4 Å molecular sieves. Celite, alumina, and 4 Å molecular sieves were activated under vacuum for four days at 350ºC. All other chemical were used as received. ^{1}H spectra were recorded on Varian 300 MHz or a Bruker 500 MHz spectrometer at ambient temperature unless

otherwise stated. ^{1}H and ^{13}C NMR are reported with reference to solvent resonances (residual C_6H_6 in C_6D_6, 7.16 ppm and 128.1 ppm or residual THF in d^8-THF, 1.72 ppm and 67.57 ppm). 2, 2', 2''-tri(diisopropylphosphinomethylamino)triphenylamine, ^{iPr}**L**, was synthesized according to the literature preparation from previous work in this group.[30]

4.5.2 Synthetic Procedures

Synthesis of ^{i}PrLFeFeCl (1): ^{iPr}L (538.4 mg, 0.792 mmol) was dissolved in Et_2O and frozen at -196 °C using liquid N_2 in the cold well. A solution of ^{n}BuLi (982 μL, 2.45 mmol) in hexanes was added slowly to the frozen solution. Upon removal from the cold well and stirring for 30 minutes, the solution was pale yellow. The pale yellow solution and a THF solution of $FeCl_2(THF)_{1.5}$ (370.5 mg, 1.58 mmol) were frozen in the cold well. The thawing ligand solution was added on top of the frozen metal solution dropwise. After addition, the ligand solution is allowed to refreeze before warming at room temperature. The solution is stirred for 4 hours at room temperature, affording a deep blue solution. The solvent is removed in *vacuo* and the residue is reconstituted in toluene and filtered through a Celite plug to remove the LiCl. The toluene is removed in *vacuo* to yield 471.8 mg (72% crude yield) of deep blue crystalline powder. Bulk crystals were obtained by layering pentane onto a concentrated toluene solution. For **1**: ^{1}H NMR (23 ^{o}C, 500 MHz, C_6D_6): δ 118.9, 97.0, 86.1, 56.7, 34.7, 19.7, 10.3, 4.4, -66.8, and -86.8 ppm. A crystal suitable for single crystal X-ray crystallography was obtained by slow vapor diffuse of hexane into a concentrated solution of benzene. Elemental Analysis was

obtained using the same crystals: Anal. Calcd for CHN: C, 56.78; H, 7.33; N, 6.79. Found: C, 56.68; H, 7.26; N, 6.72.

Synthesis of ^{i}PrLFeFe (2): ^{i}PrLFeFeCl (212 mg, 0.257 mmol) was dissolved in THF and cooled to -78 ^{o}C and a solution of PhMgCl (2M) was added dropwise. The solution is allowed to warm to room temperature slowly and a color change to deep red is observed. The solution is stirred at room temperature for an additional 8 hours. After filtering, the solvent is removed in *vacuo*, the residue is reconstituted in benzene and filtered again to remove magnesium salts. The benzene is removed in *vacuo* to yield 126.8 mg (62% crude yield) of dark powder. Bulk crystals were obtained via vapor diffusion of pentane into a concentrated toluene solution (crystalline yield: 63%). For **2**: ^{1}H NMR (23 ^{o}C, 500 MHz, C_6D_6): δ 85.9, 52.2, 27.5, 14.3, -30.2, -59.9 ppm. A crystal suitable for single crystal X-ray crystallography was obtained from a concentrated benzene solution. Elemental Analysis was obtained using the same crystals: Anal. Calcd for CHN (^{iPr}LFeFe(THF)): C, 59.94; H, 7.95; N, 6.50. Found: C, 59.86; H, 7.89; N, 6.39.

Synthesis of ^{i}PrLFeCoCl (3): ^{i}PrLFeFeCl (444 mg, 0.54 mmol) was dissolved in THF and a THF solution of $CoCl_2(THF)_{1.5}$ (105.5 mg, 0.54 mmol) was added portionwise. The solution immediately changes to a deep purple and is stirred at room temperature for 3 hours. After filtering, the solvent is removed in *vacuo*, the residue is reconstituted in toluene and filtered again to remove the LiCl. The toluene is concentrated in vacuo and subsequently layered with pentane. Purple crystalline blocks were collected in 89% yield. For **3**: ^{1}H NMR (23 ^{o}C, 500 MHz, C_6D_6): δ 150.7, 88.3, 48.3, 32.8, 15.3, 11.9, -70.7, -86.3 ppm. A crystal suitable for single crystal X-ray crystallography was obtained by

layering pentane onto a concentrated solution of toluene. Elemental Analysis was obtained using the same crystals: Anal. Calcd for CHN: C, 56.57; H, 7.30; N, 6.77. Found: C, 56.48; H, 7.38; N, 6.63.

Synthesis of ^{i}PrLFeCo (4): ^{i}PrLFeCoCl (110 mg, 0.13 mmol) was dissolved in THF and a solution of MeMgCl (3M) was added dropwise. The solution immediately changes to a dark brown orange and is stirred at room temperature for 2 hours. After filtering, the solvent is removed in *vacuo* and the residue is reconstituted in benzene and filtered again to remove magnesium salts. The benzene is removed in *vacuo* to yield 98 mg (93% crude yield) of dark powder. Bulk purification was achieved via vapor diffusion of Et_2O into a concentrated THF solution (crystalline yield: 62%). For **4**: ^{1}H NMR (23 ^{o}C, 500 MHz, C_6D_6): δ 135.8, 53.3, 26.8, 22.4, 17.0, -4.0, -34.0, -57.7 ppm. A crystal suitable for single crystal X-ray crystallography was obtained by vapor diffusion of Et_2O into a concentrated solution of THF. Elemental Analysis was obtained using the same crystals: Anal. Calcd for CHN: C, 59.10; H, 7.63; N, 7.07. Found: C, 59.19; H, 7.68; N, 6.98.

4.5.3 X-Ray Crystallographic Data Collection and Refinement of the Structures

Single crystals were grown by layering pentane onto a concentrated toluene solution for **1**, **1-Br**, and **3**, from a concentrated solution of benzene for **2** and from vapor diffusion of Et_2O into concentrated solution of THF for **2-LiCl** and **4**. Dark blue blocks of **1** (0.30 x 0.25 x 0.20 mm^3), Deep blue blocks of **1-Br** (0.40 x 0.30 x 0.20 mm^3), orange-brown plate of **2** (0.15 x 0.05 x 0.05 mm^3), red needles of **2-LiCl** (0.30 x 0.20 x 0.05 mm^3), deep purple blocks of **3** (0.30 x 0.25 x 0.20 mm^3), and yellow-brown blocks of **4** (0.25 x 0.20 x 0.20 mm^3) were placed on the tip of a glass capillary and mounted on

a Bruker APEX Platform CCD diffractometer for data collection at 173(2) K.[57] The data collection was carried out using Mo-Kα radiation (graphite monochromator). The data intensity was corrected for absorption and decay (SADABS).[58] Final cell constants were obtained from least squares fits of all measured reflections after integration (SAINT).[59] The structure was solved using SHELXS-97 and refined using SHELXL-97.[60] A direct-methods solution was calculated which provided most non-hydrogen atoms from the E-map. Full-matrix least squares / difference Fourier cycles were performed to locate the remaining non-hydrogen atoms. All non-hydrogen atoms were refined with anisotropic displacement parameters. Hydrogen atoms were placed in ideally and refined as riding atoms with relative isotropic displacement parameters. For complexes **1**, **1-Br**, the PLATON program, SQUEEZE function, was used to remove disordered solvent in the asymmetric unit.[61] For **1**, a total of 160 electrons were removed in a total volume of 794 $Å^3$ per unit cell, equally distributed between two positions at (0, 0, 0), and (0.0, 0.5, 0.5) in the asymmetric unit. The number of electrons is consistent with removal two disordered pentane molecules at each position. For **1-Br**, a total of 198 electrons were removed in a total volume of 844 $Å^3$ per unit cell, equally distributed between two positions at (0, 0, 0), and (0.0, 0.5, 0.5) in the asymmetric unit. The number of electrons is consistent with removal two disordered pentane molecules at each position. For **2**, a total of 388 electrons were removed in a total volume of 815 $Å^3$ per unit cell at the position (0, 0, 0) in the asymmetric unit. The number of electrons is consistent with removal of 8 disordered benzene molecules. For **3**, a total of 194 electrons were removed in a total volume of 764 $Å^3$ per unit cell, equally distributed between two positions at (0,

0, 0), and (0.0, 0.5, 0.5) in the asymmetric unit. The number of electrons is consistent with removal two disordered pentane molecules at each position. For **4**, a total of 72 electrons were removed in a total volume of 310 $Å^3$ per unit cell, equally distributed between two positions at (0.4, 0.6, 0.2), and (0.6, 0.0, 0.8) in the asymmetric unit. The number of electrons is consistent with removal two disordered THF molecules at each position. Crystallographic data are summarized in Table 4.1.

4.5.4 Physical Measurements

Elemental analyses were performed by Complete Analysis Laboratories, Inc. (Parsippany, NJ). Visible and near-infrared absorption data were collected on a Cary-14 spectrophotometer. UV-wavelength absorption spectra were collected on a Cary 300 Bio UV-Visible spectrophotometer. Cyclic voltammetry was conducted using a CH Instruments 600 electrochemical analyzer. The one-cell setup utilized a glassy carbon working electrode, platinum wire counter electrode, and $Ag/AgNO_3$ reference electrode in acetonitrile. Analyte solutions were prepared in a THF solution of tetra-n-butylammonium hexafluorophosphate (0.4 M) and referenced internally to the Fc/Fc^+ redox couple. Magnetic susceptibility data were measured from powder samples of solid material in the temperature range 2 to 300 K by using a SQUID susceptometer (MPMS-7, Quantum Design, calibrated with standard palladium reference sample, error <2%). The experimental data were corrected for underlying diamagnetism by use of tabulated Pascal's constants.[62,63] The susceptibility and magnetization data were simulated with the program julX.[64] ^{57}Fe Mössbauer data were recorded on an alternating constant acceleration spectrometer. The minimum experimental line width was 0.24 mm s^{-1} (full

width at half-height). The ^{57}Co/Rh source (1.8 GBq) was positioned at rt inside the gap of the magnet system at a zero-field position. Isomer shifts are quoted relative to iron metal at 300 K.

4.5.5 Computational Details

Complexes **1-4** were interrogated using density functional theory (DFT) and the complete active space self-consistent field (CASSCF) method[55] followed by a multiconfigurational second-order perturbation theory (CASPT2) method.[56] These methods have proven successful in predicting accurate results for ground and electronically excited states in several other systems studied in our group.[21,29,30] No symmetry constraints were used.

DFT Calculations. Initial starting points for geometry optimizations were derived from the experimentally determined X-ray structures of **1-4**. Gas phase geometry optimizations were performed for the corresponding possible spin states with the Perdew−Burke−Ernzerhof (PBE) exchange-correlation functional and the Turbomole 6.1 program package.[50,54] For C and H atoms, the double-ζ quality basis sets def-SV(P) was used, whereas the triple-ζ quality basis set def-TZVP was employed for N, O, and P.[53] Additional polarized functions were introduced by using def-TZVPP for Fe and Cr. The DFT calculations were performed with the broken symmetry option (unrestricted calculations) and the resolution-of-the-identity (RI) approximation.[54] Vibrational frequencies for the DFT-optimized structures were also computed at the same level of theory. Negative frequencies were not observed for any of the complexes.

CASSCF/CASPT2 Calculations. All CASSCF/CASPT2 calculations were performed

with the MOLCAS-7.4 package[65] using the DFT- optimized structures with no imposed symmetry for all possible spin states. The relativistic all-electron ANO-RCC basis sets[66,67] were used for all elements. In all of these calculations, the ANO-RCC-VTZP basis set was used for the Fe and Co, ANO-RCC-VDZP basis set was used for N and the ANO-RCC-MB basis set was used for C and H. Scalar relativistic effects were included by using the Douglas−Kroll−Hess Hamiltonian.[68] The two-electron integral evaluation was simplified by employing the Cholesky decomposition technique.[69-71] The natural orbital occupation numbers were used for the evaluation of the effective bond order (EBO), which is calculated as the difference between the total occupancies of the bonding and antibonding molecular orbitals of the M−M bond divided by two.[72,73]

CAS Choice. A complete active space was used consisting of 12 electrons in 15 orbitals (12, 15) for the ^{iPr}LFeFeCl **1**, a similar active space of 13 electrons in 15 orbitals (13, 15) was used for the ^{iPr}LFeFe **2**, and a similar active space of 14 electrons in 15 orbitals (14, 15) was used for the ^{iPr}LFeCo **4**. For ^{iPr}LFeCoCl **3**, an active space of 9 electrons in 13 orbitals was utilized due to two low lying cobalt orbitals that could not be optimized into the active space. The choice of active space was intended to comprise all the valence 3d-electrons and all the 3d orbitals from the two metals. The 15 orbitals used in the active space consist of the ten 3d-orbitals from the two metals as well as five iron 4d-orbitals that are empty and correlating.

Bibliography

Chapter 1 References

(1) World Population Prospects: The 2008 Revision http://www.un.org/esa/population/publications/popnews/Newsltr_87.pdf (accessed May 11, 2013).

(2) Inventory of U.S. Greenhouse Gas Emissions and Sinks: http://www.epa.gov/climatechange/Downloads/ghgemissions/US-GHG-Inventory-2013-Main-Text.pdf (accessed May 11, 2013).

(3) Olah, G. A. Beyond Oil and Gas: The Methanol Economy. *Angew. Chem. Int. Ed.* **2005**, *44*, 2636–2639.

(4) Carbon Dioxide at NOAA's Mauna Loa Observatory reaches new milestone: Tops 400 ppm http://researchmatters.noaa.gov/news/Pages/CarbonDioxideatMaunaLoareaches400ppm.aspx (accessed May 11, 2013).

(5) Arakawa, H.; Aresta, M.; Armor, J. N.; Barteau, M. A.; Beckman, E. J.; Bell, A. T.; Bercaw, J. E.; Creutz, C.; Dinjus, E.; Dixon, D. A.; Domen, K.; DuBois, D. L.; Eckert, J.; Fujita, E.; Gibson, D. H.; Goddard, W. A.; Goodman, D. W.; Keller, J.; Kubas, G. J.; Kung, H. H.; Lyons, J. E.; Manzer, L. E.; Marks, T. J.; Morokuma, K.; Nicholas, K. M.; Periana, R.; Que, L.; Rostrup-Nielson, J.; Sachtler, W. M. H.; Schmidt, L. D.; Sen, A.; Somorjai, G. A.; Stair, P. C.; Stults, B. R.; Tumas, W. Catalysis Research of Relevance to Carbon Management: Progress, Challenges, and Opportunities. *Chem. Rev.* **2001**, *101*, 953–996.

(6) Collman, J. P.; Wagenknecht, P. S.; Hutchison, J. E. Molecular Catalysts for Multi-electron Redox Reactions of Small Molecules: The "Cofacial Metallodiporphyrin" Approach. *Angew. Chem. Int. Ed.* **1994**, *33*, 1537–1554.

(7) Dempsey, J. L.; Esswein, A. J.; Manke, D. R.; Rosenthal, J.; Soper, J. D.; Nocera, D. G. Molecular Chemistry of Consequence to Renewable Energy. *Inorg. Chem.* **2005**, *44*, 6879–6892.

(8) Benson, E. E.; Kubiak, C. P.; Sathrum, A. J.; Smieja, J. M. Electrocatalytic and Homogeneous Approaches to Conversion of CO_2 to Liquid Fuels. *Chem. Soc. Rev.* **2009**, *38*, 89–99.

(9) Tolman, W. B., Ed. *Activation of Small Molecules*. Wiley-VCH: Weinheim, 2006.

(10) Shilov, A. E. Catalytic Reduction of Molecular Nitrogen in Solutions. *Russ. Chem. Bull.* **2003**, *52*, 2555–2562.

(11) Schrock, R. R. Reduction of Dinitrogen. *Proc. Natl. Acad. Sci.* **2006**, *103*, 1708.

(12) Yandulov, D. V.; Schrock, R. R. Reduction of Dinitrogen to Ammonia at a Well-Protected Reaction Site in a Molybdenum Triamidoamine Complex. *J. Am. Chem. Soc.* **2002**, *124*, 6252–6253.

(13) Yandulov, D. V.; Schrock, R. R. Catalytic Reduction of Dinitrogen to Ammonia at a Single Molybdenum Center. *Science* **2003**, *301*, 76–78.

(14) Greco, G. E.; Schrock, R. R. Synthesis of Triamidoamine Ligands of the Type $(ArylNHCH_2CH_2)_3N$ and Molybdenum and Tungsten Complexes That Contain an $[(ArylNCH_2CH_2)_3N]^{3-}$ Ligand. *Inorg. Chem.* **2001**, *40*, 3850–3860.

(15) Greco, G. E.; Schrock, R. R. Synthesis, Structure, and Electrochemical Studies of Molybdenum and Tungsten Dinitrogen, Diazenido, and Hydrazido Complexes that Contain Aryl-Substituted Triamidoamine Ligands. *Inorg. Chem.* **2001**, *40*, 3861–3878.

(16) Chatt, J.; Dilworth, J. R.; Richards, R. L. Recent Advances in the Chemistry of Nitrogen Fixation. *Chem. Rev.* **1978**, *78*, 589–625.

(17) Einsle, O.; Tezcan, F. A.; Andrade, S. L. A.; Schmid, B.; Yoshida, M.; Howard, J. B.; Rees, D. C. Nitrogenase MoFe-Protein at 1.16 Å resolution: A Central Ligand in the FeMo-Cofactor. *Science* **2002**, *297*, 1696–1700.

(18) Lam, O. P.; Anthon, C.; Meyer, K. Influence of Steric Pressure on the Activation of Carbon Dioxide and Related Small Molecules by Uranium Coordination Complexes. *Dalton Transactions* **2009**, *44*, 9677.

(19) Castro-Rodriguez, I.; Meyer, K. Small Molecule Activation at Uranium Coordination Complexes: Control of Reactivity via Molecular Architecture. *Chem. Commun.* **2006**, 1353–1368.

(20) Evans, W. J.; Seibel, C. A.; Ziller, J. W. Organosamarium-Mediated Transformations of CO_2 and COS: Monoinsertion and Disproportionation Reactions and the Reductive Coupling of CO_2 to $[O_2CCO_2]^{2-}$. *Inorg. Chem.* **1998**, *37*, 770–776.

(21) Castro-Rodriguez, I.; Nakai, H.; Zakharov, L. N.; Rheingold, A. L.; Meyer, K. A Linear, O-Coordinated η^1-CO_2 Bound to Uranium. *Science* **2004**, *305*, 1757–1759.

(22) Helm, M. L.; Stewart, M. P.; Bullock, R. M.; DuBois, M. R.; DuBois, D. L. A Synthetic Nickel Electrocatalyst with a Turnover Frequency Above 100,000 s^{-1}

for H_2 Production. *Science* **2011**, *333*, 863–866.

(23) Frey, M. Hydrogenases: Hydrogen-Activating Enzymes. *ChemBioChem* **2002**, *3*, 153–160.

(24) Fontecilla-Camps, J. C.; Volbeda, A.; Cavazza, C.; Nicolet, Y. Structure/Function Relationships of [NiFe]- and [FeFe]-Hydrogenases. *Chem. Rev.* **2007**, *107*, 4273–4303.

(25) Kilgore, U. J.; Roberts, J. A. S.; Pool, D. H.; Appel, A. M.; Stewart, M. P.; DuBois, M. R.; Dougherty, W. G.; Kassel, W. S.; Bullock, R. M.; DuBois, D. L. $[Ni(P^{Ph}_2N^{C6H4X}_2)_2]^{2+}$ Complexes as Electrocatalysts for H_2 Production: Effect of Substituents, Acids, and Water on Catalytic Rates. *J. Am. Chem. Soc.* **2011**, *133*, 5861–5872.

(26) Raugei, S.; Chen, S.; Ho, M.-H.; Ginovska-Pangovska, B.; Rousseau, R. J.; Dupuis, M.; DuBois, D. L.; Bullock, R. M. The Role of Pendant Amines in the Breaking and Forming of Molecular Hydrogen Catalyzed by Nickel Complexes. *Chem. Eur. J.* **2012**, *18*, 6493–6506.

(27) Smith, S. E.; Yang, J. Y.; DuBois, D. L.; Bullock, R. M. Reversible Electrocatalytic Production and Oxidation of Hydrogen at Low Overpotentials by a Functional Hydrogenase Mimic. *Angew. Chem. Int. Ed.* **2012**, *51*, 3152–3155.

(28) O'Hagan, M.; Ho, M.-H.; Yang, J. Y.; Appel, A. M.; DuBois, M. R.; Raugei, S.; Shaw, W. J.; DuBois, D. L.; Bullock, R. M. Proton Delivery and Removal in $[Ni(P^{R}_2N^{R'}_2)_2]^{2+}$ Hydrogen Production and Oxidation Catalysts. *J. Am. Chem. Soc.* **2012**, *134*, 19409–19424.

(29) Dupuis, M.; Chen, S.; Raugei, S.; DuBois, D. L.; Bullock, R. M. Comment on "New Insights in the Electrocatalytic Proton Reduction and Hydrogen Oxidation by Bioinspired Catalysts: A DFT Investigation." *J. Phys. Chem. A* **2011**, *115*, 4861–4865.

(30) Lucas, R. L.; Zart, M. K.; Murkerjee, J.; Sorrell, T. N.; Powell, D. R.; Borovik, A. S. A Modular Approach toward Regulating the Secondary Coordination Sphere of Metal Ions: Differential Dioxygen Activation Assisted by Intramolecular Hydrogen Bonds. *J. Am. Chem. Soc.* **2006**, *128*, 15476–15489.

(31) Shook, R. L.; Peterson, S. M.; Greaves, J.; Moore, C.; Rheingold, A. L.; Borovik, A. S. Catalytic Reduction of Dioxygen to Water with a Monomeric Manganese Complex at Room Temperature. *J. Am. Chem. Soc.* **2011**, *133*, 5810–5817.

(32) Gupta, R.; MacBeth, C. E.; Young, V. G.; Borovik, A. S. Isolation of Monomeric

MnIII/II−OH and MnIII−O Complexes from Water: Evaluation of O−H Bond Dissociation Energies. *J. Am. Chem. Soc.* **2002**, *124*, 1136–1137.

(33) Mayer, S. M.; Lawson, D. M.; Gormal, C. A.; Roe, S. M.; Smith, B. E. New Insights into Structure-Function Relationships in Nitrogenase: a 1.6 Å Resolution X-ray Crystallographic Study of *Klebsiella pneumoniae* MoFe-Protein. *J. Mol. Biol.* **1999**, *292*, 871–891.

(34) Peters, J. W.; Stowell, M. H. B.; Soltis, S. M.; Finnegan, M. G.; Johnson, M. K.; Rees, D. C. Redox-Dependent Structural Changes in the Nitrogenase P-Cluster. *Biochemistry* **1997**, *36*, 1181–1187.

(35) Iwata, S.; Barber, J. Structure of Photosystem II and Molecular Architecture of the Oxygen-Evolving Centre. *Curr. Opin. Struct. Biol.* **2004**, *14*, 447–453.

(36) Ferreira, K. N.; Iverson, T. M.; Maghlaoui, K.; Barber, J.; Iwata, S. Architecture of the Photosynthetic Oxygen-Evolving Center. *Science* **2004**, *303*, 1831–1838.

(37) Eames, E. V.; Betley, T. A. Site-Isolated Redox Reactivity in a Trinuclear Iron Complex. *Inorg. Chem.* **2012**, *51*, 10274–10278.

(38) Zhao, Q.; Betley, T. A. Synthesis and Redox Properties of Triiron Complexes Featuring Strong Fe-Fe Interactions. *Angew. Chem. Int. Ed.* **2011**, *50*, 709–712.

(39) Eames, E. V.; Harris, T. D.; Betley, T. A. Modulation of magnetic behavior via ligand-field effects in the trigonal clusters (^{Ph}L)Fe$_3$L*$_3$ (L* = thf, py, PMe$_2$Ph). *Chem. Sci.* **2012**, *3*, 407.

(40) Eames, E. V.; Sanchez, R. H.; Betley, T. A. Metal Atom Lability in Polynuclear Complexes. *Inorg. Chem.* **2013**, *52*, 5006-5012.

(41) Fout, A. R.; Zhao, Q.; Xiao, D. J.; Betley, T. A. Oxidative Atom-Transfer to a Trimanganese Complex To Form Mn$_6$(μ^6-E) (E = O, N) Clusters Featuring Interstitial Oxide and Nitride Functionalities. *J. Am. Chem. Soc.* **2011**, *133*, 16750–16753.

(42) Fout, A. R.; Xiao, D. J.; Zhao, Q.; Harris, T. D.; King, E. R.; Eames, E. V.; Zheng, S.-L.; Betley, T. A. Trigonal Mn$_3$ and Co$_3$ Clusters Supported by Weak-Field Ligands: A Structural, Spectroscopic, Magnetic, and Computational Investigation into the Correlation of Molecular and Electronic Structure. *Inorg. Chem.* **2012**, *51*, 10290–10299.

(43) Harris, T. D.; Betley, T. A. Multi-Site Reactivity: Reduction of Six Equivalents of Nitrite To Give an Fe$_6$(NO)$_6$ Cluster with a Dramatically Expanded

Octahedral Core. *J. Am. Chem. Soc.* **2011**, *133*, 13852–13855.

(44) Zhao, Q.; Harris, T. D.; Betley, T. A. $[(^{H}L)_2Fe_6(NCMe)_m]^{n+}$ (m= 0, 2, 4, 6; n= −1, 0, 1, 2, 3, 4, 6): An Electron-Transfer Series Featuring Octahedral Fe_6 Clusters Supported by a Hexaamide Ligand Platform. *J. Am. Chem. Soc.* **2011**, *133*, 8293–8306.

(45) Krogman, J. P.; Foxman, B. M.; Thomas, C. M. Activation of CO_2 by a Heterobimetallic Zr/Co Complex. *J. Am. Chem. Soc.* **2011**, *133*, 14582–14585.

(46) Nippe, M.; Goodman, S. M.; Fry, C. G.; Berry, J. F. Chemically Reversible Four-Electron Oxidation and Reduction Utilizing Two Inorganic Functional Groups. *J. Am. Chem. Soc.* **2011**, *133*, 2856–2859.

Chapter 2 References

(1) Breslow, R. Biomimetic Chemistry and Artificial Enzymes: Catalysis by Design. *Acc. Chem. Res.* **1995**, *28*, 146–153.

(2) Howard, J. B.; Rees, D. C. Structural Basis of Biological Nitrogen Fixation. *Chem. Rev.* **1996**, *96*, 2965–2982.

(3) Burgess, B. K.; Lowe, D. J. Mechanism of Molybdenum Nitrogenase. *Chem. Rev.* **1996**, *96*, 2983–3012.

(4) Santos, Dos, P. C.; Igarashi, R. Y.; Lee, H.; Hoffman, B. M.; Seefeldt, L. C.; Dean, D. R. Substrate Interactions with the Nitrogenase Active Site. *Acc. Chem. Res.* **2005**, *38*, 208–214.

(5) Hoffman, B. M.; Dean, D. R.; Seefeldt, L. C. Climbing Nitrogenase: Toward a Mechanism of Enzymatic Nitrogen Fixation. *Acc. Chem. Res.* **2009**, *42*, 609–619.

(6) Yandulov, D. V.; Schrock, R. R. Catalytic Reduction of Dinitrogen to Ammonia at a Single Molybdenum Center. *Science* **2003**, *301*, 76–78.

(7) Greco, G. E.; Schrock, R. R. Synthesis, Structure, and Electrochemical Studies of Molybdenum and Tungsten Dinitrogen, Diazenido, and Hydrazido Complexes that Contain Aryl-Substituted Triamidoamine Ligands. *Inorg. Chem.* **2001**, *40*, 3861–3878.

(8) Schrock, R. R. Transition Metal Complexes That Contain a Triamidoamine Ligand. *Acc. Chem. Res.* **1997**, *30*, 9–16.

(9) Cummins, C. C.; Lee, J.; Schrock, R. R.; Davis, W. D. Trigonal-Monopyramidal M^{III} Complexes of the Type [$M(N_3N)$] (M= Ti, V, Cr, Mn, Fe; N_3N=[(*t*$BuMe_2Si)CH_2CH_2]_3N$). *Angew. Chem. Int. Ed.* **1992**, *31*, 1501–1503.

(10) Pedersen, C. J. Cyclic Polyethers and Their Complexes with Metal Salts. *J. Am. Chem. Soc.* **1967**, *89*, 7017–7036.

(11) Dietrich, B.; Lehn, J. M.; Sauvage, J. P. Diaza-polyoxa-macrocycles et Macrobicycles. *Tetrahedron Lett.* **1969**, *10*, 2885–2888.

(12) Dietrich, B.; Lehn, J. M.; Sauvage, J. P.; Blanzat, J. Cryptates—X. *Tetrahedron* **1973**, *29*, 1629–1645.

(13) MacDowell, D.; Nelson, J. Facile Synthesis of a New Family of Cage Molecules.

Tetrahedron Lett. **1988**, *29*, 385–386.

(14) Krakowiak, K. E.; Bordunov, A. V.; Bradshaw, J. S. Synthesis of Hexaazacryptands Containing Furan and Benzene Groups in the Bridging Arms. *J. Heterocycl. Chem.* **1998**, *35*, 169–171.

(15) Sato, T.; Suzuki, A.; Sakai, K.; Tsubomura, T. Syntheses and Structures of a Novel Trinaphthylene Hexaimino Cryptand: Three Different Conformations of a Macrobicyclic Ligand. *Bull. Chem. Soc. Jpn.* **1996**, *69*, 379–388.

(16) Harding, C. J.; Lu, Q.; Malone, J. F.; Marrs, D. J.; Martin, N.; McKee, V.; Nelson, J. Hydrolytically-Sensitive Hexaimino and Hydrolytically-Inert Octaamino-Cryptand Hosts for Dicopper. *J. Chem. Soc., Dalton Trans.* **1995**, 1739.

(17) Alliger, G. E.; Müller, P.; Cummins, C. C.; Nocera, D. G. Cofacial Dicobalt Complex of a Binucleating Hexacarboxamide Cryptand Ligand. *Inorg. Chem.* **2010**, *49*, 3697–3699.

(18) Alliger, G. E.; Müller, P.; Do, L. H.; Cummins, C. C.; Nocera, D. G. Family of Cofacial Bimetallic Complexes of a Hexaanionic Carboxamide Cryptand. *Inorg. Chem.* **2011**, *50*, 4107–4115.

(19) Kang, S. O.; Llinares, J. M.; Powell, D.; VanderVelde, D.; Bowman-James, K. New Polyamide Cryptand for Anion Binding. *J. Am. Chem. Soc.* **2003**, *125*, 10152–10153.

(20) Jabin, I.; Reinaud, O. First C_{3v}-Symmetrical Calix[6](aza)crown. *J. Org. Chem.* **2003**, *68*, 3416–3419.

(21) Darbost, U.; Zeng, X.; Rager, M.-N.; Giorgi, M.; Jabin, I.; Reinaud, O. X-ray and Solution Structures of the First Zn Funnel Complex Based on a Calix[6]aza-cryptand. *Eur. J. Inorg. Chem.* **2004**, *2004*, 4371–4374.

(22) Blanchard, S.; Le Clainche, L.; Rager, M.-N.; Chansou, B.; Tuchagues, J.-P.; Duprat, A. F.; Le Mest, Y.; Reinaud, O. Calixarene-Based Copper(I) Complexes as Models for Monocopper Sites in Enzymes. *Angew. Chem. Int. Ed.* **1998**, *37*, 2732–2735.

(23) Darbost, U.; Rager, M.-N.; Petit, S.; Jabin, I.; Reinaud, O. Polarizing a Hydrophobic Cavity for the Efficient Binding of Organic Guests: The Case of Calix[6]tren, a Highly Efficient and Versatile Receptor for Neutral or Cationic Species. *J. Am. Chem. Soc.* **2005**, *127*, 8517–8525.

(24) Makita, Y.; Sugimoto, K.; Furuyoshi, K.; Ikeda, K.; Fujiwara, S.-I.; Shin-ike, T.; Ogawa, A. A Zinc(II)-Included Hemicryptophane: Facile Synthesis, Characterization, and Catalytic Activity. *Inorg. Chem.* **2010**, *49*, 7220–7222.

(25) Brotin, T.; Dutasta, J.-P. Cryptophanes and Their Complexes--Present and Future. *Chem. Rev.* **2009**, *109*, 88–130.

(26) Raytchev, P. D.; Perraud, O.; Aronica, C.; Martinez, A.; Dutasta, J.-P. A New Class of C_3-symmetrical Hemicryptophane Hosts: Triamide- and Tren-Hemicryptophanes. *J. Org. Chem.* **2010**, *75*, 2099–2102.

(27) Martinez, A.; Dutasta, J.-P. Hemicryptophane–oxidovanadium(V) Complexes: Lead of a New Class of Efficient Supramolecular Catalysts. *J. Catal.* **2009**, *267*, 188–192.

(28) Perraud, O.; Tommasino, J.-B.; Robert, V.; Albela, B.; Khrouz, L.; Bonneviot, L.; Dutasta, J.-P.; Martinez, A. Hemicryptophane-Assisted Electron Transfer: A Structural and Electronic Study. *Dalton Trans.* **2013**, *42*, 1530–1535.

(29) Chatelet, B.; Payet, E.; Perraud, O.; Dimitrov-Raytchev, P.; Chapellet, L.-L.; Dufaud, V.; Martinez, A.; Dutasta, J.-P. Shorter and Modular Synthesis of Hemicryptophane-tren Derivatives. *Org. Lett.* **2011**, *13*, 3706–3709.

(30) Taratula, O.; Hill, P. A.; Bai, Y.; Khan, N. S.; Dmochowski, I. J. Shorter Synthesis of Trifunctionalized Cryptophane-A Derivatives. *Org. Lett.* **2011**, *13*, 1414–1417.

(31) Perdew, J. Density-Functional Approximation for the Correlation Energy of the Inhomogeneous Electron Gas. *Phys. Rev. B* **1986**, *33*, 8822–8824.

(32) Becke, A. D. Density-Functional Exchange-Energy Approximation with Correct Asymptotic Behavior. *Phys. Rev. A* **1988**, *1988*, 3098–3101.

(33) Gosse, I.; Dutasta, J.-P.; Perrin, M.; Thozet, A. A Thiophosphorylated Hemicryptophane: Structure of the Toluene Inclusion Complex. *New J. Chem.* **1999**, *23*, 545–548.

(34) Ahlrichs, R.; Bär, M.; Häser, M.; Horn, H.; Kölmel, C. Electronic Structure Calculations on Workstation Computers: The Program System Turbomole. *Chem. Phys. Lett.* **1989**, *162*, 165–169.

(35) Bakowies, D.; Bühl, M.; Thiel, W. A Density Functional Study on the Shape of C_{180} and C_{240} Fullerenes. *Chem. Phys. Lett.* **1995**, *247*, 491–493.

(36) Johnson, B. P.; Dielmann, F.; Balázs, G.; Sierka, M.; Scheer, M. Spherical

Cluster Comprising a Four- and Six-Membered-Ring Motif. *Angew. Chem. Int. Ed.* **2006**, *45*, 2473–2475.

(37) Mebs, S.; Henn, J.; Dittrich, B.; Paulmann, C.; Luger, P. Electron Densities of Three B_{12}Vitamins. *J. Phys. Chem. A* **2009**, *113*, 8366–8378.

(38) Eichkorn, K.; Treutler, O.; Öhm, H.; Häser, M.; Ahlrichs, R. Auxiliary Basis Sets to Approximate Coulomb Potentials. *Chem. Phys. Lett.* **1995**, *242*, 652–660.

(39) Bao, M.; Nakamura, H.; Yamamoto, Y. Facile Allylative Dearomatization Catalyzed by Palladium. *J. Am. Chem. Soc.* **2001**, *123*, 759–760.

(40) Ray, M.; Hammes, B. S.; Yap, G. P. A.; Rheingold, A. L.; Borovik, A. S. Structure and Physical Properties of Trigonal Monopyramidal Iron(II), Cobalt(II), Nickel(II), and Zinc(II) Complexes. *Inorg. Chem.* **1998**, *37*, 1527–1532.

(41) Spek, A. L. Single-Crystal Structure Validation with the Program PLATON. *J. Appl. Crystallogr.* **2003**, *36*, 7–13.

(42) McGee, K. A.; Veltkamp, D. J.; Marquardt, B. J.; Mann, K. R. Porous Crystalline Ruthenium Complexes Are Oxygen Sensors. *J. Am. Chem. Soc.* **2007**, *129*, 15092–15093.

(43) Ringer, A. L.; Figgs, M. S.; Sinnokrot, M. O.; Sherrill, C. D. Aliphatic C−H/π Interactions: Methane−Benzene, Methane−Phenol, and Methane−Indole Complexes. *J. Phys. Chem. A* **2006**, *110*, 10822–10828.

(44) Dey, R. C.; Seal, P.; Chakrabarti, S. CH/π Interaction in Benzene and Substituted Derivatives with Halomethane: A Combined Density Functional and Dispersion-Corrected Density Functional Study. *J. Phys. Chem. A* **2009**, *113*, 10113–10118.

(45) Aoki, S.; Suzuki, S.; Kitamura, M.; Haino, T.; Shiro, M.; Zulkefeli, M.; Kimura, E. Molecular Recognition of Hydrocarbon Guests by a Supramolecular Capsule Formed by the 4:4 Self-Assembly of Tris(Zn^{2+}-Cyclen) and Trithiocyanurate in Aqueous Solution. *Chem.--Asian J.* **2012**, *7*, 944–956.

(46) SMART V5.054, Bruker Analytical X-ray Systems, Madison, Wi (2001).

(47) Blessing, R. H. An Empirical Correction for Absorption Anisotropy. *Acta Crystallogr.,Sect. A: Found. Crystallogr.* **1995**, *A51*, 33–38.

(48) SAINT+ V6.45, Bruker Analytical X-ray Systems, Madison, WI (2003).

(49) SHELXTL V6.14, Bruker Analytical X-ray Systems, Madison, WI (2000).

(50) PLATON, A Multi-purpose Crystallographic Tool, Utrecht University, Utrecht, The Netherlands, A. L. Spek (2000).

Chapter 3 References

(1) Unden, G.; Bongaerts, J. Alternative Respiratory Pathways of *Escherichia coli*: Energetics and Transcriptional Regulation in Response to Electron Acceptors. *Biochimi. Biophys. Acta, Bioenerg.* **1997**, *1320*, 217–234.

(2) Lehninger, A. L.; Nelson, D. L.; Cox, M. M. *Lehninger Principles of Biochemistry, 4th ed.*; W.H. Freeman & Co.: New York, 2005.

(3) Pac, C.; Ihama, M.; Yasuda, M.; Miyauchi, Y.; Sakurai, H. Tris(2,2'-bipyridine)Ruthenium(2+)-Mediated Photoreduction of Olefins with 1-benzyl-1,4-dihydronicotinamide: A Mechanistic Probe for Electron-Transfer Reactions of NAD(P)H-Model Compounds. *J. Am. Chem. Soc.* **1981**, *103*, 6495–6497.

(4) Adembri, G.; Camparini, A.; Donati, D.; Fusi, S.; Ponticelli, F.; Scotton, M. Photodimerization of N-benzyl-1,4-dihydronicotinamide. *Tetrahedron Lett.* **1983**, *24*, 5399–5402.

(5) Xu, H. J.; Liu, Y. C.; Fu, Y.; Wu, Y. D. Catalytic hydrogenation of α,β-epoxy ketones to form β-hydroxy ketones mediated by an NADH coenzyme model. *Org. Lett.* **2006**, *8*, 3449–3451.

(6) Ouellet, S. G.; Tuttle, J. B.; MacMillan, D. W. C. Enantioselective Organocatalytic Hydride Reduction. *J. Am. Chem. Soc.* **2004**, *127*, 32–33.

(7) Yang, J. W.; Hechavarria Fonseca, M. T.; Vignola, N.; List, B. Metal-Free, Organocatalytic Asymmetric Transfer Hydrogenation of α,β-Unsaturated Aldehydes. *Angew. Chem. Int. Ed.* **2005**, *44*, 108–110.

(8) Adolfsson, H. Organocatalytic Hydride Transfers: A New Concept in Asymmetric Hydrogenations. *Angew. Chem. Int. Ed.* **2005**, *44*, 3340–3342.

(9) Martin, N. J. A.; List, B. Highly Enantioselective Transfer Hydrogenation of α,β-Unsaturated Ketones. *J. Am. Chem. Soc.* **2006**, *128*, 13368–13369.

(10) Li, G.; Liang, Y.; Antilla, J. C. A Vaulted Biaryl Phosphoric Acid-Catalyzed Reduction of α-Imino Esters: The Highly Enantioselective Preparation of α-Amino Esters. *J. Am. Chem. Soc.* **2007**, *129*, 5830–5831.

(11) Li, G.; Antilla, J. C. Highly Enantioselective Hydrogenation of Enamides Catalyzed by Chiral Phosphoric Acids. *Org. Lett.* **2009**, *11*, 1075–1078.

(12) Fukuzumi, S.; Fujioka, N.; Kotani, H.; Ohkubo, K.; Lee, Y.-M.; Nam, W. Mechanistic Insights into Hydride-Transfer and Electron-Transfer Reactions by a

Manganese(IV)−Oxo Porphyrin Complex. *J. Am. Chem. Soc.* **2009**, *131*, 17127–17134.

(13) Reichenbach-Klinke, R.; Kruppa, M.; König, B. NADH Model Systems Functionalized with Zn(II)-Cyclen as Flavin Binding SiteStructure Dependence of the Redox Reaction within Reversible Aggregates. *J. Am. Chem. Soc.* **2002**, *124*, 12999–13007.

(14) Koizumi, T.; Tanaka, K. Reversible Hydride Generation and Release from the Ligand of $[Ru(pbn)(bpy)_2](PF_6)_2$ Driven by a pbn-Localized Redox Reaction. *Angew. Chem. Int. Ed.* **2005**, *44*, 5891–5894.

(15) Polyansky, D.; Cabelli, D.; Muckerman, J.; Fujita, E.; Koizumi, T. A.; Fukushima, T.; Wada, T.; Tanaka, K. Photochemical and Radiolytic Production of an Organic Hydride Donor with a RuII Complex Containing an NAD+ Model Ligand. *Angew. Chem. Int. Ed.* **2007**, *46*, 4169–4172.

(16) Tanaka, K.; Ooyama, D. Multi-electron reduction of CO_2 via Ru-CO_2, -C(O)OH, -CO, -CHO, and -CH_2OH species. **2002**, *226*, 211–218.

(17) Carelli, V.; Liberatore, F.; Scipione, L.; Di Rienzo, B.; Tortorella, S. Dithionite Adducts of Pyridinium Salts: Regioselectivity of Formation and Mechanisms of Decomposition. *Tetrahedron* **2005**, *61*, 10331–10337.

(18) Zhu, X.-Q.; Tan, Y.; Cao, C.-T. Thermodynamic Diagnosis of the Properties and Mechanism of Dihydropyridine-Type Compounds as Hydride Source in Acetonitrile with "Molecule ID Card." *J. Phys. Chem. B* **2010**, *114*, 2058–2075.

(19) Ray, M.; Hammes, B. S.; Yap, G. P. A.; Rheingold, A. L.; Borovik, A. S. Structure and Physical Properties of Trigonal Monopyramidal Iron(II), Cobalt(II), Nickel(II), and Zinc(II) Complexes. *Inorg. Chem.* **1998**, *37*, 1527–1532.

(20) Lucas, R. L.; Zart, M. K.; Murkerjee, J.; Sorrell, T. N.; Powell, D. R.; Borovik, A. S. A Modular Approach toward Regulating the Secondary Coordination Sphere of Metal Ions: Differential Dioxygen Activation Assisted by Intramolecular Hydrogen Bonds. *J. Am. Chem. Soc.* **2006**, *128*, 15476–15489.

(21) Ellis, W. W.; Raebiger, J. W.; Curtis, C. J.; Bruno, J. W.; DuBois, D. L. Hydricities of BzNADH, $C_5H_5Mo(PMe_3)(CO)_2H$, and $C_5Me_5Mo(PMe_3)(CO)_2H$ in Acetonitrile. *J. Am. Chem. Soc.* **2004**, *126*, 2738–2743.

(22) Curtis, C. J.; Miedaner, A.; Ellis, W. W.; DuBois, D. L. Measurement of the Hydride Donor Abilities of $[HM(diphosphine)_2]^+$ Complexes (M = Ni, Pt) by Heterolytic Activation of Hydrogen. *J. Am. Chem. Soc.* **2002**, *124*, 1918–1925.

(23) Frisch, M. J.; Trucks, G. W.; Schlegel, H. B.; Scuseria, G. E.; Robb, M. A.; Cheeseman, J. R.; Scalmani, G.; Barone, V.; Mennucci, B.; Petersson, G. A.; Nakatsuji, H.; Caricato, M.; Li, X.; Hratchian, H. P.; Izmaylov, A. F.; Bloino, J.; Zheng, G.; Sonnenberg, J. L.; Hada, M.; Ehara, M.; Toyota, K.; Fukuda, R.; Hasegawa, J.; Ishida, M.; Nakajima, T.; Honda, Y.; Kitao, O.; Nakai, H.; Vreven, T.; Montgomery, J. A.; Jr; Peralta, J. E.; Ogliaro, F.; Bearpark, M.; Heyd, J. J.; Brothers, E.; Kudin, K. N.; Staroverov, V. N.; Kobayashi, R.; Normand, J.; Raghavachari, K.; Rendell, A.; Burant, J. C.; Iyengar, S. S.; Tomasi, J.; Cossi, M.; Rega, N.; Millam, J. M.; Klene, M.; Knox, J. E.; Cross, J. B.; Bakken, V.; Adamo, C.; Jaramillo, J.; Gomperts, R.; Stratmann, R. E.; Yazyev, O.; Austin, A. J.; Cammi, R.; Pomelli, C.; Ochterski, J. W.; Martin, R. L.; Morokuma, K.; Zakrzewski, V. G.; Voth, G. A.; Salvador, P.; Dannenberg, J. J.; Dapprich, S.; Daniels, A. D.; Farkas, O.; Foresman, J. B.; Ortiz, J. V.; Cioslowski, J.; Fox, D. J. Gaussian09, Revision A1.

(24) Klamt, A.; Sch rmann, G. COSMO: A New Approach to Dielectric Screening in Solvents with Explicit Expressions for the Screening Energy and its Gradient. *J. Chem. Soc., Perkin Trans. 2* **1993**, 799.

(25) Steffens, J. J.; Chipman, D. M. Reactions of Dihydronicotinamides. I. Evidence for an Intermediate in the Reduction of Trifluoroacetophenone by 1-substituted Dihydronicotinamides. *J. Am. Chem. Soc.* **1971**, *93*, 6694–6696.

(26) Abeles, R. H.; Hutton, R. F.; Westheimer, F. H. The Reduction of Thioketones by a Model for a Coenzyme. *J. Am. Chem. Soc.* **1957**, *79*, 712–716.

(27) SMART V5.054, Bruker Analytical X-ray Systems, Madison, Wi (2001).

(28) Blessing, R. H. An Empirical Correction for Absorption Anisotropy. *Acta Crystallogr.,Sect. A: Found. Crystallogr.* **1995**, *A51*, 33–38.

(29) SAINT+ V6.45, Bruker Analytical X-ray Systems, Madison, WI (2003).

(30) SHELXTL V6.14, Bruker Analytical X-ray Systems, Madison, WI (2000).

(31) Spek, A. L. Single-Crystal Structure Validation with the Program PLATON. *J. Appl. Crystallogr.* **2003**, *36*, 7–13.

Chapter 4 References

(1) Benson, E. E.; Kubiak, C. P.; Sathrum, A. J.; Smieja, J. M. Electrocatalytic and homogeneous approaches to conversion of CO2 to liquid fuels. *Chem. Soc. Rev.* **2009**, *38*, 89–99.

(2) Dempsey, J. L.; Esswein, A. J.; Manke, D. R.; Rosenthal, J.; Soper, J. D.; Nocera, D. G. Molecular Chemistry of Consequence to Renewable Energy. *Inorg. Chem.* **2005**, *44*, 6879–6892.

(3) Tolman, W. B., *Activation of Small Molecules*. Wiley-VCH: Weinheim, 2006.

(4) Einsle, O.; Tezcan, F. A.; Andrade, S. L. A.; Schmid, B.; Yoshida, M.; Howard, J. B.; Rees, D. C. Nitrogenase MoFe-Protein at 1.16 Å Resolution: A Central Ligand in the FeMo-Cofactor. *Science* **2002**, *297*, 1696–1700.

(5) Mayer, S. M.; Lawson, D. M.; Gormal, C. A.; Roe, S. M.; Smith, B. E. New Insights into Structure-function Relationships in Nitrogenase: A 1.6 Å Resolution X-ray Crystallographic Study of *Klebsiella pneumoniae* MoFe-protein. *J. Mol. Biol.* **1999**, *292*, 871–891.

(6) Peters, J. W.; Stowell, M. H. B.; Soltis, S. M.; Finnegan, M. G.; Johnson, M. K.; Rees, D. C. Redox-Dependent Structural Changes in the Nitrogenase P-Cluster. *Biochemistry* **1997**, *36*, 1181–1187.

(7) Huniar, U.; Ahlrichs, R.; Coucouvanis, D. Density Functional Theory Calculations and Exploration of a Possible Mechanism of N_2 Reduction by Nitrogenase. *J. Am. Chem. Soc.* **2004**, *126*, 2588–2601.

(8) Siegbahn, P. E. M. Theoretical Models for the Oxygen Radical Mechanism of Water Oxidation and of the Water Oxidizing Complex of Photosystem II. *Inorg. Chem.* **2000**, *39*, 2923–2935.

(9) Bullock, R. M., *Catalysis Without Precious Metals*. Wiley-VCH: Weinheim, Germany, 2010.

(10) Stephan, D. W. Early-Late Heterobimetallics. *Coord. Chem. Rev.* **1989**, *95*, 41–107.

(11) Wheatley, N.; Kalck, P. Structure and Reactivity of Early-Late Heterobimetallic Complexes. *Chem. Rev.* **1999**, *99*, 3379–3420.

(12) Gade, L. H. Highly Polar Metal-Metal Bonds in "Early-Late" Heterodimetallic Complexes. *Angew. Chem. Int. Ed.* **2000**, *39*, 2658–2678.

(13) Cotton, F. A.; Murillo, C. A.; Walton, R. A., *Multiple Bonds Between Metal Atoms*. 3rd ed. Springer: New York, 2005.

(14) Collman, J. P.; Boulatov, R. Heterodinuclear Transition-Metal Complexes with Multiple Metal–Metal Bonds. *Angew. Chem. Int. Ed.* **2002**, *41*, 3948–3961.

(15) Kuppuswamy, S.; Powers, T. M.; Johnson, B. M.; Bezpalko, M. W.; Brozek, C. K.; Foxman, B. M.; Berben, L. A.; Thomas, C. M. Metal–Metal Interactions in C_3-Symmetric Diiron Imido Complexes Linked by Phosphinoamide Ligands. *Inorg. Chem.* **2012**, *52*, 4802-4811.

(16) Harris, T. D.; Betley, T. A. Multi-Site Reactivity: Reduction of Six Equivalents of Nitrite To Give an Fe6 (NO) 6 Cluster with a Dramatically Expanded Octahedral Core. *J. Am. Chem. Soc.* **2011**, *133*, 13852–13855.

(17) Cotton, F. A.; Daniels, L. M.; Murillo, C. A. Divalent Iron Formamidinato complexes: A Highly Distorted Dinuclear Compound. *Inorg. Chim Acta.* **1994**, *224*, 5–9.

(18) Cotton, F. A.; Daniels, L. M.; Matonic, J. H.; Murillo, C. A. Highly Distorted Diiron (II, II) Complexes Containing Four Amidinate Ligands. A Long and Short Metal-Metal Distance. *Inorg. Chim Acta.* **1997**, *256*, 277–282.

(19) Klose, A. Magnetic Properties Diagnostic for the Existence of Iron(II)-Iron(II) Bonds in Dinuclear Complexes Which Derive from Stepwise Insertion Reactions on Unsupported Iron-Aryl Bonds. *J. Am. Chem. Soc.* **2001**, 1–13.

(20) Fohlmeister, L.; Liu, S.; Schulten, C.; Moubaraki, B.; Stasch, A.; Cashion, J. D.; Murray, K. S.; Gagliardi, L.; Jones, C. Low-Coordinate Iron(I) and Manganese(I) Dimers: Kinetic Stabilization of an Exceptionally Short Fe-Fe Multiple Bond. *Angew. Chem. Int. Ed.* **2012**, *51*, 8294–8298.

(21) Zall, C. M.; Zherebetskyy, D.; Dzubak, A. L.; Bill, E.; Gagliardi, L.; Lu, C. C. A Combined Spectroscopic and Computational Study of a High-Spin S= 7/2 Diiron Complex with a Short Iron–Iron Bond. *Inorg. Chem.* **2012**, *51*, 728–736.

(22) Zhao, Q.; Harris, T. D.; Betley, T. A. $[(^{H}L)_2Fe_6(NCMe)_m]^{n+}$ (m= 0, 2, 4, 6; n= −1, 0, 1, 2, 3, 4, 6): An Electron-Transfer Series Featuring Octahedral Fe_6 Clusters Supported by a Hexaamide Ligand Platform. *J. Am. Chem. Soc.* **2011**, *133*, 8293–8306.

(23) Eames, E. V.; Harris, T. D.; Betley, T. A. Modulation of Magnetic Behavior via Ligand-Field Effects in the Trigonal Clusters $(^{Ph}L)Fe_3L^*_3$ (L* = thf, py,

PMe$_2$Ph). *Chem. Sci.* **2012**, *3*, 407.

(24) Gade, L. H. "Strangelove" in Cluster Chemistry: A New Class of Open-Shell Transition Metal Clusters. *Angew. Chem. Int. Ed.* **1996**, *35*, 2089–2090.

(25) Whittlesey, B. R. Xenophilic Transition Metal Clusters. *Coord. Chem. Rev.* **2000**, *206*, 395–418.

(26) Krogman, J. P.; Foxman, B. M.; Thomas, C. M. Activation of CO_2 by a Heterobimetallic Zr/Co Complex. *J. Am. Chem. Soc.* **2011**, *133*, 14582–14585.

(27) Kuppuswamy, S.; Cooper, B. G.; Bezpalko, M. W.; Foxman, B. M.; Powers, T. M.; Thomas, C. M. Synthesis and Structural Characterization of High Spin M/Cu (M = Mn, Fe) Heterobimetallic and Fe/Cu$_2$Trimetallic Phosphinoamides. *Inorg. Chem.* **2012**, *51*, 1866–1873.

(28) Kuppuswamy, S.; Bezpalko, M. W.; Powers, T. M.; Turnbull, M. M.; Foxman, B. M.; Thomas, C. M. Utilization of Phosphinoamide Ligands in Homobimetallic Fe and Mn Complexes: The Effect of Disparate Coordination Environments on Metal–Metal Interactions and Magnetic and Redox Properties. *Inorg. Chem.* **2012**, *51*, 8225–8240.

(29) Rudd, P. A.; Liu, S.; Planas, N.; Bill, E.; Gagliardi, L.; Lu, C. C. Multiple Metal-Metal Bonds in Iron-Chromium Complexes. *Angew. Chem. Int. Ed.* **2013**, *52*, 4449–4452.

(30) Rudd, P. A.; Liu, S.; Gagliardi, L.; Young, V. G., Jr; Lu, C. C. Metal–Alane Adducts with Zero-Valent Nickel, Cobalt, and Iron. *J. Am. Chem. Soc.* **2011**, *133*, 20724–20727.

(31) Rudd, P. A.; Planas, N.; Bill, E.; Gagliardi, L.; Lu, C. C. Dinitrogen Activation at Iron and Cobalt Metallalumatranes. *Eur. J. Inorg. Chem.* **2013**, *accepted.*

(32) Cotton, F. A.; Daniels, L. M.; Matonic, J. H.; Murillo, C. A. Highly Distorted Diiron (II, II) Complexes Containing Four Amidinate Ligands. A Long and Short Metal-Metal Distance. *Inorg. Chim. Acta.* **1997**, *256*, 277–282.

(33) Cotton, F. A.; Daniels, L. M.; Falvello, L. R.; Matonic, J. H.; Murillo, C. A. Trigonal-lantern Dinuclear Compounds of Diiron (I, II): The Synthesis and Characterization of Two Highly Paramagnetic Fe$_2$(amidinato)$_3$ Species with Short Metal-Metal Bonds. *Inorg. Chim. Acta.* **1997**, *256*, 269–275.

(34) Hess, C. R.; Weyhermüller, T.; Bill, E.; Wieghardt, K. [{Fe(tim)}$_2$]: An Fe-Fe Dimer Containing an Unsupported Metal-Metal Bond and Redox-Active

N_4Macrocyclic Ligands. *Angew. Chem. Int. Ed.* **2009**, *48*, 3703–3706.

(35) Nguyen, T.; Merrill, W. A.; Ni, C.; Lei, H.; Fettinger, J. C.; Ellis, B. D.; Long, G. J.; Brynda, M.; Power, P. P. Synthesis and Characterization of the Metal(I) Dimers [Ar′MMAr′]: Comparisons with Quintuple-Bonded [Ar′CrCrAr′]. *Angew. Chem. Int. Ed.* **2008**, *47*, 9115–9117.

(36) Cooper, B. G.; Napoline, J. W.; Thomas, C. M. Catalytic Applications of Early/Late Heterobimetallic Complexes. *Catal. Rev.* **2012**, *54*, 1–40.

(37) Thomas, C. M.; Napoline, J. W.; Rowe, G. T.; Foxman, B. M. Oxidative addition across Zr/Co multiple bonds in early/late heterobimetallic complexes. *Chem. Commun.* **2010**, *46*, 5790.

(38) Eames, E. V.; Hernández Sánchez, R.; Betley, T. A. Metal Atom Lability in Polynuclear Complexes. *Inorg. Chem.* **2013**, *52*, 5006–5012.

(39) Pauling, L. Atomic radii and interatomic distances in metals. *J. Am. Chem. Soc.* **1947**, *69*, 542–553.

(40) Pauling, L. *The Nature of the Chemical Bond*; 3rd ed. Cornell University Press: Ithaca, NY, 1960.

(41) Greenwood, B. P.; Rowe, G. T.; Chen, C.-H.; Foxman, B. M.; Thomas, C. M. Metal−Metal Multiple Bonds in Early/Late Heterobimetallics Support Unusual Trigonal Monopyramidal Geometries at both Zr and Co. *J. Am. Chem. Soc.* **2010**, *132*, 44–45.

(42) Zall, C. M.; Clouston, L. J.; Young, V. G., Jr; Ding, K.; Kim, H. J.; Zherebetskyy, D.; Chen, Y.-S.; Bill, E.; Gagliardi, L.; Lu, C. C. Mixed-Valent Dicobalt and Iron-Cobalt Complexes with High-Spin Configurations and Short M-Co Bonds. *Inorg. Chemistry* **2013**, *submitted*.

(43) Freedman, D. E.; Han, T. H.; Prodi, A.; Müller, P.; Huang, Q.-Z.; Chen, Y.-S.; Webb, S. M.; Lee, Y. S.; McQueen, T. M.; Nocera, D. G. Site Specific X-ray Anomalous Dispersion of the Geometrically Frustrated Kagomé Magnet, Herbertsmithite, $ZnCu_3(OH)_6Cl_2$. *J. Am. Chem. Soc.* **2010**, *132*, 16185–16190.

(44) Toby, B. H.; Dreele, Von, R. B. GSAS-II: The Genesis of a Modern Open-Source All Purpose Crystallography Software Package. *J. Appl. Crystallogr.* **2013**, *46*, 544–549.

(45) Betley, T. A.; Peters, J. C. The Strong-Field Tripodal Phosphine Donor, $[PhB(CH_2PiPr_2)_3]^-$, Provides Access to Electronically and Coordinatively Unsaturated

Transition Metal Complexes. *Inorg. Chem.* **2003**, *42*, 5074–5084.

(46) Evans, D. J.; Hughes, D. L.; Silver, J. Low-coordinate Homoleptic iron(II) Thiolates Revisited. *Inorg. Chem.* **1997**, *36*, 747–748.

(47) Sanakis, Y.; Power, P. P.; Stubna, A.; Münck, E. Mössbauer Study of the Three-Coordinate Planar Fe(II) Thiolate Complex $[Fe(SR)_3]^-$ (R = C_6H_2-2,4,6-tBu_3): Model for the Trigonal Iron Sites of the $MoFe_7S_9$:Homocitrate Cofactor of Nitrogenase. *Inorg. Chem.* **2002**, *41*, 2690–2696.

(48) Andres, H.; Bominaar, E. L.; Smith, J. M.; Eckert, N. A.; Holland, P. L.; Münck, E. Planar Three-Coordinate High-Spin Fe IIComplexes with Large Orbital Angular Momentum: Mössbauer, Electron Paramagnetic Resonance, and Electronic Structure Studies. *J. Am. Chem. Soc.* **2002**, *124*, 3012–3025.

(49) *Mössbauer spectroscopy*; Dickson, D. P. E.; Berry, F. J., Eds. Cambridge University Press: Cambridge, 2009.

(50) Perdew, J. Density-Functional Approximation for the Correlation Energy of the Inhomogeneous Electron Gas. *Phys. Rev. B* **1986**, *33*, 8822–8824.

(51) Schäfer, A.; Horn, H.; Ahlrichs, R. Fully optimized contracted Gaussian basis sets for atoms Li to Kr. *J. Chem. Phys.* **1992**, *97*, 2571.

(52) Schäfer, A.; Huber, C.; Ahlrichs, R. Fully Optimized Contracted Gaussian Basis Sets of Triple Zeta Valence Quality for Atoms Li to Kr. *J. Chem. Phys.* **1994**, *100*, 5829.

(53) Weigend, F.; Ahlrichs, R. Balanced Basis Sets of Split Valence, Triple Zeta Valence and Quadruple Zeta Valence Quality for H to Rn: Design and Assessment of Accuracy. *Phys. Chem. Chem. Phys.* **2005**, *7*, 3297–3305.

(54) Ahlrichs, R.; Bär, M.; Häser, M.; Horn, H.; Kölmel, C. Electronic structure Calculations on Workstation Computers: The Program System Turbomole. *Chem. Phys. Lett.* **1989**, *162*, 165–169.

(55) Roos, B. O.; Taylor, P. R.; Si gbahn, P. E. M. A Complete Active Space SCF Method (CASSCF) Using a Density Matrix Formulated Super-CI Approach. *Chem. Phys.* **1980**, *48*, 157–173.

(56) Andersson, K.; Malmqvist, P.-A.; Roos, B. O. Second-Order Perturbation Theory with a Complete Active Space Self-Consistent Field Reference Function. *J. Chem. Phys.* **1992**, *96*, 1218.

(57) SMART V5.054, Bruker Analytical X-ray Systems, Madison, Wi (2001).

(58) Blessing, R. H. An Empirical Correction for Absorption Anisotropy. *Acta Crystallogr.,Sect. A: Found. Crystallogr.* **1995**, *A51*, 33–38.

(59) SAINT+ V6.45, Bruker Analytical X-ray Systems, Madison, WI (2003).

(60) SHELXTL V6.14, Bruker Analytical X-ray Systems, Madison, WI (2000).

(61) Spek, A. L. Single-Crystal Structure Validation with the Program PLATON. *J. Appl. Crystallogr.* **2003**, *36*, 7–13.

(62) Weast, R. C.; Astle, M. J. *CRC Handbook of Chemistry and Physics*; CRC Press Inc: Boca Ranton, FL, 1979.

(63) O'Conner, C. J. *Magnetochemistry--Advances in theory and experimentation*; Lippard, S. J., Ed. John Wiley & Sons, Ltd.: New York, 1982; Vol. 29, pp. 203–283.

(64) Bill, E. julX.

(65) Aquilante, F.; De Vico, L.; FerrÃ, N.; Ghigo, G.; Malmqvist, P.-Ã. K.; NeogrÃ dy, P.; Pedersen, T. B.; PitonÌ Ã k, M.; Reiher, M.; Roos, B. R. O.; Serrano-AndrÃ s, L.; Urban, M.; Veryazov, V.; Lindh, R. MOLCAS 7: The Next Generation. *J. Comput. Chem.* **2010**, *31*, 224–247.

(66) Roos, B. O.; Lindh, R.; Malmqvist, P.-A.; Veryazov, V.; Widmark, P.-O. Main Group Atoms and Dimers Studied with a New Relativistic ANO Basis Set. *J. Phys. Chem. A* **2004**, *108*, 2851–2858.

(67) Roos, B. O.; Lindh, R.; Malmqvist, P.-A.; Veryazov, V.; Widmark, P.-O. New Relativistic ANO Basis Sets for Transition Metal Atoms. *J. Phys. Chem. A* **2005**, *109*, 6575–6579.

(68) Hess, B. Relativistic Electronic-Structure Calculations Employing a Two-Component No-Pair Formalism with External-Field Projection Operators. *Phys. Rev. A* **1986**, *33*, 3742–3748.

(69) Aquilante, F.; Pedersen, T. B.; Lindh, R.; Roos, B. O.; Sánchez de Merás, A.; Koch, H. Accurate *ab initio* Density Fitting for Multi-Configurational Self-Consistent Field Methods. *J. Chem. Phys.* **2008**, *129*, 024113.

(70) Aquilante, F.; Pedersen, T. B.; Lindh, R. Low-Cost Evaluation of the Exchange Fock Matrix from Cholesky and Density Fitting Representations of the Electron

Repulsion Integrals. *J. Chem. Phys.* **2007**, *126*, 194106–194106–11.

(71) Aquilante, F.; Malmqvist, P.-A.; Pedersen, T. B.; Ghosh, A.; Roos, B. O. Cholesky Decomposition-Based Multiconfiguration Second-Order Perturbation Theory (CD-CASPT2): Application to the Spin-State Energetics of Co III(diiminato)(NPh). *J. Chem. Theory Comput.* **2008**, *4*, 694–702.

(72) Roos, B. O.; Borin, A. C.; Gagliardi, L. Reaching the Maximum Multiplicity of the Covalent Chemical Bond. *Angew. Chem. Int. Ed.* **2007**, *46*, 1469–1472.

(73) Brynda, M.; Gagliardi, L.; Roos, B. O. Analysing the chromium–chromium multiple bonds using multiconfigurational quantum chemistry. *Chemical Physics Letters* **2009**, *471*, 1–10.

Appendix A

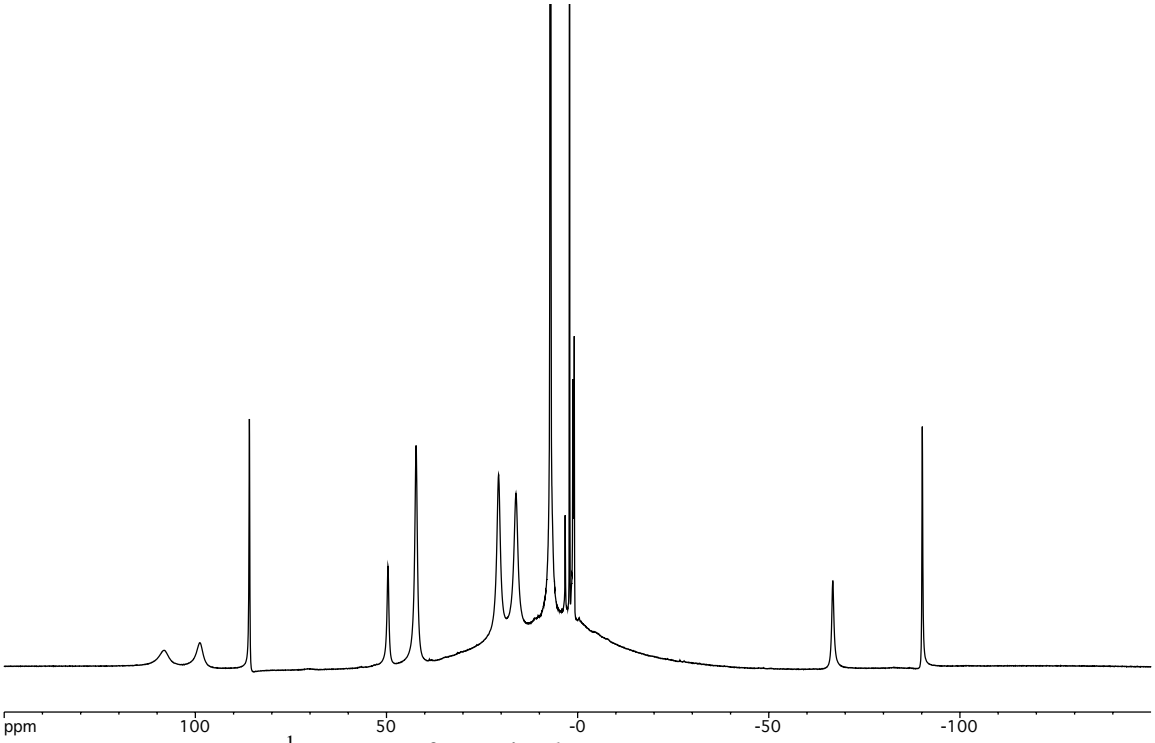

Figure A.1 500 MHz ^{1}H NMR of 1-Br in d_8-THF.

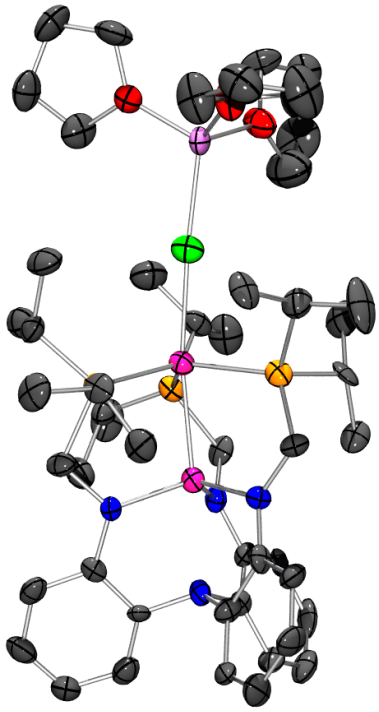

Figure A.2 Solid-state structure of **2-LiCl** at 50 % probability. Atoms are represented as follows: Fe (pink), N (blue), C (grey), P (orange), Cl (green), Li (light purple), O (red).

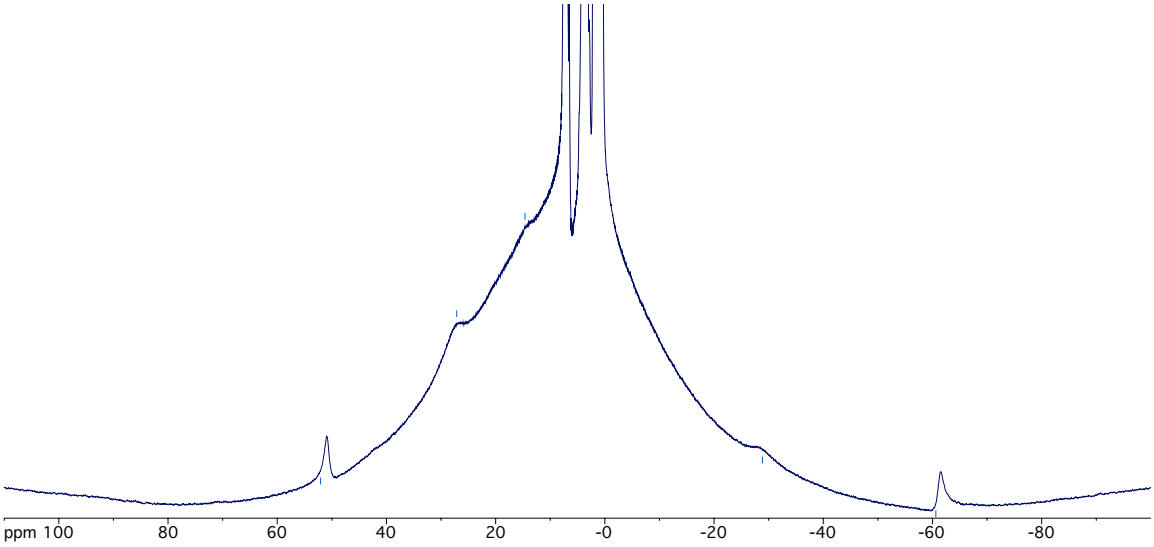

Figure A.3 500 MHz ^{1}H NMR of **2** in C_6D_6.

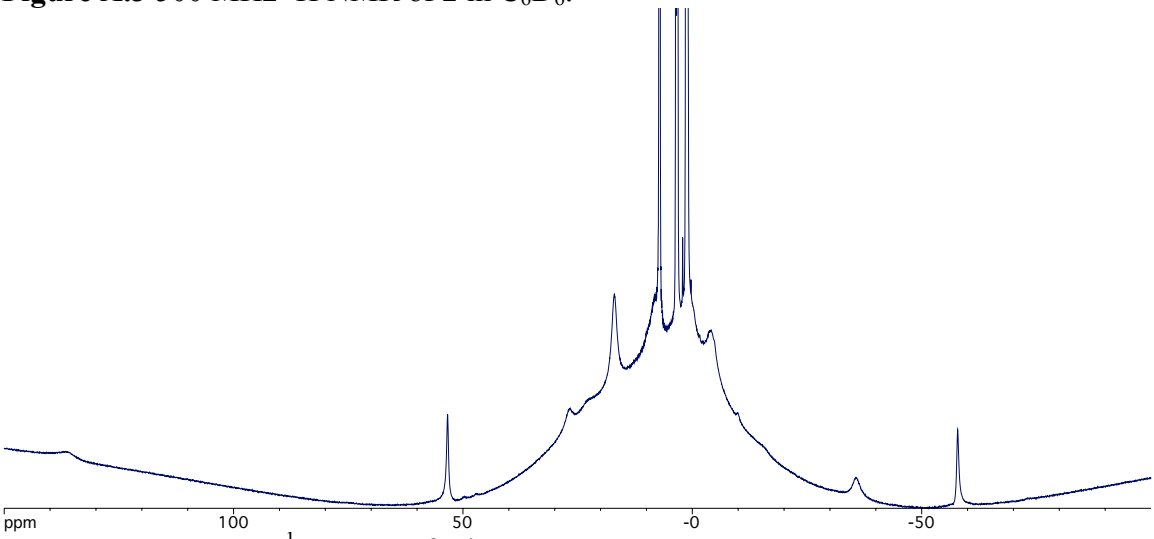

Figure A.4 500 MHz ^{1}H NMR of **4** in C_6D_6.

Table A.1 Crystallographic information for **2-LiCl**.

	2-LiCl
chemical formula	$C_{55}H_{92}N_4P_3Fe_2O_4LiCl$
formula weight	1120.33
crystal system	monoclinic
space group	$P2_1$
a (Å)	15.3390(16)
b (Å)	22.659(2)
c (Å)	17.0592(18)
α (deg)	90
β (deg)	91.217(2)
γ (deg)	90
V (Å^3)	5927.9(11)
Z	6
D_{calcd} (g cm^{-3})	1.883
λ (Å), μ (mm^{-1})	0.71073
T (K)	173(2)
Θ range (deg)	1.49 to 25.05
reflns collected	44626
unique reflns	20645
data/restraint/ parameters	20645/1/1195
R_1, wR_2 ($I > 2\sigma(I)$)	0.0751, 0.1267

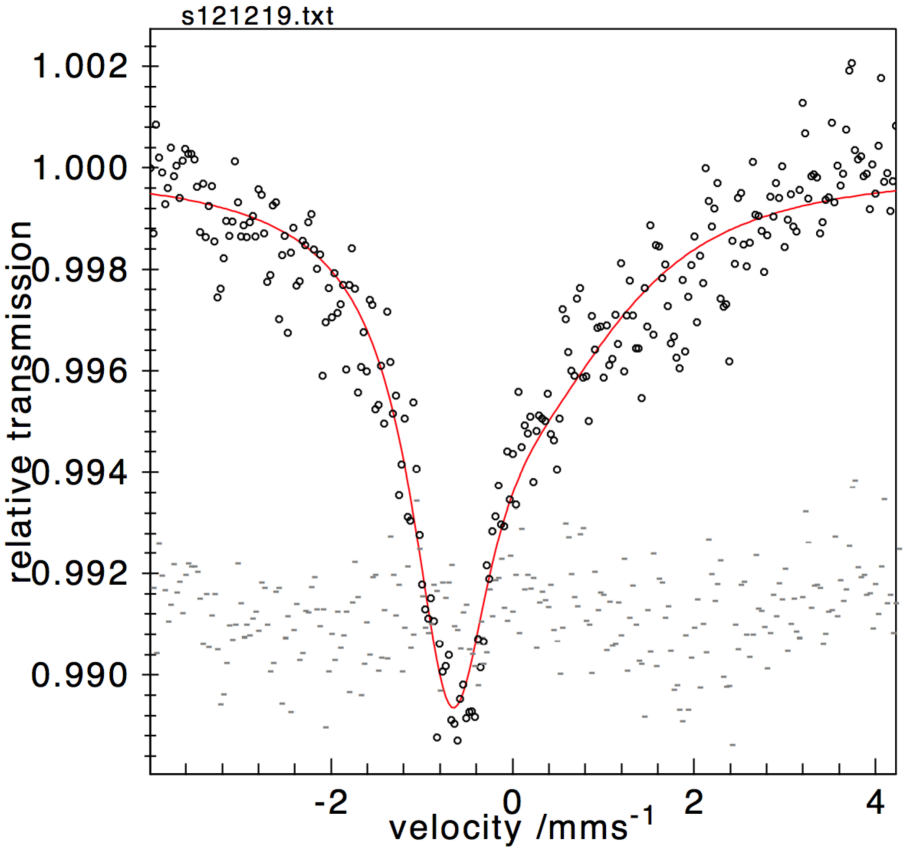

Figure A.5 Initial ^{57}Fe Mossbauer spectrum of ^{iPr}LFeCoCl **3**.

Table A.2 Comparison of bond lengths (Å) and angles (°) for solid-state structure of **3** and DFT optimized FeFeCl structure for nonet ground state.

	^{iPr}LFeFeCl **1**	Nonet
Fe-M, Å	2.6261(6)	2.5214
M-Cl, Å	2.2622(2)	2.2451
Fe–N_{eq}, Å	1.973(2)	2.0006
	1.980(2)	2.0052
	1.963(2)	1.9973
Fe–N_{ax}, Å	2.2653(9)	2.4138
M-P, Å	2.4847(9)	2.3243
	2.4568(9)	2.3040
	2.4610(9)	2.3019
N_{eq}–Fe–N_{eq}, °	114.86(9)	112.76
	117.71(9)	114.84
	116.09(9)	114.62
P–M–P, °	114.57(3)	114.12
	119.41(3)	115.81
	114.19(3)	114.29
M-M-Cl, °	168.80(3)	178.22

Table A.3 Comparison of bond lengths (Å) and angles (°) for solid-state structure of **3** and DFT optimized FeFe structure for octet ground state.

	^{iPr}LFeFe **2**	Octet
Fe-M, Å	2.3252(2)	2.3955
Fe−N_{eq}, Å	1.9879(1)	1.9874
		1.9879
		1.9858
Fe−N_{ax}, Å	2.2927(2)	2.3180
M-P, Å	2.3656(2)	2.3037
		2.3034
		2.3028
N_{eq}−Fe−N_{eq}, °	116.59(1)	115.72
		116.50
		115.72
P−M−P, °	119.40(5)	117.61
		118.02
		117.41

Table A.4 Comparison of bond lengths (Å) and angles (°) for solid-state structure of **3** and DFT optimized FeCoCl structure for octet ground state.

	^{iPr}LFeCoCl **3**	Octet
Fe-M, Å	2.5899(6)	2.5908
M-Cl, Å	2.2476(9)	2.2056
Fe−N_{eq}, Å	1.968(2)	1.9776
	1.970(2)	1.9783
	1.957(2)	1.9785
Fe−N_{ax}, Å	2.300(3)	2.3788
M-P, Å	2.3671(8)	2.2863
	2.3672(7)	2.2849
	2.4099(8)	2.2851
N_{eq}−Fe−N_{eq}, °	115.62(7)	114.31
	114.27(7)	114.69
	116.97(7)	114.26
P−M−P, °	116.36(2)	112.96
	114.78(2)	113.33
	116.35(2)	113.14
M-M-Cl, °	169.56(3)	179.54

Table A.5 Comparison of bond lengths (Å) and angles (°) for solid-state structure of **3** and DFT optimized FeCo structure for septet ground state.

	^{iPr}LFeCo **4**	Septet
Fe-M, Å	2.2599(4)	2.2973
Fe−N_{eq}, Å	1.9891(4)	1.9791
	1.9751(3)	1.9770
	1.9640(2)	1.9781
Fe−N_{ax}, Å	2.2405(4)	2.2591
M-P, Å	2.3032(4)	2.2407
	2.2945(4)	2.2347
	2.3119(3)	2.2535
N_{eq}−Fe−N_{eq}, °	115.7(2)	115.25
	117.0(2)	120.73
	118.5(2)	115.25
P−M−P, °	117.31(7)	109.95
	120.38(7)	138.23
	122.07(7)	110.46

Table A.6 XYZ coordinates for geometry optimized nonet ground state of ^{iPr}LFeFeCl **1**.

	Atom	X	Y	Z
1	Fe	4.908349	4.013833	17.7419
2	Fe	5.577894	4.084641	15.312054
3	Cl	6.23736	4.169846	13.167726
4	P	4.354836	6.038985	15.606617
5	P	4.315979	2.159572	15.414418
6	P	7.574051	3.970067	16.452581
7	N	4.581922	5.919991	18.240903
8	N	3.226276	2.922882	17.70336
9	N	4.226147	3.919979	20.055411
10	N	6.442089	3.147539	18.690169
11	C	4.596222	6.934865	17.214499
12	H	5.583229	7.45938	17.138739
13	H	3.813868	7.721332	17.360532
14	C	4.754832	7.334478	14.363154
15	C	5.159382	0.626043	15.987499
16	C	3.608898	1.628839	13.799631
17	C	2.81906	2.224966	16.506379
18	H	2.02756	2.770731	15.931576
19	H	2.425708	1.197869	16.71153
20	C	2.326232	3.106374	18.717496
21	C	0.937651	2.79007	18.646779
22	H	0.541804	2.277031	17.757107
23	C	0.062593	3.164922	19.672863
24	H	-1.009324	2.920958	19.582266
25	C	0.528382	3.865139	20.801435
26	H	-0.167822	4.170969	21.59832
27	C	1.900586	4.148091	20.916358
28	H	2.290076	4.677055	21.80075

29	C	2.797483	3.739479	19.921377
30	C	4.971914	2.782235	20.545781
31	C	6.192231	2.471696	19.852108
32	C	7.647856	2.871708	17.944051
33	H	7.705933	1.814487	17.575991
34	H	8.580502	3.065133	18.531125
35	C	8.954533	3.317662	15.42215
36	C	8.283523	5.544675	17.090321
37	C	7.00364	1.432984	20.392267
38	H	7.95892	1.180322	19.906975
39	C	6.581142	0.701001	21.508936
40	H	7.223502	-0.108145	21.895959
41	C	5.346253	0.96875	22.126805
42	H	5.013689	0.379027	22.995747
43	C	4.546084	2.016211	21.636284
44	H	3.581209	2.253108	22.11315
45	C	4.656506	5.215504	20.529961
46	C	4.988232	5.452007	21.86927
47	H	4.973785	4.610332	22.579985
48	C	5.313873	6.748642	22.304518
49	H	5.555099	6.931097	23.363779
50	C	5.304173	7.809399	21.379385
51	H	5.542033	8.83255	21.715902
52	C	5.018464	7.583121	20.027824
53	H	5.055536	8.422336	19.31635
54	C	4.727641	6.271065	19.554199
55	C	2.521557	5.932747	15.486597
56	H	9.325745	5.403205	17.453047
57	H	8.279733	6.304877	16.280366
58	H	7.649136	5.908013	17.92609
59	H	9.903054	3.25325	15.999988
60	H	8.682408	2.312237	15.038553
61	H	9.088113	3.982733	14.544173
62	H	5.839578	7.563584	14.410821
63	H	4.544174	6.931089	13.351061
64	H	4.166403	8.263389	14.532087
65	H	2.242115	5.405804	14.549596
66	H	2.141412	5.351071	16.352736
67	H	2.056719	6.943172	15.490732
68	H	5.4014	0.735575	17.065592
69	H	4.517391	-0.270747	15.842181
70	H	6.105493	0.492565	15.421302
71	H	4.439525	1.49982	13.07487
72	H	3.032172	0.681576	13.888076
73	H	2.948804	2.431628	13.409382

Table A.7 XYZ coordinates for geometry optimized octet ground state of ^{iPr}LFeFe **2**.

	Atom	X	Y	Z
1	Fe	-0.0236	9.161	14.7772
2	Fe	-0.0049	9.1618	12.3818
3	N	0.0109	9.1592	10.0639
4	C	-0.8796	6.9724	10.7545
5	C	-1.1882	5.6219	10.4364
6	H	-1.6951	4.9876	11.1807
7	C	-0.8255	5.0693	9.1972
8	H	-1.0707	4.0143	8.9864
9	C	0.1528	7.1832	8.5287
10	H	0.6957	7.8001	7.7948
11	C	-0.2273	7.7567	9.7448
12	N	-1.125	7.5723	11.9712
13	C	-0.1392	5.8341	8.2429
14	H	0.1667	5.3939	7.2805
15	C	-1.8053	6.8237	12.9941
16	H	-1.2373	5.9283	13.3676
17	H	-2.8168	6.4539	12.682
18	P	-1.9766	7.9963	14.4081
19	C	-3.4607	8.9764	13.9449
20	C	-2.6347	6.9227	15.7619
21	C	2.3439	9.4823	10.7772
22	C	3.671	9.8878	10.4703
23	H	4.4663	9.7653	11.2225
24	C	3.9807	10.4736	9.232
25	H	5.0195	10.7863	9.0302
26	C	1.6671	10.2648	8.5423
27	H	0.8684	10.4259	7.8006
28	C	1.3483	9.6531	9.7575
29	N	1.9353	8.974	11.9917
30	C	2.9848	10.6831	8.2674
31	H	3.2233	11.1642	7.3054
32	C	2.9126	8.7678	13.0276
33	H	3.4003	9.7106	13.3979
34	H	3.7413	8.0729	12.7314
35	P	1.964	8.0477	14.437
36	C	3.2044	8.0243	15.8076
37	C	-1.4327	11.0297	10.7504
38	C	-2.4392	11.9799	10.428
39	H	-2.7302	12.739	11.1709
40	C	-3.095	11.9464	9.1862
41	H	-3.8792	12.6925	8.9721
42	C	-1.7645	10.0318	8.5236
43	H	-1.5042	9.2518	7.7903
44	C	-1.0808	10.0706	9.7418
45	N	-0.7988	10.9351	11.9712
46	C	-2.7799	10.966	8.2341
47	H	-3.3111	10.9249	7.2699
48	C	-1.1099	11.897	12.9949
49	H	-2.1756	11.8626	13.3513

50	H	-0.9074	12.9572	12.6916
51	P	-0.0379	11.4366	14.4244
52	C	1.5692	12.2203	13.9969
53	C	-0.6547	12.5335	15.7785
54	H	1.9051	11.8056	13.0231
55	H	1.4632	13.324	13.912
56	H	2.3291	11.9816	14.7705
57	H	-0.6493	13.602	15.4682
58	H	-1.6917	12.242	16.0492
59	H	-0.0147	12.4179	16.6786
60	H	-1.8435	6.2228	16.1044
61	H	-2.9401	7.5518	16.6248
62	H	-3.5135	6.3334	15.4178
63	H	-3.2478	9.4914	12.9844
64	H	-4.3493	8.3186	13.8218
65	H	-3.6728	9.7387	14.724
66	C	1.8554	6.2691	13.9871
67	H	4.1323	7.4908	15.5035
68	H	3.4651	9.0658	16.0924
69	H	2.7737	7.5185	16.6975
70	H	2.8685	5.8209	13.8875
71	H	1.2827	5.7134	14.7595
72	H	1.3201	6.1932	13.0175

Table A.8 XYZ coordinates for geometry optimized octet ground state ^{iPr}LFeCoCl **3**.

	Atom	X	Y	Z
1	Fe	2.4041	12.1038	5.7885
2	Co	1.671	12.1888	8.272
3	P	2.9329	10.2928	8.0724
4	P	-0.2681	12.1163	7.0656
5	P	2.867	14.1043	7.9228
6	Cl	1.0555	12.246	10.3892
7	N	0.8836	11.2236	4.8791
8	N	4.0661	11.0308	5.8201
9	N	3.0725	12.019	3.5071
10	N	2.6715	14.0017	5.3012
11	C	-0.3301	10.9743	5.6129
12	H	-0.414	9.9282	6.0111
13	H	-1.2567	11.1687	5.0154
14	C	4.4653	10.3841	7.0431
15	H	5.2324	10.9565	7.6292
16	H	4.8777	9.3552	6.8862
17	C	4.9903	11.2419	4.8215
18	C	4.5133	11.8306	3.6055
19	C	2.6469	13.3179	3.0044
20	C	2.5132	14.358	3.9807
21	C	2.6063	15.0072	6.3296
22	H	1.612	15.5232	6.3957
23	H	3.3805	15.8083	6.2159
24	C	2.189	15.6604	3.5181
25	H	2.0925	16.4881	4.2382
26	C	1.956	15.9005	2.1539
27	H	1.6926	16.9197	1.8242
28	C	2.0351	14.8594	1.2175
29	H	1.8313	15.045	0.1509
30	C	2.3884	13.5662	1.6545
31	H	2.457	12.7359	0.9337
32	C	2.3262	10.8772	2.9975
33	C	2.718	10.1494	1.8719
34	H	3.6627	10.4083	1.3668
35	C	1.9222	9.0906	1.3892
36	H	2.2405	8.5208	0.5017
37	C	0.723	8.781	2.0469
38	H	0.0843	7.9628	1.673
39	C	0.329	9.4873	3.1949
40	H	-0.6024	9.2061	3.7111
41	C	1.1347	10.5341	3.7146
42	C	5.3999	12.1857	2.5862
43	H	5.008	12.6778	1.6819
44	C	6.7803	11.928	2.7136
45	H	7.4722	12.2133	1.9054
46	C	7.255	11.3007	3.8748
47	H	8.3309	11.0829	3.9834
48	C	6.3787	10.9613	4.9189
49	H	6.7795	10.4959	5.8331
50	C	2.718	10.1494	1.8719
51	H	-1.8001	12.2543	8.9541
52	H	-2.6031	11.4676	7.5227
53	H	-1.4164	10.5529	8.5507
54	C	-0.9063	13.6907	6.3675
55	H	-1.9513	13.5696	6.0064
56	H	-0.8779	14.4854	7.1426
57	H	-0.2564	13.99	5.5184

58	C	2.4516	15.3666	9.1923
59	H	2.6946	14.9621	10.1964
60	H	3.0125	16.3112	9.0172
61	H	1.3611	15.5696	9.1673
62	C	4.6972	14.0026	8.0375
63	H	5.149	15.0182	8.0621
64	H	4.9851	13.4522	8.9582
65	H	5.0791	13.4532	7.1515
66	C	3.5572	9.7505	9.7132
67	H	2.6935	9.546	10.3787
68	H	4.1895	8.84	9.6198
69	H	4.1465	10.5703	10.1734
70	C	2.1068	8.7811	7.4356
71	H	2.7519	7.8867	7.5789
72	H	1.1454	8.627	7.9697
73	H	1.9021	8.917	6.3528

Table A.9 XYZ coordinates geometry optimized septet ground state of ^{iPr}LFeCo **4**.

	Atom	X	Y	Z
1	CO	1.6621	0.0717	3.7873
2	FE	-0.6273	0.1013	3.5988
3	P	1.5317	2.1964	4.487
4	P	1.6289	0.0009	1.554
5	P	1.4181	-1.998	4.6446
6	N	-2.8849	0.0529	3.5308
7	N	-1.001	2.042	3.7032
8	N	-0.8871	-0.7187	1.8187
9	N	-1.0025	-1.0844	5.137
10	C	-3.2311	1.3907	3.0502
11	C	-4.4616	1.6771	2.4525
12	H	-5.1834	0.8595	2.2971
13	C	-4.7757	2.9847	2.0332
14	H	-5.7493	3.1966	1.5633
15	C	-3.8314	4.0039	2.2228
16	H	-4.0612	5.0356	1.906
17	C	-2.5791	3.7276	2.7933
18	H	-1.8466	4.5424	2.9015
19	C	-2.2338	2.4115	3.2061
20	C	0.0315	3.0418	3.8097
21	H	-0.2413	3.8942	4.4848
22	H	0.3214	3.4976	2.8249
23	C	-3.1485	-1.0341	2.5847
24	C	-4.3589	-1.7318	2.5629
25	H	-5.1274	-1.4915	3.3148
26	C	-4.596	-2.7392	1.606
27	H	-5.5557	-3.2799	1.5988
28	C	-3.5968	-3.0355	0.6671
29	H	-3.7697	-3.8142	-0.0952
30	C	-2.3626	-2.3665	0.6946
31	H	-1.5838	-2.6369	-0.0355
32	C	-2.0943	-1.3636	1.6658
33	C	0.2161	-1.0356	0.9464
34	H	0.0108	-0.8111	-0.1321
35	H	0.5372	-2.11	0.9946
36	C	-3.2421	-0.235	4.9192
37	C	-2.241	-0.893	5.7113
38	C	-2.5916	-1.2633	7.037
39	H	-1.8513	-1.7727	7.6738
40	C	-3.8555	-0.9508	7.5632
41	H	-4.093	-1.2407	8.6009
42	C	-4.8013	-0.2555	6.7955
43	H	-5.7835	0.0116	7.2168
44	C	-4.4832	0.0963	5.468
45	H	-5.2124	0.6449	4.8508
46	C	0.0098	-1.8287	5.8431
47	H	-0.3386	-2.842	6.1706
48	H	0.4066	-1.3105	6.757
49	C	3.086	-0.706	0.6674
50	H	2.9015	-0.7738	-0.4277
51	H	3.9732	-0.0609	0.8416
52	H	3.3097	-1.7193	1.0625
53	C	1.3586	1.5662	0.6209
54	H	2.1469	2.3051	0.8781
55	H	1.3633	1.3897	-0.4773
56	H	0.3707	1.9783	0.9163
57	C	2.8544	3.4608	4.2539

58	H	2.5538	4.4457	4.6751
59	H	3.7841	3.1216	4.7577
60	H	3.0702	3.5793	3.1711
61	C	1.2398	2.2849	6.3052
62	H	2.0874	1.8189	6.8507
63	H	1.1176	3.3377	6.6442
64	H	0.3132	1.7168	6.5345
65	C	2.7561	-2.7511	5.6693
66	H	2.4076	-3.679	6.1749
67	H	3.6243	-2.9986	5.0223
68	H	3.0929	-2.0239	6.4379
69	C	0.8782	-3.4236	3.62
70	H	1.6423	-3.6507	2.8472
71	H	0.7157	-4.3236	4.2528
72	H	-0.0746	-3.1524	3.1183